β-decay of hadrons in a first principle approach

Dissertation

zur Erlangung des
Doktorgrades der Naturwissenschaften (Dr.rer.nat.)

an der Karl-Franzens-Universität Graz

vorgelegt von
Walid Ahmed Mian

Betreut durch Univ.-Prof. Dipl.-Phys. Dr.rer.nat. Axel Maas

Graz, 2019

Abstract

Inspired by the non-negligible back-coupling between the electroweak and the strong interactions in neutron star mergers, we investigate some particular aspects of the dynamical back-coupling in a first principle study. This always implies the more involved tensor structure of correlation functions since the electroweak interactions break various symmetries of the QCD explicitly, especially C and P. To cope with the symmetry structure and the different scales in the system, we employ the functional methods.

As a first step, we investigate the explicit breaking of the C, P, and flavor symmetry on the simplest objects, namely the quark propagators. While at weak breaking, the qualitative effects have similar trends as in perturbation theory, even moderately strong breakings lead to qualitatively different effects, non-linearly amplified by the strong interaction. This mandates caution with perturbative extrapolation.

In the next step, we investigate the non-perturbative back-coupling at the hadronic level on the example of the weak pion decay. To avoid the additional complexity by the weak gauge bosons, we take an effective low-energy description of the weak interaction. In particular, we formulate the weak pion decay in the combined Dyson-Schwinger/Bethe-Salpeter framework, as well as in the Functional-Renormalization-Group. Since both types of approaches have different systematics, this allows us to control systematic error sources to some extent. We present an approach for accessing properties of bound states and resonances, like mass and decay width, within both frameworks and put them in perspective to each other. In particular, we test our framework for the Functional-Renormalization-Group for a QCD-assisted low-energy quark-meson model. In the end, we discuss the implications of the P-violation for the weak pion decay and outline some aspects for future investigations.

Kurzfassung

Inspiriert durch die nicht vernachlässigbare Rückkopplung zwischen der elektroschwachen und starken Wechselwirkung in Neutronen Stern Fusionen untersuchen wir in dieser Arbeit einige besondere Aspekte der dynamischen Rückkopplung in einer „first principle study". Dies impliziert eine kompliziertere Struktur für die Korrelationsfunktionen, da die elektroschwache Wechselwirkung verschiedene Symmetrien verletzt, insbesondere C und P. Um mit der Symmetriestruktur und den verschiedenen Skalen in unserem System zurechtzukommen, verwenden wir die Funktionalenmethoden.

Im ersten Schritt untersuchen wir die explizite Brechung der C-, P- und Flavorsymmetrie für das einfachste Objekt, nämlich dem Quarkpropagator. Während bei schwacher Brechung die qualitativen Effekte noch die gleiche Richtung aufweisen wie in der Störungstheorie, führt selbst eine moderat stärkere Brechung zu qualitativ anderen Effekten. Dies mahnt uns zur Vorsicht mit störungstheoretischer Extrapolation.

Im nächsten Schritt untersuchen die nicht-störungstheoretische Rückkopplung auf hadronischem Level am Beispiel des schwachen Pionzerfalls. Um zusätzliche Komplikationen durch die schwachen Eichbosonen zu vermeiden, nehmen wir eine Niederenergiebeschreibung der schwachen Wechselwirkung. Insbesondere beschreiben wir den schwachen Pionzerfall in dem kombiniertem Dyson-Schwinger/Bethe-Salpeter Rahmen als auch in der Funktionalen Renormierungs Gruppe. Da die beiden Formulierungen verschiedene Systematiken haben, erlaubt uns dies die systematischen Fehler zu einem gewissem Maße zu kontrollieren. Wir präsentieren eine Vorgehensweise für den Zugriff auf die Eigenschaften von Bindungszuständen und Resonanzen, wie Masse und Zerfallsbreite, in beiden Formulierungen und setzen diese in Verhältnis zueinander. Insbesondere testen wir unsere Vorgehensweise wird für ein QCD-unterstütztes Niederenergiemodell. Zum Abschluss diskutieren wir die Implikationen der Paritätsverletzung für den schwachen Pionzerfall und umreißen einige Aspekte für die zukünftige Forschung.

Acknowledgement

In the name of Allah, the Gracious, the Merciful.

All praise belongs to Allah, who gave me the opportunity and the ability to work on this exciting topic for the last few years.

Using this opportunity, I want to express my sincere gratitude to all the people and organizations individually for their support over the last years in the following.

First of all, I thank my advisor Prof. Dr. Axel Maas, for giving me the opportunity to work on such an inspiring topic for the last years. I am especially thankful for the time, which he took almost every week for the discussions, guidance, and constructive remarks during the research period, as well as during the writing phase of the thesis. Apart from this, I am also very thankful to him for the extended parental leave, especially for patience and forbearance during this time.

Afterward, I want to thank Prof. Dr. Jan M. Pawlowski. I had the opportunity to work with him during my six-month stay abroad at the University of Heidelberg. I am especially grateful for his guidance, helpful remarks, support, hospitality, and the possibility to work under his supervision.

I also want to thank Dr. Hèlios Sanchis-Alepuz for the long discussions, guidance, and helpful remarks on my work from which I learned a lot. I am especially grateful for his patience to go through my code and teach me the details of the numerical implementations in the DSE/BSE framework.

In this regard, I am also very thankful to Dr. Markus Q. Huber for the help and guidance; especially, for the computational implementations in the presence of various symmetry breakings with DoFun.

Besides, I am also very grateful to the working group of Prof. Dr. Jan M. Pawlowski. I had fascinating and fruitful discussions with them; especially, Nicolas Wink, Dr. Anton K. Cyrol, and Dr. Mario Mitter. I am thankful to all of them for the talks, constructive remarks on my work, and especially for the help with the numerical implementations. In this respect, I want to thank Anton Cyrol for his time and help to work with FormTracer. I want to express my special gratitude to Nicolas Wink for providing me the results from our real-time FRG project for this thesis.

I also want to thank Jordi París-Lopéz for long and fruitful discussions during the whole time of my Ph.D. thesis, and especially during the collaboration on the FRG project.

Furthermore, I thank all the members of the doctoral school Graz "Hadrons in Vacuum, Nuclei and Stars", my colleagues, and office roommates for their helpful remarks and fruitful discussions on my study; especially, during doctoral seminars and conferences. I want to mention them here individually: principal investigators: Prof. Dr. Christof Gattringer, Prof. Dr. Reinhard Alkofer, Prof. Dr. Wolfgang Schwaiger and Prof. Dr. Leonid Glozman; (former)

Ph.D. students: Dr. Romain Contant, Dr. Ouraman Hajizadeh, Dr. Pascal Toerek, Dr. Carla Marchis, Dr. Stefan Kofler, Dr. Ana Juricic, Dr. Mario Giuliani, Dr. Christian Rohrhofer, Dr. Adrian Blum, Dr. Milan Vujinovic, Ju-Hyun Jung, Angel Miramontes-Lopez and Marco Catillo; (former) roommates: Dr. Andreas Krassnig, Dr. Padmanath Madanagopalan, Dr. Thomas Hilger and Dr. Maria Gómez-Rocha. In this regard, I am especially thankful to Prof. Dr. Reinhard Alkofer for the long conversations as my mentor for the last few years. I also want to express my special gratitude to Fanny Maetz for taking care of all my bureaucratic works and thereby allowing me to focus on the research during the whole period.

Moreover, I want to thank FWF doctoral school W1203-N16 for their financial support and the University of Graz for the mobility grant at the University of Heidelberg.

I want to express my special gratitude to my friends and family members Faiq Ahmed, Andrew Walker, Mirza Noman Ahmed, and Hasanat Ahmad for proofreading (parts) of this thesis.

Last but not least, I want to express my sincere gratefulness to all the people in my private life, who have inspired me, guided me and made this possible – Starting with the Holy Prophet Muhammad (peace and blessings of Allah be upon him), his Promised Messiah Mirza Ghulam Ahmad (peace be upon him) and his Khalifas (may Allah be pleased with them and be their helper). They are the inspirations of my life and the sources of my success. "O my Lord, always shower blessings on your Prophet and his progeny, in this world and the next." (Jalal-ud-Din Shams: *The Commentary of al-Qaisdah*, Islam International Publications Ltd., U.K., 2013).

In the end, I thank my parents (Momna Naheed Mian and Wasim Ahmed Mian), my sister (Labiba Ahmed Mian), my wife (Saba Nasir), and my children (Talat Walid Mian and Qudsia Walid Mian) for their support, guidance, and patience.

Thanks to you all!

Contents

Chapter 1

Introduction

One of the most remarkable observations of the 21^{st} century is the recent detection of the gravitational waves from a binary black hole merger [1, 2] and was appreciated with the Nobel Prize of physics in 2017. Though gravitational waves were predicted a century ago by Einstein's theory of general relativity, the detection of these was possible in recent years due to the experimental demanding. This has opened a new gate for future investigations of the universe and will substantially increase our fundamental understanding.

Apart from the merger of the binary black holes, binary systems of neutron stars, and a neutron star and black hole are also sources of gravitational waves (see for further details, e.g., [3, 4], and the references therein). Therefore, various investigations have been done in this field over the last years (see, e.g., [5–7] for a review on this topic). The recent successful detection of the gravitational waves from a binary neutron star merger [8] underlines the significance of this researches.

These studies reveal the importance of microphysical details like neutrino physics, magnetic fields, etc., on the binary neutron star merger process and its outcome (see for details, e.g., [9–15]). One of the key ingredients is the neutrino back-coupling because a fraction of gravitational binding energy is released in the form of neutrinos. During the merger process, which takes place at the timescale of ms, the material inside the core is very dense and becomes opaque even for neutrinos [9]. Thus, the neutrinos react with the matter predominantly via β-decay.

At the same time, we have a very high neutrino flux, which can be measured in detectors like the future Hyper-Kamiokande [10, 16]. The analysis of [15] shows that the maximal energy of the emitted neutrinos depends on the equation of state. So by measuring the gravitational waves and the neutrinos from the merger process at the same time, we get complementary information and learn about the inner structure of neutron star mergers.

In the short timescale of the merger process, we do not have any equilibrium state. Hence, dynamical back-coupling between the electroweak interactions and the strong interaction becomes relevant. A first-principles study of this requires a fully back-coupled, non-perturbative treatment of the system. This is so far only possible at the level of comparatively simple effective models, but not yet in an ab-initio calculation due to the enormous complexity of a fully back-coupled analysis.

With this work, we aim to start the investigation in this field. Since the electroweak interactions come along with various unique features like the violation of the charge conjugation (C) and parity (P), a lot of physical aspects, as well as technical issues, have to be solved upfront; before, the fully dynamical back-coupling for a binary neutron star merger can be considered.

We will tackle some of these aspects in this work, and the future investigation will essentially allow us to give some insight into the binary neutron star mergers.

To avoid any misunderstanding, we want to make clear that the distinctive feature of our study is not the fully back-coupled aspect. Instead, we start our analysis from the quantum chromodynamics (QCD), the theory of the strong interaction; or at least, we use an effective-model and describe the systematic improvement towards QCD.

As a first step, we focus on a few particular aspects of the back-coupling from the electroweak interactions, namely, the breaking of the C, P, and flavor symmetry to the strong sector. Neutron star mergers are not the only reason to consider this problem. Beyond the known standard model also hidden sectors may exist in which strongly interacting parity-conserving and parity-breaking interactions both exist. Both these considerations motivate us to understand such back-couplings better.

Symmetries reduce, by virtue of the Wigner-Eckhart theorem, the structure of the correlation functions. Therefore, the explicit symmetry breaking induces a richer tensor structure. We focus on the simplest object, which exhibits the full additional complexity, namely the quark propagator (QP). Since we are mainly interested in how the strong interaction may amplify, or modify, the symmetry breaking effects, we will consider only an explicit source of the symmetry breaking.

For the next step, we lift the assumption of an explicit breaking term and take the weak interaction into account by investigating the weak pion decay. Regarding our motivation of the binary neutron star mergers, the most dominant process is the β-decay. At the level of the quarks and leptons, both processes have the same ingredients. The weak pion decay has the additional advantage of investigating mesons instead of baryons. This does not only simplifies the analysis significantly but also gives us the possibility to check our method because the pion is very well studied in theory and experiment. To do so, we approximate the weak interaction by a Fermi-theory in the form of an effective low-energy 4-Fermi interaction between the quarks and leptons of the first generation. This is a sufficient approximation for the weak interaction, which does not show a strong momentum-dependence at low-energies due to explicit masses of the W and Z bosons.

The inclusion of such breakings and the large differences in relevant energies already limit the possible choices of methods. Notably, the lattice gauge theory is not suitable. This is, on the one hand, due to the immense computational costs for the vastly different energy levels involved. On the other hand, there is no fully proven way yet to upgrade the static breaking considered here to the full weak interactions using lattice methods [17].

As an alternative, here we employ for this purpose a combination of functional methods: Dyson-Schwinger/Bethe-Salpeter-equations (DSEs/BSEs) [18–26] and the Functional-Renormalization-Group (FRG) [27–30]. Both methods are continuous and covariant formulations, which allow us to access high- and low-energy scales at the same time. Their major drawback is that they lead to an infinite tower of coupled non-linear integral equations, which need truncations to be solved. Nevertheless, these methods yield good results at various levels of sophistication to determine the QP (see, e.g., [18–20, 23, 24] and references therein) and the pion (see, e.g., [26, 31, 32] and the references therein).

To be more precise, we use the DSEs to investigate the effects of the explicit symmetry breaking on the QP. In the case of the weak pion decay, we imply the combined DSEs/BSEs analysis, as well as the FRG. Since both types of approaches have different systematics, this allows us to control systematic error sources to some extent. In the case of the DSEs/BSEs, we restrict ourselves to the so-called rainbow-ladder truncation. This truncation conserves the most important features for our purpose, like dynamical mass generation and the correct treatment of chiral symmetry [18–20, 23, 31, 32]. Thus, a large amount of investigation for the pion has been done using this truncation. This enables us to benchmark our results at the starting point of the analysis, where we switch off the part from the weak interaction.

This is of particular importance because the calculation of the decay-width is still an open question in the functional methods. This is owed to the fact that these methods rely on the formulation of the quantum field theory (QFT) in Euclidean space rather than Minkowski space, which is necessary to describe physical observables like the decay-width. Hence, one is left with the possibility to perform numerical extrapolation from the Euclidean data or the direct calculation in the complex plane of the corresponding momenta. We imply both techniques in this work. The latter one is preferable but comes along with immense computational costs and technical issues, which has to be solved and tested upfront.

In the DSE/BSE framework, various approaches have been developed in the recent years to perform calculations in Minkowski space (see, e.g., [33–39] and the references therein). In [39], for instance, a formalism for the calculation of the DSEs in Minkowski space is presented by reversing the Wick rotation. This is applied to the fermion propagator. The so-called Nakanishi integral representation, along with the light-front projection, is applied for the calculation of the BSEs in [36, 37] (see also the references therein for further details). We solve the BSEs on the physical pole in contrast to the other approaches, i.e., a pole in the unphysical Riemann sheet for the Minkowski space. We show the implication of such a pole for the Euclidean space and locate its right position in the complexified Euclidean space. This does not mean that the pole itself has moved, but we are looking at the same pole from another direction.

In the FRG framework, techniques have been developed recently to perform calculation in the Minkowski space, the so-called real-time FRG (see, e.g., [40–51] and the references therein). Real-time formulation, along with the dynamical hadronization [29, 52–54] are the core of our investigation in the FRG framework. Dynamical hadronization is a proper and efficient way to include our low-energy degrees of freedom, such as the pions dynamically into the system. We test our approach for a QCD-assisted low-energy effective model and outline the procedure for the weak pion decay. The final results for the weak pion decay will be revealed in the future investigation.

The results presented in this work are achieved within a collaboration. The major part of these is already published or available as a preprint. Texts and figures taken from these are not indicated explicitly.

The thesis is organized as follows. In chapter 2, we motivate our investigation in more detail and outline the physical aspects. In chapter 3, we turn to the functional methods. Since these methods are already described in various reviews, we will keep the introduction short and highlight the technical issues relevant for our investigation. More involved technical and mathematical details are shifted to the appendix A.

In chapter 4, we present the result for the explicit symmetry breaking on the QP. Probably the most relevant insight gained, aside from the necessary technology to deal with the increase of complexity, is that the fully coupled system behaves as expected from perturbation theory only at very weak breaking. Already at moderately small breaking, the amplification by the strong interaction can lead to qualitatively different behaviors for the QP than perturbatively expected. We list many further results in appendix B, providing a complete picture of the QP for a wide range of parameters and quark masses. In this chapter, we will also present information on the analytic structure of the QP using its Schwinger function, an issue that is already in QCD alone highly non-trivial.

In chapter 5 and 6, we describe the formulation of the weak pion decay in the combined DSE/BSE and FRG approach, respectively. In particular, we go into detail about the additional complexities caused by the weak interaction. In addition to this, we test our combined analyses of the real-time FRG and dynamical hadronization for a QCD-assisted low-energy model. This system is also investigated for a different level of truncations to have a better insight into the systematic errors. These results are listed in the appendix D. All of the insights and results are finally summarized, and an outlook is given in chapter 7.

Chapter 2

β-decay: Dominant process in neutron star mergers

In this chapter, we first motivate this work in more detail in section 2.1 and discuss the relevant physical basics. The theoretical foundations are based on the QFT. Hence, we first define the necessary quantities for us to fix the notation in section 2.2. We discuss the approximation for the weak interaction by a low-energy effective interaction with the right symmetry breaking properties in section 2.3. Afterward, we give a brief introduction into the QCD in section 2.4. In the end, we deal with bound states and resonances in section 2.5, which are the primary object of our investigation in this work.

Since the theoretical foundations are textbook knowledge, we keep our introduction short and highlight certain aspects relevant to our investigation. In this work, we will not deal with the renormalization theory (see, e.g., [55–62] for a detailed introduction in this topic). We imply multiplicative renormalization, as done in [26,63]. For the sake of clarity, we will suppress the multiplicative renormalization constants and state them only in the final equations of our investigation.

Before we start, let us state further definitions and conventions. We sum over double indices. Throughout this work, we work in Euclidean spacetime ($g_{\mu\nu} = \delta_{\mu\nu}$) and use the natural units, i.e., $\hbar = c = k_B = e = 1$. For example, we get for the distance:

$$1\text{m} = 10^{15}\text{fm} \approx 5.1 \cdot 10^{15} \frac{1}{\text{GeV}}. \tag{2.1}$$

For the integral in d-dimensions, we define the shorthand notation in the position-space and the momentum-space:

$$\int_x \mathrel{\hat{=}} \int \mathrm{d}\, x^d, \qquad\qquad \int_p \mathrel{\hat{=}} \int \frac{\mathrm{d}\, p^d}{(2\pi)^d}. \tag{2.2}$$

In this work, we have to deal with very lengthy expressions with multiple integrals. For the sake of brevity, we suppress the integral symbol in some cases. In this case, the index of the corresponding field also includes the momentum of that field, and the summation over double indices is understood as an integral for continuous indices. At the same time, we suppress all the delta distributions. Thus, the momentum conservation should be applied correctly at each vertex.

2.1 Motivation

The past century is characterized by scientific innovations and has significantly changed our view of the world. In particular, the physical understanding of nature is driven by improvements in observing capabilities. Recently, a new window on the universe has opened with the long-desired successful detection of the gravitational waves [1, 2, 8]. This will essentially increase our fundamental knowledge of the most exotic objects in nature, like black holes and neutron stars. Thus, a huge amount is invested in the present and future observatories for gravitational waves like LIGO [64, 65], Virgo [66], GEO [67], KAGRA [68], and LIGO-India [69].

On the theoretical side, sources for the gravitational waves have become the focus of the investigation in the past few years. Among these are binaries of black holes and/or neutron stars and under certain circumstances also gravitational collapse like the supernova (see for details, e.g., [3–7, 70] and the references therein). Neutron stars are in various aspects unique, and so is their role in physics, especially from the experimental point of view. They are not only successfully measured in the electromagnetic spectra [71–73], but also neutrinos from a supernova [74, 75] and gravitational waves from a binary neutron star merger [8] are already observed. Their understanding requires knowledge from the microphysics to the general relativity. Thus, all the four known fundamental forces of the nature play an equally important role, and their interplay with each other makes their study tricky as well as interesting. This makes them at the same time the perfect laboratory to test our theories (see for an introduction in this topic, e.g., [70, 76–82] and the references therein).

Neutrinos play an essential role in the understanding of the neutron stars during their whole life, and extraordinary during supernovae and binary neutron star mergers. This is due to the fact that a fraction of the gravitational binding energy is released in the form of neutrinos resulting in a huge neutrino flux. The neutrino luminosity can become 10^{20} times higher than the photon luminosity of our sun and under particular circumstances even higher [9, 83]. Therefore, they govern the infall dynamics of the core-collapse, trigger and fuel the explosion, and drive the cooling of the neutron star in the course of its life [83–85]. They are also the only direct probe for the dynamics inside the core due to their weakly interacting nature, and thus give information on the explosion mechanism.

The role of the neutrinos is also crucial in the case of binary neutron star mergers for the process itself and its outcome because of their reactions with the matter inside the core. This is owed to the fact that the neutron stars are already very dense objects and not far away from a black hole. During the merger process, their coalescence become more dense and opaque even for neutrinos [5, 9–15]. In particular, the form of the gravitational waves depends on the details of the neutrino back-coupling, which was shown in [14] by calculating the gravitational waves for three different equations of state. Therefore, the expected gravitational waves should provide insight into the structure of the corresponding process. At the same time, the maximum energy of the neutrinos depends on these reactions. So measuring the neutrinos and gravitational waves give us complementary information and increase our understanding of the merger process.

The so far only successful detection of the gravitational waves [8] along with the multi-messenger electromagnetic signal [86] from binary neutron star merger has already contributed to our insight in various ways, published in numerous articles. For example, implications on the equation of state for the neutron stars were made in [87]. Also, constraints on the cosmological gravity and nuclear matter parameter for neutron stars were derived (see [88, 89] and reference therein for further details).

Unfortunately, there is so far no successful detection of the neutrinos from this process at

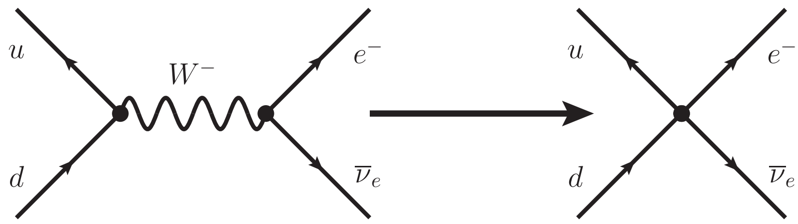

Figure 2.1: Diagrammatic representation of the β-decay at the level of the elementary particles. Down-quark (d) decays into an up-quark (u) by emitting a W^--boson, which then decays into an electron (e^-) and electron-anti-neutrino ($\overline{\nu}_e$). This is approximated with an effective low-energy interaction of the 4 fermions neglecting the intermediate exchange boson.

the present Super-Kamiokande facility [90]. It should also not be expected that a single measurement will reveal all the answers. Further observations with advanced detectors and better resolution for the gravitational waves, as well as neutrinos, will give us insight on the neutrino back-coupling during a merger process. For a detector like the future Hyper-Kamiokande, the detection number of the neutrinos is approximately 10 if the merger process happens in the distance smaller than 5 Mpc [10, 16], which is a huge amount for neutrinos.

The understanding of the merger process requires progress from the theoretical side, along with the experimental side. The theoretical analysis is very demanding due to various reasons. The merger process happens at a time scale of ms and, therefore, does not have any equilibrium state. At the same time, the environment is such dense that the dynamical back-coupling between the strong and the electroweak interactions becomes relevant [5, 9–15]. This requires a fully back-coupled, non-perturbative, first principle study of the system, which is not feasible at the moment due to the enormous complexity.

In addition to this, the weak interaction has various unique features, like C- and P-violation. Investigating these symmetry violations is a tough task even in perturbation theory. Therefore, the impact of the P-violation has just recently been included in the analysis, however, only in the context of the supernovae (see for details, e.g., [91–95] and the references therein). These results show that the kinetic theory is modified by the left-handedness of the particles, which should not be ignored.

For the merger process, this may have a significant impact. Our results, so far, also indicate that the symmetry breaking effects are amplified by the dynamical back-coupling with the strong interaction, although the strong interaction conserves these symmetries. Thus, we should be cautious with the perturbative extrapolations. We will discuss this in more detail in chapter 4. So throughout this work, we take the implicit CP-violation into account.

Considering the most dominant reactions during the merger process, which are given by [14]:

$$\nu_e + n \longleftrightarrow p + e^-, \qquad \overline{\nu}_e + p \longleftrightarrow n + e^+, \qquad \nu_e + \overline{\nu}_e \longleftrightarrow e^+ + e^-, \qquad \nu_e + \overline{\nu}_e \longleftrightarrow \gamma,$$

reveals that the β-decay in its different forms is the most dominant process for the back-coupling of the strong and weak interacting matter. The β-decay involves the both lightest baryons, namely, protons (p) and neutrons (n) along with the first generation of the leptons, namely, electrons (e) and electron-neutrinos (ν_e).

In the constituent quark model (see [96] for an introduction into the elementary particle physics), the protons and neutrons consist of the quarks from the first generation, namely, up-quark (u) and down-quark (d). At the level of the elementary particles, β-decay is a process in which the down-quark decays into an up-quark by emitting a W^--boson. The W^--boson decays in the following into an electron and anti-electron-neutrino. As a first approximation, we neglect the exchange of the W^--boson, which is a sufficient approximation at low-energies due to the heavy mass of the W-bosons. So we are left with a low-energy 4-Fermi interaction involving the quarks and leptons of the first generation. The process of the β-decay and its approximation is shown in figure 2.1.

The β-decay involves protons and neutrons and hence requires to deal with baryons. Baryons consist of three quarks. Therefore, their properties like mass and decay-width are extracted from a 6-point-function in a first principle study of a QFT. A fully back-coupled and non-perturbative analysis of this is far too complicated as a first step. Thus, we first consider the simplest and lightest hadrons, namely pions. Pions are mesons and consist of a quark and an anti-quark of the first generation. Their treatment requires knowledge of a 4-point-function, which is much simpler compared to baryons. In addition to this, the pions are very well studied in theory and experiment. Hence, they are the perfect candidate to test our method.

The pion-decay into an electron and electron-neutrino involves the same process for the quarks and leptons as the β-decay. At the level of the elementary particles, we are investigating the same process in a more general context and hence call it β-decay of hadrons. Let us note here that the charged pions dominantly decay into a muon and muon-neutrino, which is the second generation of the leptons. This is not an issue for our investigation because we vary the mass values of the leptons for different orders of magnitudes in our study. We just call them electrons and neutrinos as representants of the leptons for the sake of clearer understanding. This concludes our motivation, and we extract the β-decay of hadrons with the right C- and P-violation as our primary object of investigation in this work. We now continue with the theoretical foundations relevant to the understanding of this work, starting with the QFT.

2.2 QFT

In this section, we will define the different quantities of interest. The purpose of this section is to set up the notation for the following sections. For a detailed introduction in the QFT, we refer the reader to textbooks like [97–102].

The n-point functions are the central objects in the QFT. For our purpose, we choose the path integral formalism. First we combine all the fields of our theory in the field Φ and the corresponding sources in J. With the index i ,we access the different fields of Φ, like the fermion fields $\tilde{\psi}$ and the boson fields $\tilde{\varphi}$, where the index i includes all the internal indices of the field.

$$\Phi = \begin{pmatrix} \tilde{\varphi} & \tilde{\psi} & \overline{\tilde{\psi}} & \dots \end{pmatrix}^T , \qquad J = \begin{pmatrix} j & \overline{\eta} & -\eta & \dots \end{pmatrix}^T . \tag{2.3}$$

The n-point functions, also called correlation functions or Green's functions ($G^{(n)}$), are the time-ordered vacuum expectation values of the fields with the measure $\mathrm{e}^{-S[\Phi]}$, where $S[\Phi]$ is the action of the theory.

$$G^{(n)}_{i_1,\dots,i_n}(x_1, \dots, x_n) \equiv \langle \Phi_{i_1}(x_1) \dots \Phi_{i_n}(x_n) \rangle := \frac{\int \mathcal{D}\Phi \;\; \Phi_{i_1}(x_1) \dots \Phi_{i_n}(x_n) \, \mathrm{e}^{-S[\Phi]}}{\int \mathcal{D}\Phi \, \mathrm{e}^{-S[\Phi]}} , \tag{2.4}$$

where $\int \mathcal{D}\Phi$ denotes the path integral.

We define the generating functional $Z[J]$ of the correlation functions and the generating functional $W[J]$ of the connected diagramms ($G_c^{(n)}$), also called Schwinger functional, as follows:

$$e^{W[J]} \equiv Z\left[J\right] = \int \mathcal{D}\Phi \, e^{-S[\Phi]+\int (J\Phi)} \,.$$

$$G^{(n)}_{c,i_1,\ldots,i_n}(x_1,\ldots,x_n) \equiv \langle \Phi_{i_1}(x_1)\ldots\Phi_{i_n}(x_n)\rangle_c = \left.\frac{\delta^n}{\delta J_{i_1}(x_1)\ldots\delta J_{i_n}(x_n)} W\left[J\right]\right|_{J=0} . \tag{2.5}$$

Appropriate functional derivatives of the generating functional enable us to calculate the correlation functions, which is shown in the last line for the Schwinger functional.

With the help of the Schwinger functional, we define the generating functional of the one-particle-irreducible (1PI)-diagramms, also called the effective action, as follows:

$$\Gamma\left[\phi\right] = \sup_J \left(-W\left[J\right] + \int (J\phi)\right) \tag{2.6}$$

The field ϕ is the expectation value of the field Φ in the presence of the external source J[1].

$$\phi = \frac{\delta W\left[J\right]}{\delta J} = \frac{1}{Z[J]}\frac{\delta Z[J]}{\delta J} = \langle\Phi\rangle_J = \begin{pmatrix}\varphi & \psi & \overline{\psi} & \ldots\end{pmatrix}^T \tag{2.7}$$

For our analysis, we will use the effective action. This completes our introduction into the QFT.

In the end, we state some important relations, which will be used in the following chapters. Due to the different mathematical properties of the fields under commutation, we first define:

$$(-1)^G_{i,j,\ldots} = \begin{cases} -1 \text{ if } \{\phi_i,\phi_j,\ldots\} \text{ contains odd numbers of Grassmann valued fields,} \\ \;\;1 \text{ else} \end{cases} , \tag{2.8}$$

and get:

$$\frac{\delta\Gamma\left[\phi\right]}{\delta\phi_i} = (-1)^G_i J_i. \tag{2.9}$$

Using the equations (2.7) and (2.9) we get the relation between the propagator ($\mathcal{P}$) and the second derivative of the Schwinger functional:

$$\mathcal{P}_{ij}(x,y) := \left[\frac{\delta^2\Gamma[\phi]}{\delta\phi_j(y)\delta\phi_i(x)}\right]^{-1} = (-1)^G_i \frac{\delta^2 W[J]}{\delta J_i(x)\delta J_j(y)}. \tag{2.10}$$

Eventually, we define a shorthand notations for the n-th functional derivatives of effective action:

$$\Gamma^{(n)}_{i_1,\ldots,i_n}\left[\phi\right] := \frac{\delta^n}{\delta\phi_{i_1}\ldots\delta\phi_{i_n}}\Gamma\left[\phi\right]. \tag{2.11}$$

In the end, we state the relation for the functional derivative of the propagator:

$$\frac{\delta}{\delta\phi_k}\mathcal{P}_{ij} := -(-1)^G_{l,m}\mathcal{P}_{il}\Gamma^{(3)}_{k,l,m}[\phi]\mathcal{P}_{mj}. \tag{2.12}$$

This concludes our introduction into the QFT.

[1] Throughout this work we denote the different fields with tilde on it and their expectation values in the presence of the externel field without a tilde, where the distinction between them has a significant impact. Otherwise, we will just use the different fields without a tilde for the sake of brevity.

2.3 Effective weak interaction

We refer the reader to textbooks like [103–107] for a detailed introduction into the theory of the electroweak interactions. The weak interaction has a lot of interesting properties, like the breaking of various symmetries. Hence, we have to deal with a richer tensor structure for the n-point-functions. This hampers the analysis significantly. As a first step, we focus on particular aspects of the weak interaction, starting with the C- and P-Violation.

2.3.1 CP-violation

The definitions in this section are taken from [107], and we refer the reader to this textbook for further details on this topic. The weak interaction violates C and P symmetry, each maximally. Let us start with the P.

Parity

The P-transformation is a point reflection in space. Thus, it only acts on the space coordinates and differentiates between time and space. The symmetry transformation leaves scalars unchanged and inverts the sign of each vector like coordinates and momenta.

$$(x_0, \vec{x}) \to (x_0, -\vec{x}), \qquad\qquad (p_0, \vec{p}) \to (p_0, -\vec{p}). \tag{2.13}$$

There are also vectors, for example, the angular momentum ($\vec{L} = \vec{x} \times \vec{p}$), which does not change their sign under this transformation. Such vectors are called pseudo-vectors or axial vectors.

Analogous to this, we also classify pseudo-scalars, which change their sign under this transformation. This also leads to a classification of the fields according to their transformation behavior under the P-transformation[2] $\mathcal{P}$. The transformation properties of vector fields, axial-vector fields, scalar fields and pseudo-scalar fields are as follows:

$$\mathcal{P} A^i_\mu(p_0, \vec{p}) \mathcal{P}^{-1} = \mp A^i_\mu(p_0, -\vec{p}), \qquad\qquad \mathcal{P} \varphi(p_0, \vec{p}) \mathcal{P}^{-1} = \pm \varphi(p_0, -\vec{p}). \tag{2.14}$$

For spinors ψ the P-transformation is given by:

$$\mathcal{P} \psi(p_0, \vec{p}) \mathcal{P}^{-1} = \gamma_0 \psi(p_0, -\vec{p}), \qquad\qquad \mathcal{P} \overline{\psi}(p_0, \vec{p}) \mathcal{P}^{-1} = \overline{\psi}(p_0, -\vec{p}) \gamma_0. \tag{2.15}$$

We project out left-handed and right-handed spinor states by:

$$\psi^{L/R} = \frac{1}{2}\left(\mathbb{1} \mp \gamma^5\right)\psi, \qquad\qquad \overline{\psi}^{L/R} = \overline{\psi}\frac{1}{2}\left(\mathbb{1} \pm \gamma^5\right), \tag{2.16}$$

which are transformed as:

$$\mathcal{P} \psi^{L/R}(p_0, \vec{p}) \mathcal{P}^{-1} = \gamma_0 \psi^{R/L}(p_0, -\vec{p}), \qquad \mathcal{P} \overline{\psi}^{L/R}(p_0, \vec{p}) \mathcal{P}^{-1} = \overline{\psi}^{R/L}(p_0, -\vec{p}) \gamma_0. \tag{2.17}$$

This means that the left-handed fields are tranformed into right-handed fields and vice versa.

The weak interaction only acts on the left-handed particles and thus violates P maximally. As already mentioned symmetry breaking leads to a richer tensor structure for the correlation functions. Let us now illustrate this for the quark 2-point-function, which is the major object

[2] In the previous section, we have also defined the propagator with $\mathcal{P}$. We will only use the P-transformation in this section of the work. For the rest of the work, $\mathcal{P}$ will be used for propagators to avoid ambiguity.

of investigation in chapter 4. It has 4 different Lorentz-tensor structures, namely, the vector channel $\left(\overline{\psi}\,\mathrm{i}\,\not{p}\psi\right)$, scalar channel $\left(\overline{\psi}\mathbb{1}\psi\right)$, axial channel $\left(\overline{\psi}\,\mathrm{i}\,\not{p}\gamma^5\psi\right)$, and pseudo-scalar $\left(\overline{\psi}\gamma^5\psi\right)$. We consider the P-transformation behavior of these channels. For example, the axial channel transforms as:

$$\begin{aligned}\mathcal{P}\left(\overline{\psi}(p_0,\vec{p})\,\mathrm{i}\,\not{p}\gamma^5\psi(p_0,\vec{p})\right)\mathcal{P}^{-1} &= \overline{\psi}(p_0,-\vec{p})\gamma^0\,\mathrm{i}\left(p_0\gamma^0-\vec{p}\cdot\vec{\gamma}\right)\gamma^5\gamma^0\psi(p_0,-\vec{p})\\ &= -\left(\overline{\psi}(p_0,-\vec{p})\,\mathrm{i}\,\not{p}\gamma^5\psi(p_0,-\vec{p})\right),\end{aligned} \tag{2.18}$$

where $\vec{p}\cdot\vec{\gamma}=\sum_{i=1}^{d-1}p_i\gamma^i$. So the axial vector violates P. Analogous calculations for the other channels show that the first 2 channels are P conserving and the latter 2 are P violating. Thus, the QP has in P violating theories all the 4 Lorentz-tensors instead of 2.

Charge conjugation

The C-transformation ($\mathcal{C}$) replaces the particle by its anti-particle and lets the intrinsic properties, like the mass, spin, momentum, and energy of the particle unchanged. The common representation of this transformation is $\mathcal{C}=\mathrm{i}\,\gamma^2\gamma^0$. However, the relations stated here are independent of the representation. The transformation behavior of the spinor fields, vector fields, real-scalar fields (φ) and complex-scalar fields ($\overline{\varphi}$) are as follows:

$$\begin{aligned}&\mathcal{C}\psi\mathcal{C}^{-1}=\mathcal{C}\overline{\psi}^T, &&\mathcal{C}\overline{\psi}\mathcal{C}^{-1}=-\psi^T\mathcal{C}^{-1}, &&\mathcal{C}A^i_\mu\mathcal{C}^{-1}=-A^i_\mu,\\ &\mathcal{C}\varphi\mathcal{C}^{-1}=\varphi, &&\mathcal{C}\overline{\varphi}\mathcal{C}^{-1}=\overline{\varphi}^*, &&\mathcal{C}\overline{\varphi}^*\mathcal{C}^{-1}=\overline{\varphi}.\end{aligned} \tag{2.19}$$

In particular, the right-handed and left-handed spinor-fields tranforms as:

$$\mathcal{C}\psi^{L/R}\mathcal{C}^{-1}=\mathcal{C}\left(\overline{\psi}^{R/L}\right)^T, \qquad \mathcal{C}\overline{\psi}^{L/R}\mathcal{C}^{-1}=-\left(\psi^{R/L}\right)^T\mathcal{C}^{-1}. \tag{2.20}$$

This means that the right-handed particle is transformed into a left-handed anti-particle. The weak interaction violates C maximally by coupling left-handed particles to left-handed anti-particles. This concludes our introduction on the CP-Violation.

2.3.2 Symmetry breaking and effective interaction

The strong and electric interactions are flavor conserving in contrast to the weak interaction. During the β-decay process, the down-quark changes its flavor into an up-quark. So the last missing symmetry violation for our study is the flavor symmetry.

As a first step, we want to analyze the impact of the C, P, and flavor symmetry on the QP in chapter 4. Flavor violation within a generation is not possible without involving further particles due to electric charge conservation. During the β-decay, this is ensured by the emission of a lepton and a(n) (anti-)neutrino. So the analysis of the broken flavor symmetry requires the study at the level of a 4-point-vertex. To avoid the additional complexity of a 4-point-vertex, we model the leptons as an external background field for the study of the QP. Given that our ultimate interest is in neutron star mergers, where such a reservoir is readily available, this appears like a reasonable approximation.

The breaking of the symmetries will be realized by including an explicitly symmetry-violating term in the Lagrangian. The breaking is then generated already at tree-level. For the study of the QP, we do not want to restrict ourselves to quarks of the first generation and analyze each generation on its own. Therefore, the subscript u and d denotes up-like quarks and down-like quarks and the superscript L and R left-handed and right-handed quarks, respectively.

The strength of the weak interaction, or more precisely the coupling to the symmetry breaking external field, will be denoted by g_{W}, the effective weak strength. We will vary the value of g_{W} from small values to large values to turn on the effects smoothly. Finally, the quark fields are denoted by Q. The explicit symmetry breaking term has the form:

$$\mathcal{L}_{\mathrm{SB}} = \frac{g_w}{2} \left[\left(\overline{Q}^L_u \, \mathrm{i} \not{p} Q^L_d \right) + \left(\overline{Q}^L_d \, \mathrm{i} \not{p} Q^L_u \right) \right] . \tag{2.21}$$

Let us now discuss the implication of the breaking term for the QP. In addition to the propagation of the up-like quarks and down-like quarks, we also have the propagation from the up-like quark to a down-like quark and vice versa within a generation due to the flavor symmetry breaking. So we have also QPs for mixed flavors resulting in 4 different propagators for a single generation instead of 2. Due to the P-violation, we have for each QP 4 Lorentz-tensors instead of 2, as already shown in the previous section. Therefore, we have 16 different quantities to calculate for the QPs instead of 4 due to symmetry breakings showing the rise of complexity even for the simplest object. We will discuss this in more detail in chapter 4.

For the next step in chapter 5 and 6, we relax the assumption of a reservoir and take the weak interactions explicitly into account by including the emitted neutrinos and electrons. This will require to work on a hadronic level, which is our next aim. We start with the weak pion-decay into an electron and neutrino, according to our discussion in the motivation section. The decay process at the level of the quarks and leptons is shown in figure 2.1, which leads to the following approximation of the weak interaction in form of a 4-Fermi interaction

$$\mathcal{L}_{\text{4-Fermi}} = \frac{\alpha_w}{2} \left[\left(\overline{Q}^L_u \gamma^\mu Q^L_d \right) \left(\bar{l}^L_e \gamma^\mu l^L_\nu \right) + \left(\overline{Q}^L_d \gamma^\mu Q^L_u \right) \left(\bar{l}^L_\nu \gamma^\mu l^L_e \right) \right] , \tag{2.22}$$

where l are the lepton fields and the subscript e and ν denotes the electrons and neutrinos respectively. Here α_w denotes the effective weak coupling.

Such a 4-Fermi interaction in the Lagrangian leads to a non-renormalizable theory [97]. This issue is solved by introducing the effective weak coupling momentum-dependent with sufficient enough drop off behavior for large momenta. Therefore, we model the effective weak coupling guided by the W-boson exchange. The W-boson exchange leads in Euclidean space to a contribution of the form:

$$\alpha_w \sim \frac{\tilde{g}^2_w}{p^2 + M^2_w}, \tag{2.23}$$

where $\tilde{g}_w$ is the weak coupling. M_w, and p are the mass and the momentum of the W-boson, respectively. The coupling does not show a big momentum-dependence for $p \lesssim 10\,\mathrm{GeV}$ due to the heavy mass of the W-boson and drop off rapidly for higher momenta. Thus, modeling the effective coupling in this way will ensure renormalizability. This concludes our discussion on the weak interaction, and we proceed further with the strong interaction.

2.4 QCD

QCD is the theory of the strong interaction. For an introduction in this topic, see for example [107–111] and the reference therein. The quarks are the only matter particles in the

Standard Model of the elementary particles, which interact strongly via the gluons. Let us first describe the QCD and discuss its features afterward. QCD is a non-abelian gauge theory with the gauge group SU($N_c = 3$). Although we state the theoretical description for SU(3), the following characterization is also valid for a simple Lie group (see textbooks like [112–114] for an introduction in this topic).

The quarks are charged under the gauge group called the color charge. They are fermions with spin 1/2 and come in 6 different flavors (f) namely up (u), down (d), charm (c), strange (s), top (t) and bottom (b). They interact via the gluon gauge field $A_\mu = A^i_\mu t^i$, where t^i are the generators of the corresponding gauge group (see the appendix A.2 for further details of the SU(N)-algebra).

The Lagrangian of the QCD is given by:

$$\mathcal{L}_{\mathrm{QCD}} = \overline{Q}_f \left(\not{D} + m_f \right) Q_f + \frac{1}{4} F^i_{\mu\nu} F^i_{\mu\nu}, \tag{2.24}$$

where $\not{D} = \gamma_\mu D_\mu$ with the gamma matrices γ_μ (see the appendix A.3 for details) and the covariant derivative:

$$D_\mu = \partial_\mu - \mathrm{i}\, g_s A^i_\mu t^i. \tag{2.25}$$

Here g_s is the strong coupling. The field strength tensor is given by:

$$F^i_{\mu\nu} = \partial_\mu A^i_\nu - \partial_\nu A^i_\mu + g_s f^{ijk} A^j_\mu A^k_\nu, \tag{2.26}$$

where f^{ijk} is the total anti-symmetric structure constant.

The so defined Lagrangian is then by construction invariant under the gauge transformations:

$$Q_f \to U Q_f, \qquad \overline{Q}_f \to \overline{Q}_f U^\dagger, \qquad A_\mu \to U A_\mu U^\dagger - \frac{i}{g_s} (\partial_\mu U) U^\dagger, \tag{2.27}$$

where U is an element of the Lie group given by:

$$U = \exp\left[-\mathrm{i}\, t^i \theta^i(x) \right], \tag{2.28}$$

with $N_c^2 - 1$ functions $\theta^i(x)$.

2.4.1 Gauge fixing

The gauge transformations in (2.27) relate infinite number of physically equivalent field configurations. Thus, we have to single out physically inequivalent gauge configurations from the equivalent one, called gauge fixing. Technically, this is achieved by applying a gauge fixing condition $G^i[A] = 0$ (see for details, e.g., [97]). We insert this condition into the functional integral with the help of the identity (the so called Faddev and Popov trick [115]):

$$1 = \int \mathcal{D}G \delta(G) = \int \mathcal{D}\theta(x) \delta\left(G^i \left[A^\theta \right] \right) \det \left(\frac{\delta G^i \left[A^\theta \right]}{\delta \theta^j} \right), \tag{2.29}$$

where δ is the functional dirac delta.

For covariant gauges given by:

$$G^i[A] = \partial_\mu A^i_\mu(x) - \omega^i(x) = 0, \tag{2.30}$$

with an arbitrary function $\omega^i(x)$, we obtain the ghost fields $c = c^i t^i$ and the anti-ghost field $\bar{c} = \bar{c}^i t^i$ from the Faddev-Popov determinant using the relation $\frac{\delta G^i}{\delta \theta^j} = \frac{\delta G^i}{\delta A^k_\mu} \frac{\delta A^k_\mu}{\delta \theta^j}$ along with (2.27):

$$\det\left(\frac{\delta G^i\left[A^\theta\right]}{\delta\theta^j}\right) = \det\left(\frac{1}{g_s}\partial_\mu D^{ij}_\mu\right) = \int \mathcal{D}c\mathcal{D}\bar{c}\exp\left[\int \bar{c}^i\partial_\mu D^{ij}_\mu c^j\right],$$
$$D^{ij}_\mu = \delta^{ij}\partial_\mu - g f^{ijk} A^k_\mu. \tag{2.31}$$

The ghost fields violate the spin-statistic theorem and, therefore, are unphysical states. Their remit is to cancel the unphysical degrees of freedom.

For the final step, we integrate over the ω^i with a Gaussian weight ($\int \mathcal{D}\omega \exp(-\int(\omega^i)^2/(2\xi))$) and eliminate the delta function. As a result of this, we obtain our gauge fixed action of the theory with the gauge fixing parameter ξ. An explicit construction shows that this does not fix the gauge uniquely beyond perturbation theory. Thus, we have to deal with the so-called, Gribov copies [116], whose role is still an open question in the non-perturbative approaches. We refer the reader to [117–125] and the references therein for further details on this topic.

For a better understanding of the different contributions, we split the the Lagrangian of the QCD in the matter part $\mathcal{L}_\mathrm{M}$, part for the gauge-fields $\mathcal{L}_\mathrm{G}$, gauge fixing part $\mathcal{L}_\mathrm{GF}$, and the ghost part $\mathcal{L}_\mathrm{Gh}$:

$$\mathcal{L}^\text{gauge-fixed}_\text{QCD} = \underbrace{\overline{Q}_f\left(\not{D} + m_f\right)Q_f}_{\mathcal{L}_\mathrm{M}} + \underbrace{\frac{1}{4}F^i_{\mu\nu}F^i_{\mu\nu}}_{\mathcal{L}_\mathrm{G}} + \underbrace{\frac{1}{2\xi}(\partial_\mu A^i_\mu)^2}_{\mathcal{L}_\mathrm{GF}} + \underbrace{\bar{c}^i\partial_\mu D^{ij}_\mu c^j}_{\mathcal{L}_\mathrm{Gh}}. \tag{2.32}$$

The matter part contains all the contributions from the quarks, which are the free propagation of the quarks and the interaction part for the quarks via the gauge fields. This part is independent of gauge fixing. The gauge part is the Yang-Mills part of the theory without gauge fixing. The last two parts are the additional contributions from gauge fixing procedure.

The gauge field propagator in momentum-space is given by the inverse of the 2-point functions. The tree-level propagator (D^A) has the following form:

$$D^{A,ij}_{\mu\nu}(p) = \left[\frac{\delta^2}{\delta A^j_\nu(p')\delta A^i_\mu(p)} S^\text{gauge-fixed}_\text{QCD}[\phi]\Bigg|_{\phi=0}\right]^{-1} = \frac{\delta^{ij}}{p^2}\left[\Pi^\perp_{\mu\nu}(p) + \xi\Pi^\parallel_{\mu\nu}(p)\right]. \tag{2.33}$$

Here, we split the contributions into the longitudinal ($\Pi^\parallel$) and transverse ($\Pi^\perp$) direction given by:

$$\Pi^\parallel_{\mu\nu}(p) = \frac{p_\mu p_\nu}{p^2}, \qquad \Pi^\perp_{\mu\nu}(p) = \delta_{\mu\nu} - \Pi^\parallel_{\mu\nu}(p). \tag{2.34}$$

Throughout this work, we choose the Landau-gauge ($\xi \to 0$) for our investigations due to its several advantages. The obvious one is that the gluon propagator has only a transverse direction. The most important benefit for our study is that we have the minimal amount of terms possible (see, e.g., [126] and the reference therein). Therefore, most of the investigations are done in this gauge and allow comparison with other results. This concludes the formal part of the QCD, and we highlight some essential features of the theory in the following.

2.4.2 Properties

Confinement, along with dynamical chiral symmetry breaking, build the core for the formation of the hadrons and their properties. Thus, they play an essential role in our understanding of the QCD. This understanding is driven by the collider experiments, e.g., at the LHC and calculations from the perturbation theory. The possibility of the perturbative calculations is owed to the asymptotic freedom feature of the QCD. So we occupy ourselves with these properties in the following starting with the asymptotic freedom.

Asymptotic freedom

Asymptotic freedom is a crucial ingredient for the success of the QCD as the theory for the strong interaction. Therefore, It has a fundamental role in the Standard Model of the elementary particle physics. The importance was first realized in the work of David Gross, Frank Wilczek, and David Politzer [127, 128] and was essentially appreciated with the Nobel Prize of physics in 2004. Asymptotic freedom states that an interaction vanishes asymptotically rather than diverges for increasing energy scales.

As a consequence of this, the value of the strong coupling becomes small enough to be in the validity range of perturbation theory for sufficient high-energies. This makes QCD predictive up to the highest orders and ultraviolet (UV) complete. This feature allows a QFT and, in particular, QCD to be a fundamental theory of the nature. Let us note here that in contrast to the QCD, the theory of the electroweak interaction, by Abdus Salam and Steven Weinberg [129,130], is not asymptotically free and thus breaks down at sufficiently-high energy scales. Therefore, the Standard Model is not a fundamental theory of the nature despite all its success. So the QCD is, at the moment, the only theory of the nature with this feature.

Confinement

While the coupling of the QCD vanishes asymptotically in the UV, it is strong in the infrared (IR). In particular, it binds the quarks together to color neutral bound states called hadrons and does not allow to single out color charged objects. Thus, only hadrons are observed in the detectors and not the quarks and gluons, which is the essential difference to the other observed fundamental particles and forces we know. This property of QCD is referred to as the color confinement or just confinement. The more profound understanding of why this happens is still far from being solved. Numerous studies are dealing with the confinement problem, and a rigorous proof of it is one of the unsolved millennium prize problems (see [131] and the references therein for details on this topic).

Dynamical chiral symmetry breaking

Chiral symmetry is an exact symmetry of the QCD for massless quarks. This symmetry is explicitly violated in nature due to the finite mass of the quarks. In addition to the explicit violation, it is is also broken dynamically. The dynamical chiral symmetry breaking is responsible for the large constituent quark masses, hence heavy hadrons. Let us, in the following, illustrate how the dynamical breaking of the chiral symmetry endows the quarks with the mass in the chiral limit. This procedure uses the Hubbard-Stratanovich transformation, which helps us to understand better the features of the dynamical hadronization, one of the key features in our analysis using FRG.

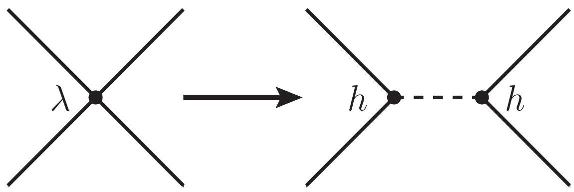

Figure 2.2: Diagrammatic representation of partial bosonization procedure by the Hubbard-Stratanovich transformation. The transformation enables us to replace the 4-Fermi interaction (coupling λ) by a Yukawa interaction of the quarks and bosons (coupling h).

For this purpose, we consider the case of a single massless quark with the dynamically generated chiral symmetric 4-Fermi interaction in the scalar minus pseudo-scalar channel by the quark-gluon interaction. The scalar channel is related to the sigma meson and the pseudo-scalar channel to the pion, which are the lightest mesons [132]. Thus, these channels for the 4-Fermi interaction are the most dominant ones.

The Lagrangian is given by:

$$\mathcal{L}_{\text{chiral}} = (\overline{Q}\partial\!\!\!/ Q) + \frac{\lambda}{2}\left[(\overline{Q}Q)^2 - (\overline{Q}\gamma_5 Q)^2\right], \tag{2.35}$$

and the chiral transformation by:

$$\overline{Q} \mapsto \overline{Q}\exp\left[-\tfrac{\mathrm{i}}{2}\gamma_5\Theta\right], \qquad Q \mapsto \exp\left[-\tfrac{\mathrm{i}}{2}\gamma_5\Theta\right]Q, \tag{2.36}$$

where θ is chiral rotation angle. Let us note here that the combination of scalar minus pseudo-scalar channel is chiral symmetric and not each channel on its own, seen by a straight forward calculation.

The Hubbard-Stratanovich transformation is given by an identity insertion in the path integral of the form:

$$\mathbb{1} = \mathcal{N}\int \mathcal{D}\varphi_1\mathcal{D}\varphi_2 \exp\left[-\int \frac{1}{2}m_\sigma^2\left\{\left(\varphi_1 + \frac{h}{m_\sigma^2}(\overline{Q}Q)\right)^2 + \left(\varphi_2 - \frac{h}{m_\sigma^2}(\overline{Q}\,\mathrm{i}\,\gamma_5 Q)\right)^2\right\}\right], \tag{2.37}$$

where $\mathcal{N}$ is a normalization constant. We call the field φ_1 sigma and φ_2 pion, which will be clear later on.

To obtain the bosonized action we cancel the 4-Fermi interaction by setting $\lambda = -\frac{h^2}{m_\sigma^2}$ and get the bosonized Lagrangian of the form:

$$\mathcal{L}_{\text{chiral}}^{\text{bosonized}} = (\overline{Q}\partial\!\!\!/ Q) + \frac{m_\sigma^2}{2}\left(\varphi_1^2 + \varphi_2^2\right) + h\left[\varphi_1(\overline{Q}Q) - \varphi_2(\overline{Q}\,\mathrm{i}\,\gamma_5 Q)\right]. \tag{2.38}$$

This bosonization procedure enables us to replace the 4-Fermi interaction by a Yukawa interaction with a boson exchange, which is shown diagrammatically in figure 2.2. However, the 4-point interaction is dynamically generated again into the system by the same diagrammatical process reversely. Thus, we have the Yukawa interaction, as well as the 4-point interaction, in the system.

This is the well known double-counting problem of the Hubbard-Stratanovich transformation. The dynamical hadronization avoids this problem by allowing the identity transformation at the level of the full effective action. We will introduce this procedure in section 3.3.1 and discuss its advantages at that point.

Let us now turn back to the dynamical chiral symmetry breaking. According to the Noether-Theorem, there exists a conserved charge for each symmetry [133]. For the chiral symmetry, this is given by:

$$Q_5 = \frac{1}{2}\int \mathrm{d}^3 x \;\; \overline{Q}(x)\gamma_0\gamma_5 Q(x). \tag{2.39}$$

According to the Nambu-Goldstone-Theorem, symmetry breaking is characterized by (see, e.g., [107] and the references therein):

$$0 \neq \left\langle \left[\mathrm{i}\, Q_5, \overline{Q}\,\mathrm{i}\,\gamma_5 Q\right]\right\rangle \sim \left\langle \overline{Q}Q \right\rangle, \tag{2.40}$$

i.e., non-vanishing chiral condensate. The Euler-Lagrange-equations of the bosonized fields yield:

$$\frac{\delta S}{\delta\varphi_1} = m_\sigma^2\varphi_1 + h\overline{Q}Q = 0, \qquad\qquad \frac{\delta S}{\delta\varphi_2} = m_\sigma^2\varphi_2 + h\overline{Q}\gamma_5 Q = 0. \tag{2.41}$$

So the non-vanishing chiral condensate implies a non-vanishing expectation value for the sigma field ($0 \neq \left\langle \overline{Q}Q \right\rangle \sim \langle\varphi_1\rangle$).

The Euler-Lagrange-equation for the quark evaluated at the expectation values for the bosonic fields yield:

$$\left.\frac{\delta S}{\delta\overline{Q}}\right|_{\varphi_1=\langle\varphi_1\rangle,\varphi_2=0} = (\partial\!\!\!/ + m_Q)Q = 0, \qquad \text{with} \qquad m_Q = h\,\langle\varphi_1\rangle \sim \left\langle \overline{Q}Q \right\rangle \neq 0. \tag{2.42}$$

This shows that the dynamical breaking generates the constituent quark masses. Thus, hadron masses are predominantly caused by the binding energy. In particular, we get a massive mode, namely, the sigma.

According to the Nambu-Goldstone-Theorem, we also have a massless particle, the Nambu-Goldstone-boson, which is the pion in our case. So pion would be massless and absent from the physical space if chiral symmetry were not broken explicitly in the nature. This explains why the pion is so much lighter than the other hadrons and, therefore, plays a unique role in the hadron spectrum. This concludes our brief introduction to the QCD. We now deal with the bound states and resonances, which are the primary object of investigation in this work.

2.5 Bound states and resonances

The strong interaction bounds the quark and gluons to hadrons. Thus, we observe bound states in nature instead of the quarks, which is related to the well-known confinement property of the QCD. Our knowledge about the strong force and to some extent of the weak force is derived from the hadrons and their decays. Therefore, bound states and resonances play a crucial role in the understanding of nature (see, e.g., [134–139] and the references therein for further details).

Bethe and Salpeter already made one of the critical works to determine the properties of bound states in the early ’60s [140, 141]. Although we have made significant progress since then in the understanding of the bound states and their properties, the quantitative precision of their properties is still a big challenge. In QCD, this is even more hampered because the coupling becomes strong in the IR and thus requires a non-perturbative treatment (see [18] and the references therein for further details).

Almost all quantitative non-perturbative approaches are formulated in Euclidean space. So we are left with two options. Either, we extract the bound state properties from subleading exponential tails of the Euclidean correlation functions; or we continue our formulation from the Euclidean space to the Minkowski space and calculate the correlation functions direct in Minkowski space. While the latter one is more desired, it is not possible for the large part of the bound states at the moment due to the immense computational power required for this.

In this work, we will imply both techniques. We will deal with the technical details for the investigation of the bound states and resonances in the following chapters, whilst introducing the different methods. Let us now turn to the analytical structure of the correlation functions, which is directly related to the properties of bound states and resonances.

2.5.1 Resonances: Poles in the second Riemann sheet

Before we start with the analytical structure, let us first define the Riemann sheets. They come into play when dealing with multi-valued complex functions[3]. We will discuss the Riemann sheets for the root function, which is relevant to our study and refer the reader to the textbooks, like [142–144] for a general mathematical introduction into this topic.

The square function maps the complex variable z and its negative to the same complex number. Thus, the inverse function

$$f\colon \mathbb{C} \to \mathbb{C}, \quad z \mapsto \sqrt{z} \tag{2.43}$$

is multi-valued. The issue of a well-defined inverse function can easily be solved by restricting the image of f. Therefore, we cut the complex plane along the negative real axis[4]. The upper and lower half of the complex plane is then defined as the first and second Riemann sheet, also called the physical and unphysical sheet, respectively.

The function f is now well defined on each Riemann sheet. We depict the imaginary part of f on booth sheets in figure 2.3. The orange and blue area shows the first and second Riemann sheet, respectively. Both sheets are disconnected along the cut but connected to each other along the same cut. So we change from one sheet to the other, when we move in a circle around the origin. This is of particular interest when performing contour integrals in the complex plane. Let us now turn back to the analytical structure of the correlation functions.

The analytical structure of the correlation functions is the consequence of causality on the scattering matrix[5] (for details see, e.g., [134–139, 147–150] and references therein.). Bound states and resonances manifest themselves as poles in the scattering matrix. To be more precise, let $s = P_M^2$ be the total momentum (P_M) squared of the incoming particles, which form the bound state, in Minkowski space. Then resonances are poles in the second Riemann sheet, and stable particles are poles on the real axes of the variable $\sqrt{s}$.

[3]The word "function" is not correct, because function implies that the mapping is well-defined and not multi-valued. Nevertheless, we stick to the standard notation in the literature and call it a function.

[4]The cut is not unique. Any path which connects the brunch points (in this case ∞ and 0) can be chosen as a cut. However, we choose the standard definition for the Riemann sheets in this case.

[5]A rigorous proof of this exists only within a non-relativistic scattering, relativistic perturbation theory, and axiomatic field theory [139]. For relativistic scattering beyond perturbation theory this is only an hypothesis (Mandelstam hypothesis [145, 146]).

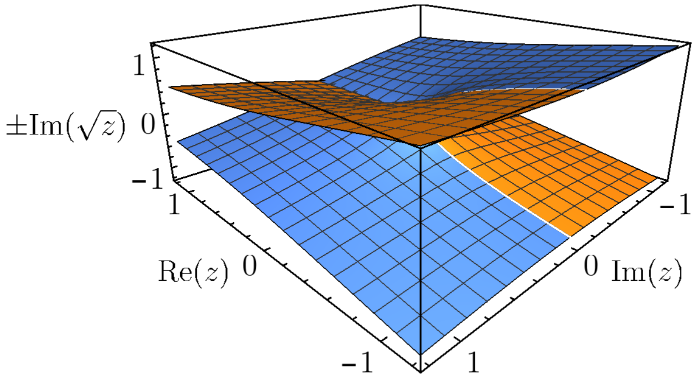

Figure 2.3: The imaginary part of the root function for the both Riemann sheets. The orange (+) and blue (−) represents the image on the first and second Riemann sheet, respectively.

The pole position also reveals the mass (M) and decay-width (Γ) of the particle, given by ($\sqrt{s_{\mathrm{Pole}}} = M - \mathrm{i}\,\frac{\Gamma}{2}$)[6]. For a better understanding, we show the pole position of stable particles and resonances in the complex $\sqrt{s}$-plane (left panel) and the resulting pole positions in the complex s-plane (right panel) in figure 2.4. The red point shows the position of the pole in the first Riemann sheet of the corresponding resonance.

We conclude that from the pole positions of the corresponding correlation function or the propagator, we may extract properties of the bound states and resonances. The BSEs make use of this by evaluating the correlation functions on the pole (particle is on-shell). In the FRG framework, we use the propagators of the mesonic-fields, which are introduced into the system by dynamical hadronization, to extract the pole position. For the propagator, we use the direct calculation in the Minkowski space with the real-time FRG, as well as an extrapolation of the Euclidean propagators into the real-time momentum region. For the latter one, we calculate numerical Padé-like analytical continuation and the Schwinger function of the propagator.

2.5.2 Analytical structure from numerical continuation

Let us now introduce these two extrapolation mechanisms briefly.

Padé-like analytical continuation

In this work, we use a modified version of standard Padé approximant, which follows Schlessinger's point method [151] nested function ($C^N(p)$), to fit the propagators. The approximating function $C^N(p)$ is a rational function given by the expression:

$$C^N(p) = \cfrac{z_1}{1 + z_2 \cfrac{p-p_1}{1+z_3\frac{p-p_2}{1+\dots}}}, \tag{2.44}$$

where the coefficients $z_{1,\dots,N}$ are determined from the input data for the Euclidean propagator on the momentum grid $p_{1,\dots,N}$, see [151, 152] for more details. This allows us to continue the

[6] The mass and decay-width of resonances are also defined by Breit-Wigner parametrization in the literature. The Breit-Wigner is only a good parametrization for particles with $\Gamma \ll M$. This has led to a lot of controversy on the sigma meson due to its large decay-width (see, e.g., [139] for a review on this topic). So we use the pole position for the characterization, which is mathematically well-defined, but maybe less intuitive.

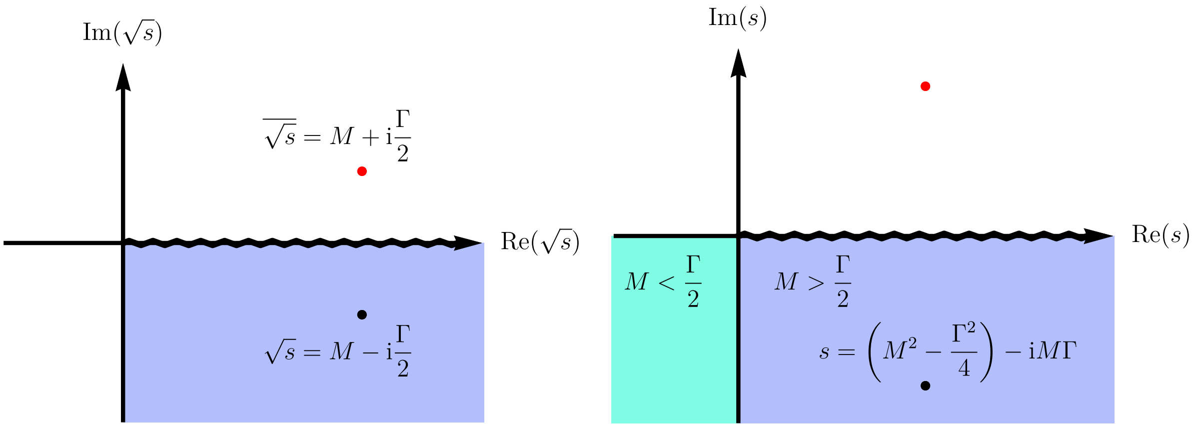

Figure 2.4: The pole positions for stable particles (wiggly line) and resonances (blue area) in the complex $\sqrt{s}$-plane (left panel) and the implication for the resonances in the complex s-plane (right panel). Stable particles are poles on the real axes and resonances are poles in the second Riemann sheet in the complex $\sqrt{s}$-plane. The red point shows the position of the pole in the first sheet of the corresponding resonance.

function in the complex p-plane, thus obtaining poles. We determine the poles numerically, hence the pole masses and the decay-width of the particle.

Schwinger function

Let us now briefly introduce the Schwinger function (for more details see [153, 154]). The Schwinger function $\Delta(t)$ is defined as

$$\Delta(t) = \frac{1}{\pi} \int_0^\infty \mathrm{d}\, p_4 \cos(tp_4) \sigma(p_4^2), \tag{2.45}$$

where $\sigma(p_4^2)$ is one of the dressing functions[7] from the propagator evaluated at zero spatial momentum ($\vec{p} = 0$).

The dressing function with a real pole ($P_{\text{Pole}} = M$) in timelike momenta ($p_4^2 < 0$) yields for the Schwinger function the following:

$$\sigma(p_4^2) \sim \frac{1}{p_4^2 + M^2} \qquad \Rightarrow \qquad \Delta(t) \sim \frac{1}{|M|}\, \mathrm{e}^{-|M|t} \tag{2.46}$$

For a complex conjugate poles $P_{\text{Pole}} = M \pm \mathrm{i}\,\frac{\Gamma}{2}$ we get

$$\Delta(t) \sim \mathrm{e}^{-|M|t} \cos\left(\frac{\Gamma}{2} t + \delta\right), \tag{2.47}$$

where δ is a phase shift.

[7] The QP has a dressing function for each Lorentz-tensor. The Schwinger function calculated from different dressing functions differs quantitatively. The mass and the decay-width are extracted from the exponential tail and oscillation behavior of the Schwinger function, which is the same for the different dressing function of the QP. So it does not matter which dressing function we take. However, the dressing function of the scalar channel is numerically more stable, especially in the chiral limit due to the dynamical chiral symmetry breaking. Thus, we use the scalar channel for our analysis.

The Schwinger function of a real stable particle is an exponential decay function with the decay rate giving the mass of the particle. For a resonance, we get an oscillating exponential decay function. The oscillation frequency is related to the decay-width of the particle. Although the propagator looks very similar in the euclidean space, they differ significantly in their Schwinger function. So the Schwinger function is an excellent quantity to investigate the analytical structure.

In the end let us note another more detail parametrization of the propagators by a meromorphic function of the form:

$$\sigma(p_4^2) = \frac{e^2 + f p_4^2}{p_4^2 + 2m^2\cos(2\theta)p_4^2 + m^4}. \tag{2.48}$$

This parametrization is also often used, like in [154]. This leads to the following Schwinger function:

$$\Delta(t) = \frac{e^2}{2m^3\sin(2\theta)} e^{-tm\cos(\theta)} \left(\sin(\theta + tm\sin(\theta)) + \frac{fm^2}{e^2}\sin(\theta - tm\sin(\theta)) \right). \tag{2.49}$$

We will fit our results using both types of parametrizations. Let us note here that both parametrizations lead to the same results for the poles. However, one parametrization is sometimes more suited for fitting to numerical data. In the latter parametrization, $m\cos(\theta)$ is the real part of the pole and $m\sin(\theta)$ is the imaginary part of the pole. This concludes our brief introduction to the physical background of the thesis, and we turn to the formal part.

Chapter 3

Functional methods

In this chapter, we will focus on the functional methods in the form of the DSEs, BSEs, and the FRG. These approaches are well-known, and hence various aspects are discussed in detailed reviews. So we will keep our introduction short. Some of the more involved technical details are shifted to the appendices for the sake of simplicity.

3.1 DSEs

The DSEs are equations of motions for the correlation functions (see, e.g., [18–22,155–161] and the references therein for a detail introduction in this field). They are the consequence of the invariant measure for the path integral under translation for each field $\Phi_i \to \Phi_i + \epsilon_i$. This leads to the condition, that the total derivative of each field vanishes.

$$
\begin{aligned}
0 &= \int \mathcal{D}\Phi \frac{\delta}{\delta\Phi_i}\, \mathrm{e}^{-S[\Phi]+\int (J\Phi)} = \int \mathcal{D}\Phi \left\{ \left(-\frac{\delta}{\delta\Phi_i} S\left[\Phi\right] + (-1)^G_i J_i \right) \mathrm{e}^{-S[\Phi]+\int (J\Phi)} \right\}, \\
&= \left(-\frac{\delta S}{\delta\Phi_i}\Big|_{\frac{\delta}{\delta J}} + (-1)^G_i J_i \right) Z[J]
\end{aligned}
\tag{3.1}
$$

The first term in the parenthesis in the second line means that the first derivative of the action is evaluated at the derivative of the corresponding sources $\frac{\delta}{\delta J}$. In the standard literature, this is denoted as $\frac{\delta S}{\delta\Phi_i}\left[\frac{\delta}{\delta J}\right]$, and we are also going to use this notation in the following.

Multiplying both sides with $\mathrm{e}^{-W[J]}$ from the left and applying the derivatives correctly yields:

$$
0 = \left(-\frac{\delta S}{\delta\Phi_i}\left[\frac{\delta W[J]}{\delta J} + \frac{\delta}{\delta J} \right] + (-1)^G_i J_i \right) 1. \tag{3.2}
$$

After using the equations (2.7), (2.9), and (2.10); we get the master equation for the 1PI-generating functional:

$$
\frac{\delta\Gamma\left[\phi\right]}{\delta\phi_i} = \frac{\delta S}{\delta\Phi_i}\left[\phi + (-1)^G \int \mathcal{P} \frac{\delta}{\delta\phi} \right] 1. \tag{3.3}
$$

From this equation, all the equations for the n-point functions are derived via suitable derivatives. We will compare some features of the DSEs with the FRG in the last section of this chapter. Hence, conclude our introduction into the DSEs for the moment.

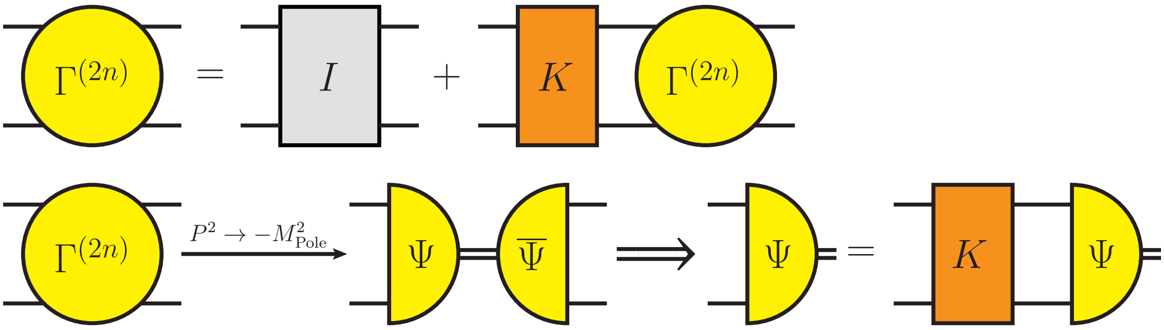

Figure 3.1: Graphical derivation of the BSEs. The first line shows the general expression for n-incoming particles going to n-outgoing particles, described by the $2n$-point-function. Its contributions are splitted in parts, which do not contain the same $2n$-point function with the right pole structure and those who do. The second line shows the extraction of the BSA at the pole. See text for further details.

3.2 Bound states and decays in the Bethe-Salpeter-approach

The full information of the bound states and resonances is encoded in the corresponding Greens function, e.g., from the 4-point function, we may extract masses and decay-width of the mesons. In this work, we are interested in the mass and decay-width of the pion; thus, we will focus on the 4-point functions. Nevertheless. let us be more general in this introductory section (see, e.g., [23–26, 140, 141] and the references therein for a detailed introduction into this topic).

First, consider the evolution of n-incoming particles into n-outgoing particles, which is described by the $2n$-Greensfunction and its amputated counterpart the scattering matrix $T^{(2n)}$:

$$G^{(2n)} = G_0^{(2n)} + G_0^{(n)} T^{(2n)} G_0^{(n)}, \tag{3.4}$$

where $G_0^{(2n)}$ is the disconnected product of $2n$-propagators. Starting point is the finding in the QFT that stable particles or resonances appear as poles (M_{Pole}) in the scattering matrix and correlation functions (see e.g [99, 100, 139, 162] and the referencies therein for more details):

$$T^{(2n)} \propto \frac{\Psi\overline{\Psi}}{P_M^2 - M_{\text{Pole}}^2}, \tag{3.5}$$

where Ψ is the Bethe-Salpeter-amplitude (BSA) and P_M the total momentum of the n-particles in Minkowski space which forms the bound-state or resonance.

Due to the fact that the functional methods are formulated in the Euclidean space, we need to calculate the Greens functions on the complex plane to access quantities from Minkowski space. Unfortunately, such a calculation is too complicated and not feasible at the moment. Luckily, the DSEs of the corresponding Greens functions are simplified if the particle is on-shell and are called the homogeneous BSEs. In the following, we will illustrate how these equations are derived from the DSEs of the 1PI-correlation functions. This derivation is also shown diagrammatically in figure 3.1 for a better understanding.

To be more formal, let P be the total momentum of the particle in Euclidean space. Then, the relation (3.5) transforms into:

$$\Gamma^{(2n)} = \mathcal{N} \frac{\Psi\overline{\Psi}}{P^2 + M_{\text{Pole}}^2}, \tag{3.6}$$

where $\mathcal{N}$ is renormalization constant. Taking appropriate derivatives of the master equation (3.3) yields a DSE for $\Gamma^{(2n)}$. For the following steps, we make use of the condition that only few Greensfunctions on the right hand side of the master equation exhibits a pole for the n-incoming particles.

Diagrammatically, the contributions to the $2n$-point function are splitted in parts containing the same $\Gamma^{(2n)}$ with the right pole structure or not (first line in figure 3.1). Therefore, we multiply this equation with $(P^2 + M^2_{\text{Pole}})$ and take the limit $P^2 \to -M^2_{\text{Pole}}$:

$$\mathcal{N}\Psi\overline{\Psi} = \lim_{P^2 \to -M^2_{\text{Pole}}} \left\{(P^2 + M^2_{\text{Pole}})\Gamma^{(2n)}\right\} = \lim_{P^2 \to -M^2_{\text{Pole}}} \left\{(P^2 + M^2_{\text{Pole}})\frac{\delta^{2n-1}}{\delta\phi^{2n-1}}\frac{\delta S}{\delta\Phi}\right\}. \tag{3.7}$$

From the last step follows that only terms on the right hand side contribute, which have the same pole structure, and the rest vanishes. This simplifies the equation drastically.

For example, only one term remains for the pion in the pure QCD case (see appendix C for further details). From the last equation, we extract BSA and gets the desired homogeneous BSEs, which has the general form (second line in figure 3.1):

$$\Psi = KG_0^{(n)}\Psi, \tag{3.8}$$

where K is the interaction kernel derived from DSEs in our case.

The same procedure can also be used in the nPI-formalism to derive the interaction kernel (see for details [24–26]). The kernel might not be the same using different formalisms, but the result is for an untruncated system. This concludes our introduction into the BSEs, and we proceed with the FRG.

3.3 FRG

The modern formulation of the FRG is based on the Wilsonian idea of integrating out the quantum fluctuation step by step, instead, of doing it at once like for the DSEs (see, e.g., [27–30, 163, 164] for a detailed introduction into this topic). Technically, we regularize the fluctuations below the renormalization group (RG) scale k. This is achieved by introducing an additional term ΔS_k with a regulator R_k, which determines how the quantum fluctuations are integrated out.

Hereby, we get IR-regularized generating functionals:

$$Z_k[J] = \mathrm{e}^{W_k[J]} = \int \mathcal{D}\Phi\, \mathrm{e}^{-S[\Phi]-\Delta S_k[\Phi]+\int(J\Phi)}. \tag{3.9}$$

For practical use, a regulator quadratic in fields is choosen. We will also do this in our study (see [29] for a discussion on a general type of regulator):

$$\Delta S_k[\Phi] = \frac{1}{2}\int_q \Phi(-q)R_k(q)\Phi(q) = \frac{1}{2}\int_q \tilde{\varphi}(-q)R_k^B(q)\tilde{\varphi}(q) + \int_q \overline{\tilde{\psi}}(q)R_k^F(q)\tilde{\psi}(q) + \dots, \tag{3.10}$$

where R_k^B and R_k^F are the bosonic and fermionic regulators respectively. In general, they have the following form:

$$R_k^B(q^2) \propto q^2 r_B(q^2/k^2), \qquad R_k^F(q^2) \propto \not{q}\, r_F(q^2/k^2), \tag{3.11}$$

where r_B and r_F are the regulator shape functions for the bosonic and fermionic case, respectively.

Apart from some conditions, the regulator can be chosen arbitrary, which are:

i) For $k \to 0$, all the quantum fluctuations are integrated out. So we get the full theory, and hence the regulator term should vanish:

$$\lim_{\frac{k^2}{q^2} \to 0} R_k(q) = 0. \tag{3.12}$$

ii) The regulator should act as a mass term in the infrared to ensure the IR regularization:

$$\lim_{\frac{q^2}{k^2} \to 0} R_k(q) > 0. \tag{3.13}$$

iii) The last condition with the UV-cutoff Λ is:

$$\lim_{k^2 \to \Lambda^2 \to \infty} R_k(q) \to \infty \tag{3.14}$$

and ensures, that the classical fields dominate the path integral for $k \to \infty$.

These properties of the regulators translates into boundary conditions for the regularized effective action:

$$\lim_{\Lambda \to \infty} \lim_{k \to \Lambda} \Gamma_k[\phi] = S[\phi], \qquad \lim_{k \to 0} \Gamma_k[\phi] = \Gamma[\phi], \tag{3.15}$$

and thus enable us to flow smoothly from the classical theory S at $k = \Lambda \to \infty$ to the full quantum effective action at $k = 0$.

The derivation of the flow equation, also called the Wetterich's equation, with all its details and with the dynamical hadronization is shifted to the appendix D. The standard form (without the additional term from the dynamical hadronization) is then given by:

$$\partial_t \Gamma_k [\phi] = \frac{1}{2} \operatorname{STr} \left[(\partial_t R_k) \mathcal{P}_k \right], \tag{3.16}$$

where $t = -\ln(\frac{k}{\Lambda})$ is the RG time and $\mathcal{P}_k$ is the propagator in the presence of the regulator:

$$\mathcal{P}_k = \left[\Gamma_k^{(2)} [\phi] + R_k \right]^{-1}. \tag{3.17}$$

In this work, we are interested in the hadron decays, especially of the pion. This requires calculations in Minkowski space called real-time FRG and the concept of the dynamical hadronization. We will deal with the real-time FRG later in chapter 6. So let us now introduce in the following subsections the idea of the dynamical hadronization.

3.3.1 Dynamical hadronization

As already mentioned, bound states and resonances in QFT manifest themselves in resonant momentum channels of the corresponding correlation functions. In effective field theories, such a channel can be described by an exchange of a particle, which is well known as the Hubbard-Stratanovich transformation in the case of local 4-point interaction, already introduced in section 2.4.2. This idea is now generalized for the dynamical hadronization (also sometimes called dynamical bosonization or condensation). For a detailed introduction, see e.g., [29,52–54] and for QCD related application [165–168] and the references therein.

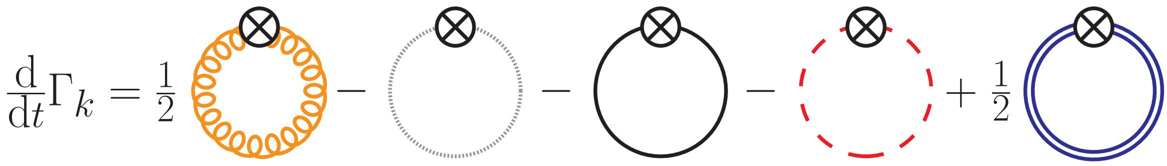

Figure 3.2: Diagrammatic representation of the Wetterich equation. The brown-wiggly, grey-dotted, black-solid, red-dashed, and double blue-solid lines represent the gluons, ghosts, quarks, leptons, and mesons from the dynamical hadronization, respectively. The blob with an x in it shows the regulator insertion.

Due to the fact that the intermediate particle may be created at different scales during the flow, it is introduced into the system scale-dependent. In this way, the FRG avoids the well-known double counting problem of the for the Hubbard-Stratanovich transformation by allowing the identity transformation on the level of the full effective action at each RG step. Let us emphasize that the dynamical hadronization is now developed for a general type of transformation and is no longer restricted to Hubbard-Stratanovich type transformations. Although for our purpose, Hubbard-Stratanovich type transformations are sufficient.

Technically, this is achieved by formulating the transformation rule for the infinitesimal RG step. Let us define $\hat{\Phi}$ as the part of the fields introduced by the dynamical hadronization. Then, we give the relation of how the bound state is formed by the fundamental fields as a function $F[\phi]$:

$$\partial_t \hat{\Phi} = \dot{A}_k F[\phi], \tag{3.18}$$

where $\dot{A}_k$ is the scale-dependency of the transformation and can be chosen arbitrarily.

For example, the σ is a scalar formed of up-antiup and down-antidown, and hence the transformation rule is given by

$$\partial_t \tilde{\sigma} = \dot{A}_k \overline{Q} Q. \tag{3.19}$$

If the transformation rule obeys the following condition, which it does in the example mentioned above:

$$\left\langle \partial_t \hat{\Phi}_i(q) \right\rangle_J = \partial_t \hat{\phi}_i(q). \tag{3.20}$$

Then, the flow equation gets an extra term on the left-hand side from the scale-derivative of the new scale-dependent fields:

$$\frac{\mathrm{d}}{\mathrm{d}\,t}\Gamma_k[\phi] = \partial_t\big|_{\hat{\phi}_k} \Gamma_k[\phi] + \partial_t \hat{\phi} \frac{\delta}{\delta \hat{\phi}} \Gamma_k\left[\phi\right] = \frac{1}{2}\,\mathrm{STr}\left[(\partial_t R_k)\mathcal{P}_k\right] \tag{3.21}$$

For the detailed derivation of the flow equation, see appendix D.

We show the diagrammatic representation of the flow equation (3.21) in figure 3.2 with the different contributions for our study. The first contribution is given by the QCD in the form of the gluons (brown-wiggly lines), ghosts (grey-dotted lines), and quarks (black-solid lines). In the presence of the effective electroweak interaction, we also have leptons (red-dashed lines). The last contribution is from the mesons (double blue-solid line) in the form of the pions and sigma, which are introduced into the system via the dynamical hadronization[1]. The blob with an x in it represents the regulator insertion. We will use this convention for the representation of the different fields throughout this work.

Let us mention the advantage of such a procedure in the following. Strongly correlated systems like QCD are typically investigated in systematic vertex expansions [167–170] (details on the expansion will be discussed in the next section). The higher-order vertices (vertices with no classical part) are generated dynamically into the system in the first place from vertices or diagrams with the classical part. These diagrams have a rapid decay behavior in momentum-space for asymptotically free theories as QCD. This leads to very efficient suppression of the diagrams after the angle integration.

Resonances in the interaction channel, on the other hand, do not have such behavior if their regularized mass is of the same order as the cutoff or below. The advantage of the dynamical hadronization procedure is twofold. First, we resolve the pole behavior in the resonant interaction channel and get well-controlled behavior. This is of particular importance for numerical implementation. The second advantage is the reduction to a lower-order vertex, which is even more important for applications.

For example, in the case of the mesons, the 4-quark-vertex can be reduced to a 2-quark-1-boson-vertex. A 3-point-vertex has a smaller tensor basis and also fewer momentum variables, i.e., any 3-point-vertex depends on two independent external momenta from which one constructs three Lorentz-invariants, as the two momenta squared and the angle between them. On the other hand, a 4-point-vertex depends on three external independent momenta resulting in six Lorentz-invariants.

This also emphasizes the power of the dynamical hadronization procedure. Nevertheless, let us make clear that dynamical hadronization does not entail the reduction to a low-energy effective field theory. It is only a convenient and efficient reparametrization in the dynamical low-energy degree of freedom.

3.4 Properties and comparison of the DSEs and FRG frameworks

FRG in the form of the Wetterich equation and DSE are very close to each other with their assets and drawbacks. Both yield exact equations for the correlation functions and thus are non-perturbative formulations. In both cases, we get an infinite tower of coupled, non-linear equations, which needs to be truncated at some stage for the practical calculations. Before we state some remarks on properties and the truncation scheme, let us first give some definitions.

For our study, we employ the vertex expansion of the effective action in terms of the correlation functions. It can be seen as a generalization of the multidimensional Taylor series for the fields. Thus, it provides us with a systematic expansion scheme for error control in terms of apparent convergence. Usually, the series is expanded around vanishing fields, but the best convergence is achieved by expanding around the minimum of the corresponding potential. We will do this in chapter 6 for the mesonic potential and hence introduce the series for a non-vanishing expansion point.

We have to deal with the tree-level and full quantities. So we define the tree-level n-point-

[1]We do not use different diagrammatic representations for the sigma and pion fields throughout this work.

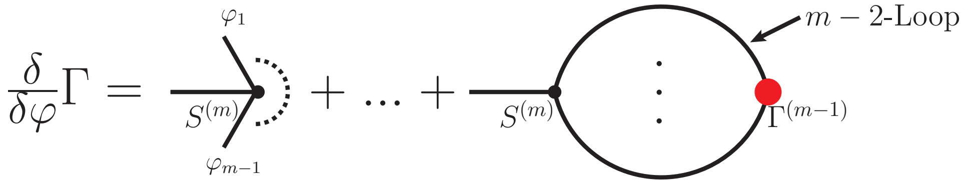

Figure 3.3: Diagrammatic representation of the DSE (3.26). $\varphi_1 \ldots \varphi_m$ indicate the internal fields in the master equation. Small black blobs and big red blobs represent the tree-level and full vertex, respectively, denoted with $S^{(m)}$ and $\Gamma^{(m-1)}$.

vertex with $S^{(n)}$:

$$S^{(n)}_{i_1,\ldots,i_n}[\phi] := \frac{\delta^n}{\delta\phi_{i_1}\ldots\delta\phi_{i_n}} S[\phi]\,, \qquad S^{(n)}_{i_1,\ldots,i_n} \equiv S^{(n)}_{i_1,\ldots,i_n}\left[\phi = \phi^{(0)}\right], \tag{3.22}$$

where $\phi^{(0)}$ is the expansion point for the fields. The full vertex $\Gamma^{(n)}$ is defined analogous[2].

The tree-level and full propagators of the field ϕ at the expansion point will be denoted with D^ϕ and P^ϕ, respectively.

$$D^\phi_{ij} := \left[\frac{\delta^2}{\delta\phi_j\delta\phi_i} S[\phi]\bigg|_{\phi=\phi^{(0)}}\right]^{-1}, \qquad P^\phi_{ij} := \mathcal{P}_{ij}\big|_{\phi=\phi^{(0)}} = \left[\frac{\delta^2}{\delta\phi_j\delta\phi_i}\Gamma[\phi]\bigg|_{\phi=\phi^{(0)}}\right]^{-1}. \tag{3.23}$$

The vertex expansion for the effective action is given by:

$$\Gamma[\phi] = \sum_{n=0}^{\infty} \frac{1}{n!}\Gamma^{(n)}_{i_1,\ldots,i_n}\Delta\phi_{i_1}\ldots\Delta\phi_{i_n} \tag{3.24}$$

where $\Delta\phi = \phi - \phi^{(0)}$. Here, we have used the sloppy notation of $n!$ in the expansion, which is not correct if different fields are involved. To be correct, let n_j be the amount of the different fields with $n = n_1 + \ldots$ then by $n! = n_1! \times \ldots$ the right expression is yield.

In the end, let us state some conventions for the diagrammatic representations of the equations in both frameworks. We will use the convention of a small black blob and big red blob for the diagrammatic representation of the tree-level and full vertex throughout this work. The distinction between the tree-level and full quantities is only relevant in the DSE/BSE framework. In the FRG, all the quantities are full. For the sake of a consistent notation, we will use the big red blob also in the context of the FRG.

Let us also note here that all the internal propagators in the DSE/BSE framework, as well as in the FRG, are full propagators. Therefore, we will not use an extra big red blob for the propagators to indicate a full propagator, which is usually done in the DSE/BSE literature. All the internal propagators are understood to be full propagators.

Let us now compare some properties. The significant differences between both methods are owed to the fact that the classical action of the theory is the starting point for all the functional derivatives of the effective action (right-hand side of the master equation for the DSEs (3.3)). As a consequence of this, each term on the right-hand side has one classical vertex, and hence a bare coupling.

[2] We have already defined the full n-point-vertex and propagator in the presence of the fields in equation (2.10) and (2.11)

The flow equation, on the other hand, is a relation for the effective action and thus has only full vertices and dressed quantities. In figure 3.2, we see the diagrammatic representation of the flow equation, which is an exact equation with a one-loop structure.

The amount of the loops in a DSE depends on the order of the interactions in the theory. For a better illustration of this, let us consider a pure bosonic classical action with an interaction of the order m:

$$S[\tilde{\varphi}] = \int g\tilde{\varphi}^m = \int \frac{1}{m!} S^{(m)} \tilde{\varphi}^m, \qquad\qquad S^{(m)} = m!g \tag{3.25}$$

where g is the corresponding coupling. The master equation yields:

$$\begin{aligned}\frac{\delta\Gamma\left[\varphi\right]}{\delta\varphi} &= \frac{\delta S}{\delta\tilde{\varphi}}\left[\varphi + \mathcal{P}\frac{\delta}{\delta\varphi}\right]1. = mg\left(\varphi + \mathcal{P}\frac{\delta}{\delta\varphi}\right)^{m-1}1 \\ &= \frac{S^{(m)}}{(m-1)!}\left(\varphi^{m-1} + \ldots + \Gamma^{(m-1)}[\phi]\mathcal{P}^{m-1}\right).\end{aligned} \tag{3.26}$$

Here, we suppress the integrals and the indices of the particles for the sake of brevity.

The diagrammatic representation of this equation is shown in figure 3.3. We see each term on the right-hand side has one classical vertex ($S^{(m)}$) with the bare coupling g. The last term in the parenthesis shows that an interaction of the order m in general causes a $(m-2)$-loop on the right-hand side of the master equation, which is connected to a full vertex of the order $m-1$ ($\Gamma^{(m-1)}$).

The Greens function of the order 1 (left-hand side) requires the knowledge of the Greens function of the order $m-1$, which is the highest order appearing on the right-hand side. In general, the n-point correlation functions are related to $n+m-2$-point correlation functions, where m is the highest order of the interactions in the classical action with the corresponding field. Thus, the amount of the loops, as well as the correlation to higher-order Greens functions, depends on the theory under consideration in the DSE.

These numbers are fixed in the FRG. The Wetterich equation relates the effective action with its second derivative. Taking further derivatives of the effective action yields equations of n-point functions, which depends at most on $n+2$-point functions.

A further difference is that each field in the theory has its own master equation for the DSEs (3.3); whereas, the Wetterich equation is one equation for the effective action. Therefore, for a vertex with different kinds of fields, there exist different DSEs starting with different master equations for each field type [126]. The equations are different but equivalent. This provides us with the so-called transverse Ward-Takahashi identities, which says that the difference between these equations should vanish.

For example, the DSE for the quark-gluon-vertex can be derived starting from the master equation for the quarks or gluons. The difference should already be evident by comparing the loop-orders. We have a four-gluon interaction in the classical action. Thus, starting with the gluon field will yield an equation with a 2-loop structure. The quark fields have the maximal interaction term of the order 3 in the classical action. This leads to an equation of 1-loop structure. For some practical use, one equation may be more convenient than the other and thus can be used as a practical advantage. This concludes our presentation of the properties for the different formalisms. In the following, we introduce the truncation procedure used in functional methods.

3.4.1 Truncation

In the context of the truncation, it is also important to discuss the tensor basis of a given vertex. The different kinds of fields in the theory have various attributes, like flavor and color for the quark fields[3]. So the correlation functions and the n-point vertices are tensor-valued.

They are expanded in tensor basis according to their structure in different spaces:

$$\Gamma^{(n)}_{i_1,\dots,i_n} = \sum_m f^m(p_1,\dots,p_n)\tau^m_{i_1,\dots,i_n}, \qquad S^{(n)}_{i_1,\dots,i_n} = \sum_m g^m \tau^m_{i_1,\dots,i_n}, \tag{3.27}$$

where τ^m are the tensor basis with the corresponding scalar dressing functions f^m. They depend on the external momenta of the vertex[4]. For the tree-level vertex, we have the tree-level coupling g^m instead of dressing functions. In general, the contributions of the most tensor basis at tree-level vanishes ($g^m = 0$ for most of the m's) but are generated dynamically into the system at the level of the full vertices ($f^m \neq 0$).

For a better understanding, let us consider the 4-gluon-vertex. It has 136 Lorentz-tensors, which can be reduced to 41 in the Landau-gauge. In addition to these, we have different tensors in the color space, which depend on the amount of the colors and grow exponentially with N_c. For SU(3), we have 8 tensors resulting in a basis of 328 tensors for this vertex (see, e.g., [126]). This is only for the four-gluon-vertex in pure QCD. P-violation, in addition, enlarges the tensor basis of the vertices.

The functional methods yield equations for each dressing function, which is, in general, coupled non-linear to all other dressing functions. So even for one vertex, we have to derive 328 equations in pure QCD, which can not be done by hand. Thus, different Mathematica tools, like DoFun [171, 172] and FormTracer [173], have been developed in the past few years, which makes the most of the calculation automatized. However, these tools are developed in the context of the QCD, and special care has to be taken in the presence of additional symmetry breakings present in this work. The equations are then solved with various numerical methods.

This leads us to the next challenge while calculating the dressing functions numerically. The dressing function depends on all the external momenta at this vertex: for the 4-gluon-vertex, on three independent external momenta from which one constructs six Lorentz-invariants. Even a tiny grid of $32 = 2^5$ points in each direction will lead us to a $32^6 = 2^{30}$ grid points in the momentum-space for each dressing function. Taking all these into account is not feasible at the moment. This example illustrates very well the complexity one has to deal with in the functional methods. Thus, truncating such an extensive system of equation is a necessary step in functional methods.

The truncation is usually done threefold. First of all, we only take $\Gamma^{(n)}$ till to a maximum N into account and neglect all higher-orders ($\Gamma^{(n)} = 0$ for $n \geq N$). This may be guided by the physical intuition or from the perturbation theory that some particular vertices are more dominant for the given question at hand, or the restriction is just given by the technical feasibility.

For a given n-point-vertex, we may also take only a sub-part of the tensor basis. Finally, we may not take the full momentum-dependencies into account and choose particular momentum

[3]We make the following conventions for the rest of this work. We use the indices $\{a, b, c, d\}$, $\{e, f, g, h\}$, $\{i, j\}$, $\{\alpha, \beta\}$ and $\{\mu, \nu, \rho, \sigma\}$ for the colors, flavors, adjoint in color-space, adjoint in flavor-space and Lorentz-space, respectively; if nothing else is stated.

[4]Note that we suppress the delta function for the momenta throughout this work and thus only $n-1$ momenta are independent. Hence, we may denote sometimes only (n-1) momenta for the dressing functions.

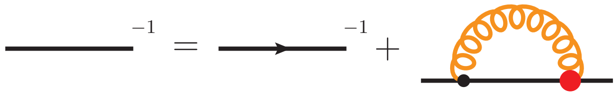

Figure 3.4: Diagrammatic representation of the DSE for the QP (3.28). This is given by all the possibilities how a quark can propagate from one place to an other in QCD. The black line with an arrow on it represents the tree-level propagator.

channels, which may be more dominant for the question at hand. This concludes our introduction to functional methods. In the end, we present the rainbow-ladder truncation [18, 19, 23] for the QP and the pion BSE, which we use for our study.

Rainbow-ladder truncation

Applying the master equation (3.3) on the QCD action from eq. (2.32) yields the following DSE for the QP:

$$\left(P^{Q}\right)^{-1} \equiv \Gamma^{(2),Q} = S^{(2),Q} + \int S^{(3),A,Q,\overline{Q}} P^{Q} \Gamma^{(3),A,Q,\overline{Q}} P^{A}. \tag{3.28}$$

Here, we have suppressed all the internal indices of the different fields for the sake of clarity. The diagramatical representation of this equation is shown in figure 3.4. The inverse full QP is given by the inverse tree-level QP and the way how a quark can propagate in QCD viz. by emitting a gluon and absorbing it.

The equation shows that the QP needs the knowledge of the full gluon propagator (P^A) and the full quark-gluon-vertex, which have their own DESs depending on higher-order n-point functions. These two full quantities couple the matter sector with the Yang-Mills sector. The fully back-coupled analysis of the Yang-Mills sector and the matter sector is very complicated and a current field of investigation on its own (see, e.g., [20, 167, 174–178] and the references therein for the role of the quark-gluon-vertex).

Thus, we will not dynamically back-couple these both sectors, but rather take the tree-level tensor structure for the quark-gluon-vertex, which is the rainbow-ladder truncation[5] [18,19,23], with an effective coupling for the strong interaction, the well-known Maris-Tandy coupling [179].

To be more precise, the tree-level quark-gluon-vertex[6] is given by:

$$S^{(3),A,Q,\overline{Q}}_{(i,\mu),(a,e),(b,f)} = -\,\mathrm{i}\, g_s t^i_{ba} \gamma^\mu \delta_{ef} = g_s \tau^1, \qquad \tau^1_{(i,\mu),(a,e),(b,f)} = -\,\mathrm{i}\, t^i_{ba} \gamma^\mu \delta_{fe}. \tag{3.29}$$

The basis of the full quark-gluon-vertex has 12 basis tensors, which are reduced to 8 in Landau-gauge, and only one of them (τ^1) has a non-vanishing contribution at tree-level. So we take only this part of the basis for the full quark-gluon-vertex and combine this with the full gluon propagator to an effective interaction with tree-level tensor structure.

$$P^A(q)\Gamma^{(3),A,Q,\overline{Q}}_{(i,\mu),(a,e),(b,f)}(q, p-q, p) = \frac{\alpha_s(q^2)}{g_s^2} D^A(q) S^{(3),A,Q,\overline{Q}}_{(i,\mu),(a,e),(b,f)}. \tag{3.30}$$

[5] Applying this truncation for the QP is called the rainbow truncation. Since the same structure for vertices is also present in the BSEs (see, e.g., the pion BSE in section 5.4), the same truncation is also applied for the BSE, which is called the ladder truncation. Therefore, the self-consistent truncation is called the rainbow-ladder truncation.

[6] The tree-level gluon propagator D^A is already stated in equation (2.33)

The Maris-Tandy coupling α_s is given by

$$\alpha_s(q^2) = \frac{\pi}{\omega^6} D q^4 \,\mathrm{e}^{-\frac{q^2}{\omega^2}} + \frac{2\pi\gamma_m [1 - \exp(-\frac{q^2}{m_t^2})]}{\ln[\mathrm{e}^2 - 1 + (1 + \frac{q^2}{\Lambda_{\mathrm{QCD}}^2})^2]} \tag{3.31}$$

Here, the parameters are adapted to describe pions in the vacuum adequately. In the literature these parameters are fitted for degenerate masses of up and down-quarks [180]. For a detailed analyses of different parameter sets, see e.g., [181, 182].

To allow for comparison, we choose here one such set, namely $\Lambda_{\mathrm{QCD}} = 0.234\,\mathrm{GeV}$, $m_t = 1.0\,\mathrm{GeV}$, $\omega = 0.4\,\mathrm{GeV}$, and $D = 0.93\,\mathrm{GeV}^2$. $\gamma_m = 12/(11N_c - 2N_f)$ is the anomalous dimension of the QP. Because we consider each quark generation on its own, we choose $N_f = 2$ and $N_c = 3$. The last term for the Maris-Tandy coupling is to ensure the right perturbative behaviour of the strong coupling in the far UV.

In the end, let us mention that the rainbow-ladder truncation is quite successful in determining the light meson and baryon sector, as shown in these works [18–20, 23, 24, 26, 31, 32, 183–188]. This is owed to the fact that coupling conserves the most important features for our purpose, like dynamical mass generation and the correct treatment of chiral symmetry. Therefore, this is sufficient for our study (see, e.g., [26, 189–191] and the references therein for investigations beyond the rainbow-ladder truncation). This concludes our introduction to the formal part of the thesis. We now present the results in the following chapters starting with the QP.

Chapter 4

Quark propagator with broken C, P, and flavor symmetry

In this chapter, we will investigate the influence of the broken C, P and flavor symmetry on the QP. For this purpose, we insert an explicitly symmetry-violating term in the Lagrangian. Using our ansatz in equation (2.21) and (2.32) leads us to the following Lagrangian:

$$\mathcal{L}_{ESB} = \mathcal{L}_{\text{QCD}}^{\text{gauge-fixed}} + \mathcal{L}_{\text{SB}} = \overline{Q}_f \left(\not{D} + m_f \right) Q_f + \frac{g_w}{2} \sigma_{ef} \left(\overline{Q}_e^L \, \mathrm{i} \not{p} Q_f^L \right) + \mathcal{L}_{\text{Rest}}, \tag{4.1}$$

where σ_{ef} is only 1 for mixed flavour within a generation else 0. $\mathcal{L}_{\text{Rest}}$ is the remainder of the QCD Lagrangian and does not play a specific role in the following.

First, we focus on the modification of the QP caused by the additional symmetry violation and compare it with the pure QCD case in section 4.1. Afterward, we present the numerical results of the different quantities for the QP in section 4.2. We will also present an analysis of the analytical structure of the QP using its Schwinger function, as well as Padé-like analytical continuations. In particular, we will put these both methods in perspective to each other.

We list many further results in appendix B, providing a complete picture of the QP in this setup for a wide range of parameters and quark masses. All of the insights and results are finally discussed in section 4.3. The major part of the results presented here are already published in [192, 193].

4.1 Quark propagator

In this section, we first analyze the general structure of the QP, which has additional non-vanishing contributions due to symmetry violation in section 4.1.1. The significant contributions to the QP caused by these are already visible at the tree-level QP. Thus, we deal with them in section 4.1.2. Afterward, we turn towards the full QP and analyze the coupled system of the DSEs in 4.1.3.

4.1.1 Structure of the quark propagator

The breaking of the explicit flavor symmetry results in non-vanishing QPs (P_{ef}^{Q}) from flavor e to f. In addition to this, each QP also has non-vanishing axial and pseudo-scalar channels. In particular, the QP and its inverse have the same tensor basis. The standard notation for the vector and scalar channel dressing functions of the inverse Propagator in the literature is

A and B. We will keep this and denote the dressing functions for the axial and pseudo-scalar channels of the inverse propagator with C and D. The corresponding dressing functions of the propagator are expressed by a tilde.

We can write the QP in a matrix form, where the diagonal elements are the QPs for pure flavor, and the off-diagonal elements are the QPs for mixed flavors. So we combine the flavor elements in a matrix, e. g., for the vector channel as:

$$A = \begin{pmatrix} A_{uu} & A_{ud} \\ A_{du} & A_{dd} \end{pmatrix}, \tag{4.2}$$

which allows for a compact notation. Writing the propagator and its inverse in terms of these matrices yields:

$$\begin{aligned} P^Q(p^2) &= \tilde{A}(p^2)\,\mathrm{i}\not{p} + \tilde{B}(p^2)\mathbb{1} + \tilde{C}(p^2)\,\mathrm{i}\not{p}\gamma^5 + \tilde{D}(p^2)\gamma^5, \\ \left(P^Q(p^2)\right)^{-1} = \Gamma^{(2),Q} &= -A(p^2)\,\mathrm{i}\not{p} + B(p^2)\mathbb{1} + C(p^2)\,\mathrm{i}\not{p}\gamma^5 + D(p^2)\gamma^5. \end{aligned} \tag{4.3}$$

The dressing functions of the propagator and its inverse are related with each other. In general, the dressing functions of the propagator depends on all the dressing functions of the inverse propagator in a complicated way, and generically denoted as:

$$\tilde{A}_{ef} = \tilde{A}_{ef}(A_{gh}, B_{gh}, C_{gh}, D_{gh}). \tag{4.4}$$

This relation is simplified drastically in pure QCD, where only the vector and scalar channel of the pure flavour contributes. It is given by:

$$\tilde{A}_{ee}(p^2) = \frac{A_{ee}(p^2)}{A_{ee}^2(p^2)p^2 + B_{ee}^2(p^2)}, \qquad \tilde{B}_{ee}(p^2) = \frac{B_{ee}(p^2)}{A_{ee}^2(p^2)p^2 + B_{ee}^2(p^2)}. \tag{4.5}$$

This is no longer true in our case. The fundamental relation:

$$P^{-1}P = \mathbb{1}. \tag{4.6}$$

for the propagator and its inverse yields the general relations between the matrix-valued dressing functions:

$$\begin{aligned} A\tilde{A}p^2 + B\tilde{B} + C\tilde{C}p^2 + D\tilde{D} &= \mathbb{1}, & -A\tilde{B} + B\tilde{A} + C\tilde{D} - D\tilde{C} &= 0, \\ -A\tilde{D} - D\tilde{A} + B\tilde{C} + C\tilde{B} &= 0, & A\tilde{C}p^2 + C\tilde{A}p^2 + B\tilde{D} + D\tilde{B} &= 0. \end{aligned} \tag{4.7}$$

While this is a system of linear equations for either the matrix elements of the propagator or its inverse, an explicit solution is of little use. The expressions become incredibly lengthy and, therefore, prohibitively expensive to evaluate during numerical calculations. Thus, in our investigations, we always solved such equations numerically at double precision.

For the analysis of the P-violation, it is more convenient to split the Lorentz-channels into left-handed $\tilde{L}(p^2)$ and right-handed $\tilde{R}(p^2)$ contributions to the QP, instead of splitting it into the vector and axial channels:

$$P(p^2) = \frac{1}{\sqrt{2}}\tilde{L}(p^2)\,\mathrm{i}\not{p}(\mathbb{1} - \gamma^5) + \frac{1}{\sqrt{2}}\tilde{R}(p^2)\,\mathrm{i}\not{p}(\mathbb{1} + \gamma^5) + \tilde{B}(p^2)\mathbb{1} + \tilde{D}(p^2)\gamma^5, \tag{4.8}$$

with the relations:

$$\tilde{L}(p^2) = \frac{1}{\sqrt{2}}\left(\tilde{A}(p^2) - \tilde{C}(p^2)\right), \qquad \tilde{R}(p^2) = \frac{1}{\sqrt{2}}\left(\tilde{A}(p^2) + \tilde{C}(p^2)\right). \tag{4.9}$$

To assess the consequences for the left-handed and right-handed contributions, it is useful to define their relative ratio as:

$$\tilde{r}_{ef}(p^2) = \frac{\tilde{L}_{ef}(p^2) - \tilde{R}_{ef}(p^2)}{\tilde{L}_{ef}(p^2) + \tilde{R}_{ef}(p^2)} = -\frac{\tilde{C}_{ef}(p^2)}{\tilde{A}_{ef}(p^2)}. \tag{4.10}$$

We will analyze this quantity for the effects on the P-violation in section 4.2.5. Let us now turn to the tree-level QP first.

4.1.2 The tree-level quark propagator

The tree-level propagator already reveals the major contributions for the QPs. They are separated in the different channels at tree-level, but will mix in the full case. Thus, for a better understanding, let us state the QPs at tree-level, which are given by:

$$\begin{aligned}
D^Q_{uu}(p^2) =& \frac{1}{N(p^2)}\left[(m_d^2 + (1-2g_\mathrm{w}^2)p^2)\,\mathrm{i}\,\not{p} + m_u(m_d^2 + p^2)\mathbb{1} + 2g_\mathrm{w}^2 p^2\,\mathrm{i}\,\not{p}\gamma^5\right],\\
D^Q_{dd}(p^2) =& \frac{1}{N(p^2)}\left[(m_u^2 + (1-2g_\mathrm{w}^2)p^2)\,\mathrm{i}\,\not{p} + m_d(m_u^2 + p^2)\mathbb{1} + 2g_\mathrm{w}^2 p^2\,\mathrm{i}\,\not{p}\gamma^5\right],\\
D^Q_{\substack{ef,\\ e\neq f}}(p^2) =& \frac{g_\mathrm{w}}{N(p^2)}\left[(m_e m_f - p^2)\,\mathrm{i}\,\not{p} - (m_e + m_f)p^2\mathbb{1} - (m_e m_f + p^2)\,\mathrm{i}\,\not{p}\gamma^5 - (m_e - m_f)p^2\gamma^5\right],
\end{aligned} \tag{4.11}$$

where the common denominator is given by:

$$N(p^2) = m_d^2 m_u^2 + (m_u^2 + m_d^2)p^2 + (1-4g_\mathrm{w}^2)p^4 = (1-4g_\mathrm{w}^2)(p^2 + M_l^2)(p^2 + M_h^2). \tag{4.12}$$

Here, we have factorized the denominator to see both poles of the tree-level propagator.

The poles are given by:

$$M_{l/h} = \sqrt{\frac{m_u^2 + m_d^2 \mp \sqrt{(m_u^2 - m_d^2)^2 + 16 g_\mathrm{w}^2 m_u^2 m_d^2}}{2(1-4g_\mathrm{w}^2)}}. \tag{4.13}$$

For $g_\mathrm{w} \to 0$, M_l goes to the mass of the lighter quark, and M_h to the mass of the heavier quark. By increasing g_w, the value of M_l is decreased and M_h is increased and thus increases the effect of the mass splitting.

Note that M_l and M_h diverge at $g_w = 0.5$. At this point, the poles turn imaginary, indicating a breakdown of the trivial vacuum around which the perturbative expansion is performed. This feature will not be lifted in the full non-perturbative treatment. Hence, we are only able to find solutions as long as $g_\mathrm{w} \lesssim 0.4$. Since this is a very large breaking, probably far too strong for the setting of neutron star mergers guiding this work, we did not endeavor to find out what happens beyond this point, thus restricting ourselves to breaking strengths below this value.

The explicit chiral symmetry breaking by the tree-level masses manifests itself in the scalar channel of the pure and mixed flavors. In the chiral limit, the scalar channel vanishes at tree-level, but due to dynamical chiral breaking, the scalar channel does not vanish for the full propagator.

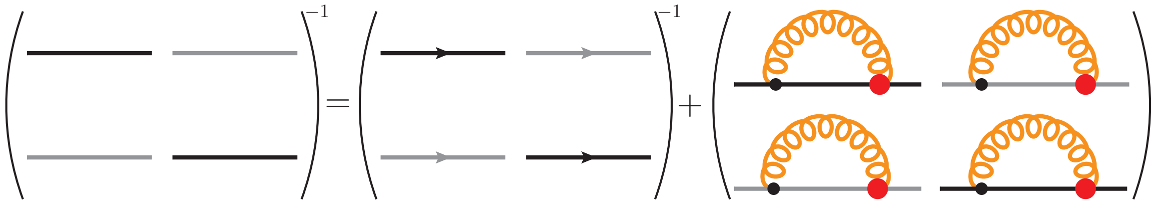

Figure 4.1: Diagrammatic representation of the DSEs for the QPs. The black- and grey-solid lines represent QPs for pure and mixed flavors, respectively.

The vector channel of the mixed propagator is proportional to $g_{\mathrm{w}}(m_u m_d - p^2)$, which changes its sign for $p^2 > m_u m_d$. The influence of this is a contribution in different directions for high- and low-momenta. For heavier bare quark masses, this contribution is shifted to higher momenta.

The most remarkable contribution, a difference of both quark masses, appears in the pseudo-scalar channel of the mixed propagator. This will have a significant impact on the full propagator. Remarkably, this contribution appears with an opposite sign for the propagator from up-like quarks to down-like quarks and the other way around: Although we have taken the same strength for the propagation of both mixed QPs in our ansatz, we get a difference, if the quarks have different masses. This concludes our analysis on the tree-level propagator, and we proceed with the full propagator and consider their DSEs.

4.1.3 The DSEs of the quark propagator

A graphical representation of the DSEs in the presence of the additional symmetry violations is shown in figure 4.1. The equations look similar to those of QCD (see figure 3.4), where the QP can also be given in a matrix form, but with vanishing off-diagonal elements. It is only the appearance of the off-diagonal tree-level elements, which gives rise to all differences.

Due to the similarities, we employ the same rainbow-ladder truncation as stated in equation (3.30) to this system of equations resulting in:

$$\begin{aligned}\Gamma_{ef}^{(2),Q}(p^2,\mu^2) =& \sqrt{Z_{2,e}(\mu^2,\Lambda^2)Z_{2,f}(\mu^2,\Lambda^2)}S_{ef}^{(2),Q} + \frac{Z_{2,e}(\mu^2,\Lambda^2)Z_{2,f}(\mu^2,\Lambda^2)}{3\pi^3}\times \\ &\times \int^{\Lambda} \mathrm{d}^4 q \frac{\alpha_s(k^2)}{k^2}\left(\delta_{\nu\rho} - \frac{k_\nu k_\rho}{k^2}\right)\gamma_\nu P_{fe}(q^2,\mu^2)\gamma_\rho, \end{aligned} \tag{4.14}$$

where $Z_{2,e}$ and $Z_{2,f}$ are the quark wavefunction-renormalization constants for flavor e and f. $\int^\Lambda$ represents a translationally-invariant regularization with the UV-cutoff Λ. μ is the renormalization point and $k = q - p$.

By inserting the form of the QPs from eq. (4.3) in (4.14), we extract the equations for the dressing function. The detailed expressions are stated in the appendix B.1. For our study, we take for the bare quark masses $m_{\mathrm{up}} = 2.3\,\mathrm{MeV}$, $m_{\mathrm{down}} = 4.8\,\mathrm{MeV}$, $m_{\mathrm{strange}} = 95\,\mathrm{MeV}$, $m_{\mathrm{charm}} = 1.275\,\mathrm{GeV}$, $m_{\mathrm{bottom}} = 4.18\,\mathrm{GeV}$ and $m_{\mathrm{top}} = 160\,\mathrm{GeV}$ from the PDG [194]. Besides, we will also consider the chiral limit, as well as degenerate cases.

Let us note here that the PDG values are in a different renormalization scheme, actually even different schemes for different flavors, and at different renormalization points for the different flavors. Here, we aim to compare different flavors directly. Therefore, we chose as a uniform renormalization scheme that our quark masses should equal the values listed above at $\mu = 10^6$ GeV, and use a miniMOM-type scheme.

At the perturbative resumed one-loop level in our miniMOM scheme, this amounts to a difference of about $25 - 35\%$ larger masses, depending on flavor, compared to the PDG renormalization scheme. Note that the small difference is due to the appearance of the running coupling at the renormalization point in this scheme. At the qualitative level of our study, this will make little difference. Ultimately, if we would be able to solve the DSEs exactly, the scheme would anyhow not matter for physical observables.

4.2 Numerical results

For each quark generation, we have 2 propagators for pure flavor and 2 propagators for mixed flavor, and each has 4 Lorentz-channels, resulting in 16 dressing functions. We will consider 6 cases in total, the chiral limit and three physical quark generations, and two cases of degenerate masses. Therefore, we have numerical results for 192 dressing functions and each of them as a function of the weak strength.

In addition to that, we also have the Schwinger function for each dressing function. To avoid cluttering up the main text, most of these results are relegated to appendix B. Here, only the qualitatively most remarkable results will be analyzed. The results in the appendix do not add any conceptual new to this section.

The result for the QP in QCD are usually given in terms of the wavefunction renormalization $Z(p^2) = 1/A(p^2)$ and massfunction $M(p^2) = B(p^2)/A(p^2)$ [18,23,153]. For ease of comparison, the case with $g_\mathrm{w} = 0$ will serve as a reference. Therefore, in section 4.2.2 the results for Z and $\tilde{A}_{AA}$ will be explored. Afterward, the massfunction and the related $\tilde{B}_{AA}$ will be discussed in section 4.2.3.

We will analyze the pole structure of the QPs in section 4.2.4. In section 4.2.5, we will investigate the results for the axial channel $\tilde{C}_{AA}$, and study the impact of P-violation. But first, it is necessary to discuss the involved scales, as the problem is now a multi-scale one. Note that in the chiral limit, there is no difference between the up-like quark and down-like quark, and thus the flavor-diagonal elements coincide. In these cases, always the up-type one will be shown.

4.2.1 Relative scales

g_w is dimensionless. Thus, a possibility for the comparison of the breaking strength with the strong interaction is given by g_w and the average strength of the Maris-Tandy coupling $\overline{\alpha}$ in the IR region. Neglecting the perturbative part of the Maris-Tandy coupling, we get:

$$\overline{\alpha} = \int \frac{\mathrm{d}\,x}{2\pi} \alpha(x) \approx 5.5, \tag{4.15}$$

where $x = q^2/\omega^2$ and the integration region for the average is taken from $q = 0$ to $q = 1$ GeV. The weak coupling is constant throughout. The smallest values of the weak strength $g_\mathrm{w} = 10^{-6}$ is many order of magnitude smalle than $\overline{\alpha}$ and thus represent the natural case. The largest value of $g_\mathrm{w} = 0.4$, which is only one order of magnitude smaller than $\overline{\alpha}$, substantially deviates from nature. This also justifies our choice to restrict to not too large values of g_w. However, such effects may play a role in theories with strongly-interacting chiral sectors.

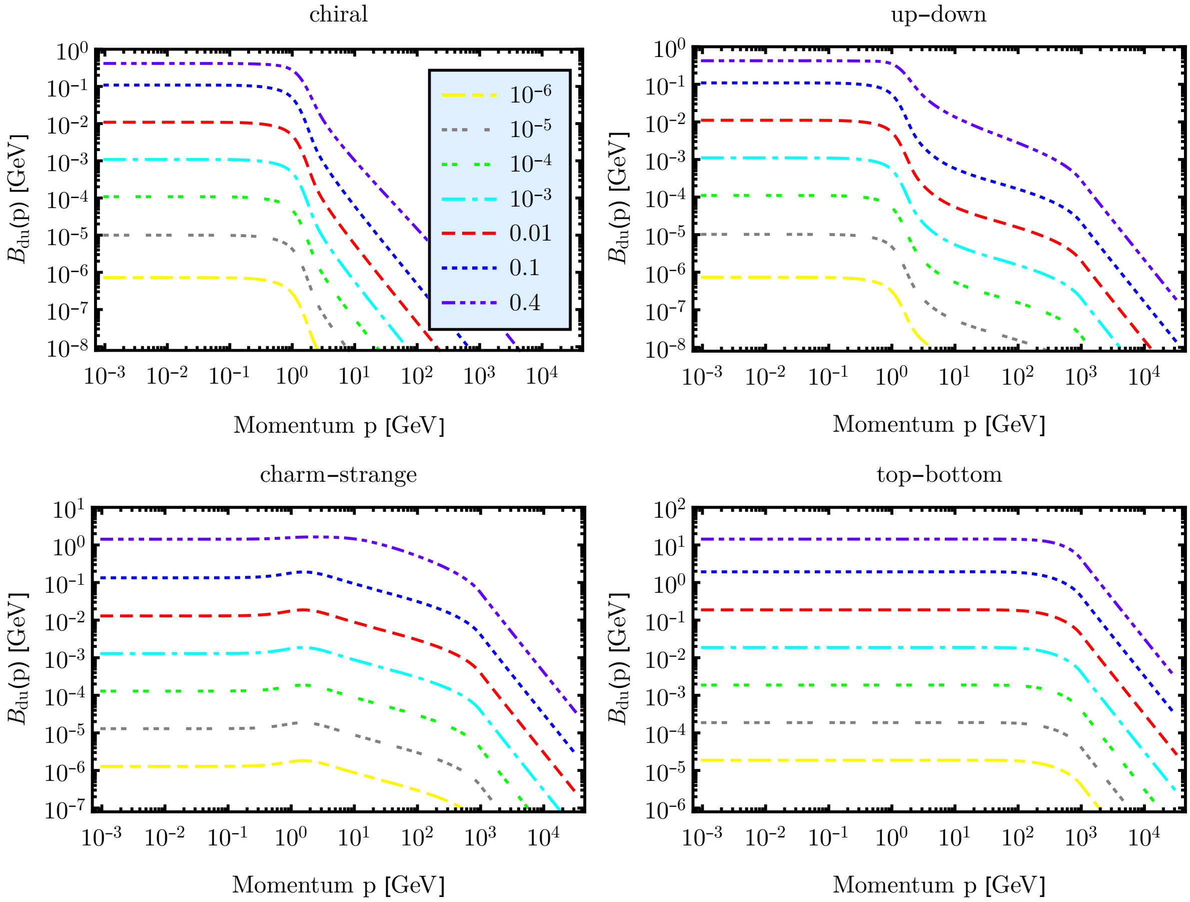

Figure 4.2: The scalar channel for the inverse mixed propagator in the chiral limit and for all three quark generations.

The interaction also manifests itself into a momentum-scale, in particular, appearing in the scaler channel. The weak strength is transmuted into a momentum-scale in the flavor off-diagonal-element, which is zero without breaking. It is shown for various quark masses in figure 4.2.

It is seen that in the IR this dressing function is approximately proportional to the weak strength for $g_\mathrm{w} \leq 0.1$. Note that the generated scale depends on the quark masses. For both light generations, the difference to the chiral limit is small. For the top- and bottom-quark, the generated scale is one order of magnitude bigger at the same g_w. Thus, there is a linking of the different involved scales.

4.2.2 Wavefunction renormalization function

From equation (B.3) follows that A_{uu} and $\tilde{A}_{uu}$ are directly linked with each other, and thus $Z = 1/A_{uu}$ is also directly related to $\tilde{A}_{uu}$. These dressing functions are shown in figure 4.3 for different values of g_w and different flavors. Starting in the chiral limit (subfigure 4.3a), we see no appreciable effect for values of $g_\mathrm{w} \lesssim 0.01$. At larger values $\tilde{A}_{uu}$ slightly increases in the UV when increasing g_w. In the mid momenta regime, it is slightly decreased, and in the IR,

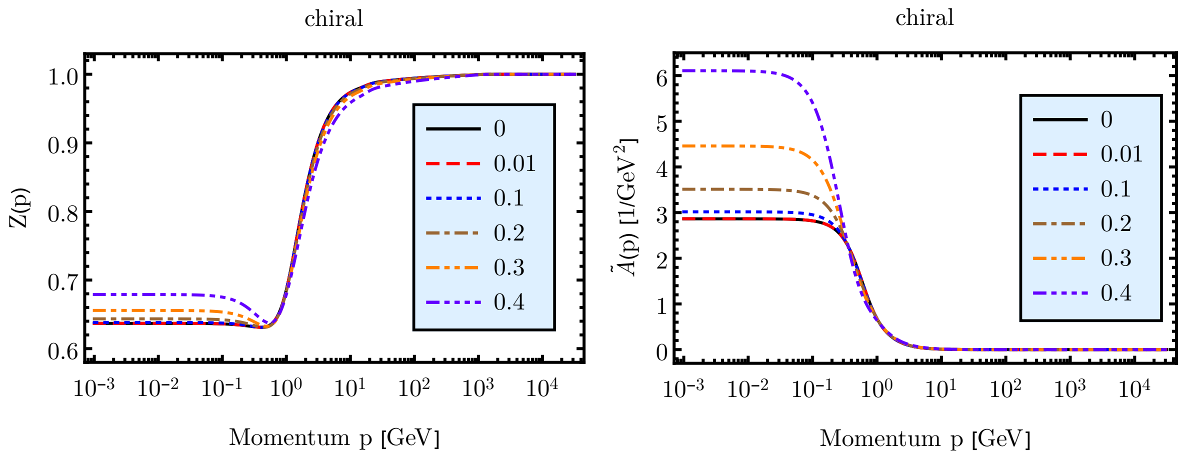

(a) The Wavefunction renormalization (left panel) and the vector channel of the QP (right panel) for different values of g_{w} in the chiral limit.

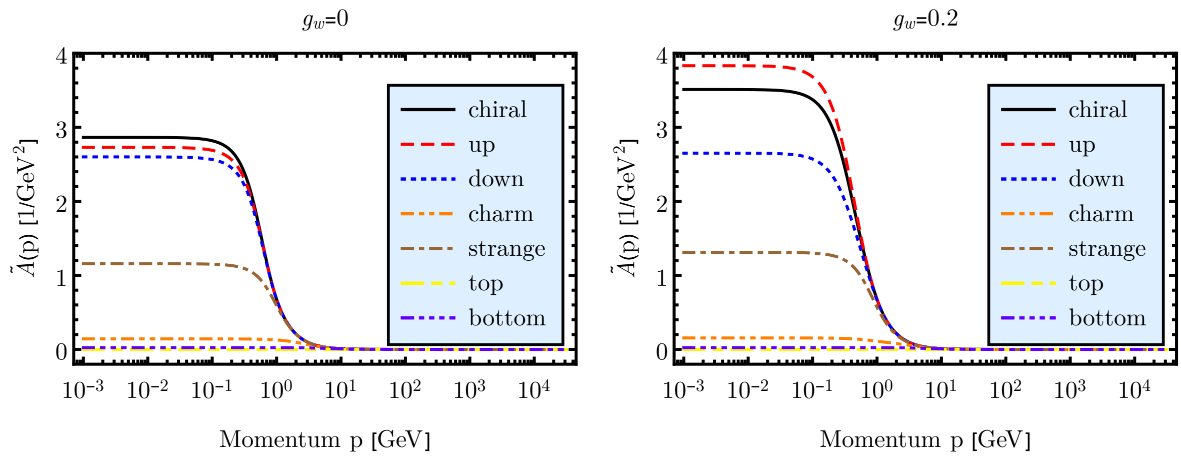

(b) The flavor-diagonal vector channel without (left panels) and with (right panel) explicit breaking.

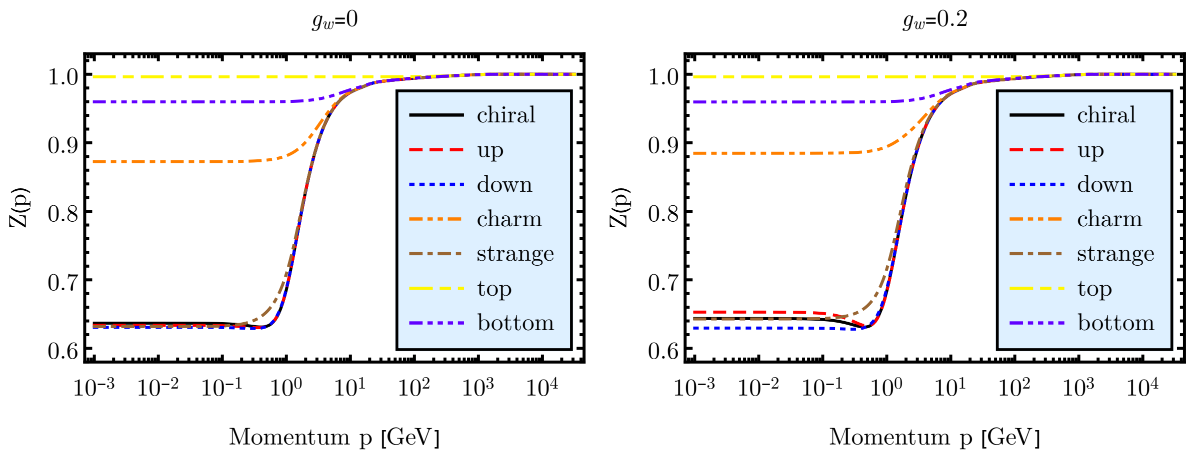

(c) The wavefunction renormalization without (left panels) and with (right panel) explicit breaking.

Figure 4.3: The wavefunction renormalization and the flavor-diagonal vector channel.

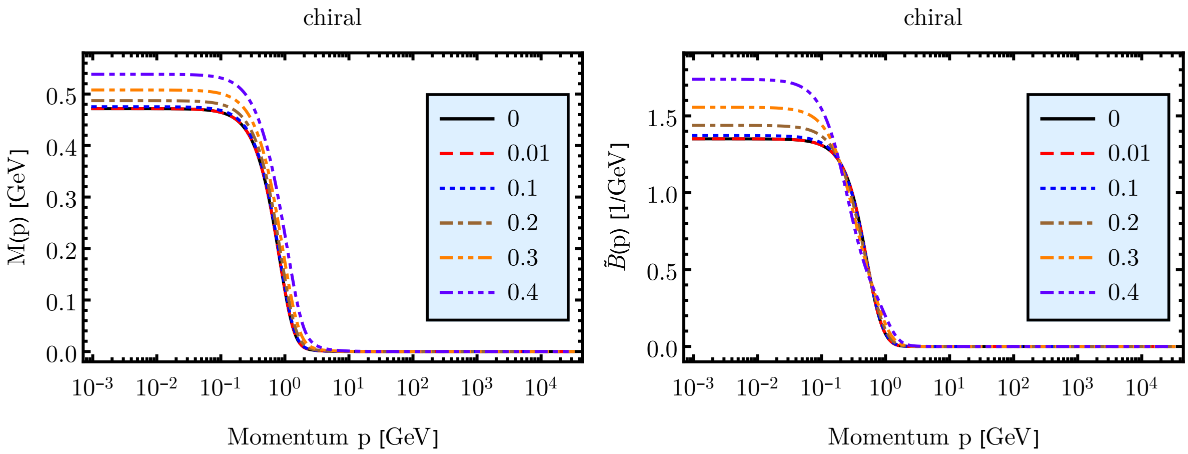

Figure 4.4: The massfunction (left panel) and the flavor-diagonal scalar channel (right panel) for different values of g_w in the chiral limit.

it is significantly increased. A consequence of this is that Z also increases in the IR. This can be understood from equation (B.3), as A_{uu} is obtained from integrating $\tilde{A}_{uu}$ multiplied with a kernel over all momenta. Because $\tilde{A}_{uu}$ is increased in the UV very little and more decreased in the mid-range, Z is slightly decreased in the UV range due to the integration. For the same reason, Z is not increased as much as $\tilde{A}_{uu}$ is increased in the IR.

For other quark masses, the same behavior is seen, as shown in the second and third panel of figure 4.3. The graph shows that $\tilde{A}$ is increased in the IR for all quark flavors, and thus Z is also increased.

The effect comes from different sources. One is from g_w and the other from a combination of g_w and the bare quark masses. Especially, A and Z are increased for the up quarks more than in the chiral limit. The value for up-like quarks is increased, in general, more than for down-like quarks. This is also seen in figure B.1 in appendix B.3.1 in more detail.

This can be understood from equation (4.11) for the tree-level case. One of the contributions arises from the bare quark masses and another from mass splitting with different signs. This creates the cross-talks leading to the observed effects. We will return to this later in section 4.2.5. In addition, the absolute value is decreased for higher bare quark masses, as anticipated because the masses of the quarks enter in the denominator of the QP. This can be seen already for the tree-level propagator in equation (4.12).

4.2.3 Massfunction

The relations between the dressing functions of the QP and its inverse are more involved as in QCD, as already discussed in 4.1.1. In QCD, the relation is given in equation (4.5), which is expressed in the standard literature in the following form:

$$\tilde{A}_{ee}(p^2) = \frac{Z_{ee}(p^2)}{p^2 + M_{ee}^2(p^2)}, \qquad \tilde{B}_{ee}(p^2) = \frac{Z_{ee}(p^2)M_{ee}(p^2)}{p^2 + M_{ee}^2(p^2)}. \tag{4.16}$$

To be able to compare, we therefore choose to define a (pseudo) massfunction as:

$$M_{ee}(p^2) = \frac{B_{ee}(p^2)}{A_{ee}(p^2)}, \tag{4.17}$$

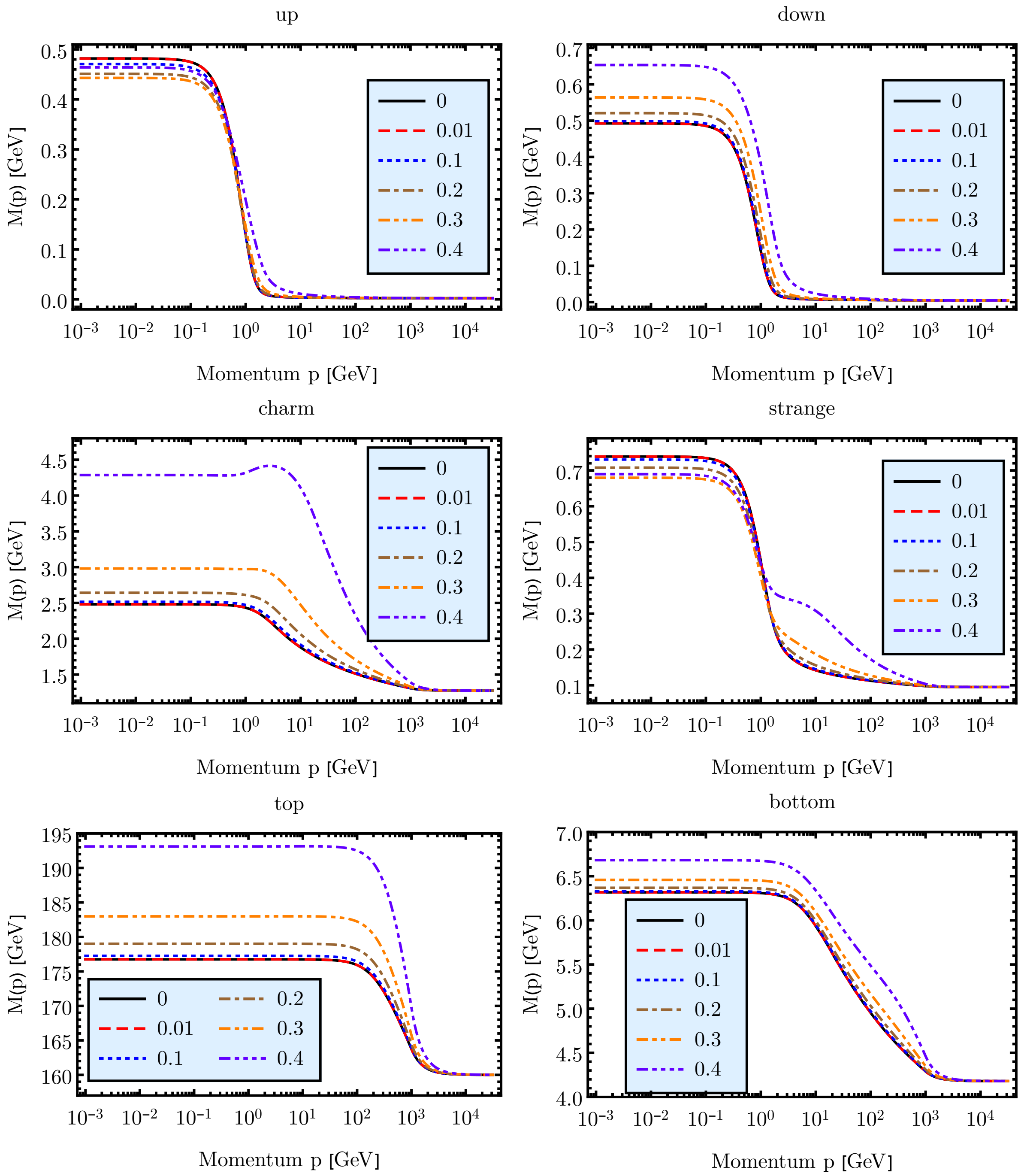

Figure 4.5: The massfunction for different values of g_{w}. From top to bottom generations one to three are shown, and the left-hand panels show up-type quarks, and the right-hand panels down-type quarks.

which by construction coincides with the usual one in the QCD case. Of course, neither in QCD nor here this function needs to coincide with the actual mass. Any such statement requires the analysis of the pole positions in section 4.2.4. Nonetheless, we will stick here with the usual convention and call this quantity massfunction.

The dependence on g_w of this massfunction in the chiral limit is shown in the left panel of figure 4.4. As in QCD, the massfunction is non-zero, indicative of chiral symmetry breaking. The massfunction starts to change appreciably for $g_\mathrm{w} \gtrsim 0.01$, like the wavefunction renormalization. The same is true for $\tilde{B}_{uu}$, which is also shown in the right panel of figure 4.4. Since the connection between B_{uu} and $\tilde{B}_{uu}$, due to equation (B.3), is similar as for A_{uu} and $\tilde{A}_{uu}$, the same analysis as before applies, and the response to g_w follows the same pattern.

At non-zero masses, the picture changes. This is shown in figure 4.5 for all quark flavors. The massfunction M of the up quark is decreased by increasing g_w for $g_\mathrm{w} \lesssim 0.3$. For larger values, it increases again, but here our approximations start to break down. This replicates the result of the tree-level propagator in section 4.1.2. The mass of the heavier quark in a generation is increased, and the mass of the lighter quark is decreased.

The second generation follows the pattern of the first, but not the third. In the latter case, the massfunction of both quarks increases. This implies different contributions to the massfunctions. One increases the massfunction of the heavier quark and decreases the one of the lighter quark. The other contribution increases with the mass of both quarks. An indication of this is already seen in the second generation, albeit not creating a qualitative change.

4.2.4 Poles of the quark propagator

In this section, we will analyze the pole structure of the QPs with the Schwinger function, as well as with a Padé-like analytical continuation, as described in section 2.5.2.

Schwinger function

Let us first consider the Schwinger function equation (2.45) in the chiral limit for the flavor-diagonal dressing function $\tilde{B}$. The other flavor-diagonal dressing functions do not lead to qualitatively new results and are even quantitatively similar, so these will be skipped here. The results are shown in the top panel of figure 4.6. The Schwinger function shows an oscillatory behavior, consistent with the form (2.47), and thus complex conjugate poles, as in pure QCD for the rainbow-ladder truncation [153]. In fact, a fit using a more detailed ansatz of this type, see equation 2.49, works very well, as is also shown in the top-left panel of figure 4.6. The values of the fit parameters are listed, for completeness, in appendix B.3.6.

However, the oscillation period starts to increase substantially for $g_\mathrm{w} > 0.01$, up to a point where at large g_w the first zero-crossing has moved to a time which we can no longer numerically resolve reliably. Thus, the imaginary part shrinks with increasing breaking. The curvature at short distances is still not quite right for a physical particle. A similar behavior, though with suppression of oscillations for decreasing interaction strength, has already been observed for adjoint scalar particles [195, 196]. This strongly suggests that the interaction strength plays a crucial role for the scale at which negative norm contributions become relevant, even though the coupling does not differentiate between positive-norm and negative-norm states.

At the same time, the steepness decreases, making the real part smaller. Thus, the increase in g_w moves in total the poles closer to the origin, as both real and imaginary parts decrease.

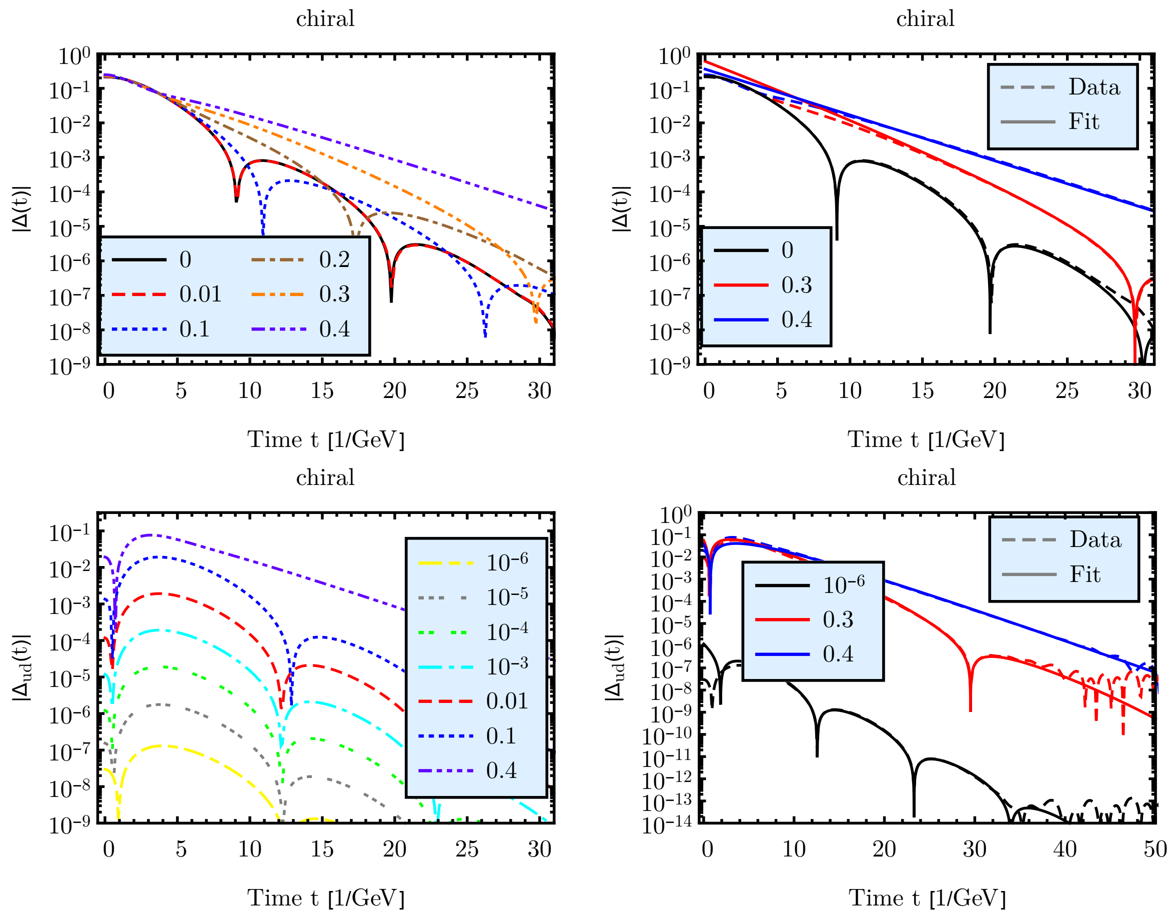

Figure 4.6: Flavor-diagonal(top panel) and off-diagonal (bottom panel) Schwinger function in the chiral limit for different g_{w} (left panel) and with fits (right panel).

The flavor-off-diagonal Schwinger function, again only the scalar part as the others are very similar, is shown in the bottom panel of figure 4.6. In principle, it shows a very similar behavior as for the flavor-diagonal part, except that it always retains a first zero-crossing, relatively independent of g_{w}, at very short times. It is still possible to fit it using the same fit form. The results for the fit are also listed in appendix B.3.6. It is found that the zero-crossing at small momenta comes from the phase shift δ in (2.47). It is very close to $\pi/2$ and causes the sign change for the Schwinger function at a small t. Still, the position of the pole also moves towards the origin with increasing breaking strength. The Schwinger function for the first two generations show the same behavior as in the chiral limit, see figure B.8 in appendix B.3.6. For the third generation, the fall-off was too fast, due to the large real part, as that any unambiguous statements could be drawn before numerical noise drowns out the signal.

It is quite an interesting result that the breaking pushes the poles closer to the origin. As we expect a change of physics when crossing the threshold $g_W \gtrsim 0.4$, this could be the first indication of a drastic change at strong breaking. However, this is probably not of relevance to neutron star physics. On the downside, the decreasing distance to the origin will create additional problems in any mesonic correlators in rainbow-ladder calculations [18, 19, 23]. In these cases, more elaborate schemes will be necessary than a tree-level breaking, which we are

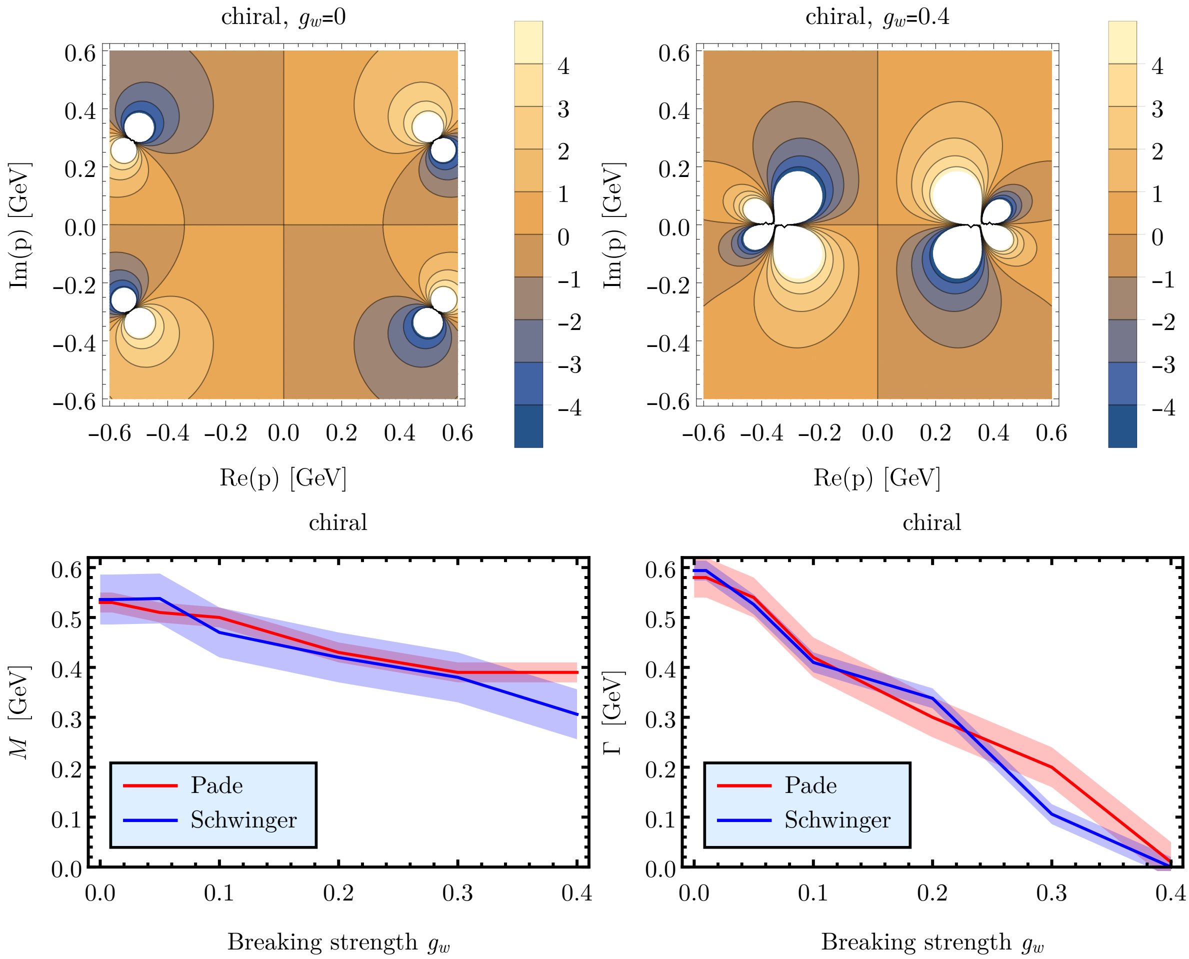

Figure 4.7: The pole positions in a contour plot without (top-left panel) and with $g_w = 0.4$ breaking strength (top-right panel). Real (bottom-left panel) and imaginary part (bottom-right panel) of the poles from the Schwinger method and Padé-like continuation.

currently developing.

Padé-like continuation

Let us now consider the Schlessinger point continuation (equation (2.44)) for flavor-diagonal dressing function $\tilde{A}$. The other flavor-diagonal dressing functions are again very similar, so these will be skipped here. The contour plot of the imaginary part in the chiral limit is shown in the top panel of figure 4.7. We obtain 4 poles for the QP at the positions $P_{\text{Pole}} = \pm\left(M \pm \mathrm{i}\,\frac{\Gamma}{2}\right)$.

Let us mention here, that the dressing functions of the QPs are functions of momentum squared $\tilde{A}(p^2)$ and hence do not differentiate between p and $-p$. Therefore, any numerical continuation using these data should be symmetric under this transformation. We see this in the top panel of figure 4.7. Thus, for each pole also its negative is a pole. This is also true for the Schwinger function. We see in equation (2.47) that only the absolute value of the real part enters in the form of the Schwinger function. The imaginary part of the pole comes in the cosine, which has an additional parameter for the phase shift δ. Hence, the Schwinger function

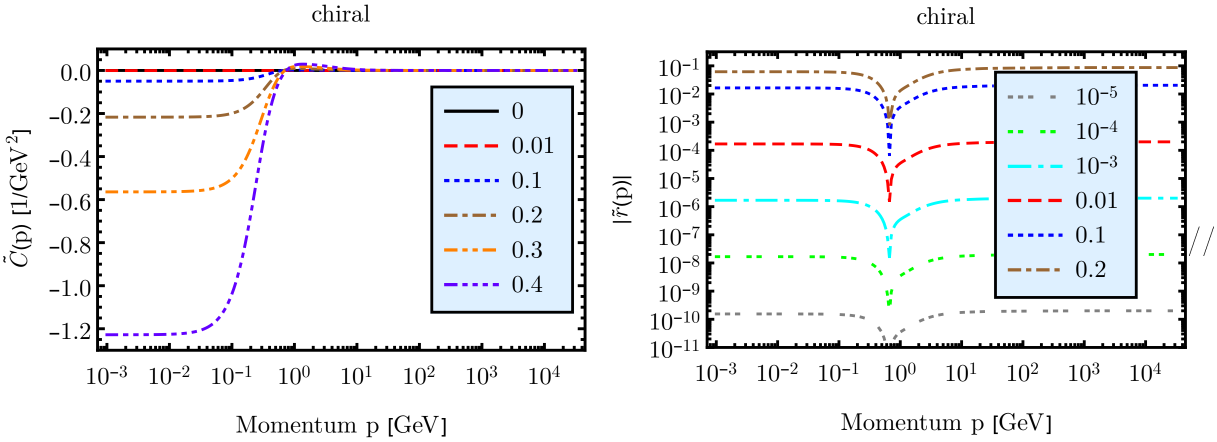

(a) Flavor-diagonal axial channel (left panel) and the ratio (right panel) in the chiral limit.

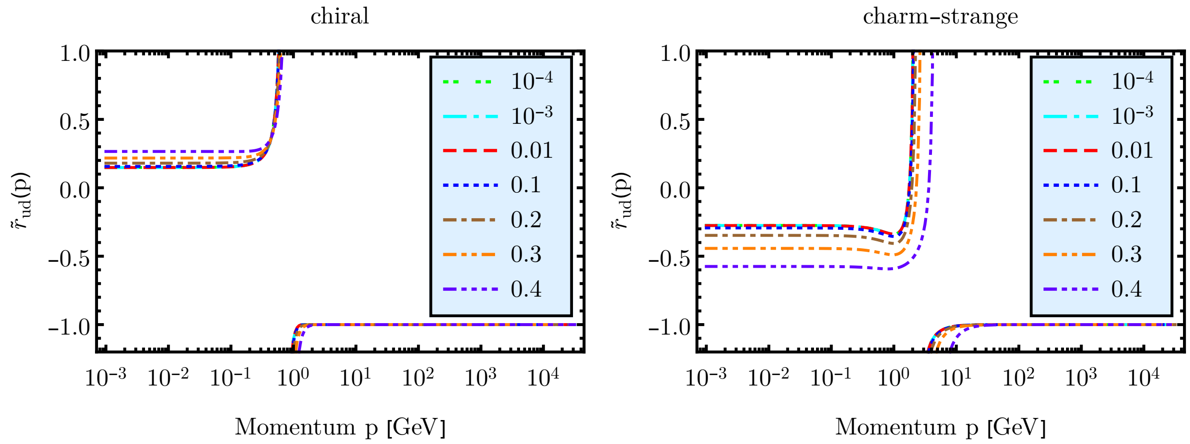

(b) The flavor-off-diagonal ratio in the chiral limit (left panel) and for the second generation (right panel)

Figure 4.8: Axial channel and the ratio (4.10) for different values of g_{w}.

with a negative Γ can be fitted with the same positive Γ using the phase shift $\delta' = \delta \pm \pi$. So the amount of the poles from the Schwinger function is the same as for the Padé-like continuations. We just neglect the part with the negative mass guided by physics.

We see in the bottom panel of figure 4.7 that the poles from the Schwinger function and the Schlessinger point method agree within the error also quantitatively. Let us note here that the poles with the negative mass are just artifacts from the numerical continuation of the Euclidean data. The direct calculation of the QP in the complex plane has only complex conjugate poles on the left side of the complexified Euclidean space (see left panel of figure 5.2).

We do not show further results for the other QPs as they agree with the results in the last section. Due to the fact that the Schlessinger point method is far easier for the numerical implementation, we will use this for our remaining analysis in this work. This concludes our analysis of the pole structure. We now turn to the investigation of the P-violation.

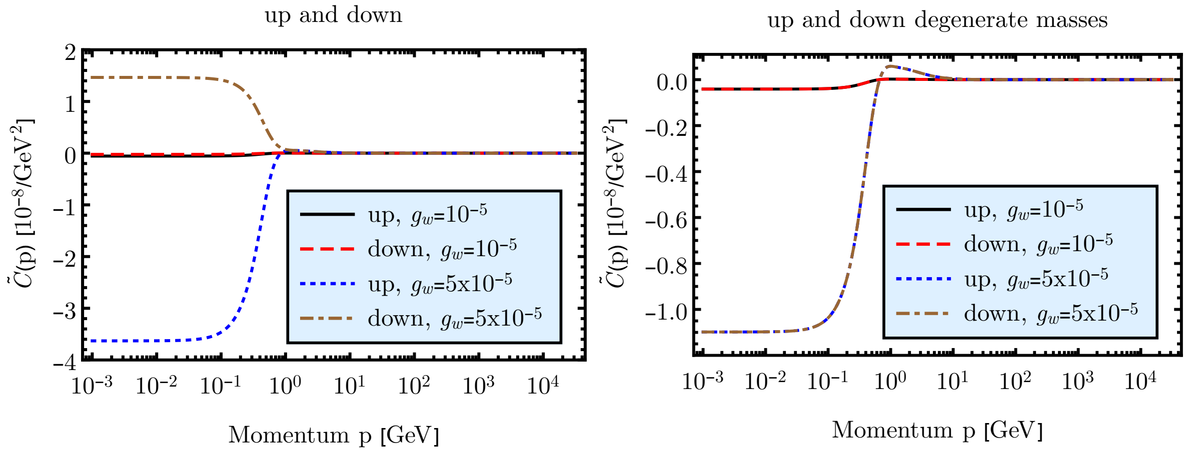

(a) The axial dressing function for the up quark and down quark at two different breaking strengths.

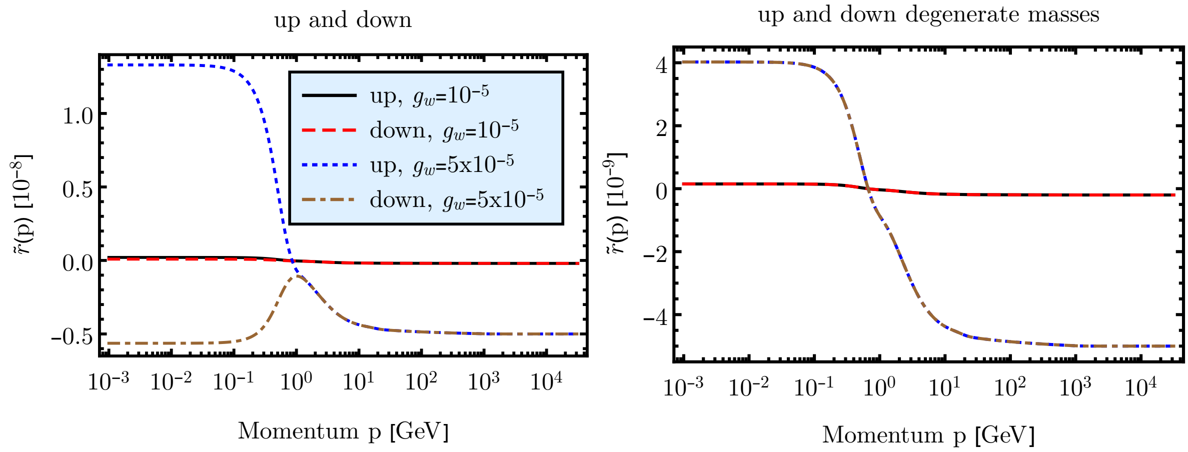

(b) The ratio for the up quark and down quark at two different breaking strengths.

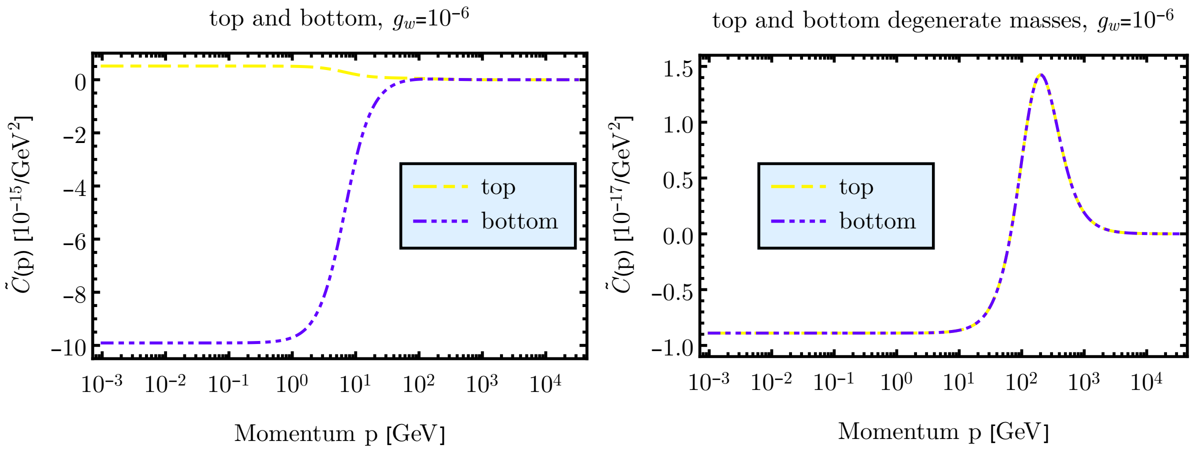

(c) The axial channel for the top and bottom quark.

Figure 4.9: The axial dressing function and the ratio (4.10) for the physical masses (left panels) and degenerate masses (right panels).

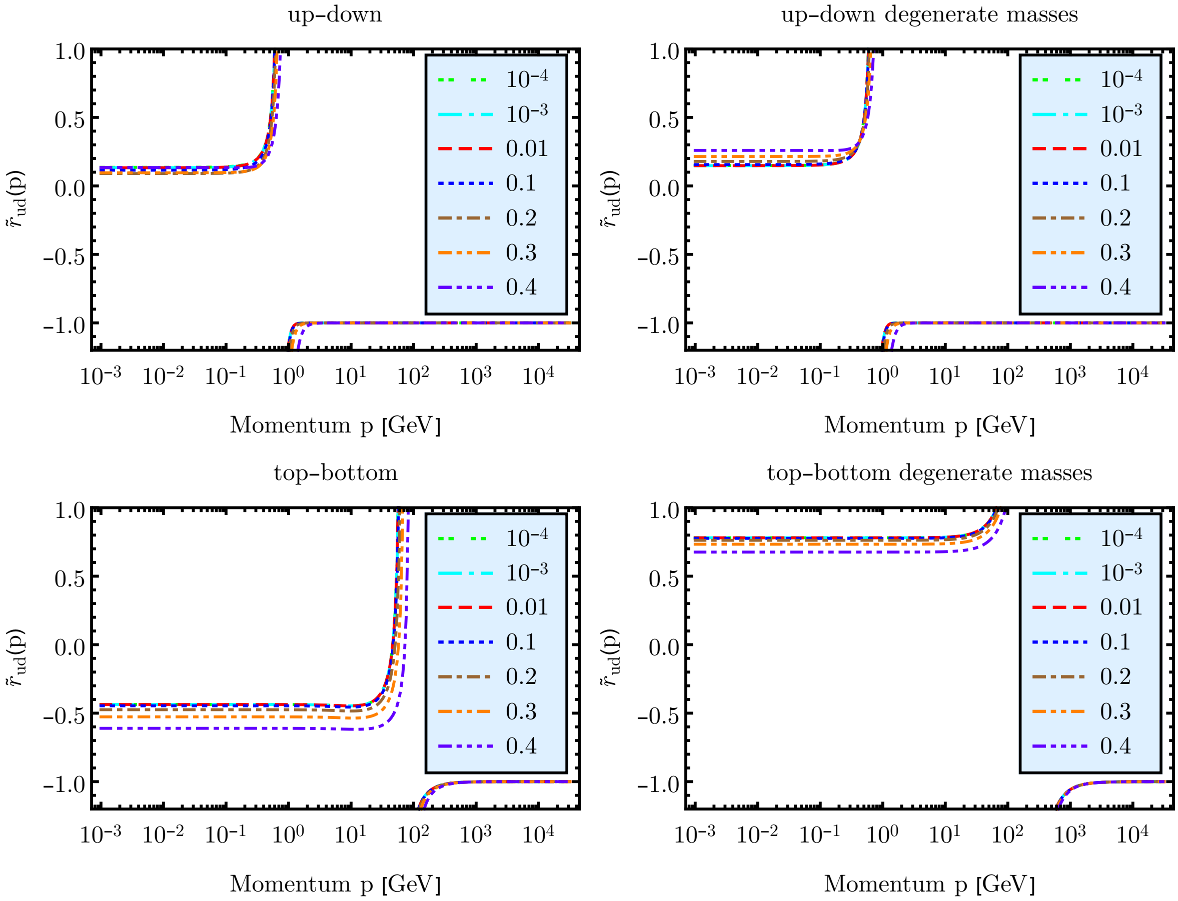

Figure 4.10: The flavor-off-diagonal ratio (4.10) for different g_{w} for the first generation (top panels) and third generation (bottom panels) for physical mass splittings (left panels) and degenerate masses (right panels).

4.2.5 P-violation

In the following, the handiness of the quarks is investigated, using the definition (4.9). This requires the axial channel, shown in the left panel of the subfigure 4.8a for the chiral limit. The corresponding dressing function $\tilde{C}$ is for the flavor-diagonal elements found to be positive for higher momenta and negative in the IR. At the same time, for increasing g_{w} the absolute value of $\tilde{C}$ also increases. Of course, at large momenta, the dressing function goes to its tree-level part, which from equation (4.11) is:

$$\tilde{C}_{0,AA} = \frac{2g_{\mathrm{w}}^2 p^2}{N(p^2)}, \tag{4.18}$$

which is positive, actually for all momenta. Therefore, the back-coupling to QCD forces it to be negative in the IR. This happens at a transition scale of approximately 1 GeV, which is the typical QCD scale.

To assess the consequences of this for the left-handed and right-handed contributions, we use the relative ratio from equation (4.10). Since $\tilde{A}$ is always positive, the sign of $\tilde{r}$ is given by the sign of $\tilde{C}$. This already entails a change of sign, and that the left-handed part is larger in the infrared. This is also shown in the right panel of the subfigure 4.8a. The effect increases non-linearly with g_w: For $g_\mathrm{w} \lesssim 0.1$, the absolute value $|\tilde{r}|$ in the UV and IR is increased by two order of magnitudes, when g_w is increased by one order of magnitude.

The flavor-off-diagonal $\tilde{C}$ is always negative in the chiral limit, but $\tilde{A}$ changes its sign, see figures B.2 and B.5 in appendix B.3. At the same transition scale of approximately 1 GeV as for the flavor-diagonal case, and in the chiral limit, $\tilde{A}$ has a zero-crossing and $\tilde{C}$ not. This leads to a diverging $\tilde{r}_{ud}$ at this scale. Thus, there is a transition from right-handed in the UV to left-handed in the IR in this case also. This is shown in the left panel of the subfigure 4.8b.

Increasing the mass, the situation for up and down quarks is shown in the left panel of the subfigure 4.9a. The absolute value of $\tilde{C}$ is different for up- and down-quark, but their behavior is as in the chiral case for $g_\mathrm{w} = 10^{-5}$. Slightly, increasing g_w to $5 \cdot 10^{-5}$ entails a drastic qualitative change. For the up-quark, $\tilde{C}$ is still positive in the UV and negative in the IR, but for the down-quark, it remains positive for all momenta. Therefore, the up-quark still flips its chirality at long distances, but the down-quark does not do so.

To understand the origin of this effect, it is helpful to study the degenerate mass case, also shown in the right panel of the subfigure 4.9a. There is no (numerically detectable) difference between up- and down-quark[1], and $\tilde{C}$ changes sign again, as in the chiral limit. For higher values of g_w, the absolute value of $\tilde{C}$ just increases in the IR. This implies that the different behavior of $\tilde{C}$ for the non-degenerate case is due to the mass splitting of the quarks. Since at tree-level only in the pseudoscalar channel, a contribution proportional to the mass splitting occurs, this effect must have been propagated by the QCD interaction to the axial channel. Moreover, the effect becomes already important at the, compared to QCD, very small mass splitting and a very small breaking scale of $g_\mathrm{w} \approx 5 \cdot 10^{-5}$. This can only happen if there is a strong non-linear amplification mechanism is at work. This implies that the QCD medium strongly affects the helicity at long ranges, but only for non-degenerate quark masses. That was certainly not expected.

The same is true for the other quark generations, see for the second generation the left panel of the subfigure 4.8b. The effect is still there for the third generation, with its very large mass splitting, see subfigure 4.9c, and there occurs already at an even smaller breaking strength of $g_\mathrm{w} = 10^{-6}$. Thus, the absolute value of the involved mass scales amplifies the non-linear back-coupling, such that it occurs at weaker breaking strength.

The corresponding relative ratios are shown in figure B.7 in appendix B.3. These graphs support the existence of a transition scale, where the left-handed and right-handed contribution change their relative contribution.

For the mixed flavor case, the effect is solely driven by the absolute value of the mass splitting, and the breaking strength plays only a minor role. This is shown in figure 4.10. Whether there is a mass-splitting or not plays only a role if the mass splitting is large enough, i.e., in the third generation. Only then the behavior with or without mass splitting differs qualitatively in the infrared. Already, the second generation is sufficient for this, as can be seen in subfigure 4.8b.

4.3 Discussion and implications for physics

We have calculated the QP in the presence of explicit C, P, and flavor symmetry breaking. Moreover, we took into account the non-linear back-coupling from QCD in the rainbow-ladder

[1] Which is not trivial, as even at tree-level the flavor propagation is not symmetric.

truncation. The latter leads to qualitative effects, even for relatively small explicit breaking strengths, at long (hadronic) distances. They also couple in a highly non-trivial way the various dressing functions to each other. This was particularly visible in the way how effects from mass splitting and mass averages surfaced in various dressing functions. The non-linear amplification also surfaced in other ways. This is a crucial insight: external perturbations can, even in rainbow-ladder truncation, be substantially amplified by the strong interactions. This must be regarded as a warning that even small effects can play a non-perturbatively significant role when QCD is involved.

From the point of view of physics, another exciting insight is obtained when considering how left-handed and right-handed particle propagation changes. Under particular conditions, flips between handedness can be amplified at long distances by the strong interaction. This can deplete or enlarge the available particles in some handedness. As the weak interactions only couple to a particular handedness, this can increase or decrease the reservoir of particles, which are weakly interacting in a system. If this pertains to the full system, this can influence the dynamics in forming or merging neutron stars, as this could alter, e.g., the opacity for neutrinos. This is even more important as the typical range where this occurs is only of the size of a hadron.

Concluding, this investigation showed that weak interaction effects, even if themselves small, can be amplified by the strong interactions, and this back-coupling can have a qualitative impact. Keeping this in mind will be important in the next step, when relaxing the assumption of a reservoir, and taking the weak interactions explicitly into account, by including the emitted neutrinos and electrons. This will require to work on a hadronic level, which we do in the next chapter.

Chapter 5

The weak pion decay in the Bethe-Salpeter-approach

In this chapter, we will focus on the weak pion decay in the combined DSE/BSE framework. So before we deal with the pions, let us first state the implications of the right pole structure for the correlation functions from the Mikowski space, as stated in section 2.5 to the Euclidean space in the first section 5.1. In the second section 5.4, we will discuss the BSE for the weak pion decay. Some parts of the findings are already published in [197]. The final results of the decay process will be presented in future investigations. Technical details of the derivation are shifted to the appendix C for the sake of reproducibility.

5.1 Poles in the second Riemann sheet

The homogeneous BSEs (3.8) are derived from the DSEs of the corresponding n-point function under the condition that the particle is on-shell, as outlined in section 3.2. Thus, the BSE has only solutions for particular momentum configurations, which gives us access to the properties of the bound state and resonances. The momenta are given by the pole positions of corresponding n-point functions. From the pole position, we extract the mass and decay-width of the particle. Stable particles are poles on the real axes, and resonances are poles in the second Riemann sheet in the Minkowski space ($M_{\text{Pole}} = M - \mathrm{i}\,\frac{\Gamma}{2}$) as already introduced in section 2.5.

As a consequence of this, the real-valued momenta in Euclidean space are not sufficient to determine the bound state properties. Therefore, we complexify the Euclidean space. To avoid any misunderstanding, let us note here that we still work in the Euclidean metric, as stated in the conventions for the thesis in chapter 2. Since any momentum squared in Euclidean space is the negative of the momentum squared in Minkowski space, the left and right half-plane of the complexified Euclidean space is called the Minkowski and Euclidean space, respectively, in the standard functional method literature. To avoid any confusion, we will not use these expressions in this manner as we deal with the actual Minkowski and Euclidean space for the discussion of the pole position.

Let us now discuss the consequences of the pole positions in Minkowski space, as stated in section 2.5, for the complexified Euclidean space because solving the BSEs, essentially, boils down to find the right pole position in the complex plane. To be more formal, let P and P_M be the total momenta of the incoming particles in Euclidean and Minkowski space, respectively; and $P^2 = s_E$ and $P_M^2 = s$. In the rest frame of the resonance ($\vec{P}_M = 0$), we get in Minkowski

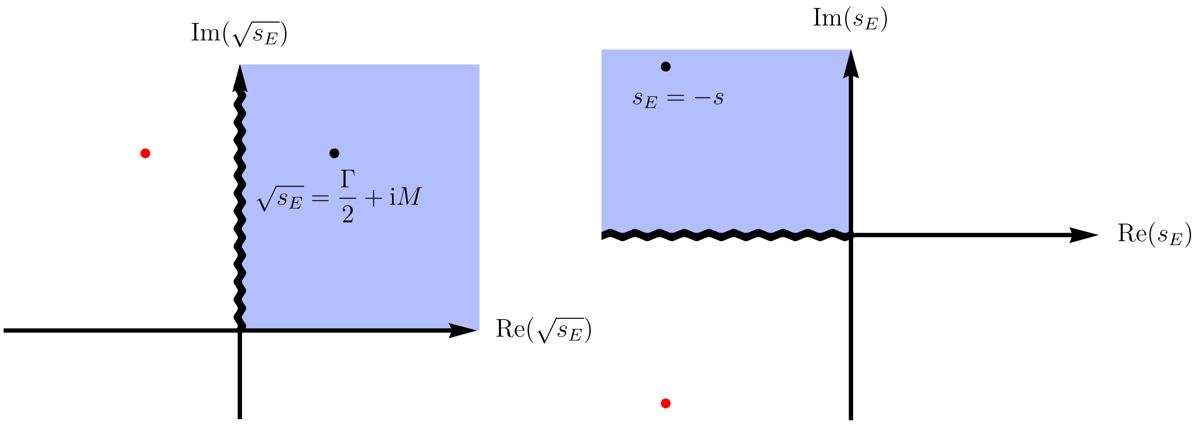

Figure 5.1: The pole positions for stable particles (wiggly line) and resonances (blue area) in the complex $\sqrt{s_\mathrm{E}}$-plane (left panel) and the implication for the resonances in the complex s_E-plane (right panel).

space:

$$P_{M,0} = M_\mathrm{Pole} = M - \mathrm{i}\,\tfrac{\Gamma}{2}. \tag{5.1}$$

This is directly related to the fourth component in the Euclidean space through the Wick rotation [39]. Thus, we get the following for the momentum and its squared in Euclidean space:

$$P_4 = \mathrm{i}\,P_{M,0} = \mathrm{i}\,M_\mathrm{Pole} = \mathrm{i}\,M + \tfrac{\Gamma}{2}, \quad \Rightarrow s_E = -s = -M^2_\mathrm{Pole} = \left(-M^2 + \frac{\Gamma^2}{4}\right) + \mathrm{i}\,M\Gamma. \tag{5.2}$$

For a better understanding, we depict an analogous figure 5.1 to the figure 2.4 for the pole positions in the complexified Euclidean space. The figure shows the pole position of stable particles (wiggly lines) and resonances (blue area) in the complex $\sqrt{s_\mathrm{E}}$-plane (left panel) and the complex s_E-plane (right panel). We have emphasized that the pole of a resonance is in the second Riemann sheet in Minkowski space. In figure 5.1, we see the same pole in the first quadrant of $\sqrt{s_\mathrm{E}}$-plane. The pole has not moved; instead, we are looking at the same pole from another position. This is directly visible by looking at the relative position of the pole in the first and second sheet to the stable particles[1].

We work in the complex s_E variable for our study, and hence the pole is located on the upper left quadrants for particles with $M > \Gamma/2$, which is the case for the pions. Thus, for physical stable or unstable particles, we must search for poles on the negative real axes or the upper half of it in the complexified Euclidean space.

Although solving the BSEs does not sound very difficult, in practice, it is a tough task, especially for decaying particles. For stable particles, we must search for a pole on a line, which is much simpler than searching in a plane. To do so, we will start in the pure QCD case, where the pole position is well-known, and turn on the weak interaction smoothly. At the same time, we will make the leptons much heavier than the pion. Hence, the decay can not take place. In the end, we will go smoothly to lighter leptons masses and thereby turn on the decay process.

[1] Starting from the position of a stable particle, we have to move in the opposite mathematical direction for the pole of a resonance. We see this in figure 2.4 and 5.1 for Minkowski and Euclidean space, respectively.

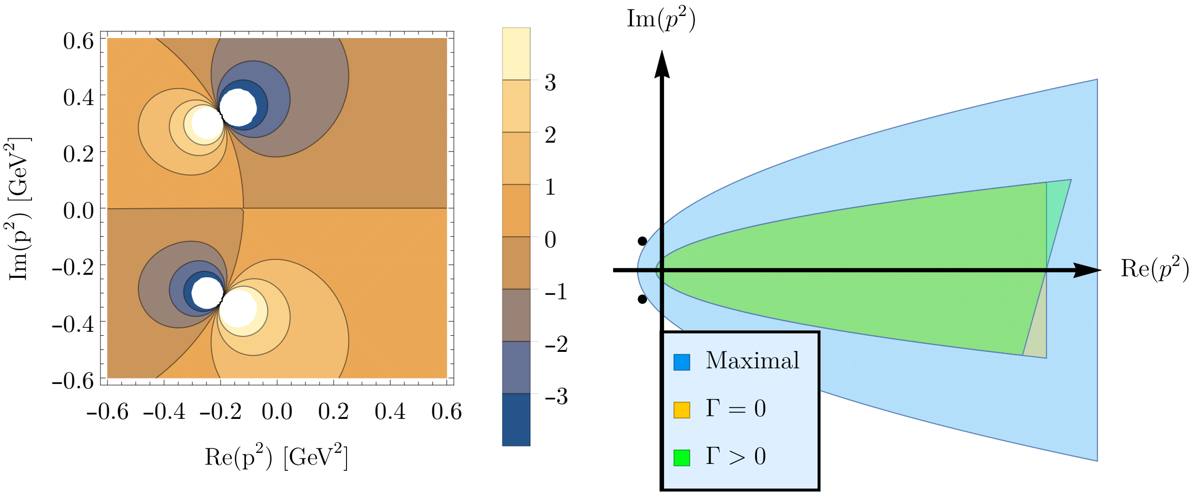

Figure 5.2: The pole position of the QP in the complex plane for the up-quark from the Padé-like analytic continuation (left panel) and the required area of the QP in the complex plane for the BSEs (right panel). The maximal area is restricted by the poles of the QP in the complex plane (blue area). This maximal area should contain the whole area for stable particles (yellow) as well as resonances (green) during the integration of the the BSE.

This will move the pole in the upper half, which we can follow. This concludes our discussion on the pole positions in the complexified Euclidean space. Let us, in the following section, discuss the implications of the pole position for the QP.

5.2 Quark propagator in the complex plane

The BSEs are derived under the condition that the particle is on-shell. Thus, the total momentum of the incoming particle is fixed and given by the equation (5.2). Especially, the total momentum is complex-valued. As a consequence of this, at least one of the particle forming the bound state has complex-valued momentum. Therefore, studying the BSEs of the pion requires the knowledge of the QP in the complex plane. So let us deal with this issue in the following and consider the case of the mesons.

We define $k_\pm$ as the momenta of quark and anti-quark, respectively. Using the relative momentum k (real-valued) between both quarks, we may write:

$$k_\pm = k \pm \eta_\pm P, \qquad k = \eta_- k_+ + \eta_+ k_- \qquad \eta_+ + \eta_- = 1, \tag{5.3}$$

where the parameter $\eta_\pm$ allows us to share the complex-valued momentum P between the quark and anti-quark. For example, $\eta_+ = 1$ means that the whole complex-valued part of the total momentum is in the quark momentum, and the momentum of the anti-quark is pure real-valued.

The dressing function of the QPs depends on the Lorentz-invariants of their momenta, which are:

$$k_\pm^2 = \left(k^2(1-z^2) + (kz \pm \frac{\eta_\pm}{2}\Gamma)^2 - \eta_\pm^2 M^2\right) \pm 2\,\mathrm{i}\,\eta_\pm M \left(kz \pm \frac{\eta_\pm}{2}\Gamma\right), \tag{5.4}$$

where $z = \cos(\theta)$ and θ is the angle between P and k. This relation describes the area confined by a parabola in the complex p^2-plane ($p^2 = k_\pm^2$) shown on the right panel in figure 5.2. The parabola is opened horizontally on the right-side with its apex at $-\eta_\pm^2 M^2$ on the left-side.

The direct calculation in the complex plane yields complex conjugate poles for the QP on the left side of the complex p^2-plane. These agree very well with the poles from the Padé-like analytic continuation, which are depicted on the left panel for the up-quark. The poles yield a maximum for the Parabola apex before they come inside the parabola region (blue). For parabola containing these poles, we need more advanced and sophisticated numerical techniques, which are currently being developed to go stepwise beyond this limitation (see [26] and the references therein for further details on this topic).

Using the standard numerical techniques, we are restricted to a maximum parabola given by the poles. This is directly related to a maximum mass M_{max} for the bound state and resonance. In the case of the light quarks, the maximum is given by:

$$M_{\text{max}} \approx \min\left[\frac{0.5}{\eta_\pm}\text{GeV}\right]. \tag{5.5}$$

Fortunately, the poles do not hinder our study as the pions are very light ($M_\pi \approx 0.14\,\text{GeV}$) and we can use the standard numerical techniques for our study.

The BSEs are integral equations, and the integrals are usually calculated till a UV-cutoff Λ in the renormalization theory. Thus, we need the QP for a finite region. So calculating the QP in an area that includes the entire integration region and is smaller than the maximal region is sufficient for the analysis. For stable particles $\Gamma = 0$, the area (yellow) is mirror symmetric. However, for resonances (green), the region is dominated by the upper half of the complex plane for quark, as well as anti-quark. This concludes our brief analysis of the QP in the complex plane. For further technical details on the numerical implementation in the complex plane, see [22, 25, 26, 198] and the references therein.

5.3 Poles in the second Riemann sheet and BSEs

We have emphasized throughout this work on the fact that physical resonances are poles in the second Riemann sheet and not in the first sheet. Thus, it is crucial to analyze the properties, which the BSEs must at least fulfill, to distinguish between both sheets in general. A pole in the first Riemann sheet can be realized by applying the transformation $\Gamma \to -\Gamma$ in our recent analysis with $\Gamma > 0$.

As a consequence of this, the pole of the resonance is transformed to its complex conjugate ($s_{\text{E}} \to \overline{s_{\text{E}}}$). This means that the pole is located on the lower half of the s_{E}-plane (see the red point on the right panel in figure 5.1). Thus, the condition that the pole is in the second sheet and not in the first sheet implies that for a given s_{E} its complex conjugate $\overline{s_{\text{E}}}$ can not be a solution of the BSE at the same time.

Let us be more formal in the following. We can write the BSEs equation (3.8) as a general eigenvalue problem of the form:

$$\lambda(s_{\text{E}})\Psi(s_{\text{E}}) = \mathcal{M}(s_{\text{E}})\Psi(s_{\text{E}}). \tag{5.6}$$

We may call $\mathcal{M}$ the BSE matrix[2], which contains the BSE Kernel and the QPs. Solutions of the BSEs are given by all the momentas $s_{\text{E}} \in \mathbb{C}$ with $\lambda(s_{\text{E}}) = 1$.

[2] In practice, the BSA is calculated on a grid and hence $\mathcal{M}$ is finite dimensional square matrix. Solving the BSEs boils down to finding the eigenvalues and eingenvectors of this matrix.

In particular, if $s_{\rm E}$ is a solution of the BSE with the BSA Ψ and $\mathcal{M}$ fulfills the following property:

$$\mathcal{M}(\overline{s_{\rm E}}) = \overline{\mathcal{M}(s_{\rm E})}. \tag{5.7}$$

Then $\overline{s_{\rm E}}$ is a solution of the BSE with the complex conjugate BSA[3] $\overline{\Psi}$. This can be seen from a straight forward calculation:

$$\mathcal{M}(\overline{s_{\rm E}})\Psi(\overline{s_{\rm E}}) = \mathcal{M}(\overline{s_{\rm E}})\overline{\Psi(s_{\rm E})} = \overline{\mathcal{M}(s_{\rm E})\Psi(s_{\rm E})} = \overline{\lambda(s_{\rm E})\Psi(s_{\rm E})} = 1 \times \overline{\Psi(s_{\rm E})}. \tag{5.8}$$

So the necessary but unfortunately not sufficient condition to distinguish between the poles from the first and second sheet is that the BSE matrix violates the relation (5.7).

Let us now check which part of the BSE matrix does not transform in agreement to this relation and hence could be a source to violate this relation for the whole BSE matrix. For this purpose, we start with the different momenta in our system.

In the rest frame of the resonance, we may write the transformation for going from the second sheet to the first sheet as follows:

$$P_M \to \overline{P_M}, \qquad P \to -\overline{P}, \qquad s_{\rm E} \to \overline{s_{\rm E}}, \qquad k \to k = \overline{k}, \qquad k_\pm \to \overline{k \mp \eta_\pm P}. \tag{5.9}$$

We note that the momenta P and $k_\pm$ are not transformed into their complex conjugate momenta and hence can be one of the sources to violate the relation (5.7).

The momenta of the quark and anti-quark are transformed into the complex conjugate of each other for the typical case $\eta_+ = \eta_- = \frac{1}{2}$. Since the dressing function of both QPs come in combination, their combination might still transform according to the relation (5.7), especially, in the case of degenerate quark masses, where both QPs agree.

The investigation of the pion is done for degenerate quark masses and $\eta_+ = \eta_- = \frac{1}{2}$ in the standard literature. Therefore, we will also start our analysis in this case to benchmark our results. So it is essential to distinguish between both sheets also in this case. In the next step, we will go to the physical quark masses. Thus, let us in the following discuss this case.

The dressing function $\tilde{A}$ and $\tilde{B}$ are real-valued on the real axis. Thus, for the analytic continuation of these function we get :

$$\tilde{A}\big(\overline{p^2}\big) = \overline{\tilde{A}\big(p^2\big)}, \qquad\qquad \tilde{B}\big(\overline{p^2}\big) = \overline{\tilde{B}\big(p^2\big)}, \tag{5.10}$$

from the Schwarz reflection principle. So the dressing functions of the QP has the transformation behaviour accordint to the relation (5.7) in the case of the degenerate masses.

The dressing functions come along with scalar products in various combinations of the momenta. In particular, there are scalar products in the BSE matrix, which contain an odd or an even amount of the momenta P. The scalar products with an even amount transform according to (5.7) and with odd momenta transforms with an additional minus sign. Especially, linear combinations of these provide us with the possibility that the whole BSE matrix can not transform according to (5.7).

We see this in the case of the pion BSE on the example of the matrix element $M_{1,2}$:

$$M_{1,2} = 2\,\mathrm{i}\left(2m^-(P\cdot q) - m^+P^2\right) \to \overline{2\,\mathrm{i}\left(2m^-(P\cdot q) + m^+P^2\right)} \neq \overline{M_{1,2}}, \tag{5.11}$$

[3]We will use only in this section $\overline{\Psi}$ to denote the complex conjugation of the BSA.

where q is the relative momentum of the internal quarks. m^- and m^+ are multiplications and additions of the QP's dressing functions (see the section 5.4 and appendix C.2 for further details and exact definitions). As a consequence of this, the BSEs can have the property to distinguish between the first and second Riemann sheet in general. Notably, the BSE of the pion violates the relation even in the degenerate case. Therefoe, the BSEs may have the property to distinguish between both sheets in our study. We will check this for the weak pion decay.

In the end, let us mention that the BSA of the pion in pure QCD is real though the matrix is complex-valued. This is owed to the fact that the QP in the complex plane enters the matrix. However, the complex part cancels out during the calculation of the BSA (see, e.g., [26,31,32] and the references therein). This is no longer true for the weak pion, and hence the BSA will be complex-valued. This concludes our general consideration. We now turn to the BSEs of the weak pion decay.

5.4 Coupled system of BSEs

The pions play a crucial role in nature and thus are very well studied from the theoretical side, as well as the experimental side. This is owed to the fact that they are the lightest hadrons and, therefore, mediate the longe range interaction between them. Their unique role is emphasized through the fact that they are Goldstone bosons of the chiral symmetry, which makes them very much lighter than the rest of the hadrons. They would be absent from the physical spectrum if the chiral symmetry would be exactly realized in nature. Therefore, without the right treatment of the chiral symmetry, it is not possible to describe the light-quark meson spectrum qualitatively correct, and "fine-tuning" is necessary (see [31,32,132] for further details on this topic).

This is of particular importance for the truncation scheme in the DSE/BSE approach. The rainbow-ladder truncation applied in this work does have the right treatment for the chiral symmetry. Nevertheless, let us briefly deal with this issue first, before we analyze the BSEs of the weak pion decay.

The BSA of the pion in pure QCD is given by (see for the derivation in the appendix C and the equation (5.18)):

$$\Psi = \int K^{Q,\overline{Q},Q,\overline{Q}} P^Q P^Q \Psi, \qquad\qquad K^{Q,\overline{Q},Q,\overline{Q}} = S^{(3),A,Q,\overline{Q}} P^A \Gamma^{(3),A,Q,\overline{Q}} \tag{5.12}$$

with the Kernel K. The solution of the BSA requires the knowledge of the full QP, the full gluon propagator, and the full quark-gluon-vertex, which has there own DSEs.

The DSE of the QP in pure QCD is stated in equation (3.28) and also requires the knowledge of the full gluon propagator and the full quark-gluon-vertex. In particular, both quantities appear in the same form. Hence, the truncation scheme for the QP and the pion BSA has to be self-consistent. Especially, the truncation scheme must respect the underlying symmetries of the theory, realized via the Ward-Takahashi or Slavnov-Taylor identities for global or local symmetries, respectively.

The axial-vector Ward-Takahashi identity ensures the right treatment of the chiral symmetry. So any truncation on the DSE of the QP has a direct impact on the pion BSE. This has been studied extensively in [31,32]. We refer the reader to this paper for further details on this topic[4].

The inclusion of the (effective) weak interaction breaks the chiral symmetry. Hence, the axial-vector Ward-Takahashi identities are modified. Going along the lines of [31, 32] for the modified axial-vector Ward-Takahashi identities is far too complicated for the explorative study here as we have already seen the rising of the complexity for the QPs due to the additional symmetry violations.

It is believed that the impact is low as far as the strength of the weak interaction is small. Therefore, this will be postponed to future investigations. In this regard, it is important to note that the chiral symmetry is also broken in the QCD due to the finite mass of the quarks, which may have a more significant impact than the weak interaction. The chiral symmetry is restored in the limit of vanishing quark masses and weak interaction, and the rainbow-ladder truncation has the correct implementation of the chiral symmetry in this limit, which is sufficient for our study.

5.4.1 BSEs of the weak pion decay

Let us now turn to the derivation of the BSE for the weak pion decay and be more formal in the following. The pions are pseudo-scalar mesons and hence directly related to the pseudo-scalar channel of the quark anti-quark pair[5]:

$$\pi^\alpha \sim \left(\overline{Q}\gamma_5 T^\alpha Q\right), \tag{5.13}$$

where T^α are the generators of the $\mathrm{SU}(N_f)$ flavor space. In our case ($N_f = 2$), we choose the Pauli matrices.

The π^α does not contain the charged pions, which are the major object of the investigation in this study. We get the charged pions via:

$$\pi^\pm = \pi^1 \mp \mathrm{i}\,\pi^2 \sim \left(\overline{Q}\gamma_5\left(T^1 \mp \mathrm{i}\,T^2\right)Q\right), \tag{5.14}$$

and we define

$$\tilde{T}^1 = T^1 - \mathrm{i}\,T^2, \qquad \tilde{T}^2 = T^1 + \mathrm{i}\,T^2. \tag{5.15}$$

Due to the fact that the $\pi^{1/2}$ and the charged pions $\pi^\pm$ are related via a simple linear combination to each other, we can study any of them. Therefore, we will use both fields throughout this work and switch between both representation at will[6]. Anyhow, explicit calculation are easier for $\pi^{1/2}$, because the algebra of the Pauli matrices is well known and implemented in different computational tools.

The approximation of the weak interaction from equation (2.22) together with the Lagrangian of the QCD from equation (2.32) yields for the matter part[7]:

$$\begin{aligned}\mathcal{L}_W = \mathcal{L}_\mathrm{M} + \mathcal{L}_l + \mathcal{L}_\text{4-Fermi} &= \overline{Q}\left(\not{D} + m_f\right)Q + \bar{l}\left(\not{\partial} + m_f\right)l + \frac{\alpha_w}{2}\left[\left(\overline{Q}^L\gamma^\mu\tilde{T}^\alpha Q^L\right)\left(\bar{l}^L\gamma^\mu\tilde{T}^\alpha l^L\right)\right] \\ &= \overline{Q}\left(\not{D} + m_f\right)Q + \bar{l}\left(\not{\partial} + m_f\right)l + \frac{\alpha_w}{2}\left[\left(\overline{Q}^L\gamma^\mu T^{\tilde{\alpha}} Q^L\right)\left(\bar{l}^L\gamma^\mu T^{\tilde{\alpha}} l^L\right)\right],\end{aligned} \tag{5.16}$$

[4] In particular, the conditions on the renormalization constants have also been investigated in detail.

[5] We will use this relation in the next chapter for the dynamical hadronization.

[6] We will use the Pauli matrices T and modified version of them $\tilde{T}$ throughout this work. Therefore, we make the following convention for the adjoint flavor index: α and $\tilde{\alpha}$ is $\{1,2\}$ in the case of $\tilde{T}$ and T, respectively.

[7] Here, we show the expression only once in both representation for a better understanding of our conventions.

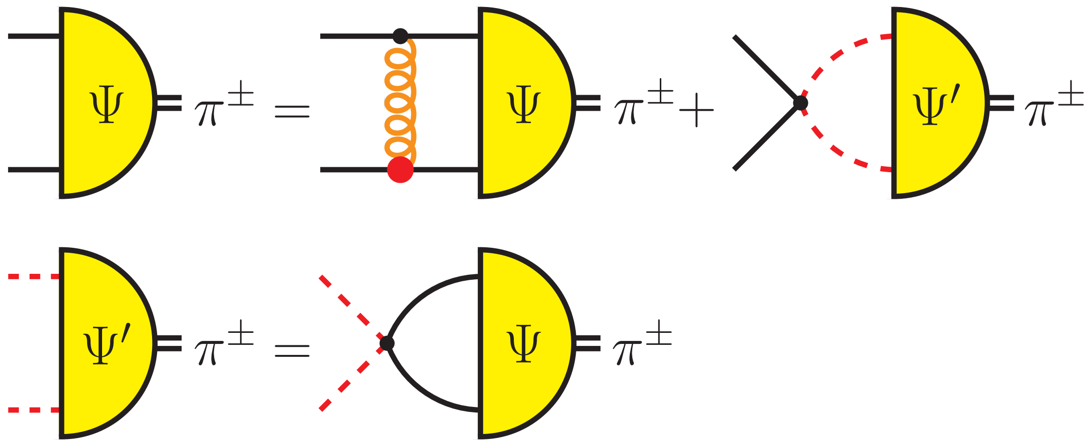

Figure 5.3: Diagrammatic representation of the weak pion BSE (5.18).

where $\mathcal{L}_l = \bar{l}\,(\not{\partial} + m_f)\,l$ is the pure leptonic part and given by the free propagation of the leptons.

Using this Lagrangian, we derive the BSE from the DSE of the 4-point functions, as mentioned in section 3.2. To be more precise, we have to consider two BSAs, namely one pion amplitude (Ψ) without the decay coming from the pure QCD and the additional amplitude for the decay process (Ψ') into the leptons from the inclusion of the electroweak interactions. The former one is derived from the DSE of the 4-quark-point function and the latter one from the 2-quark-2-lepton-point function. We will call them in the following the pure amplitude and decay amplitude, respectively.

$$\Gamma^{(4),Q,\overline{Q},Q,\overline{Q}} = \mathcal{N}\frac{\Psi\overline{\Psi}}{P^2 + M^2_{\pi,\mathrm{Pole}}}, \qquad \Gamma^{(4),l,\bar{l},Q,\overline{Q}} = \mathcal{N}\frac{\Psi'\overline{\Psi}'}{P^2 + M^2_{\pi,\mathrm{Pole}}}, \tag{5.17}$$

where $M_{\pi,\mathrm{Pole}}$ is the pole of the pion.

We derive the equations for the BSAs from the DSE of the both 4-point functions, as outlined in equation 3.7. The derivation of this is illustrated diagrammatically in the appendix C.1, and we get:

$$\begin{aligned}\Psi &= \int \left\{ K^{Q,\overline{Q},Q,\overline{Q}} P^Q P^Q \Psi + S^{(4),Q,\overline{Q},l,\bar{l}} P^l P^l \Psi' \right\}, \\ \Psi' &= \int \left\{ S^{(4),l,\bar{l},Q,\overline{Q}} P^Q P^Q \Psi \right\},\end{aligned} \tag{5.18}$$

where the Kernel K is the same as in the pure QCD (see equation (5.12) or the more detailed expression in the appendix C.2).

Diagrammatic representation of these equations is shown in figure 5.3. The first equation is the usual description in pure QCD but has now an additional term describing that the pion has a leptonic intermediate state. The second equation provides the actual decay of the pion into leptons. Note that there is also a non-trivial equation for a pole in the 4-lepton channel and related to this 2-lepton-2-quark channel in our approximation. However, this is decoupled from the 4-quark and 2-quark-2-lepton-channel system and, therefore, does not influence the weak pion decay process in our study.

Let us now look closer into different ingredients for the solution and start with the QP P^Q. The inclusion of the proposed (effective) weak interaction has no direct impact on the DSE of the QP. This is owed to the fact that the 4-Fermi interaction (equation (5.16) or (2.22)) is related to the QPs of different flavors within a generation, which is not possible in the Standard Model due to the charge conservation. So we are left with the QPs in the pure QCD case, and the rainbow-ladder truncation is possible. They are required in self-consistent truncation in the complex plane, as already discussed in detail.

We also need the full lepton propagator P^l. The only interaction term for the leptons in our theory is effective 4-Fermi interaction (equation (5.16)). For the same reasons as for the quarks, this term does not impact the DSE of the lepton propagators, and we are left with the free propagation for the leptons. Thus, the full propagator is given by:

$$P^l(p) = D^l(p) = \frac{1}{p^2 + m_f^2} \left(\mathrm{i}\not{p} + m_f \mathbb{1}\right). \tag{5.19}$$

This is owed to our simple ansatz in the lepton sector. This is sufficient for the first step since we want to see how the opening of the leptonic decay channels influences the pole position of the BSEs.

This simple form of the propagator is especially helpful regarding the pole position. Analog to the QP in section 5.2, we also require the lepton propagator in the complex plane inside a parabola. This lepton propagator has a pole at $-m_f^2$. The pole is outside the parabole as long as the leptons are heavy enough that the pions can not decay. Opening the decay channel moves the pole inside the integration region. We can avoid the pole by deforming our integration contour as outlined in [38, 199, 200]. So this is technically feasible, especially for such a simple propagator like in our case. We refer the reader to [38, 199, 200] for more details on this and proceed further.

The Kernel K is given by the pure QCD part and hence is truncated, according to rainbow-ladder. Apart from this, we also need the tree-level 2-quark-2-lepton-vertex, which must not be calculated as it is given by our ansatz. Thus, all the ingredients of the BSEs are known, and we can calculate the BSA.

5.4.2 Bethe-Salpeter-amplitude of the weak pion decay

The BSA of pseudo-scalar mesons has, in general, a four-dimensional basis in the Lorentz-space [201]. Hence, we have four dressing functions for each BSA ($f_1, \ldots, f_4$ and $g_1, \ldots, g_4$). The dressing functions depend on the Lorentz-invariants of the external BSA momenta. The BSAs of mesons depends on two external momenta from which one can form three Lorentz-invariants.

Due to the fact that the particle is on-shell, it is convenient to use the total momentum squared P^2 as it is fixed during the calculation. For the remaining two, we choose the relative momentum squared k^2 and the cosine of the angle between them ($z = \cos(\theta)$, i.e., $f_i(P^2, k^2, z)$ and analog for g_i). Combining this with the flavor and color structure of the pions yields for the pure and decay amplitude the following:

$$\begin{aligned}
\Psi^\alpha &= T^\alpha \mathbb{1}_c \frac{\gamma^5}{2} \left(f_1 \mathbb{1} + f_2\, \mathrm{i}\not{P} + f_3\, \mathrm{i}\not{k} + f_4 P_\mu k_\nu \sigma_{\mu\nu}\right), \\
\Psi^{\alpha'} &= T^\alpha \frac{\gamma^5}{2} \left(g_1 \mathbb{1} + g_2\, \mathrm{i}\not{P} + g_3\, \mathrm{i}\not{k} + g_4 P_\mu k_\nu \sigma_{\mu\nu}\right),
\end{aligned} \tag{5.20}$$

where $\mathbb{1}_c$ is the identity in color space.

We insert the general form in equation (5.18). Moreover, we take suitable traces to project out the different dressing functions and get:

$$\begin{aligned} f_i &= \int_q \left\{ C_1 \frac{\alpha_s((k-q)^2)}{(k-q)^2} M_{i,j} f_j + C_2 \alpha_w((k-q)^2) \tilde{M}_{i,j} g_j \right\}, \\ g_i &= \int_q \left\{ C_2 \alpha_w((k-q)^2) M'_{i,j} f_j \right\}, \end{aligned} \tag{5.21}$$

where C_1, C_2 are constants from the trace and $M_{i,j}$, $\tilde{M}_{i,j}$, $M'_{i,j}$ are the matrix elements containing the dressing functions of the fermion propagators and traces of the momenta (see appendix C.2 for the detailed expressions).

In particular, we get:

$$g_1 = g_4 = 0. \tag{5.22}$$

Hence, only the axial channel (g_2, g_3) of the decay amplitude contributes. This is directly related to the CP-violation, which is seen straight forward in the FRG framework and comes out after a long calculation in DSE/BSE framework. Therefore, we discuss this issue using the analogy of both frameworks.

In the FRG framework, the bound states are most straightforwardly described using dynamical hadronization, as outlined in 3.3.1. Thus, we have the pion fields explicitly in the system. The pure and the decay amplitude in the BSE framework describes the relation of the pions with the quarks and leptons at the pion pole, respectively. So the BSAs are connected to the 3-point functions of the pions with quarks or leptons, respectively.

$$\Psi = \Gamma^{(3),\pi,Q,\overline{Q}}\Big|_{P=M_{\pi,\mathrm{Pole}}}, \qquad \Psi' = \Gamma^{(3),\pi,l,\bar{l}}\Big|_{P=M_{\pi,\mathrm{Pole}}}. \tag{5.23}$$

In particular, 3-point function and the BSA have the same tensor structure in the flavor, color, and Lorentz-space. So the general form of the full vertex is given by:

$$\Gamma^{(3),\pi,l,\bar{l}} \pi^\alpha \bar{l}^L l^L = \pi^\alpha \bar{l}^L \left[T^\alpha \frac{\gamma^5}{2} \left(g_1 \mathbb{1} + g_2 \,\mathrm{i}\, \not{P} + g_3 \,\mathrm{i}\, \not{k} + g_4 P_\mu k_\nu \sigma_{\mu\nu} \right) \right] l^L. \tag{5.24}$$

Due to the fact that only left-handed fields are involved, we get in the FRG framework straight forward the desired result for g_1 and g_4. They are related to:

$$g_1 \sim \bar{l}^L \left[T^\alpha \frac{\gamma^5}{2} \right] l^L = 0, \qquad g_4 \sim \bar{l}^L \left[T^\alpha \frac{\gamma^5}{2} \sigma_{\mu\nu} \right] l^L = 0. \tag{5.25}$$

Taking also the right-handed fields ($l = l^L + l^R$) into account shows that the channel of g_1 and g_4 are related to contributions involving different handedness, and the channel of g_2 and g_3 are related to contributions involving the same handedness:

$$g_1 \sim \bar{l}^R \left[T^\alpha \frac{\gamma^5}{2} \right] l^L + \bar{l}^L \left[T^\alpha \frac{\gamma^5}{2} \right] l^R, \qquad g_2 \sim \bar{l}^L \left[T^\alpha \frac{\gamma^5}{2} \,\mathrm{i}\, \not{P} \right] l^L + \bar{l}^R \left[T^\alpha \frac{\gamma^5}{2} \gamma_\mu \right] l^R, \tag{5.26}$$

analog for g_3 and g_4. The same is true for f_1 to f_4. This has important implications for the physics.

The different channel gives us access to the handedness of the particles, and hence we can investigate the impact of the P-violation. Our study for the QP in chapter 4 reveals the possibility of changing the handedness of the particles. To be more precise, we got different contributions for the handedness of the heavier and lighter quarks within a generation above a threshold breaking strength caused by the mass difference between both quarks. Such behavior, if still persists in the full system, would result in a non-vanishing pseudo-scalar and tensor channel (g_1 and g_4).

Our naive intuition could be that this would screen the decay process since the weak decay involves only left-handed particles. However, the dynamical back-coupling can cause new effects even at moderate strengths, as seen during the investigation of the QP. Thus, we require also a back-coupled analysis with the leptonic sector. In particular, we need to go beyond the free lepton propagator and include the weak gauge bosons. This is far too complicated as a first step and will be done in future investigations. This concludes our treatment of the BSA of the weak pion decay. In the end, we summarize our findings in the following section.

5.5 Summary and discussion

The combined DSE/BSE framework makes the use of the poles for bound states and resonances. The axiomatic field theory demands that the pole of a resonance is located in the second Riemann sheet of the Minkowski space. So it is of particular importance that we translate the pole positions from the Minkowski space to the complexified Euclidean space correctly. Thus, the first part of the investigation was devoted to this issue and its generic implications on the BSEs.

Our findings reveal the pole position on the negative upper half of the complexified Euclidean space. It is important to note that the pole position has not moved. Instead, we are looking at the same pole from another direction. In the next step, we have studied the possibility for the BSEs to distinguish between both sheets in general by looking for a necessary condition. We found one condition for this purpose, which could be fulfilled in a general BSE and was fulfilled in the case of the pions.

In the second part, we have formulated the weak pion decay in the DSE/BSE framework and discussed the various technical issues while solving these equations. In particular, we have studied the impact of the additional leptonic decay channel for the BSAs, which has revealed two vanishing and two non-vanishing channels related to the handedness of the particles.

The two non-vanishing channels are in agreement with the previous studies for the leptonic decay constant [32]. Anyhow, we also get an impact on the two vanishing channels (g_1 and g_4) from our examination of the QP in the previous chapter. In particular, the channel g_1 and g_4 are related to contributions from the leptons with different handedness and vanish in perturbation theory. This is owed to the fact that the weak interaction only couples to the left-handed particles.

In the analysis of the QP with broken symmetries, we have seen that for sufficient breaking strengths and degenerate masses, there is a change of the contributions in the handedness for the lighter and heavier quarks. So we have already alerted that the non-perturbative back-coupling may deplete or enlarge the available particle is some handedness. We see here that the impact of such behavior would result in a non-vanishing g_1 and g_4.

Since all the channels of the BSAs are coupled with each other, this would directly impact the leptonic decay constant and, therefore, the pole position of the pion. There is nothing a priori we can say about the effect of this on the decay process itself. From our naive intuition, one could believe that the decay process would be screened, resulting in a more stable pion. So the decay-width of the pion would decrease as it was the case for the quarks in the previous chapter.

Anyhow, one should be cautious with such statements as we have already seen that the non-perturbative back-coupling can cause new effects even at very small strengths. To investigate this, we must go beyond the free propagation of the leptons and dynamically back-couple the effects of the strong interaction to the electroweak interactions in the leptonic sector as well. This is far too complicated in the first place and will be shifted to future investigations. This completes our formulation of the weak pion decay in the DSE/BSE framework. We now consider the same process in the FRG framework and compare them with each other. The final results of both methods will be presented in the future.

Chapter 6

Bound states and resonances in the FRG-approach

In this chapter, we will deal with bound states and resonances in the FRG framework. Our analysis is based on two key ingredients, namely, the concept of dynamical hadronization [29, 52–54] and the calculation of the real-time correlation functions [40–51]. Let us also note here that an FRG approach very close to the BSE-DSE framework has been put forward in [202, 203]. However, we will not discuss this approach here and refer the reader to [204, 205] for recent works in this direction.

As a first step, we will test both key ingredients on the QCD-assisted low-energy quark-meson model (QMM), starting with the dynamical hadronization in the first section 6.1. The major parts of these results are already published in [206, 207]. We will introduce the real-time FRG in section 6.2. Afterward, we combine both techniques in section 6.3 to formulate the weak pion decay in the FRG framework analog to the DSE/BSE framework. Some parts of the findings are already published in [197]. In the end, we will summarize our findings and discuss the physical implications.

6.1 Quark-meson model

In the FRG framework, we start with the classical action of the theory at the cutoff-scale Λ and integrate out step by step the quantum fluctuations. As a result of this, all the correlation functions of the theory are generated dynamically into the system. This includes all the related particles of the corresponding theory. Dynamical hadronization is an appropriate and efficient way to include them as the effective degrees of freedom, diagrammatically shown as double lines in figure 3.2.

The stepwise integration of the quantum fluctuation is done by lowering the cutoff-scale k. In particular, all the single loops in figure 3.2 are suppressed if the cutoff-scale drops below the mass gap m of the respective propagator. This essentially means that at a given scale, k_0 particles with heavier mass gaps ($k_0 < m$) effectively decouples from the system. Thus, they can be dropped, and particles with lighter mass gain in importance.

We may use these as the effective fields ϕ_{EFT} to get an effective low-energy description of the initial theory. This describes a natural way to embed an effective theory into the more fundamental theory, where the cutoff k_0 is the natural UV-cutoff of the effective theory

($\Lambda_{\mathrm{EFT}} = k_0$). We may write this as:

$$S_{\mathrm{EFT},\Lambda_{\mathrm{EFT}}}\left[\Phi_{\mathrm{EFT}}\right] = \Gamma_{\mathrm{FT},k_0}\left[\phi_{\mathrm{EFT}}\right], \tag{6.1}$$

where S_{EFT} is the classical action of the effective theory and Γ_{FT} is the regularized effective action of the more fundamental theory at the scale k_0.

In this work, we use this procedure to get a QCD-assisted low-energy effective theory (see, e.g., [166–168] and the references therein for further details in the context of the QCD). Notably, we may get an effective theory, where the gauge sector is decoupled from the matter sector. This is owed to the fact that the gluons in the Landau-gauge have a mass gap of almost 1 GeV, and hence below the cutoff-scale of $k_0 \lesssim 1\,\mathrm{GeV}$, they are decoupled from the system. So the gluons can be dropped. Since the ghost fields only couple to the matter sector via the gluons in leading order, the ghost fields can also be dropped.

We are left with the quarks, leptons, and hadrons with masses below 1 GeV. The pions and sigma are the lightest hadrons and thus play the most crucial role. As a first step, we ignore the leptons and take only pions and sigma into account. This leads us to the QMM. This concludes our discussion of the QCD-embedding of the low-energy effective theory. We now proceed with the investigation of the QMM.

In the first section 6.1.1, we will present the action of the QMM. Afterward, we will discuss the flow equation in section 6.1.2. We show the numerical results in section 6.1.3 and compare them with the QCD correlation functions from [168]. In the end, we will use the numerical extrapolations of the propagators to determine their poles in section 6.1.5.

6.1.1 Ansatz

In section 5.4, we have already emphasized the importance of the symmetries for the truncation scheme in the context of the chiral symmetry for the pions. In the DSE/BSE framework, the most challenging complication is to find the right approximation for the kernel, which is, on the one hand, treatable and, on the other hand, keeps the most important symmetries of the underlying physics intact.

This is much easier in the FRG framework based on dynamical hadronization. This is owed to the fact that the correlation functions are not treated as in the DSE/BSE approach, partly including the off-shell behavior and partly restricting to on-shell properties. Instead, all the correlation functions originate from common effective action. Naturally, such a unified approach resolves the challenge of self-consistent truncations, which is of crucial relevance in the DSE-BSE framework, by construction. As a consequence of this, a chiral symmetric ansatz for the regularized effective action is sufficient for our study of the pions.

Let us now start with the construction of the right ansatz for our study, which is minimal on the one hand and captures all the relevant physics, on the other hand. This requires to include the sigma in addition to the pions to realize the symmetry appropriately (see our example for the dynamical chiral symmetry breaking in 2.4.2).

Apart from the kinetic terms for the different fields, we can divide the effective action into three parts, namely the quark-self-interaction part, the pure mesonic-self-interaction part and the connection between them. Let us first state our ansatz and discuss the different parts afterward:

$$\Gamma_k = \int \Bigg\{ Z_{Q,k} \left(\overline{Q}\partial\!\!\!/ Q\right) + \frac{1}{2} Z_{\sigma,k} (\partial_\mu \sigma)^2 + \frac{1}{2} Z_{\pi,k} (\partial_\mu \pi^\alpha)^2 + V_k\left[\rho\right] - c\sigma$$
$$+ h_k \overline{Q} \left(\mathrm{i}\,\gamma_5 T^\alpha \pi^\alpha + \frac{1}{\sqrt{2N_f}} \sigma \right) Q + \lambda_k \left[\frac{1}{2N_f} \left(\overline{Q}Q\right)^2 - \left(\overline{Q}\gamma_5 T^\alpha Q\right)^2 \right] \Bigg\}. \tag{6.2}$$

We start our discussion with the part for the quark-self-interactions. During the flow of the effective action for the QCD, all the quark-self-interactions are generated dynamically and in leading order the four-quark interactions. The scalar minus the pseudo-scalar channel is related to the lightest mesons, as presented in our example for the chiral symmetry breaking in section 2.4.2. Hence, they are the most dominant interaction channels. In addition to this, they are also symmetric under the chiral transformation, as illustrated in section 2.4.2 and are, therefore, our choice for the interaction channels in the pure quark sector.

From the dynamical hadronization, we obtain a Yukawa interaction term between the mesons and quarks with the Yukawa coupling h_k. This expression is the generalization of the relations obtained in section 2.4.2. We follow [168] and parametrize the scale-dependence of the auxiliary field as:

$$\partial_t \tilde{\sigma}(p) = \frac{1}{\sqrt{2N_f}} \int_q \dot{A}_k\left(p-q,q\right) \left(\overline{Q}(p-q) Q(q)\right),$$
$$\partial_t \tilde{\pi}^\alpha(p) = \int_q \dot{A}_k\left(p-q,q\right) \left(\overline{Q}(p-q)\,\mathrm{i}\,\gamma_5 T^\alpha Q(q)\right). \tag{6.3}$$

Here, we introduce the quantities for arbitrary amount of flavors, but the final calculation is done for $N_f = 2$.

The mesonic-self-interaction is described by the potential $V_k[\rho]$, which is $O(4)$-symmetric indicated by $\rho = \frac{1}{2}\kappa^2$ with $\kappa = (\sigma, \pi^\alpha)$ as the isospin symmetry remains unbroken. A non-vanishing expectation value of ρ signals condensation of the sigma meson ($\langle\rho\rangle = \frac{1}{2}\langle\sigma\rangle^2 \neq 0$), thus spontaneous symmetry breaking.

The term $c\sigma$ is an appropriate shift of the sigma field caused by the current quark masses, which breaks the $O(4)$-symmetry explicitly. This effectively alters the expectation value of the sigma meson by tilting the effective potential ($U_k = V_k - c\sigma$) and hence results in a finite mass of the Goldstone modes (pions).

As a consequence of this, it is more convenient to use a Taylor expansion for the potential V_k about the IR minimum $\rho_0 = \frac{1}{2}\langle\sigma\rangle^2$ of the corresponding effective potential U_k (see [208] for further details). So we may write the potential as follows:

$$V_k[\rho] = \sum_{i=1}^{N} \frac{v_{k,i}}{i!} (\rho - \rho_0)^i, \qquad U_k'[\rho]\big|_{\rho=\rho_{\min,k}} = 0, \qquad \rho_0 = \rho_{\min,0} = \tfrac{1}{2}\langle\sigma\rangle^2, \tag{6.4}$$

where $v_{k,i}$ are the momentum-independent couplings. The order of the Taylor expansion N is chosen large enough to achieve apparent convergence. The expansion point is kept fix throughout the flow to increase the stability of the flow equations [208].

Before we conclude our discussion on the ansatz, let us look closer to quark-meson interaction. From our ansatz we get for the quark-pion-vertex:

$$\Gamma^{(3),\pi,Q,\overline{Q}} = \mathrm{i}\, h_k \gamma_5 T^\alpha. \tag{6.5}$$

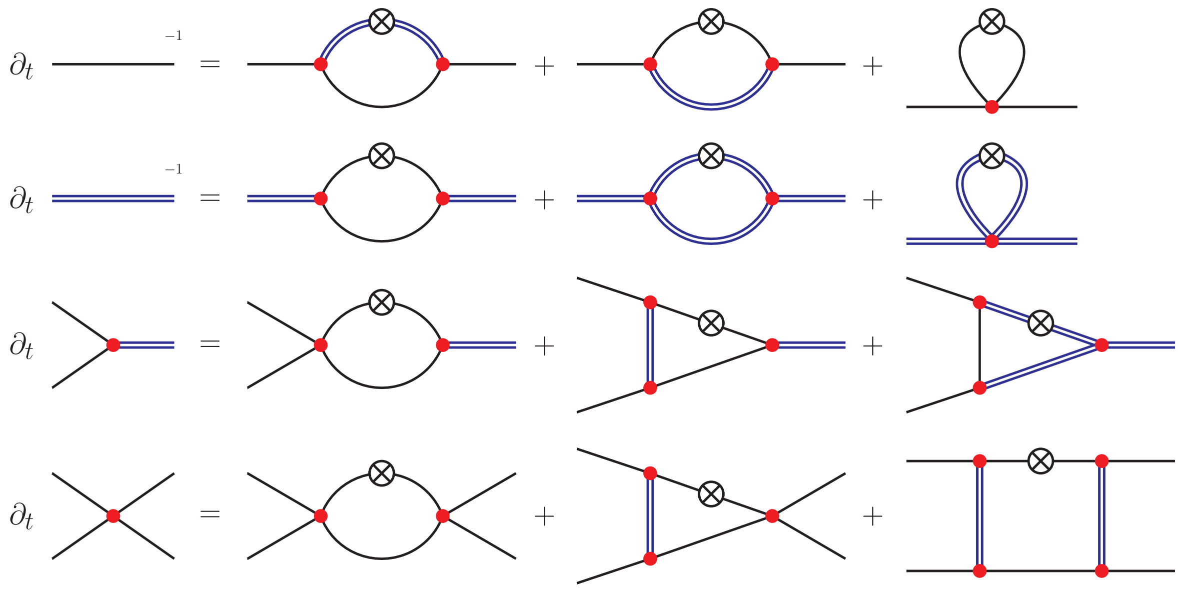

Figure 6.1: Diagrammatic representation of the flow equations for the propagators, Yukawa coupling, and 4-quark interaction. For the sake of brevity, we suppress the different permutations of the diagrams for the Yukawa coupling and 4-quark interaction.

This vertex is directly related to the BSA of the pion, as already outlined in the last chapter (see equation (5.23) and (5.20)). The BSA of the pion has 4 Lorentz-channels, and we are taking only the most dominant of those in our ansatz ($h_k \hat{=} f_1$). The channel f_2 and f_3 play an important role for the weak pion decay as presented in section 5.4.2 and hence will be taken into account for the study of the decay process in section 6.3. Since we just start to build our setup in this section, our approximation for the quark-pion-vertex is sufficient. To summarize, our ansatz captures within a reasonable approximation the leading behavior of the two flavor QCD at low momenta. We close our consideration on the ansatz and turn to the flow equations.

6.1.2 Flow equations

Let us now turn to the different quantities in our ansatz and consider their flow equations. First of all, we have the wavefunction renormalization functions for the mesons $Z_{\pi,k}(p)$, $Z_{\sigma,k}(p)$ and quarks $Z_{Q,k}(p)$, the Yukawa coupling $h_k(p_1, p_2)$, 4-quark coupling $\lambda_k(p_1, p_2, p_3)$, and the couplings of the mesonic potential $v_{k,i}$. We take the latter one momentum-independent and all the other quantities momentum-dependent.

The flow equations of these quantities are obtained by inserting our ansatz from equation (6.2) in the Wetterich equation (3.21) evaluated at the IR minimum for the sigma field. For example, the wavefunction renormalization functions are obtained from the corresponding 2-point functions. Further technical details on the derivation and the explicit expressions of the flow equations are shifted to the appendix D.3.3.

The diagrammatic representation of the flow equations is shown in figure 6.1. Let us start with the 4-quark interaction λ_k (last line in figure 6.1). First of all, we see that the exchange of the mesons via Yukawa interaction (box-diagram) generates λ_k dynamically into the system even if we start our flow for vanishing 4-quark interactions $\lambda_\Lambda = 0$, which is the famous double-counting problem of the Hubbard-Stratanovich transformation as already mentioned.

With the help of $\dot{A}_k$ from the parametrization of the dynamical hadronization we can avoid this issue. To be more precise, due to the modified Wetterich equation for the dynamical hadronization case (see the extra term on the left hand side of equation (3.21)) we get:

$$\partial_t \lambda_k = \text{Flow}\lambda_k - \dot{A}_k h_k, \qquad \partial_t h_k = \text{Flow} h_k - \dot{A}_k \Gamma^{(1),\kappa}. \tag{6.6}$$

We avoid the dynamical generating of the 4-quark coupling by canceling its flow and hereby shifting all the contributions to the Yukawa coupling.

$$\partial_t \lambda_k = 0, \qquad \Rightarrow \dot{A}_k = \frac{\text{Flow}\lambda_k}{h_k}, \qquad \Rightarrow \partial_t h_k = \text{Flow} h_k - \frac{\text{Flow}\lambda_k}{h_k}\Gamma^{(1),\kappa}. \tag{6.7}$$

As a consequence of this, the interaction vanishes $\lambda_k \equiv 0$. Moreover, we can drop all the diagrams with the 4-quark-vertex[1]. This simplifies the coupled set of equations significantly, and we are left with the flow equations of the 2-point functions and the 2-quark-meson-vertex.

In the second last line of figure 6.1, we see the flow of the 2-quark-meson-vertex. The 2-quark-pion-vertex is related to the BSA of the pion, as already discussed in section 6.1.1 and 5.4.2. We will compare this vertex with the BSA in section 6.3 in more detail, and hence turn to the 2-point-functions.

The flow of the inverse QP (first line) is similar to the DSE of the QP, shown in figure 3.4. Apart from the regulator insertion and all vertices being full vertices, the major difference is the exchange of the mesons, which are the effective low-energy degree of freedom, instead of the gluons. As an advantage of this, we can take the dynamical back-coupling of the light meson sector to some extent into account since it is easier than the dynamical back-coupling of the gauge sector. So we also have the flow of the inverse meson propagators (second line) and also the flow of the mesonic potential. This concludes our discussion on the flow equations, and we proceed with the numerical results.

6.1.3 Numerical results

In the following, we differentiate between the bare and renormalized quantities, which will be denoted by a bar. The renormalization conditions are imposed at vanishing momenta (which is the simplest choice) by requiring

$$\bar{Z}_{\pi,k}(p=0) = 1, \qquad \bar{Z}_{\sigma,k}(p=0) = 1, \qquad \bar{Z}_{Q,k}(p) = Z_{Q,k}(p), \tag{6.8}$$

As a result, all dressed quantities are RG-invariant, while the bare ones are not[2]. Further details on renormalizing the different quantities are shifted to the appendix D.

[1]This does not mean that the flow equation of the 4-quark coupling is irrelevant. The box-diagram plays an essential role as its contributions are shifted to the Yukawa coupling. For further details, see analysis of the different truncation schemes in appendix D.3.4

[2]Note that the quark wavefunction renormalization ($Z_{Q,k}$) is not renormalized in the IR, like the meson wavefunction renormalization, rather in the UV ($Z_{Q,k}(p_{\max}) = 1$) in our convention. This is due to the nature of the quarks as they are free at high-energies (asymptotic freedom) and confined in hadrons at low-energies (confinement). This is also done for the quark wavefunction renormalization in the DSE framework (see chapter 4). In this regard, let us also note that the quark wavefunction renormalization is defined in the FRG framework as the inverse of the one in the DSE framework ($Z_{\text{FRG}} = 1/Z_{\text{DSE}}$) in the standard literature. We keep the standard definitions from the literature throughout this work for the sake of comparison.

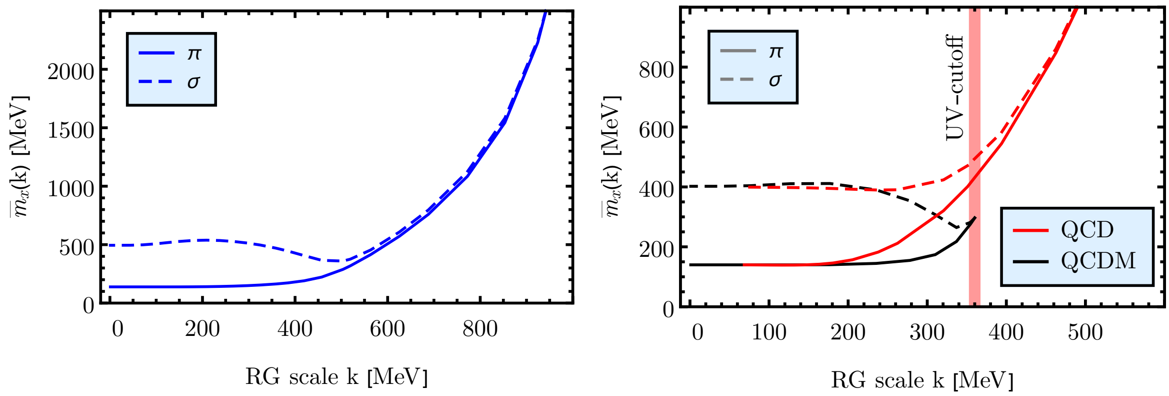

Figure 6.2: The flow of the curvature masses (PM left panel and QCDM right panel) for the mesons. The flow is started in the chiral symmetric regime. During the flow, chiral symmetry is broken dynamically, and thus the masses of pion and sigma run apart in the QMM. In the right panel the results for the QCDM and those in full QCD from [168] are compared.

We solve the flow equations for two different sets of parameters in the IR ($k \to 0$). The first set corresponds to the values of the physical observables and the second one to the first-principle calculation of the QCD with the FRG presented in [168]. The latter one has the advantage of testing the validity of low-energy effective descriptions of bound states in QCD.

For the first one, we set the curvature masses in the IR to the following values:

$$\overline{m}_\pi = 138.7\,\text{MeV}, \qquad \overline{m}_\sigma = 495\,\text{MeV}, \qquad \overline{m}_Q(0) = 297\,\text{MeV}, \qquad f_\pi = 93\,\text{MeV}, \tag{6.9}$$

where the running curvature masses are defined at the minimum of the potential:

$$\begin{aligned} m^2_{\pi,k} &= V_k'[\rho]\big|_{\rho=\rho_{\min,k}}, \qquad\qquad m^2_{\sigma,k} = \left[V_k'[\rho] + 2\rho V_k''[\rho]\right]\big|_{\rho=\rho_{\min,k}}, \\ m_{Q,k}(p) &= \frac{h_k(p,-p)}{\sqrt{2N_f}}\sigma_{\min,k}. \end{aligned} \tag{6.10}$$

The pion decay constant f_π will be calculated from the σ condensate based on an approximation provided by the Gell-Mann-Oakes-Renner relation. The accuracy of this strongly simplified way to determine the pion decay constant is sufficient for the purpose of the exploratory investigation presented here.

The second set of parameter is given by:

$$\overline{m}_\pi = 140\,\text{MeV}, \qquad \overline{m}_\sigma = 402\,\text{MeV}, \qquad \overline{m}_Q(0) = 409\,\text{MeV}, \qquad f_\pi = 79.3\,\text{MeV}. \tag{6.11}$$

In the following, we will refer to the results from the first and second parameter set as the physical model (PM) and the QCD related model (QCDM) respectively. The latter one will always be compared with the results from the first principle calculation of the QCD in FRG from [168] and referred as the QCD results in the following.

Before we start, let us state some technical details. The Yukawa coupling depends on two external momenta $h_k(p_1, p_2)$, where p_1 and p_2 are the momenta of the anti-quark and quark,

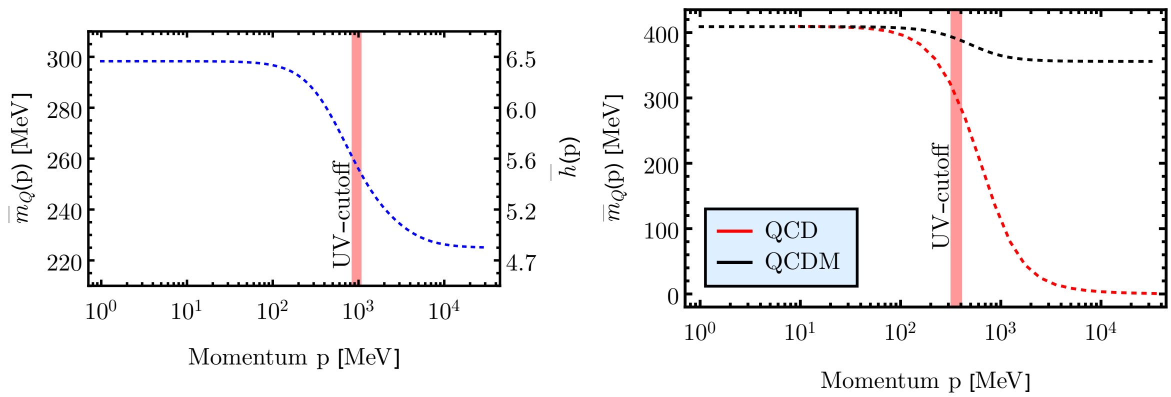

Figure 6.3: Momentum-dependent quark massfunction (PM left panel and QCDM right panel) and the Yukawa coupling for the PM (left panel). The right panel shows a comparison of the same quantity between the QCDM and QCD.

respectively. Previous studies in QCD [168] have shown that a weighted sum between total and relative momenta captures the full momentum-dependence quite accurately.

$$h_k(p_1, p_2) \to h_k\left(\sqrt{\frac{1}{4}(p_1 - p_2)^2 + (p_1 + p_2)^2}\right). \tag{6.12}$$

The same also holds for $\dot{A}(p_1, p_2)$. So this will be employed for our study of the QMM.

Let us note here, that for the comparison of the Yukawa coupling with the dressing function from the BSA, we need the full momentum-dependence of the Yukawa coupling at the pion pole. So restricting h_k to one momentum channel is not sufficient for the study of the weak pion decay. Therefore, we will take the full momentum-dependence in section 6.3 into account. Further technical details are shifted to appendix D.

Let us start with the flow of the mesonic curvature masses, depicted in figure 6.2. This is a key ingredient in all diagrams as it sets the dominant scale in the diagrams. In the left panel, we depict the results for the PM and in the right panel for the QCDM, along with the QCD results. Flows of the masses starts in almost chiral symmetric region ($\rho_{\min,\Lambda} \approx 0$)[3] for all three models. Hence, the curvature masses of pion and sigma are almost identical (see equation (6.10)). During the flow, chiral symmetry is broken dynamically ($\rho_{\min,k} > 0$) resulting in heavier masses for sigma. The results from the PM are qualitatively very similar to the previous calculations in the QMM (see, e.g., [208, 209]).

In the context of our work, the description of bound states and resonances (i.e., low-energy degree of freedom) is of significant interest. In particular, the hallmark of our study is the non-perturbative study of hadrons starting from the QCD. Therefore, the comparison with the

[3]Note that the term $c\sigma$ in the effective action alters the expectation value by tilting the effective potential, thus $\rho_{\min,k} > 0$ for all scales k. The term $c\sigma$ is the appropriate shift caused by the current quark masses. The finite quark masses break the chiral symmetry explicitly, which is small for quarks of the first generation. $\rho_{\min,\Lambda} \approx 0$ just outlines this fact. For the chiral symmetric case (without the term $c\sigma$, thus $U_k = V_k$), the pion mass flows towards zero ($m_\pi = V_0'|_{\rho=\rho_{\min,0}} = U_0'|_{\rho=\rho_{\min,0}} = 0$) as the pions are the Goldstone bosons. Therefore, pions would be absent from the physical spectrum. This case is not very interesting for us since we want to study the pions.

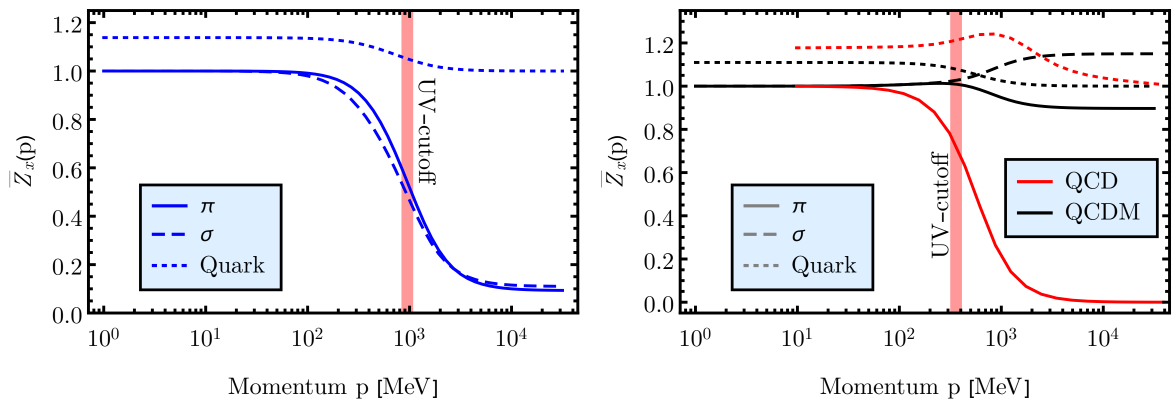

Figure 6.4: Momentum-dependent wavefunction renormalization (PM left panel and QCDM right panel). The right panel shows a comparison of the same quantity between the QCDM and QCD.

QCD results is of particular importance. We plot the results for the different quantities on the right panels of figures 6.2, 6.3, and 6.4. For small and moderate scales, or low-momenta regions; our results are in good agreement with the low-energy QCD results. However, these results can only be achieved by using a very small UV-cutoff, namely $\Lambda_{UV} \sim 360\,\mathrm{MeV}$ (see also [210]). With a higher UV-cutoff, it is not possible to decrease the sigma mass further while keeping f_π, m_π and m_Q fixed. This is most likely linked to the triviality of the O(N) model, which shrinks the values of possible IR values for a given cutoff when increasing the truncation. This has already been observed in [43, 211].

Let us, in the following, compare the different quantities in more detail and state their implications for physics, starting with the curvature masses in figure 6.2. The mesonic degrees of freedom decouple considerably faster in QCD, which is also visible in figure 6.3 for the quark masses or in figure 6.4 wavefunction renormalization. Besides, the sigma mass in QCD does not show the dip towards smaller masses in the region where chiral symmetry is restored, which is also related to the steeper rise of the massfunction in QCD. This feature has potentially important consequences for the details of chiral symmetry restoration at finite temperature, thus deserves further investigation.

There, the low UV-cutoff scale additionally results in a relatively low highest temperature that can be considered due to the thermal range of these models, see [212]. More generally, the necessary modification of the initial effective action for large external scales such as temperature, chemical potential, external background (chromo-) magnetic and electric fields has to be considered, for a detailed discussion see [213].

In all plots, the red vertical line denotes the UV-cutoff used in our calculation. The slow decay for large momenta is not very surprising in the QMM as there is no other scale involved, which could potentially suppress the mesonic degrees of freedom. Nevertheless, it is one of the most prominent differences to the full QCD calculation, resulting in a rather small range of momenta, where the QMM accurately describes all dynamics of full QCD. However, this does not imply that the description at larger momenta is wrong, merely that the question depends strongly on the observable at hand. This concludes our presentation of the results for Euclidean momenta. Let us now briefly discuss systematic improvements of the QMM towards full QCD on a quantitative level.

6.1.4 Systematic improvements towards QCD

In our system, we consider apart from the couplings of the mesonic potential four quantities, namely, the wavefunctions of the mesons and quark, and the Yukawa coupling. The wavefunction of the quark stays practically at unity for all scales. The bump in QCD at the scale of the gluon mass gap corresponds only to a sub-leading quantitative correction. Therefore, we can neglect the wavefunction of the quarks and concentrate our discussion on the remaining quantities. In particular, the difference in the wavefunctions of sigma and quark does not play an essential role in the following discussion. So we focus on the mesonic wavefunction $\bar{Z}_\kappa(p)$ and Yukawa coupling $\bar{h}(p_1, p_2)$.

Let us start with the wavefunction. We observe significant differences between the QMM and the QCD results; see figure 6.4. However, the leading diagrams that generate momentum-dependence are the same in both cases (the first two diagrams in the second line of figure 6.1). As a result, the main difference between the QMM and QCD results must be generated by $\bar{h}(p_1, p_2)$.

To see this, we also consider the leading diagrams for the momentum-dependence of the Yukawa coupling and get three leading diagrams of the triangle form. The first two triangle-diagrams with the quark and meson exchange are again self-consistently contained in the QMM (second and last term in line three of figure 6.1). However, the diagram with the gluon exchange, see the right panel in figure 6.5, is not. It is not possible to include this diagram without the knowledge of the gluon propagator and the quark-gluon-vertex building up the one gluon exchange coupling, but QCD-assisted models can be constructed with this input.

Let us note here that in the DSE/BSE framework, we also model the quark-gluon-vertex and the gluon propagator according to the rainbow-ladder truncation. The model for the interaction is given by the Maris-Tandy coupling. Thus, including these as an external input would result in an analogous truncation scheme like the rainbow-ladder truncation in the DSE/BSE framework.

We conclude from this analysis that the QMM can be systematically improved towards QCD by either including the QCD Yukawa coupling as external input or the gluon exchange coupling (right panel in figure 6.5). This underlines the strength of the current setting of systematically improvable QCD-assisted low-energy effective theories. This concludes our discussion on the systematic improvements towards QCD, and we proceed with the poles from the numerical extrapolation.

6.1.5 Poles from the numerical extrapolation

In this section, we determine the pole positions of the mesonic and quark propagators using Schlessinger's point method. We skip the Schwinger function since we have already seen that both methods lead to similar results in the context of the QPs in chapter 4. The pole position from the direct calculation in Minkowski space is done in the next section 6.2.2. So the numerical values of the masses and decay-width for both methods are stated in table 6.1 after introducing the FRG approach to real-time correlation functions.

The pion is the lightest degree of freedom in the QMM, thus stable. For the sigma meson, it is found in the present calculation that its pole mass slightly exceeds the two pion decay threshold. Therefore, we expect the mass to be dominated by a pole close to the timelike axis

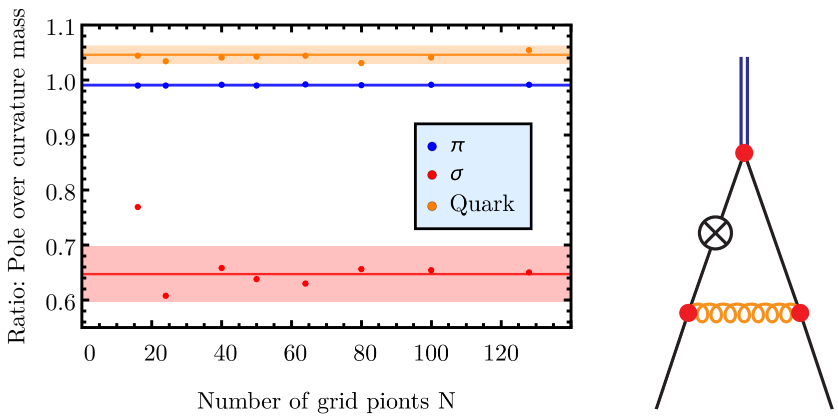

Figure 6.5: The ratios of the pole masses m_{pole} from the numerical extrapolation using Schlessinger's point method and curvature masses m_{cur} for different grid points (left panel) and the dominant diagram contributing to the Yukawa coupling in QCD (up to permutations of the regulator) and not included in the QMM (right panel). The ratio (left panel) is stable for the pion and for the quarks. For the sigma it converges slowly, but eventually.

on the second Riemann sheet of the retarded propagator and, therefore, accessible within this framework to good accuracy.

The quarks also have a pole very close to the timelike axis on the second Riemann sheet. This is in contrast to the pair of complex conjugate poles in the DSE framework (see top panel of figure 4.7). The complex conjugate poles are associated with confined states under the assumption of unbroken BRST symmetry (see [153,162,214–217] and the references therein for a detailed discussion on this topic). The confinement property for the quarks requires the gauge-sector, which is dropped in the low-energy QMM. Therefore, the pole on the second Riemann sheet for the quarks is not a contradiction within our truncation. The finite decay-width of the quarks is related to the possibility of forming pion and sigma via dynamical hadronization.

The numerical error of the reconstruction is checked by computations with different numbers of grid points. The resulting masses are displayed relative to the curvature masses in the left panel of figure 6.5. As expected from analytical arguments, the pole mass of the pion agrees well with its renormalized curvature mass [43,212], and its decay width is zero within numerical uncertainties.

As outlined above, the sigma meson features in our calculation within the QMM only a small decay width, $\Gamma/M \ll 1$, validating our reconstruction approach. Furthermore, the relative difference between the pole and curvature mass is significant at $\sim 35\%$. Such an order of magnitude agrees qualitatively with previous studies [43] in which the momentum-dependence of the propagators was not fed back into the equations. This has obvious consequences for low-energy effective theories of QCD, where the mass of the sigma meson is often used to fix the free parameters. This concludes our presentation of the results, and we proceed with the real-time FRG.

6.2 Real-time FRG

After years of extensive development for the calculation of the real-time correlation functions, we have now a very well real-time version of the FRG at hand [40–51]. This makes use of the well-known Euclidean correlation functions of the theories. We may find all the key ideas for the real-time FRG in the work of [41], which is the fundament of this study. In [41], the real-time version is applied to a bosonic theory. Thus, additional complexities arising from the fermions are not discussed there. Here, we briefly mention the key ideas of [41] in section 6.2.1 and apply them to the QMM in section 6.2.2. The technical issues arising from the insertion of the fermions are shifted to the appendix D.4. We refer the reader to [41] and the references therein for a detailed introduction.

6.2.1 Introduction

First of all, the calculation of the real-time correlation functions is not a conceptional issue in the functional methods rather a technical problem. In the FRG framework, the regulator insertion introduces additional unphysical poles in the propagator (see equation 3.17). We may write the propagator of a bosonic field[4] ϕ as follows:

$$P_k^{\phi} = \frac{1}{\Gamma_k^{(2),\phi} + R_k} = \frac{1}{\Delta\Gamma_k^{(2),\phi} + m^2 + R_k}. \tag{6.13}$$

Here, we split the contributions from the 2-point functions $\Gamma^{(2),\phi}$ in the part for the mass m and the rest $\Delta\Gamma^{(2),\phi}$.

We have already seen that the pole position of the QPs limits the calculation of the BSA in the DSE/BSE framework, and going beyond the poles requires advanced numerical methods (see section 5.2). The significant difference is that the poles in the FRG framework are scale-dependent and, therefore, move during the flow. The Wetterich equation is integrodifferential-equation. Hence we have to perform momenta integration on contours.

The naive idea of deforming the contours to avoid the poles would lead to changing the contours in each RG-step, which is not practical. The second option is to avoid the unphysical poles by introducing a regulator, which only depends on spatial momenta. However, this would break Euclidean and Minkowski symmetry, and regulators that preserve $\mathrm{SO}(1,3)$ Lorentz-symmetry are of paramount importance [40–43]. Therefore, this option is also not possible.

The way out of this problem is the freedom of choice for the regulators. We may modify the regulator with an additional $\Delta M(k)$ term to shift the poles outside the contours:

$$\begin{aligned} &R_k \to R_k + \Delta M^2(k), \\ \Rightarrow\ &P_k^{\phi} = \frac{1}{\Delta\Gamma_k^{(2),\phi} + m^2 + R_k + \Delta M^2(k)} = \frac{1}{\Delta\Gamma_k^{(2),\phi} + R_k + M^2}, \end{aligned} \tag{6.14}$$

where $M^2 = m^2 + \Delta M^2$ is the effective mass. We see that this shifts the position of the pole. The modified regulator $R_k + \Delta M^2$ must still obey the three conditions for the regulator (see section 3.3). This rather simple idea works as shown in [41] and is sufficient for our study.

[4]For the illustration, we use the bosonic case since it is simpler. For the fermions, we may extract a common denominator from the different Lorentz-channels, which is similar to the form in equation (6.13). See our example for the effective scalar QP in appendix D.3.2.

In the fermionic case, we have different Lorentz-channels for the 2-point function. The naive idea of introducing the additional mass-term in the scalar channel would break the chiral symmetry explicitly. This is not desirable since the symmetry is of paramount importance for our study. All the Lorentz-channels contribute to the poles. Thus, they are present in all the Lorentz-channels of the propagator. Therefore, we can pull a common denominator out consisting of the poles.

We define this as the effective scalar propagator ($\hat{P}$). It has the following general form (see, e.g., the QP in equation (D.27)):

$$\hat{P}(p) = \frac{1}{\left[Z_{r,k}(p)\right]^2 p^2 + m^2(p)}, \qquad Z_{r,k}(p) = Z_k(p) + \hat{R}_k^F(p), \tag{6.15}$$

where $\hat{R}$ is the scalar contribution to the fermionic regulator (without the Lorentz-structure). So taking the ΔM term in the vector channel as:

$$R_k^F(p) = \tilde{R}_k^F(p) + \Delta M(k)\not{p}, \tag{6.16}$$

shifts also the pole position. This concludes our introduction into the real-time FRG and further technical details are stated in the appendix D and [41].

6.2.2 Poles for the quark-meson model from the real-time FRG

Our major quantity of investigation is the spectral function from which we may extract the pole of the particles. The spectral function ρ is given by:

$$\rho(p) = -2\mathrm{Im}G_R(p), \tag{6.17}$$

and directly related to real-time retarded propagator (G_R). The retarded propagator can be obtained via the reverse wick rotation from the Euclidean propagator[5]:

$$G_R(p_0, \vec{p}) = -\lim_{\epsilon \to 0} P(\vec{p}, -\mathrm{i}(p_0 + \mathrm{i}\,\epsilon)). \tag{6.18}$$

So in practice, we calculate the propagator along the vertical axes in the complex plane to obtain the spectral function for different ϵ's.

The flow of the propagators is depicted in figure 6.1. As a first step, we truncate our coupled system of flow equations at the level of the propagators. This means we only calculate the propagators for complex momenta and use the already calculated Euclidean data for the higher-order n-point functions. This is analog to the rainbow-ladder truncation in the DSE/BSE framework, where we calculated the QP in the complex plane using Maris-Tandy coupling as the external input. This provides us also with a systematic truncation scheme since we can include the real-time higher-order correlation functions step by step into the system.

We calculate the spectral functions for the mesons and quark (at $\epsilon = 2\,\mathrm{MeV}$). Moreover, We normalize the spectral functions such that the maximum of the function is 1 for a better illustration since these differentiate in orders of magnitude. We show our preliminary results in figure 6.6 for the frequencies ($\omega = -p_0$). For the sake of comparison, we plot the spectral function using the propagator from the numerical extrapolation via Schlessinger's point method

[5]We study the case for vanishing temperatures, Hence, the Euclidean Feynman propagator coincides with the uniquely defined analytical continuation of the Minkowski Feynman propagator. For finite temperatures, see the detailed discussion in [41].

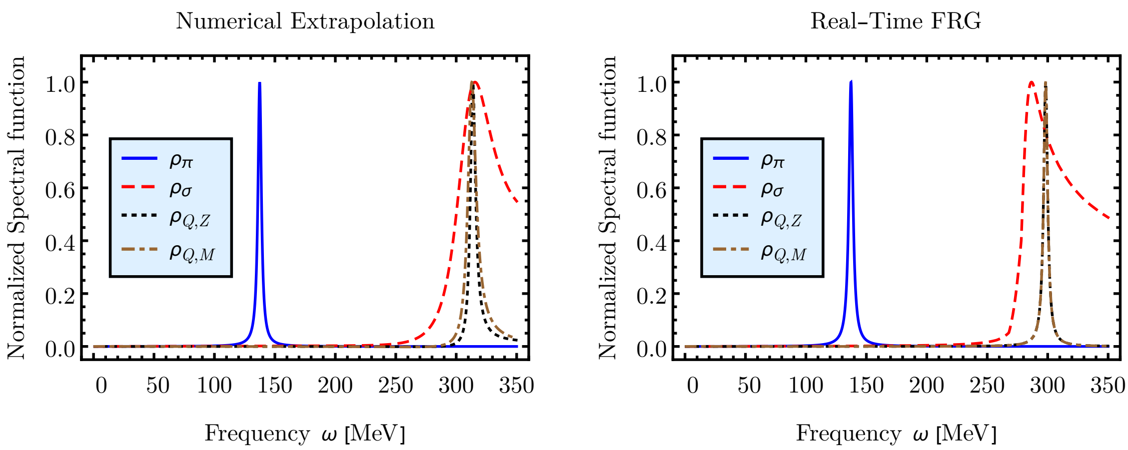

Figure 6.6: The normalized spectral function of pion (blue-solid line), sigma (red-dashed line), and quark for imaginary frequencies ω and $\epsilon = 2\,\mathrm{MeV}$. $\rho_{Q,Z}$ (brown-dotted line) and $\rho_{Q,M}$ (black-dot-dashed line) are the spectral functions of the vector and scalar channel, respectively. The spectral function are normalized such that the maximum of the function is 1 for a better illustration. Results from the numerical extrapolation (left panel) and real-time FRG (right panel).

(left panel) and real-time FRG (right panel). At this point, we again express our sincere gratitude to Nicolas Wink for providing us the numerical data of the spectral functions from the real-time FRG calculation.

The spectral function for the pion agrees quantitatively very well within both methods resulting in similar pole masses and decay-widths for the pion. This is just the expression of the fact that the Padé-like analytic continuations work very well for the lowest state.

The maximum for the sigma is shifted to lower frequencies resulting in smaller values for pole mass. This will move the pole mass closer to two pion threshold and hence is a correction of the results in the right direction. The same holds for the quarks. In addition to this, the spectral functions of the vector and scalar channel also agree very well quantitatively in the real-time FRG resulting in a more precise value for the pole position for the quark.

We use reconstruction methods for the pole positions in the real-time framework since we only have the functions along a vertical line and not in the plane. Further results on the complex plane are currently being calculated and will be presented in future studies. Results for the poles from the numerical extrapolation shows that $\Gamma \ll M$ is a reasonable assumption. Thus, we use the Breit-Wigner parametrization for the spectral function to fit the data. The parametrization is given as follows:

$$\rho_{BW}(\omega) \sim \frac{1}{(\omega^2 - M^2)^2 + M^2\Gamma^2}. \tag{6.19}$$

We listed the values for the masses and decay-width from the fit in table 6.1.

The pole masses of pion and quark are very close to the curvature masses. We get a stable pion within the numerical error as it is the lightest particle. The quark is almost stable. The biggest difference is seen for the sigma pole mass, which is now very close to the two pion threshold within the errors ($2m_\pi \approx 275\,\mathrm{MeV} \approx 290 \pm 15\,\mathrm{MeV}$). Our preliminary results already show that using the real-time FRG yields quantitatively better results for the pole positions.

		Numerical Extrapolation		Real-Time FRG	
Particle	Curvature mass	Pole mass	Decay-width	Pole mass	Decay-width
Pion	138.7	137.4 ± 0.5	0.5 ± 0.5	137.6 ± 0.1	0.5 ± 0.5
Sigma	494.5	320 ± 25	36 ± 5	290 ± 15	40 ± 10
Quark	298.3	312 ± 8	13 ± 5	299 ± 1	2 ± 1

Table 6.1: Curvature mass, pole mass and decay-width are given in MeV. For the numerical extrapolation, we have used the full momentum-dependencies of the respective propagator in the complex plane. In the case of the real-time FRG, we fitted the data to the Breit-Wigner representation of the respective spectral function.

This concludes our presentation of the preliminary results using real-time FRG, and we proceed with the weak pion decay.

6.3 Formulating the weak pion decay

Let us now formulate the weak pion decay in the FRG framework. For this purpose, we first deal with the minimal extension of the QMM from section 6.1.1 in the first section 6.3.1. Afterward, we will deal with the flow equations in section 6.3.2.

6.3.1 Ansatz

For the study of the weak pion decay, we include effective weak interaction as proposed in section 2.3 in our ansatz. As a consequence of this, the pion can now decay into leptons. Thus, we also have to include 2-lepton-pion-vertex in our ansatz. This also requires the propagation of the lepton in our system.

The QMM model proposed in section 6.1 has the charged, as well as the neutral pion, and sigma included for the right implementation of the chiral symmetry. The effective weak interaction violates the chiral symmetry explicitly. We take an explicit chiral violating ansatz, as already discussed in the DSE/BSE framework. Since we are interested in the weak pion decay of the charged pions, this will split each dressing function related to pions in part for the neutral pion and part for the charged pions[6].

For example, the 2-quark-pion-vertex consists of a tensor basis with 4 Lorentz-channel as it is directly related to the BSA (see section 5.4.2). Now we have 4 dressing function $h_{i,k}$ and $f_{i,k}$ for the neutral and charged pions, respectively (see equation (6.5) and (5.20)). For this purpose, we define the 4 tensor basis related to the pions and 1 to the sigma as follows:

$$\tau_1^\alpha = \mathrm{i}\,\gamma_5 T^\alpha \mathbb{1}_c, \qquad \tau_2^\alpha = \tau_1^\alpha \not{P}, \qquad \tau_3^\alpha = \tau_1^\alpha \not{k}, \qquad \tau_4^\alpha = \tau_1^\alpha P_\mu k_\nu \sigma_{\mu\nu}, \qquad \tau_0 = \frac{1}{\sqrt{2N_f}}\mathbb{1}, \tag{6.20}$$

where P and k are the total and relative momenta of the fermions, respectively. Taking all this

[6] This is also true for the parametrization for the scale-dependence of the auxiliary field in equation (6.3). This parametrization can straightforwardly be generalized for the splitted contributions for the neutral and charged pion. Thus, it is not stated explicitly in this work.

into account results in the following ansatz for our action:

$$\Gamma_k = \int \Bigg\{ Z_Q \left(\overline{Q}\partial\!\!\!/ Q\right) + \frac{1}{2} Z_\sigma (\partial_\mu \sigma)^2 + \frac{1}{2} Z_{\pi^n} (\partial_\mu \pi^3)^2 + \frac{1}{2} Z_{\pi^c} (\partial_\mu \pi^{\tilde{\alpha}})^2 + \bar{l} \left(Z_l \partial\!\!\!/ + m_l\right) l$$
$$+ U_k[\rho] + h_1 \sigma \left(\overline{Q}\tau_0 Q\right) + h_i \pi^3 \left(\overline{Q}\tau_i^3 Q\right) + f_i \pi^{\tilde{\alpha}} \left(\overline{Q}\tau_i^{\tilde{\alpha}} Q\right) + g_i \pi^{\tilde{\alpha}} \left(\bar{l}^L \tau_i^{\tilde{\alpha}} l^L\right)$$
$$+ \lambda^n \left[\left(\overline{Q}\tau_0 Q\right)^2 + \left(\overline{Q}\tau_1^3 Q\right)^2\right] + \lambda^c \left(\overline{Q}\tau_1^{\tilde{\alpha}} Q\right)^2 + \alpha_w \left(\overline{Q}^L \gamma_\mu T^{\tilde{\alpha}} Q^L\right) \left(\bar{l}^L \gamma_\mu T^{\tilde{\alpha}} l^L\right) \Bigg\}. \quad (6.21)$$

Here, we have suppressed the index for the RG-scale k for all the dressing functions for the sake of clarity.

The first line consists of the kinetic part for the different fields. The last line consists of different 4-Fermi interactions. The first term in the second line is the mesonic potential, which is unmodified. The second line consists of all the interactions between the meson sector and the fermion sector. In particular, the h's, f's and g's[7] are related to BSA of the neutral pion, charged pion and decay amplitude, respectively (see section 5.4.2). Taking all these into account results in 16 momentum-dependent dressing functions in our system instead of 4 in the QMM. This concludes our discussion for the ansatz of the effective action, and we proceed with the flow equations.

6.3.2 Flow equations

The diagrammatic representation of the flow equations for the weak pion decay is depicted in figure 6.7. We have two 4-fermion-vertices in our system – one for the quark-self-interaction and one arising from the weak interaction. The latter one is modeled by the 2-quark-2-lepton-vertex, according to 2.3. This means that the weak interaction is taken as an external model. Thus, the flow of the 2-quark-2-lepton is not taken into account.

The contributions from the flow of the 4-quark coupling are shifted to the Yukawa coupling via the dynamical hadronization, as described in 6.1.2. Therefore, the 4-quark-coupling vanishes for all scales. So we do not show contributions of this vertex to the flow of the other vertices. We depict the flow of the 4-quark-vertex (last line) containing only those diagrams, which generates this vertex dynamically back into the system as these contributions are required for the dynamical hadronization procedure.

The flow of the QP (first line) remains the same as in the QMM (see figure 6.1) as the effective weak interaction only contributes to flavor changing propagators within a generation, which is not possible due to the charge conservation. This was already observed in the DSE/BSE framework. Note, the flow of the QP is only identical at the diagrammatic level. Since the Yukawa coupling in the 2-quark-meson-vertex is split into parts for the neutral pion and charged pion, the explicit expression of the flow equation from the equation (D.37) changes.

The flow of the meson propagators (second line) gets an additional contribution from the lepton-loop. The flow of the lepton propagator (third line) also has a lepton-meson-loop contribution, and thus the lepton propagator is not the free propagator as in the DSE/BSE framework.

The 2-quark-pion-vertex and 2-lepton-pion-vertex are directly related to the BSAs (figure 5.3). Hence, we compare these two quantities in the following. The pure amplitude (Ψ) has

[7]Note that the only g_2 and g_3 are non-vanishing as discussed in section 5.4.2.

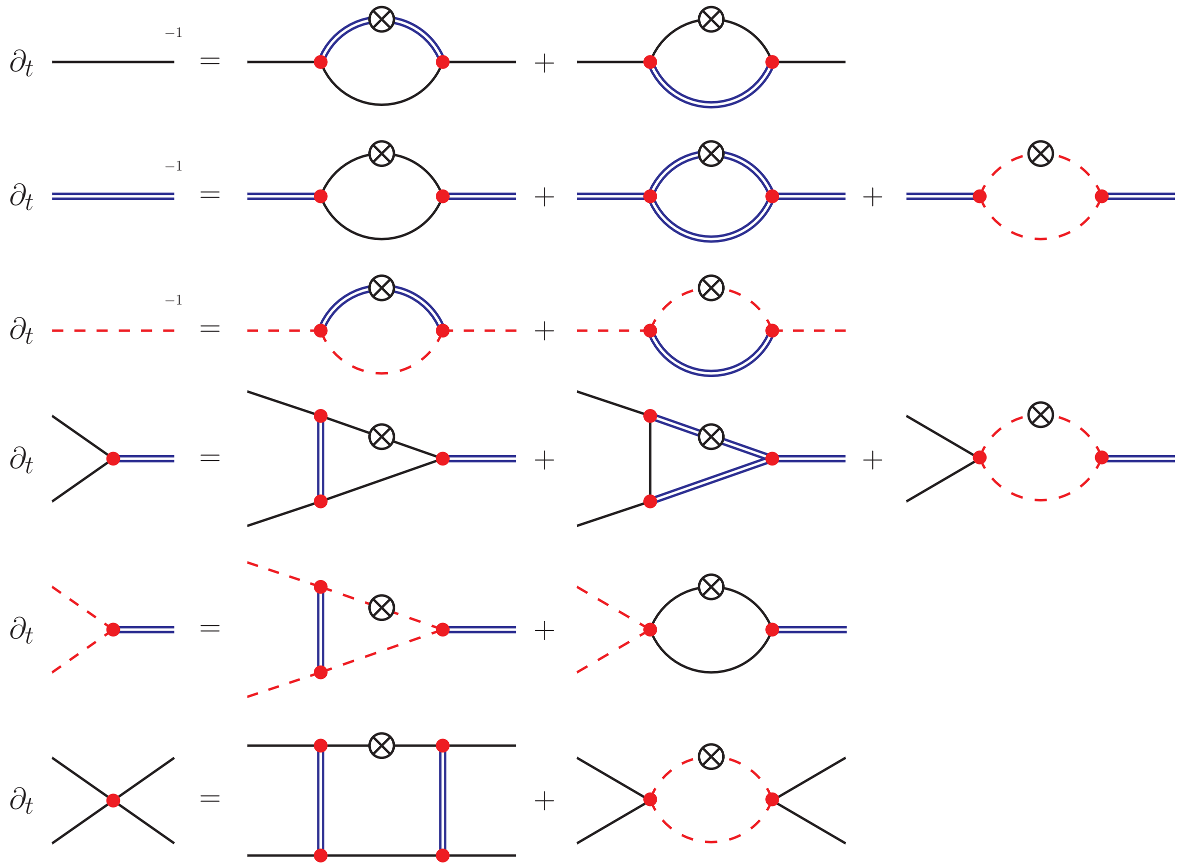

Figure 6.7: Relevant part of the flow equations for the propagators, Yukawa coupling, and 4-Fermi interaction. For the sake of brevity, we suppress the different permutations of the diagrams for the Yukawa coupling and 4-quark interaction.

one contribution from the QCD given by the gluon exchange and one contribution from the decay amplitude given by the effective weak interaction. The contribution from the QCD to the 2-quark-pion-vertex (fourth line) is now given by the mesons (first and second term) since they are an effective degree of freedom at low-energy and gluons are decoupled from the system.

Apart from these, the 2-quark-pion-vertex has also contributions from the effective weak interaction. The difference is that in the FRG framework, the 2-quark-2-lepton-vertex is a full vertex, and in the DSE/BSE framework, it is a tree-level vertex. As long as we model this vertex in the FRG framework, they both agree. Taking the flow of this vertex would take some effects of the dynamical back-coupling of the strong sector to the effective weak sector into account, which will be done in future investigations.

The 2-lepton-pion-vertex (second last line) is related to the decay amplitude. Thus, both have a similar contribution from the weak interaction (last term). Due to the dynamical hadronization, we have a Yukawa interaction between the leptons and pions in our system. This allows for a self-interaction between the leptons via a pion exchange (first term), and hence 2-lepton-pion-vertex has this additional contribution in contrast to the DSE/BSE framework, where the leptons are free.

The inclusion of the pions via the dynamical hadronization generates the dynamical back-coupling between the quark-meson sector and the lepton sector to some amount. This is in contrast to the DSE/BSE framework and highlights the power of the dynamical hadronization procedure. Anyhow, the Yukawa interaction is small, and the contributions of these are suppressed.

Let us, in the following, consider the implication of these in a little bit more detail. The 2-lepton-pion-vertex has contributions involving different and same handedness (see discussion in section 5.4.2). In particular, contributions to g_1 and g_4 vanishes as the weak interaction only couples to left-handed particles. The explicit breaking of the C, P, and flavor symmetry at the level of the QP showed that under particular circumstances, the handedness of the particles could be changed by the non-perturbative back-coupling. So the channel g_1 and g_4 can be generated by the dynamical back-coupling of the strong and weak interactions. As a consequence of this, the decay process may be suppressed, and the dynamics of the neutron star mergers may be significantly modified. We have set up a framework where we can tackle this issue step by step.

At the moment, these equations are solved, and the results will be reported elsewhere. This concludes our presentation of the weak pion decay in the FRG framework, and we summarize and discuss our findings in the following section.

6.4 Summary and discussion

We have set up the technical foundation to study the weak pion decay within the FRG framework. This approach is based on two key features, namely the dynamical hadronization and the real-time calculation of the correlation functions. The former one comes with the great advantage that the information of bound states can be mapped to lower-order n-point functions in a systematic manner. Besides, this simplifies the procedure of building self-consistent truncations compared to the DSE/BSE framework.

This is owed to the fact that the correlation functions originate from a common effective action; instead, stemming from an approach treating the correlation functions partly off-shell and partly on-shell, like in the DSE/BSE framework. Therefore, many problems are avoided when expressing the bound states exclusively in terms of their constituents.

Apart from these rather technical advantages, the inclusion of the effective degrees of freedom in the form of the pions and sigma generates an interaction between the leptons via mesons exchange. So this enables us to take some part of the dynamical back-coupling from the strong sector also in the lepton sector into account. To do this in the DSE/BSE framework involves the weak gauge bosons, which is highly non-trivial, highlighting the power of the dynamical hadronization procedure.

We first used this procedure within a QCD-assisted low-energy QMM and compared these results with a recent study of a full QCD calculation [168] to test the validity of our truncation. We found good quantitative agreement at low-energies $\lesssim 250\,\mathrm{MeV}$. Above these scales, qualitative differences start to appear, which could be traced back to missing contributions in the Yukawa coupling. Especially, the implementation of the chiral symmetry and dynamical mass generation was correct, which is of paramount importance for the study of the pions. So using a low-energy effective model is reasonable to describe the dynamics of pions at low-energies, which is sufficient for our work.

Therefore, we used the second set of parameters for the QMM to produce results with physical observables in the IR. In particular, we extracted the pole masses of the quarks and mesons from there propagator using numerical extrapolation via Padé-like approximation, as well as from the spectral function of the particles via real-time FRG. Since the pion was the lowest-lying state in our system, it was found stable in both procedures.

The most significant difference was observable in the pole mass of the sigma, where the numerical extrapolation yields a heavier mass for the two pion decay threshold. This was not only corrected qualitatively but also quantitatively by our preliminary results using the real-time FRG framework. So our real-time FRG set up works very well in the QMM model. Thus, we will use it for future investigations of the weak pion decay.

In the end, we extended our QMM, including the leptons, hence the effective weak interaction. In particular, we compared the 3-point-vertices with BSAs from the DSE/BSE framework since they are related to each other. The pure BSA and the 2-quark-pion-vertex have similar contributions with the difference that the quark-self-interaction is given by the meson exchange instead of the gluon exchange as we consider the QMM and not the full QCD.

The most important difference arises in the decay channel, wherein the FRG framework, we have contributions for the leptonic-self-interaction originating from the dynamical hadronization procedure. These enable us to take the dynamical back-coupling between the quark-meson sector and the lepton sector into account. In particular, we can investigate the dynamical back-coupled influence of the P-violation on the decay process to some amount. This concludes the presentation of our results so far. The numerical results are currently on their way and will be stated in future works. In the end, we summarize our complete findings and give an outlook for future studies in the following chapter.

Chapter 7

Summary and outlook

Motivated by the non-negligible back-coupling between the strong and electroweak sector of the standard model in very dense environments, like the neutron star mergers, we started the investigation in this field by analyzing particular aspects of the non-perturbative back-coupling. The theory of the electroweak interactions comes along with various unique features like C- and P-violation, which significantly increases the complexity of such research. Therefore, we started our analysis with the breaking of the C, P, and flavor symmetry. To be more precise, we examined the effects of the non-perturbative back-coupling for the strong sector at the level of the simplest object, namely the QP.

The QP was calculated within the rainbow-ladder truncation using a non-linear model for the strong coupling. This model had the correct implementation of the chiral symmetry and dynamical mass generation, which is of paramount importance for our study. Our study showed that the explicit breaking couples the various dressing functions of the QP in a highly non-trivial way. This can lead to qualitative effects at long hadronic distances, even for moderate breaking strengths. Thus, we should be cautious with perturbative extrapolation. This was especially observable for the effects from the mass splitting leading to exciting insight from the physical point of view.

Under particular conditions, the mass splitting effects can be amplified by the strong interaction changing the handedness of different particles. This can deplete or enlarge the available particles in some handedness. Since the electroweak interactions couple only to the left-handed particles, this can increase or decrease the reservoir of the weak interacting particles leading to modified dynamics of the neutron star merger. Anyhow, such a statement requires a dynamical back-coupled study at the hadronic level.

Thus, for the next step, we took a low-energy description for the weak sector with the right C- and P-violation to study the weak pion decay in the combined DSE/BSE, as well as FRG framework. We outlined the mechanism to extract observables like mass and decay-width of the particles in these frameworks. These quantities are related to the pole position of the corresponding correlation functions. So we first discussed the implication for a pole position from the Minkowski space to the complexified Euclidean space.

In this context, we analyzed the general structure of BSEs to distinguish between the first and second Riemann sheet. Notably, we found that the BSEs, in general, may have this property, which is fulfilled for the BSEs of the weak pion decay. This is of particular importance since physical resonances are poles in the second Riemann sheet. While the pole position in the BSEs arises directly from the self-consistency condition, in the FRG, it is necessary to extract the pole position from the resulting propagator, i.e., the pion propagator in our case.

We introduced the pions into the system via dynamical hadronization, as the effective low-energy degree of freedom, in the FRG framework. The dynamical hadronization procedure comes along with many benefits from the technical, as well as the physical point of view. In particular, it enables us to take some part of the dynamical back-coupling for the lepton sector into account, which requires to work with weak gauge bosons in the DSE/BSE framework. Thus, the dynamical hadronization, along with the real-time FRG are the core of our bound state investigation in the FRG framework. The latter is a convenient way to circumvent technical difficulties while calculating real-time correlation functions.

We tested our set up in the FRG framework for a QCD-assisted low-energy effective quark-meson model. Especially, the results were compared with a recent FRG study [168] showing good quantitative agreement for low-energies $\lesssim 250\,\mathrm{MeV}$, which is sufficient for our study of the pion. In the end, we calculated the masses and decay-width of the pion using numerical extrapolation and real-time FRG. Our preliminary results for the masses and decay-widths using real-time FRG revealed not only qualitative correction but also good qualitative results. Especially for the sigma, which mass was found close to the two pion threshold.

Apart from some rather technical issues, we also discussed the implication of the P-violation on the weak pion decay in both frameworks and put them in perspective to each other. We extracted different contributions for the BSA originating from the same handedness and different handedness. In the standard analysis, the contributions for the different handedness vanishes as the weak interaction only involves left-handed particles.

In a fully back-coupled analysis, this may not vanish since we saw the possibility of changing the handedness for different particles in the study of the QP. We can investigate this possibility in the FRG framework without more ado in contrast to the DSE/BSE approach. This is owed to the fact that the dynamical hadronization procedure induces lepton-self-interaction via the pions, and hence enables us to dynamically back-couple the quark-meson and lepton sector.

Recent studies on the impact of the P-violation in the context of the supernova showed a non-negligible modification of the kinetic theory [91–95]. Keeping this in mind may lead to a significant influence on the dynamics of the neutron star mergers by the dynamical changing of the handedness. This is currently under investigation, and results will be presented in the future.

Concluding, this investigation was a starting point of a new field, which will grow in the near future due to the developments in the gravitational waves observatories. We tackled a few technical, as well as physical aspects, showing that the effects of weak interaction can lead to qualitatively different behavior even for small strengths. While this gives us a warning with perturbative extrapolation, on the one hand, it may lead us to new interesting physical phenomena on the other hand. Anyhow, there are still various aspects to be tackled before we can deal with the β-decay of the protons and neutrons for the neutron star mergers, like the inclusion of the finite temperature and density.

Appendix A

Definitions, conventions and mathematical relations

A.1 Fourier-transformation

We use the following conventions for the Fourier-transformations in the d- dimensional Euclidean space for the fermion fields ψ and boson fields φ:

$$\psi(x) = \int_p \psi(p) \exp(\mathrm{i}\, px), \quad \overline{\psi}(x) = \int_p \overline{\psi}(p) \exp(-\mathrm{i}\, px), \quad \varphi(x) = \int_p \varphi(p) \exp(\mathrm{i}\, px), \tag{A.1}$$

and the relation:

$$\int_x \exp(-\mathrm{i}\, px) = (2\pi)^d \delta^{(d)}(p). \tag{A.2}$$

A.2 SU(N)-algebra

Let $\left\{t^i, i = 1, ..., N^2 - 1\right\}$ be the generators of the corresponding Lie-algebra of SU(N). The generators fulfill the following commutator and anti-commutator relations:

$$\left[t^i, t^j\right] = \mathrm{i}\, f^{ijk} t^k, \qquad \left\{t^i, t^j\right\} = 2\frac{c}{N}\delta_{ij}\mathbb{1} + d^{ijk} t^k, \tag{A.3}$$

where f^{ijk} and d^{ijk} are the total anti-symmetric and symmetric structure constants, respectively. In particular, we have $f^{iij} = 0$ without summing over the same indices and $d^{iij} = 0$ after summation over the same indices. For the traces we get:

$$\mathrm{Tr}\left(t^i t^j\right) = c\delta_{ij}, \tag{A.4}$$

where c is a constant depending on the representation, with $c = \frac{1}{2}$ in the fundamental representation. In the following, we state some fundamental and important relations for the calculation.

Completeness relation:

$$t^i_{ab} t^i_{cd} = c\delta_{ad}\delta_{bc} - \frac{c}{N}\delta_{ab}\delta_{cd}. \tag{A.5}$$

Fierz identity:

$$t^i_{ab} t^i_{cd} = \frac{c(N^2-1)}{N^2} \delta_{ad}\delta_{cb} - \frac{1}{N} t^i_{ad} t^i_{cb}. \tag{A.6}$$

Jacobi identity:

$$\begin{aligned} \left[\left[t^i, t^j\right], t^k\right] + \left[\left[t^k, t^i\right], t^j\right] + \left[\left[t^j, t^k\right], t^i\right] &= 0, \\ f^{ijl} f^{kml} + f^{kil} f^{jml} + f^{jkl} f^{iml} &= 0. \end{aligned} \tag{A.7}$$

Some relations for the trace:

$$\begin{aligned} \mathrm{Tr}\left(t^i t^i\right) &= c(N^2-1), & \mathrm{Tr}\left(t^i t^j t^k\right) &= \frac{c}{2}(d^{ijk} + \mathrm{i}\, f^{ijk}), \\ f^{ijk}\, \mathrm{Tr}\left(t^i t^j t^k\right) &= \mathrm{i}\, c^2 N(N^2-1), & d^{ijk}\, \mathrm{Tr}\left(t^i t^j t^k\right) &= \frac{c^2(N^2-1)(N^2-4)}{N}, \\ \mathrm{Tr}\left(t^i t^i t^j t^k\right) &= \frac{c^2(N^2-1)}{N}\delta^{jk}, & \mathrm{Tr}\left(t^i t^j t^i t^k\right) &= -\frac{c^2}{N}\delta^{jk}, \qquad \text{(A.8)} \\ \mathrm{Tr}\left(t^i t^i t^j t^j\right) &= \frac{c^2(N^2-1)^2}{N}, & \mathrm{Tr}\left(t^i t^j t^i t^j\right) &= \frac{c^2(1-N^2)}{N}. \qquad \text{(A.9)} \end{aligned}$$

Some results for the structure constants:

$$\begin{aligned} f^{ijl} f^{kml} &= 4\frac{c}{N}(\delta^{ik}\delta^{jm} - \delta^{im}\delta^{jk}) + d^{kil} d^{jml} - d^{jkl} d^{iml}, & f^{ijl} f^{kjl} &= 2cN\delta^{ik}, \\ f^{ijl} f^{ijl} &= 2cN(N^2-1), & d^{ijl} d^{kjl} &= 2\frac{c(N^2-4)}{N}\delta^{ik}, \\ d^{ijl} d^{ijl} &= 2\frac{c(N^2-4)(N^2-1)}{N}, & f^{ijl} d^{kjl} &= 0. \end{aligned} \tag{A.10}$$

A.3 Dirac-algebra in $d = 4$

Let $\gamma^0, ..., \gamma^3$ be the gamma matrices. We define the following matrices:

$$\begin{aligned} t^1 &= \mathbb{1} && \text{the scalar channel,} \\ t^{2,\ldots,5} &= \gamma^{0,\ldots,3} && \text{the vector channel,} \\ t^{6,\ldots,11} &= \sigma_{03}, \sigma_{13}, \sigma_{23}, \sigma_{01}, \sigma_{12}, \sigma_{02} && \text{the tensor channel,} \\ t^{12,\ldots,15} &= \mathrm{i}\,\gamma^{0,\ldots,3}\gamma^5 && \text{the axial channel,} \\ t^{16} &= \gamma^5 && \text{the pseudo-scalar channel,} \end{aligned} \tag{A.11}$$

with:

$$\gamma^5 = \gamma^0\gamma^1\gamma^2\gamma^3, \quad \sigma_{\mu\nu} = \frac{\mathrm{i}}{2}\left[\gamma^\mu, \gamma^\nu\right], \quad \{\gamma^\mu, \gamma^\nu\} = 2\delta^{\mu\nu}\mathbb{1}, \quad \mathrm{Tr}\left(t^A t^B\right) = 4\delta^{AB}. \tag{A.12}$$

The matrices $t^1, \ldots, t^{16}$ defines a basis. Let us note here, that for the basis we only take the matrices $\sigma_{\mu\nu}$ with $\nu > \mu$ for the tensor channel. Otherwise, the matrices will get linearly dependent due to the relation $\sigma_{\mu\nu} = -\sigma_{\nu\mu}$.

We get the complete commutator and anti-commutator relations for the different channels:

$$
\begin{aligned}
[\gamma^\mu,\sigma_{\nu\rho}] =& 2\,\mathrm{i}\,(\delta^{\mu\nu}\gamma^\rho-\delta^{\mu\rho}\gamma^\nu)\,, & \{\gamma^\mu,\sigma_{\nu\rho}\} =& -2\epsilon_{\mu\nu\rho\alpha}\,\mathrm{i}\,\gamma^\alpha\gamma^5,\\
\left[\gamma^\mu,\mathrm{i}\,\gamma^\nu\gamma^5\right] =& 2\,\mathrm{i}\,\delta^{\mu\nu}\gamma^5, & \left\{\gamma^\mu,\mathrm{i}\,\gamma^\nu\gamma^5\right\} =& \epsilon_{\mu\nu\alpha\beta}\sigma_{\alpha\beta},\\
\left[\gamma^\mu,\gamma^5\right] =& -2\,\mathrm{i}\,\mathrm{i}\,\gamma^\mu\gamma^5, & \left\{\gamma^\mu,\gamma^5\right\} =& 0,\\
\left[\sigma_{\mu\nu},\mathrm{i}\,\gamma^\rho\gamma^5\right] =& 2\,\mathrm{i}\left(\delta^{\nu\rho}\,\mathrm{i}\,\gamma^\mu\gamma^5-\delta^{\mu\rho}\,\mathrm{i}\,\gamma^\nu\gamma^5\right), & \left\{\sigma_{\mu\nu},\mathrm{i}\,\gamma^\rho\gamma^5\right\} =& 2\epsilon_{\mu\nu\rho\alpha}\gamma^\alpha,\\
\left[\sigma_{\mu\nu},\gamma^5\right] =& 0, & \left\{\sigma_{\mu\nu},\gamma^5\right\} =& -\epsilon_{\mu\nu\alpha\beta}\sigma_{\alpha\beta},\\
\left[\mathrm{i}\,\gamma^\mu\gamma^5,\mathrm{i}\,\gamma^\nu\gamma^5\right] =& -2\,\mathrm{i}\,\sigma_{\mu\nu}, & \left\{\mathrm{i}\,\gamma^\mu\gamma^5,\mathrm{i}\,\gamma^\nu\gamma^5\right\} =& 2\delta^{\mu\nu}\mathbb{1},\\
\left[\mathrm{i}\,\gamma^\mu\gamma^5,\gamma^5\right] =& 2\,\mathrm{i}\,\gamma^\mu, & \left\{\mathrm{i}\,\gamma^\mu\gamma^5,\gamma^5\right\} =& 0,\\
\left[\gamma^5,\gamma^5\right] =& 0, & \left\{\gamma^5,\gamma^5\right\} =& 2\mathbb{1},
\end{aligned}
\tag{A.13}
$$

$$
\begin{aligned}
[\sigma_{\mu\nu},\sigma_{\alpha\beta}] =& \,\mathrm{i}\,\delta^{\nu\alpha}\sigma_{\mu\beta}-\mathrm{i}\,\delta^{\nu\beta}\sigma_{\mu\alpha}+\mathrm{i}\,\delta^{\mu\beta}\sigma_{\nu\alpha}-\mathrm{i}\,\delta^{\mu\alpha}\sigma_{\nu\beta},\\
\{\sigma_{\mu\nu},\sigma_{\alpha\beta}\} =& 2\left(\delta^{\mu\alpha}\delta^{\nu\beta}-\delta^{\mu\beta}\delta^{\nu\alpha}\right)\mathbb{1}-2\epsilon_{\mu\nu\alpha\beta}\gamma^5.
\end{aligned}
$$

A.4 C operator

We state here some relations for the C-operator for the completeness. These relations are taken from [107].

$$
\begin{aligned}
\mathcal{C}^\dagger &= \mathcal{C}^{-1}, & \mathcal{C}^T &= -\mathcal{C}, & \mathcal{C}^* &= -\mathcal{C}^{-1},\\
\mathcal{C}^{-1}\gamma^\mu\mathcal{C} &= -(\gamma^\mu)^T, & \mathcal{C}^{-1}\gamma^5\mathcal{C} &= (\gamma^5)^T, & \mathcal{C}^{-1}\gamma^5\gamma^\mu\mathcal{C} &= (\gamma^5\gamma^\mu)^T,\\
\mathcal{C}^{-1}\sigma^{\mu\nu}\mathcal{C} &= -(\sigma^{\mu\nu})^T, & \mathcal{C}^{-1}t^i\mathcal{C} &= (t^i)^T.
\end{aligned}
\tag{A.14}
$$

A.5 Integrals

DSEs and FRGEs consist of loop integrals. For the explicit calculation, we choose polar coordinates. In appropriate coordinate systems, the integrands are independent of some angle direction. Hence, these angle integrations can be performed upfront. So we will state some remarks on the polar coordinates in the first section. Afterward, we will mention the details for the numerical implementation for the sake of replicability.

A.5.1 Polar coordinates

Let $x \in \mathbb{R}^d$ and $f\colon \mathbb{R}^d \to \mathbb{R}$ be a function. We define the usual transformation from the Euclidean coordinates $(x_1,\dots,x_d)$ to polar coordinates $(r,\theta_0,\theta_1,\dots,\theta_{d-2})$. For the integral in the polar coordinates we get:

$$
\int \mathrm{d}^d\,x f(x) = \int \mathrm{d}(r,\theta_0,\theta_1,\dots,\theta_{d-2})\left\{r^{d-1}\prod_{i=1}^{d-2}\sin^i(\theta_i)f(r,\theta_0,\theta_1,\dots,\theta_{d-2})\right\}. \tag{A.15}
$$

Let us define $I_{\text{angle}}(j)$ the integral over the first j angles ($j\in\{1,\dots,d-1\}$):

$$
I_{\text{angle}}(j) = \left(\int_0^{2\pi}\mathrm{d}\,\theta_0\right)\prod_{i=1}^{j-1}\left(\int_0^{\pi}\mathrm{d}\,\theta_i\sin^i(\theta_i)\right). \tag{A.16}
$$

As a special case, we define $I_{\text{angle}}(0) = 2$ if the function depends on all the polar coordinates. With the help of the Γ-function:

$$\Gamma(z) = \int_0^\infty \mathrm{d}\,t\; t^{z-1} \exp(-t), \tag{A.17}$$

we can calculate this expression:

$$I_{\text{angle}}(j) = \frac{2\pi^{(j+1)/2}}{\Gamma((j+1)/2)} = \begin{cases} 2\frac{\pi^{(j+1)/2}}{((j-1)/2)!} & \text{for j odd,} \\ 2\frac{(2\pi)^{j/2}}{(j-1)!!} & \text{for j even.} \end{cases} \tag{A.18}$$

The values for the some j's are listed in the table.

j	0	1	2	3	4	5	6	7
$I_{\text{angle}}(j)$	2	2π	4π	$2\pi^2$	$\frac{8}{3}\pi^2$	π^3	$\frac{16}{15}\pi^3$	$\frac{1}{3}\pi^4$

For the explicit calculations, we substitute $y = r^2$ and $z_j = -\cos(\theta_j)$ for ($j \in \{1, \ldots, d-2\}$). Using this in equation (A.15) yields for the integral:

$$\int \mathrm{d}^d\, x f(x) = \int \mathrm{d}(y, \theta_0, z_1, \ldots, z_{d-2}) \left\{ \frac{1}{2} y^{\frac{d-2}{2}} \prod_{i=1}^{d-2} (1 - z_i^2)^{\frac{i-1}{2}} f(y, \theta_0, z_1, \ldots, z_{d-2}) \right\}. \tag{A.19}$$

A.5.2 Numerical implementation

The numerical integration is performed using Gauss-Legendre or Gauss-Chebychev quadrature. For the radial direction, we use nodes v_r and weights w_r from Gauss-Legendre and distribute them equally over the different order of magnitudes for the integration region. Therefore, we also choose an IR-cutoff $\kappa \leq 10^{-8}$ GeV in addition to the UV-cutoff Λ for the radial direction. The function for the distribution is given as:

$$g_r(t) = \sqrt{\kappa\Lambda}\, \mathrm{e}^{\ln\left(\frac{\Lambda}{\kappa}\right) t}. \tag{A.20}$$

We checked, that the results are independent of the cutoffs. So we get for the integral in the radial direction:

$$\int_\kappa^\Lambda \mathrm{d}\,y\; y^{\frac{d-2}{2}} f(y, \ldots) \to \sum_{i=1}^{N_r} w_r^i g_r'(v_r^i) g_r(v_r^i)^{\frac{d-2}{2}} f(g_r(v_r^i), \ldots). \tag{A.21}$$

For the angle direction, we can also choose Gauss-Legendre for the nodes and weights. But in $d = 4$ dimensions the angle integration in z_2 direction has an additional factor of $\sqrt{1 - z_2^2}$ from the Jacobi determinant. The Gauss-Chebychev 2 quadrature has this factor already included. Thus, for the z_2 direction it is more convenient to choose the Gauss-Chebychev 2:

$$\int_{-1}^1 \mathrm{d}\, z_2 \sqrt{1 - z_2^2} f(\ldots, z_2) \to \sum_{i=1}^{N_2} w_2^i f(\ldots, v_2^i). \tag{A.22}$$

The last two angle directions do not have any additional factor from the Jacobi determinant. Thus, Gauss-Legendre nodes and weights are taken for these directions for the explicit calculation.

Appendix B

DSEs of the quark propagator

B.1 Coupled set of equations

In this section, we state the detail expressions of the different dressing functions of the QP. We first define the following two kernels:

$$
\begin{aligned}
K_1(p,q,k) &= 12\pi C_F \frac{\alpha(k^2)}{k^2}, \\
K_2(p,q,k) &= 4\pi C_F \frac{\alpha(k^2)}{k^2 p^2}\left[(p\cdot q) + 2\frac{(p\cdot k)(q\cdot k)}{k^2}\right],
\end{aligned} \tag{B.1}
$$

where $C_F = (N_c^2-1)/2N_c$ and N_c is the number of colors, i.e. $N_c = 3$. We further define the functional Π_i for $i = 1,2$ as:

$$
\Pi_{i,e}(f,p^2) = Z_{2,e}(\mu^2,\Lambda^2)\int^{\Lambda}\frac{\mathrm{d}^4 q}{(2\pi)^4}\left\{K_i(p,q,k)f(q^2,\mu^2)\right\}. \tag{B.2}
$$

This yields the DSEs of the the different dressing functions for flavor-diagonal elements $e \in \{u,d\}$:

$$
\begin{aligned}
A_{ee}(p^2,\mu^2) &= Z_{2,e}(\mu^2,\Lambda^2)\left[1 + \Pi_{2,e}(\tilde{A}_{ee},p^2)\right], \\
B_{ee}(p^2,\mu^2) &= Z_{2,e}(\mu^2,\Lambda^2)\left[m_e + \Pi_{1,e}(\tilde{B}_{ee},p^2)\right], \\
C_{ee}(p^2,\mu^2) &= Z_{2,e}(\mu^2,\Lambda^2)\Pi_{2,e}(\tilde{C}_{ee},p^2), \\
D_{ee}(p^2,\mu^2) &= Z_{2,e}(\mu^2,\Lambda^2)\Pi_{1,e}(\tilde{D}_{ee},p^2),
\end{aligned} \tag{B.3}
$$

where $m_e = Z_{m,e}(\mu^2,\Lambda^2)m_{\mathrm{bare},e}$ with $Z_{m,e}$ being the mass renomalization constant and $m_{\mathrm{bare},e}$ the bare quark mass for flavor e. For the mixed flavors, we get $(e,f \in \{u,d\}, e \neq f)$:

$$
\begin{aligned}
A_{ef}(p^2,\mu^2) &= \sqrt{Z_{2,e}(\mu^2,\Lambda^2)Z_{2,f}(\mu^2,\Lambda^2)}g_{\mathrm{w}} + Z_{2,f}(\mu^2,\Lambda^2)\Pi_{2,e}(\tilde{A}_{fe},p^2), \\
B_{ef}(p^2,\mu^2) &= Z_{2,f}(\mu^2,\Lambda^2)\Pi_{1,e}(\tilde{B}_{fe},p^2), \\
C_{ef}(p^2,\mu^2) &= \sqrt{Z_{2,e}(\mu^2,\Lambda^2)Z_{2,f}(\mu^2,\Lambda^2)}g_{\mathrm{w}} + Z_{2,f}(\mu^2,\Lambda^2)\Pi_{2,e}(\tilde{C}_{fe},p^2), \\
D_{ef}(p^2,\mu^2) &= Z_{2,f}(\mu^2,\Lambda^2)\Pi_{1,e}(\tilde{D}_{fe},p^2).
\end{aligned} \tag{B.4}
$$

B.2 Numerical implementation on the real axis

Let us now state some detail on the numerical implementation of the coupled set of DSEs from the previous section. This system of equation is technically very similar to the ordinary rainbow-ladder truncation. Therefore, a numerical solution using standard fixed-point iteration schemes is possible and was done here. The integrals are performed, as stated in A.5. Only the QP was numerically inverted at every step due to the more involved structure, as already discussed.

There are, however, a few more subtle numerical issues to be mentioned. To perform the integral for $\Pi_{i,e}$, the dressing functions $\tilde{A}$, $\tilde{B}$, $\tilde{C}$, and $\tilde{D}$ are evaluated for various momenta using interpolation. We performed our calculations using linear and cubic interpolation. If we use a precision of 5×10^{-5}, which is considered to be sufficient in the standard fixed-point iteration scheme, for A, B, C, and D, we get different numerical solutions for linear and cubic interpolation. By increasing the precision, the solution from the linear interpolation approaches the solution from the cubic interpolation for all dressing functions except for D_{ee} and $\tilde{D}_{ee}$. Especially using linear interpolation, we get different solutions for D_{ee} and $\tilde{D}_{ee}$ by using different start values for the iteration. In contrast to this, we get the same solutions for different start values using cubic interpolation. Thus, we consider the solutions from the cubic interpolation as stable and used them throughout this work.

In addition, we used a precision of 5×10^{-7}, instead of the standard value, for A, B, C, and D and $2^8 = 256$ grid points. In this case, the difference for the solutions from the linear and cubic interpolation was at most in the third significant digit and thus led essentially to the same results.

Let us note that our precision for the iteration procedure is for the dressing functions of the inverse propagator (A, B, C, and D). The dressing functions of the propagator ($\tilde{A}$, $\tilde{B}$, $\tilde{C}$, and $\tilde{D}$) are calculated by a numerical inversion, with a precision of roughly 10^{-20}.

B.3 Numerical results

B.3.1 Vector channel

The results are shown in figure B.1 and B.2. A comparison between the different generations, the chiral limit, and tree-level for the flavor-off-diagonal vector dressing function is shown in subfigure B.2a for a fixed value $g_{\mathrm{w}} = 0.2$. The tree-level value is given by, see equation (4.11):

$$\tilde{A}_{0,ud} = \frac{g_{\mathrm{w}}(m_u m_d - p^2)}{N(p^2)}. \tag{B.5}$$

This demonstrates that at tree-level, the dressing function is negative for momenta $p^2 \geq m_u m_d$ and positive for lower momenta. The full dressing function exhibits the same behavior, but the absolute value is substantially larger. Note especially that in the chiral limit, the tree-level propagator is proportional to $-p^2$, thus negative for all momenta. The full dressing function is, however, positive in the IR. As the masses of up- and down-quark are comparatively small, the result for them is close to the one in the chiral limit.

The dependence on the generation and g_{w} is shown in subfigure B.2b. In every generation $\tilde{A}_{ud}$ increases with g_{w}. The zero of $\tilde{A}_{ud}$ shifts to higher momenta for heavier masses. This is already the case for the tree-level propagator, where the zero is determined by the condition $p^2 = m_u m_d$.

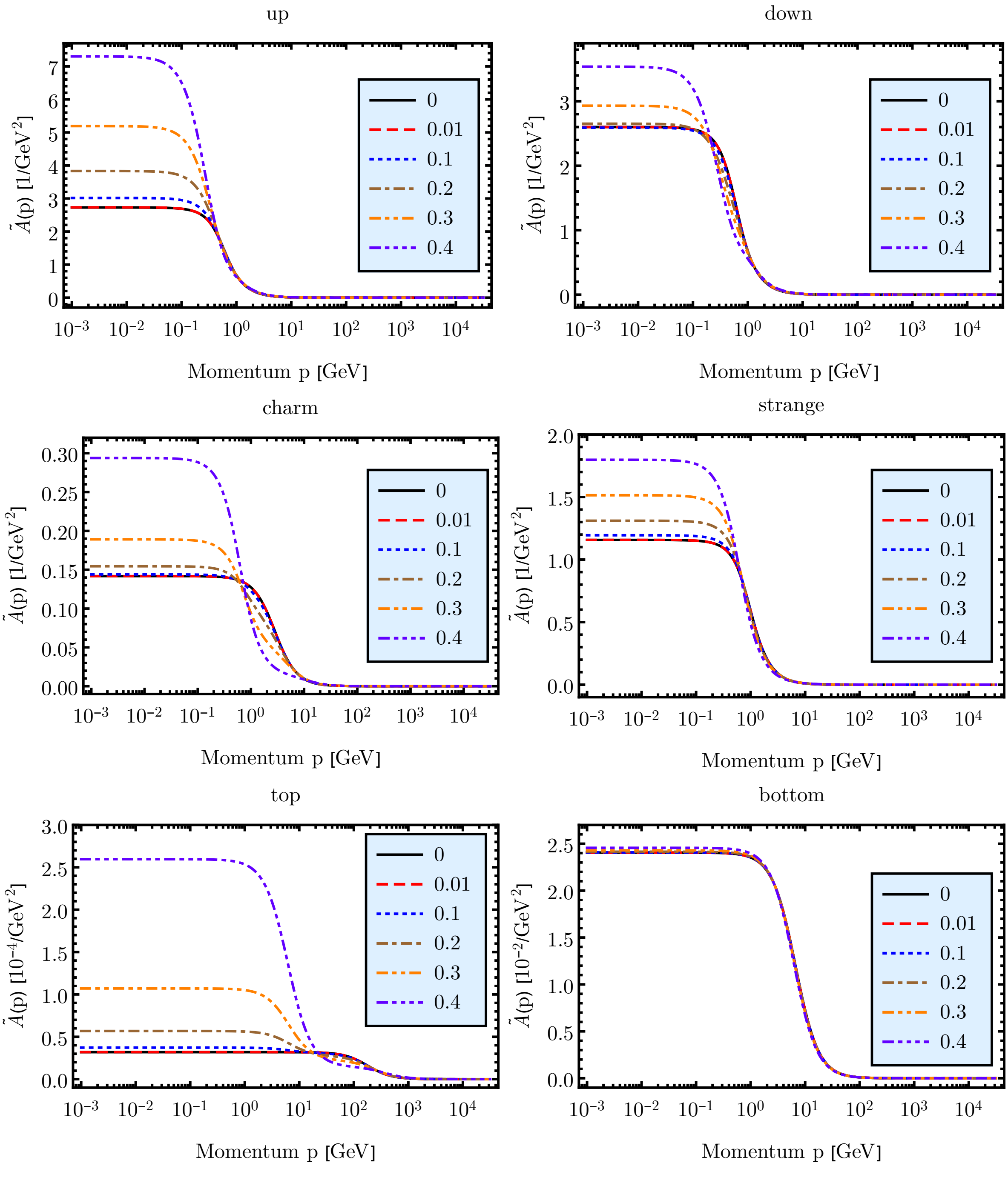

Figure B.1: The flavor-diagonal vector dressing function for different values of g_w. From top to bottom generations one to three are shown, and the left-hand panels show up-type quarks, and the right-hand panels down-type quarks.

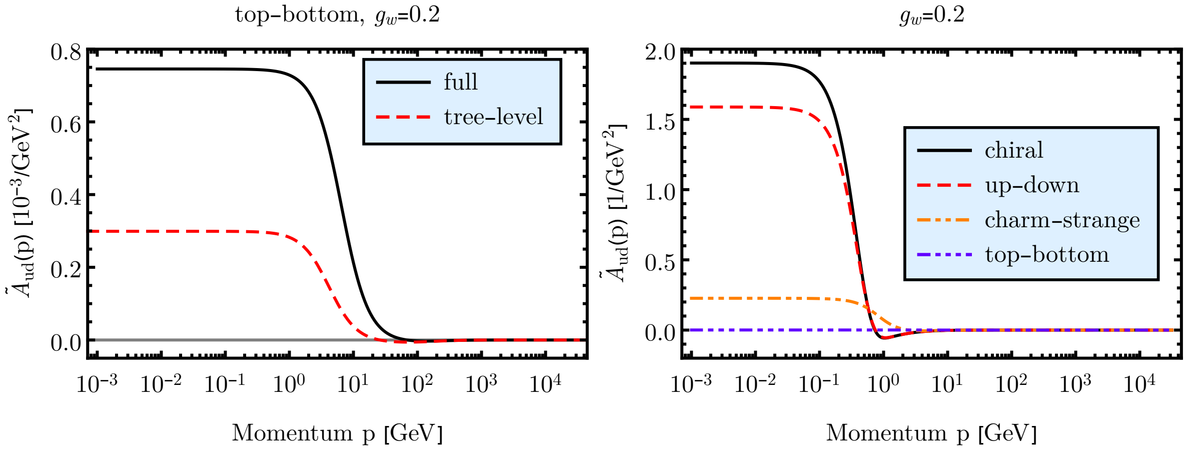

(a) The third generation in comparison to tree-level (left panel) and different generations (right panel) at $g_\mathrm{w} = 0.2$.

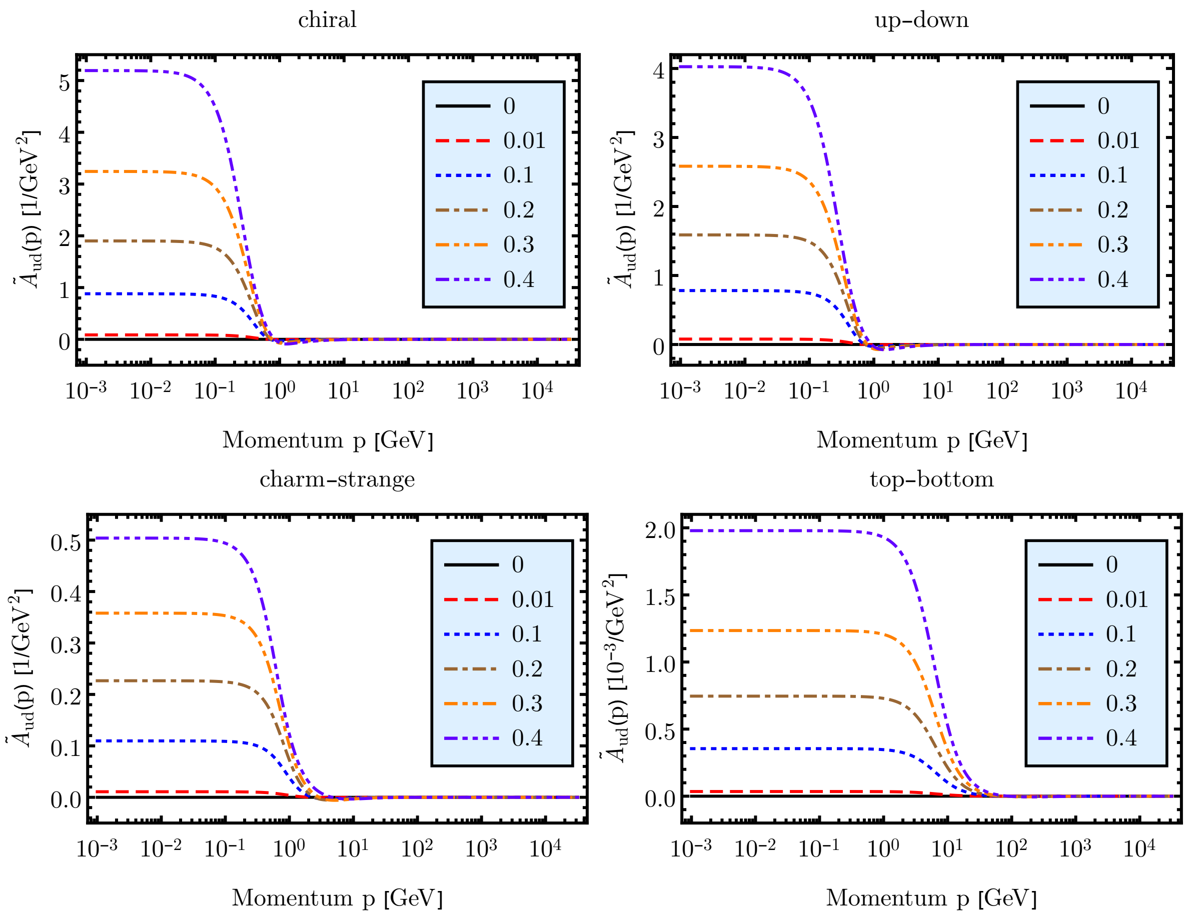

(b) In the the chiral limit and the different generations for different g_w.

Figure B.2: The flavor-off-diagonal vector dressing function.

B.3.2 Scalar channel

Complementing the results in section 4.2.3 the flavor-diagonal scalar dressing functions for the different quarks are shown in figure B.3.

The results for the flavor-off-diagonal scalar dressing function are shown in figure B.4. A comparison to the tree-level case of the third generation flavor-off-diagonal scalar dressing function is shown in subfigure B.4a. Note that the tree-level result is, see equation (4.11):

$$\tilde{B}_{0,ud} = -\frac{g_{\mathrm{w}}(m_u + m_d)p^2}{N(p^2)}. \tag{B.6}$$

Thus, at tree-level $\tilde{B}_{0,ud}$ is negative for all momenta, in particular in the UV. The latter is also seen in the full case. But it switches to a positive value in the IR. This qualitative behavior is also seen for the other generations, as is also plotted in subfigure B.4a, but at differing absolute values. This persists even in the chiral limit. The value of this quantity is also found to increase when increasing g_{w}, which is shown in subfigure B.4b.

B.3.3 Axial channel

The results are shown in figure B.5. The flavor-off-diagonal axial dressing function is shown for the various generations and the chiral limit in comparison to tree-level in subfigure B.5a at fixed $g_{\mathrm{w}} = 0.2$. The tree-level propagator takes the form, see equation (4.11):

$$\tilde{C}_{0,ud} = -\frac{g_{\mathrm{w}}(m_u m_d + p^2)}{N(p^2)}. \tag{B.7}$$

Therefore, the full dressing function becomes negative in the UV. In the IR, it is positive for the third and second generation, as is visible from subfigure B.5a, but remains negative for the first generation and the chiral limit. The change of the relative ratio between the left-handed and right-handed contribution is related to the sign of $\tilde{C}$, see equation (4.10). For the second and third generation, the contribution from the mass splitting is high enough to make $\tilde{C}$ positive in the IR. A detailed discussion is given in section 4.2.5.

In subfigure B.5b the dependence on g_{w} is shown for the different generation and the chiral limit. The higher the value of g_{w}, the larger the dressing function. However, the qualitative behavior is unchanged, and therefore entirely controlled by the masses.

B.3.4 Pseudo-scalar channel

The results are shown in figure B.6. At tree-level, the flavor-diagonal pseudo-scalar dressing function vanishes. The full dressing function has a finite value, which is depicted in the left panel of subfigure B.6a for all quarks at $g_{\mathrm{w}} = 0.2$.

The flavor-off-diagonal dressing function at tree-level is zero for degenerate quark masses,

$$\tilde{D}_{0,ud} = -\tilde{D}_{0,du} = -\frac{g_{\mathrm{w}}(m_u - m_d)p^2}{N(p^2)}, \tag{B.8}$$

as can be obtained from equation (4.11). This is also true for the full case, also shown in the right panel of subfigure B.6a, and especially so for the chiral limit. For non-degenerate quark masses, the dressing function does no longer vanish. This is in as far remarkable as

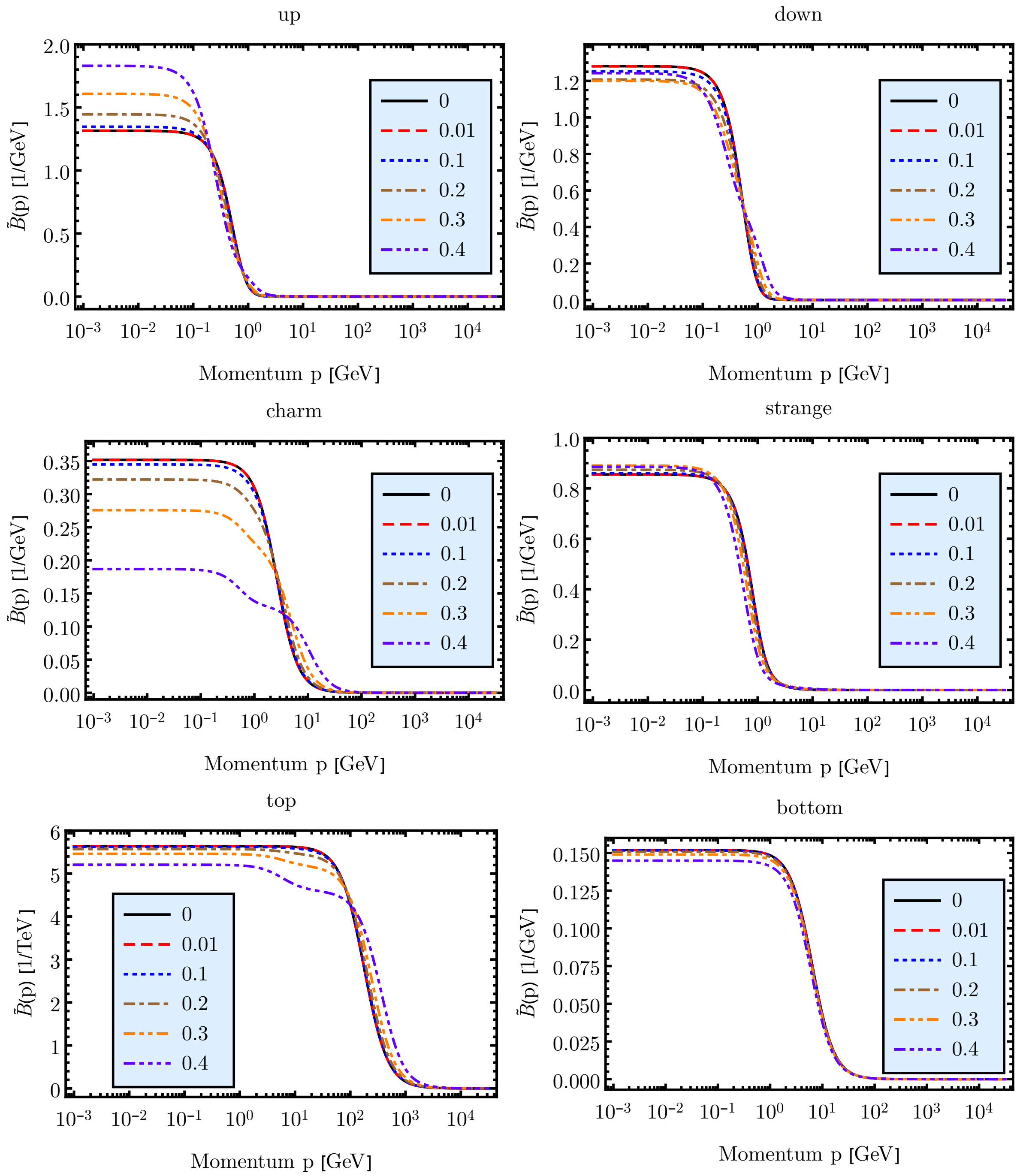

Figure B.3: The flavor-diagonal scalar dressing function for different g_{w}. From top to bottom generations one to three are shown, and the left-hand panels show up-type quarks, and the right-hand panels down-type quarks.

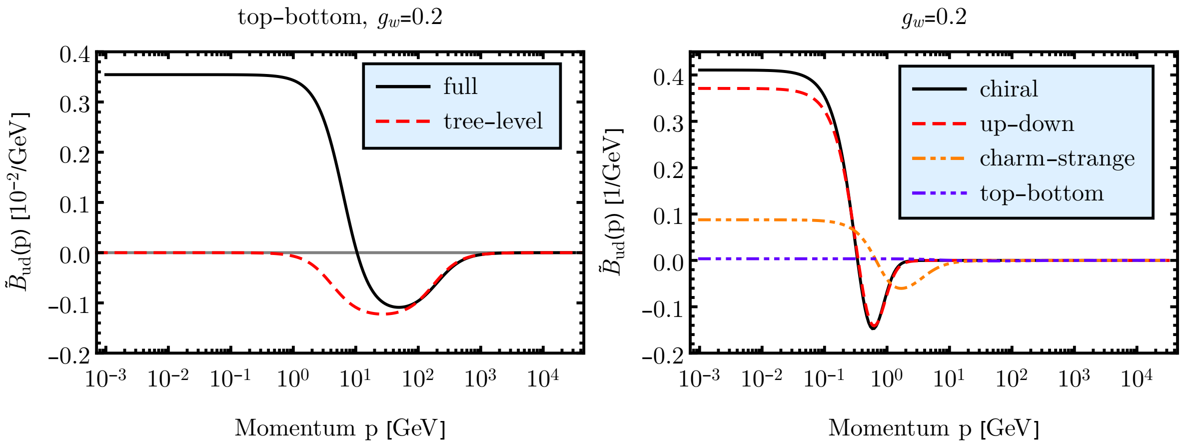

(a) The third generation in comparison to tree-level (left panel) and different generations (right panel) at $g_{\mathrm{w}} = 0.2$.

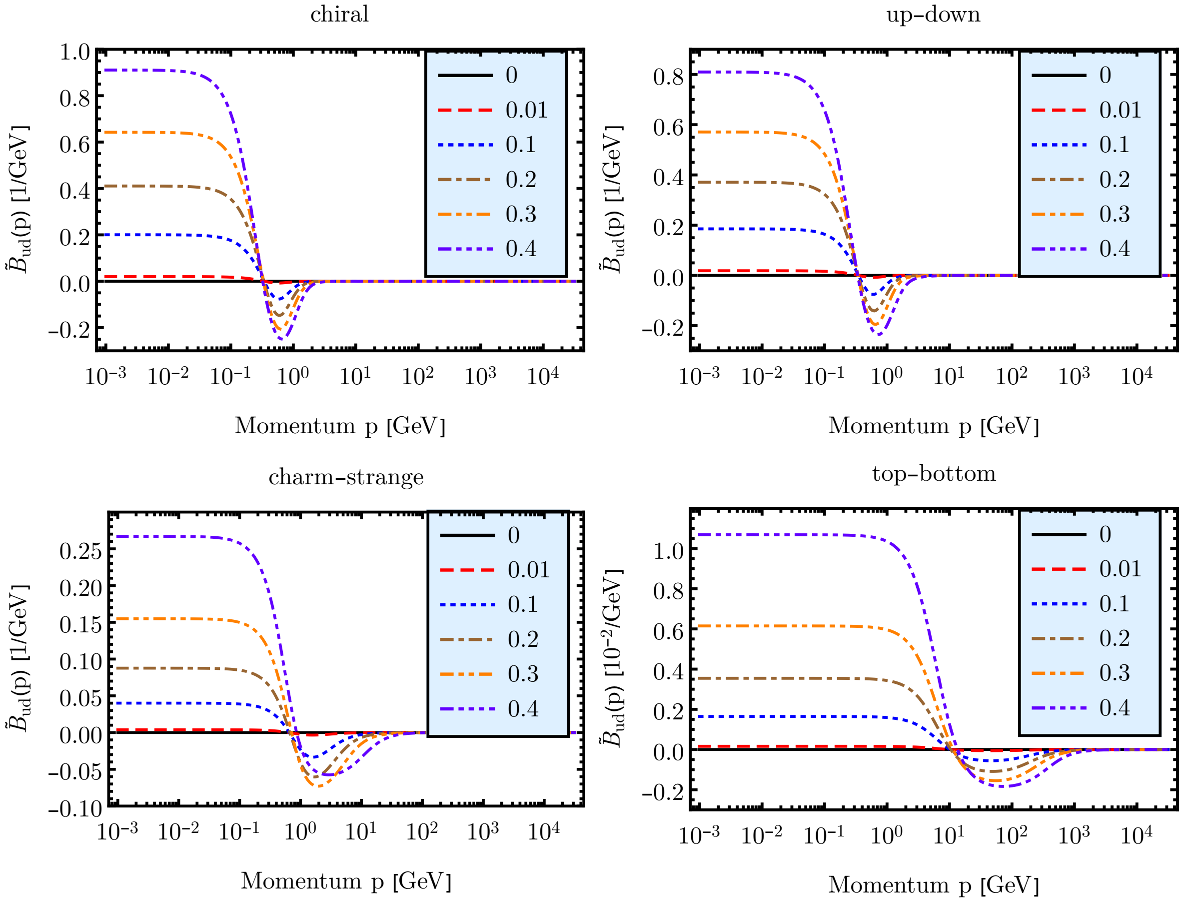

(b) In the the chiral limit and the different generations for different g_{w}.

Figure B.4: The flavor-off-diagonal scalar dressing function.

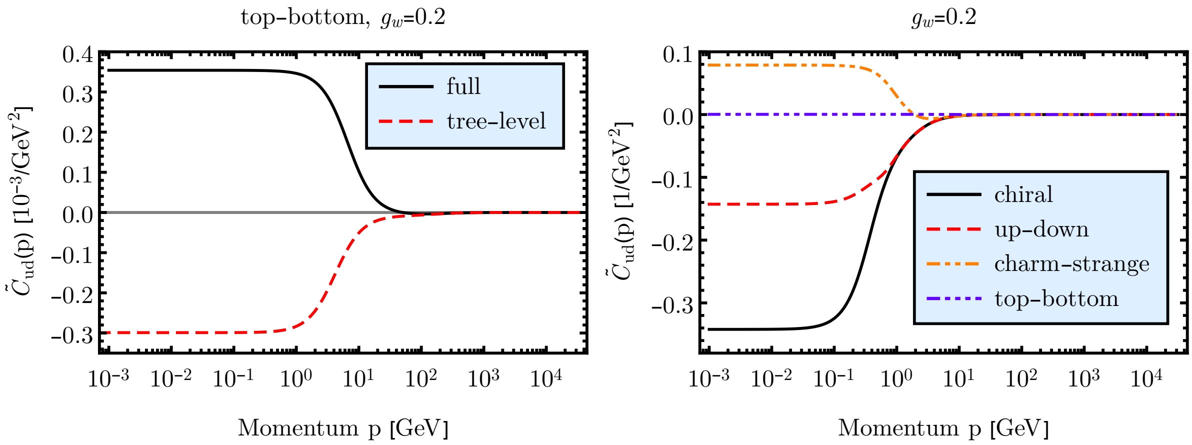

(a) The third generation in comparison to tree-level (left panel) and different generations (right panel) at $g_{\mathrm{w}} = 0.2$.

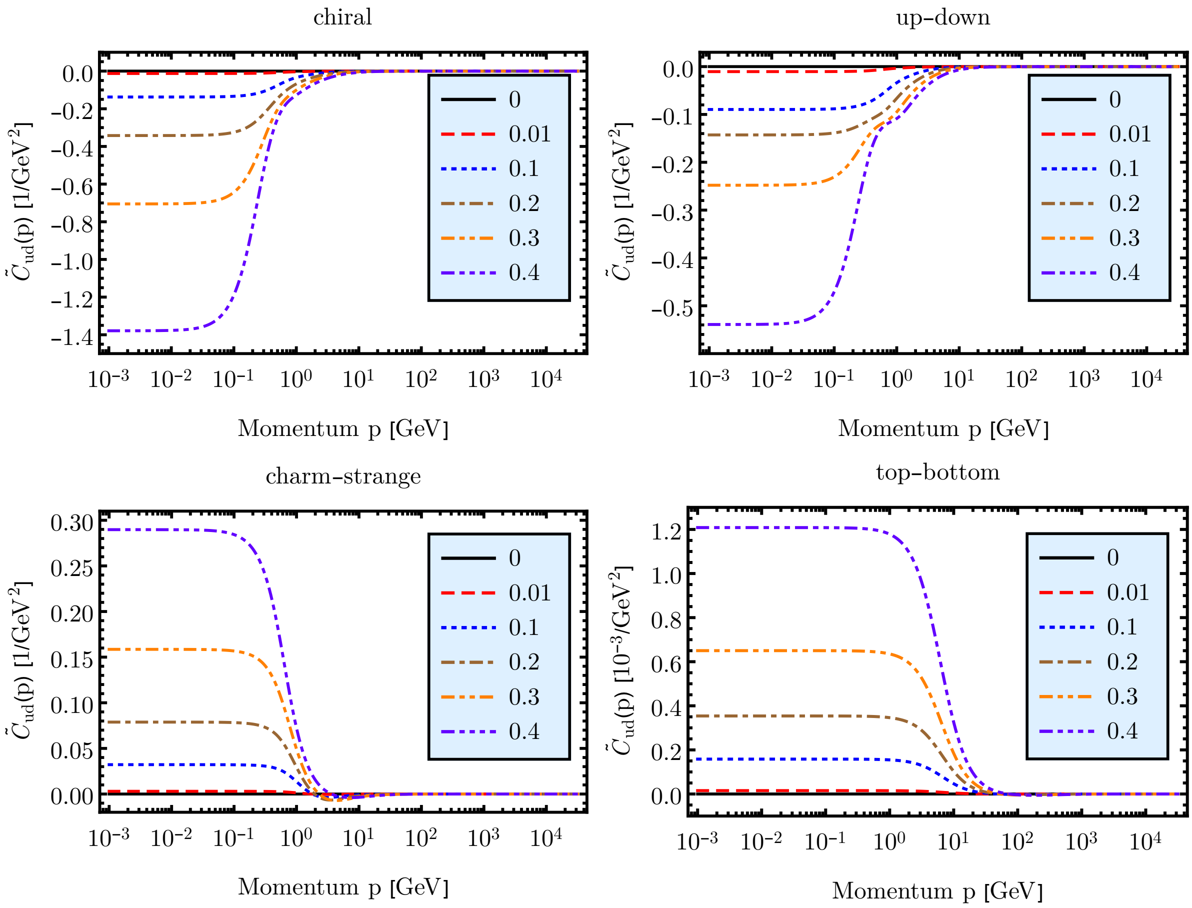

(b) In the the chiral limit and the different generations for different g_{w}.

Figure B.5: The flavor-off-diagonal axial dressing function.

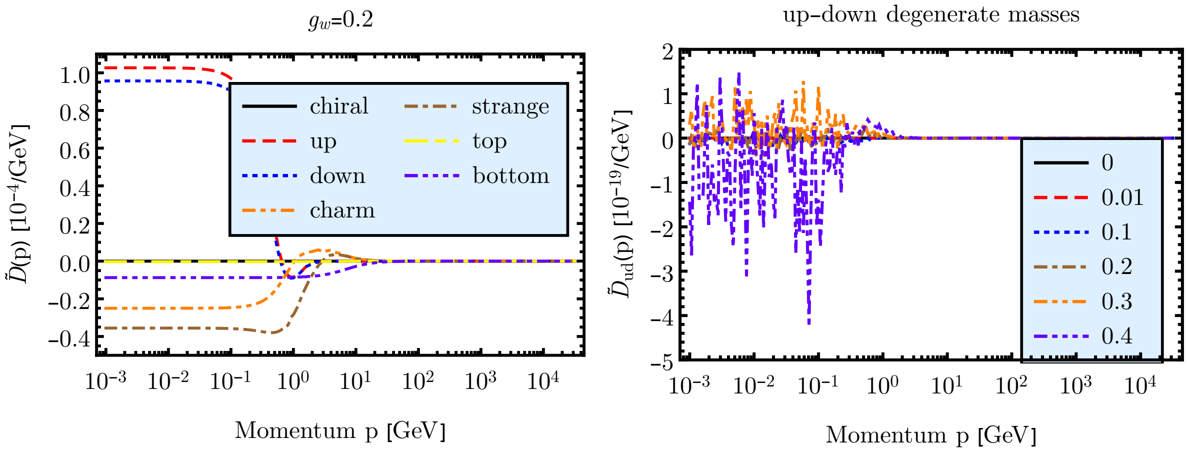

(a) The flavor-diagonal (left panel) for the different quark flavors at $g_\mathrm{w} = 0.2$ and the flavor-off-diagonal (right panel) dressing function for degenerate (here: up and down) quarks masses.

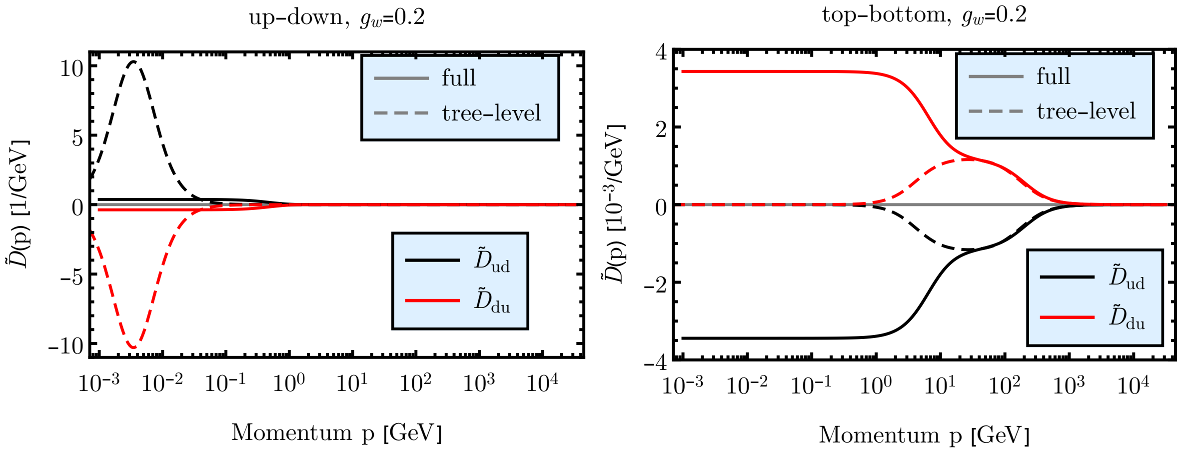

(b) The flavor-off-diagonal dressing function in comparison to tree-level for the first (left panel) and third (right panel) generation.

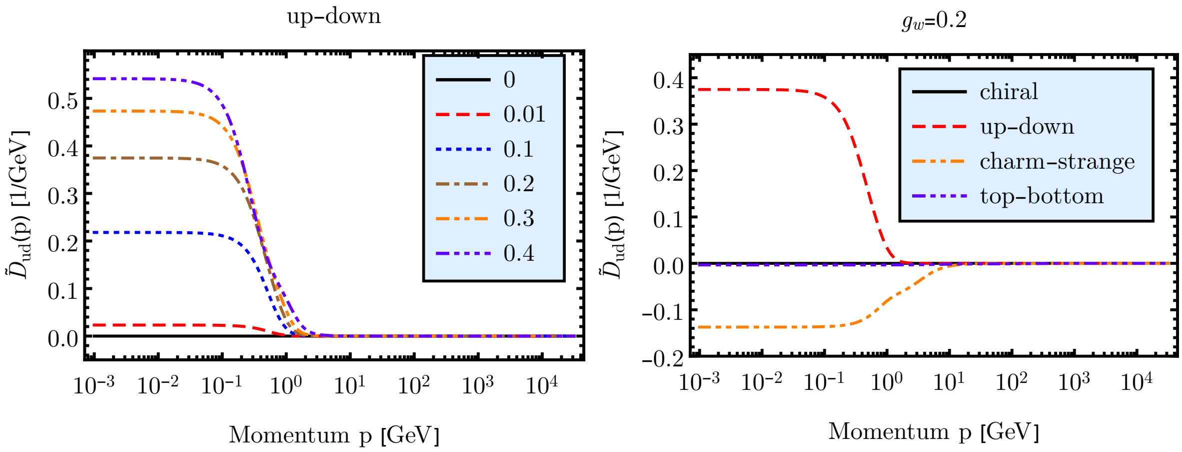

(c) The flavor-off-diagonal dressing function for the first generation (left panel) at different g_w and for the different generations at $g_\mathrm{w} = 0.2$ (right panel).

Figure B.6: The pseudo-scalar dressing function.

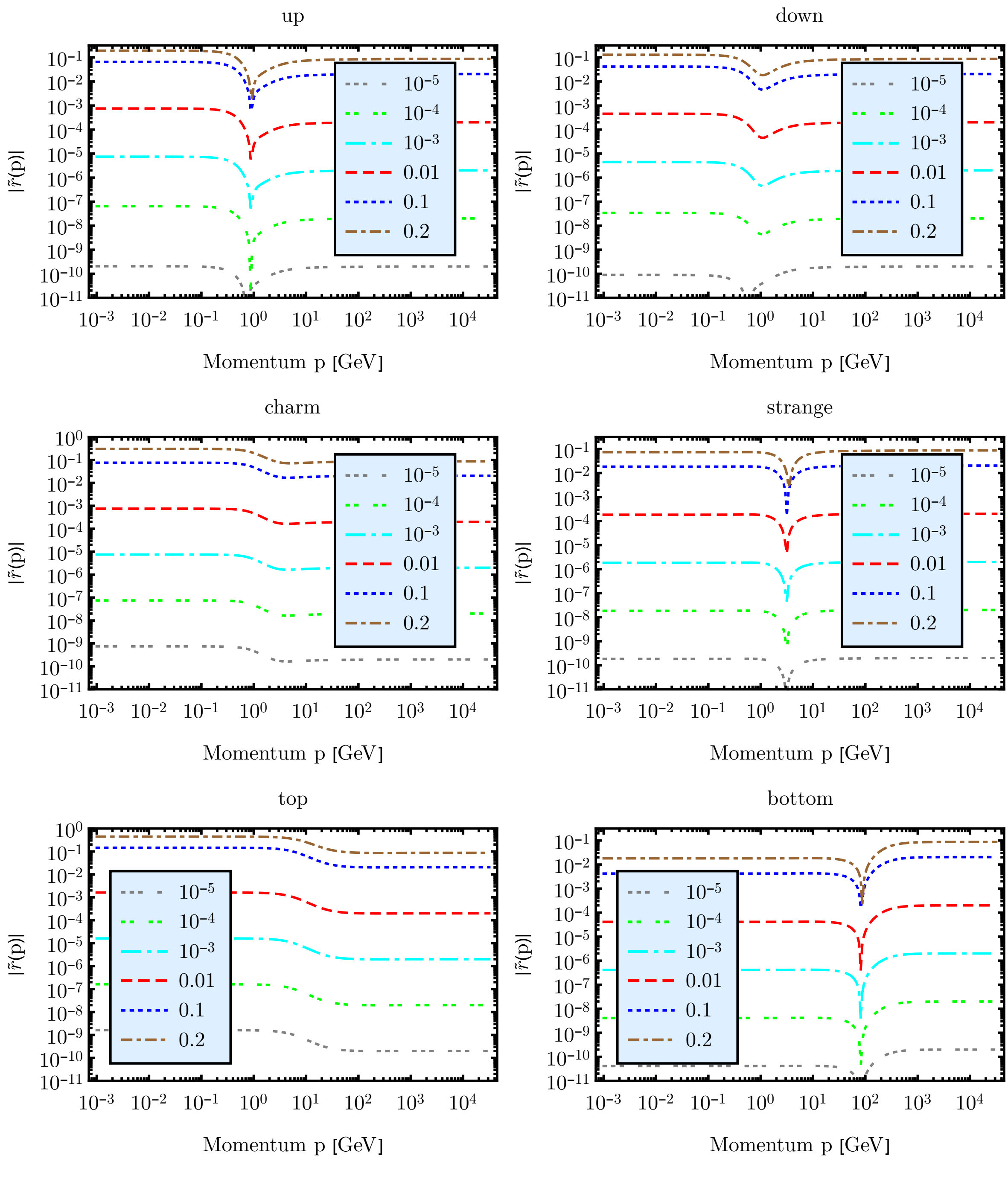

Figure B.7: Ratio (4.10) for the left-handed and right-handed flavor-diagonal quark propagator for different values of g_w. From top to bottom generations one to three are shown, and the left-hand panels show up-type quarks, and the right-hand panels down-type quarks.

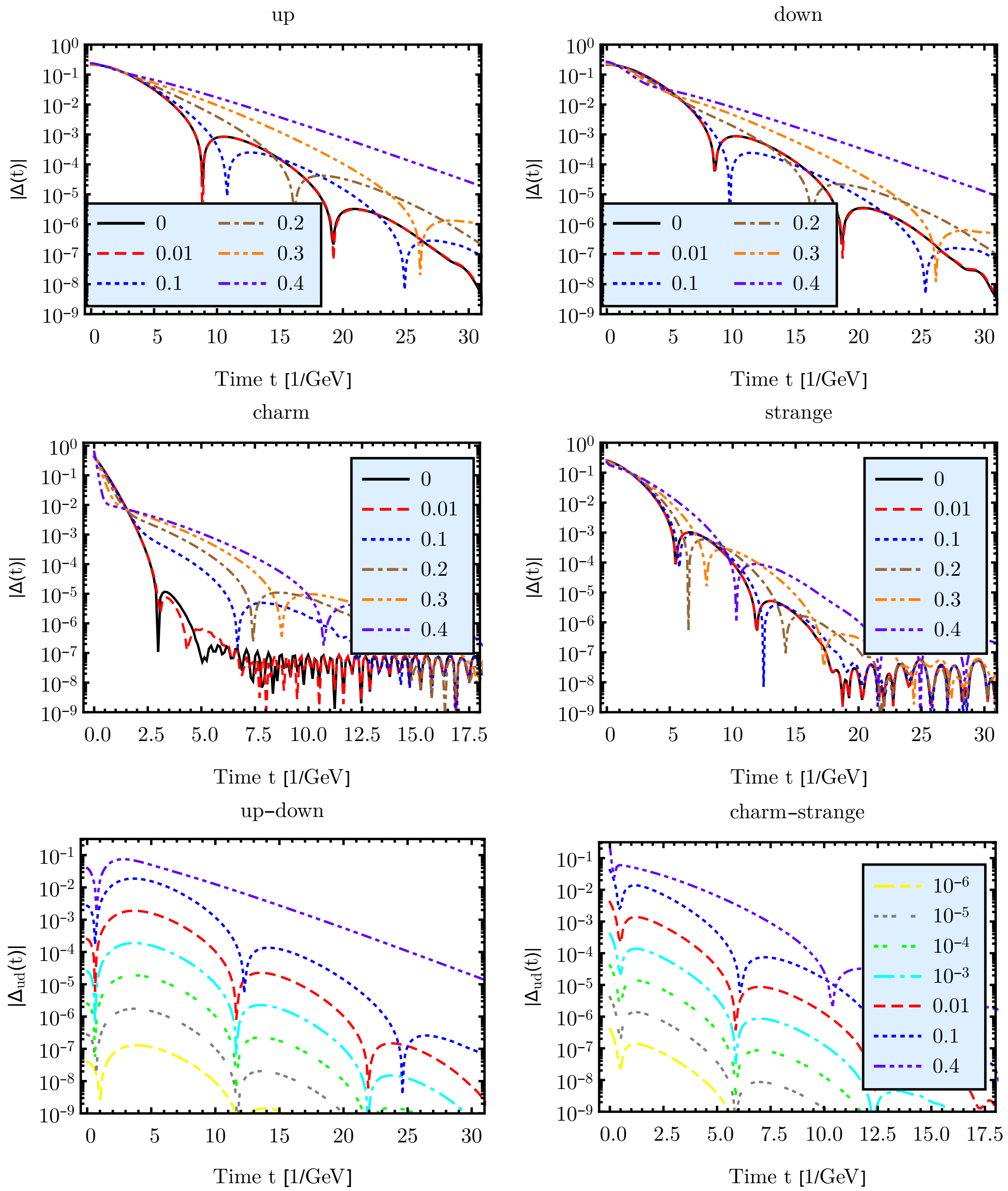

Figure B.8: The Schwinger function for different values of g_{w}. Top and middle panels show generations one and two and the left-hand panels show up-type quarks, and the right-hand panels down-type quarks. The bottom panels show the flavor-off-diagonal elements for the first (left panel) and second (right panel) generation.

	g_{w}	M	$\frac{\Gamma}{2}$	δ	m	θ
chiral	0	0.54 ± 0.05	0.30 ± 0.01	-1.13 ± 0.05	0.61 ± 0.05	0.51 ± 0.05
	0.01	0.54 ± 0.05	0.30 ± 0.01	-1.13 ± 0.05	0.61 ± 0.05	0.51 ± 0.05
	0.05	0.54 ± 0.05	0.26 ± 0.01	-0.90 ± 0.05	0.60 ± 0.05	0.46 ± 0.05
	0.1	0.47 ± 0.05	0.21 ± 0.01	-0.66 ± 0.05	0.51 ± 0.05	0.41 ± 0.05
	0.2	0.42 ± 0.05	0.17 ± 0.01	-0.14 ± 0.05	0.45 ± 0.05	0.38 ± 0.05
	0.3	0.38 ± 0.05	0.05 ± 0.01	0 ± 0.05	0.38 ± 0.05	0.14 ± 0.05
	0.4	0.31 ± 0.05	$10^{-7} \pm 0.01$	0 ± 0.05	0.31 ± 0.05	$10^{-9} \pm 0.05$
up	0	0.54 ± 0.05	0.31 ± 0.01	-1.13 ± 0.05	0.63 ± 0.05	0.51 ± 0.05
	0.01	0.54 ± 0.05	0.31 ± 0.01	-1.13 ± 0.05	0.63 ± 0.05	0.51 ± 0.05
	0.05	0.54 ± 0.05	0.27 ± 0.01	-0.92 ± 0.05	0.60 ± 0.05	0.47 ± 0.05
	0.1	0.49 ± 0.05	0.22 ± 0.01	-0.82 ± 0.05	0.53 ± 0.05	0.43 ± 0.05
	0.2	0.45 ± 0.05	0.17 ± 0.01	-1.15 ± 0.05	0.48 ± 0.05	0.36 ± 0.05
	0.3	0.39 ± 0.05	0.06 ± 0.01	0 ± 0.05	0.39 ± 0.05	0.14 ± 0.05
	0.4	0.34 ± 0.05	$10^{-7} \pm 0.01$	0 ± 0.05	0.34 ± 0.05	$10^{-9} \pm 0.05$
down	0	0.56 ± 0.05	0.32 ± 0.01	-1.13 ± 0.05	0.64 ± 0.05	0.51 ± 0.05
	0.01	0.56 ± 0.05	0.32 ± 0.01	-1.13 ± 0.05	0.64 ± 0.05	0.51 ± 0.05
	0.05	0.56 ± 0.05	0.28 ± 0.01	-0.86 ± 0.05	0.63 ± 0.05	0.46 ± 0.05
	0.1	0.50 ± 0.05	0.20 ± 0.01	-0.40 ± 0.05	0.54 ± 0.05	0.39 ± 0.05
	0.2	0.46 ± 0.05	0.19 ± 0.01	-1.45 ± 0.05	0.49 ± 0.05	0.39 ± 0.05
	0.3	0.39 ± 0.05	0.06 ± 0.01	0 ± 0.05	0.40 ± 0.05	0.15 ± 0.05
	0.4	0.34 ± 0.05	$10^{-7} \pm 0.01$	0 ± 0.05	0.34 ± 0.05	$10^{-9} \pm 0.05$

Table B.1: Fit values for the flavor-diagonal Schwinger functions.

non-trivial effects due to (non-)degeneracy propagate in other dressing functions, as discussed in the main text. We also find that the difference between the up-to-down and down-to-up dressing function, as discussed in section 4.1, also persists in the full case, and both differ by a sign. This effect does not propagate to other dressing functions, where we do not find any difference.

The dependence of the flavor-off-diagonal pseudo-scalar dressing function on generation (right panel subfigure B.6c) and g_{w} (left panel subfigure B.6c), also in comparison to tree-level (subfigure B.6b), is shown. Here also the sign switch between up-to-down and down-to-up is shown. Note that the sign in the infrared is again different for the first generation and the second and third generation. This is because of the switch of relative sign in the mass difference from the first to the other generation, as is already the case at tree-level in equation (B.8). The size, but not the qualitative features, increase again with g_{w}. The size of the dressing function also decreases with increasing quark mass.

B.3.5 Relative ratio

In figure B.7 the relative ratio (4.10) for the flavor-diagonal elements are shown, see section 4.2.5 for a detailed discussion.

	g_{w}	M	$\frac{\Gamma}{2}$	δ	m	θ
chiral	10^{-6}	0.48 ± 0.05	0.29 ± 0.01	-2.12 ± 0.05	0.56 ± 0.05	0.55 ± 0.05
	10^{-5}	0.47 ± 0.05	0.29 ± 0.01	-2.03 ± 0.05	0.55 ± 0.05	0.56 ± 0.05
	10^{-4}	0.47 ± 0.05	0.29 ± 0.01	-2.00 ± 0.05	0.55 ± 0.05	0.56 ± 0.05
	10^{-3}	0.47 ± 0.05	0.29 ± 0.01	-2.00 ± 0.05	0.55 ± 0.05	0.56 ± 0.05
	10^{-2}	0.47 ± 0.05	0.29 ± 0.01	-2.00 ± 0.05	0.55 ± 0.05	0.56 ± 0.05
	0.05	0.48 ± 0.05	0.28 ± 0.01	-1.93 ± 0.05	0.56 ± 0.05	0.53 ± 0.05
	0.1	0.49 ± 0.05	0.24 ± 0.01	-1.57 ± 0.05	0.55 ± 0.05	0.46 ± 0.05
	0.2	0.43 ± 0.05	0.19 ± 0.01	-1.68 ± 0.05	0.47 ± 0.05	0.41 ± 0.05
	0.3	0.42 ± 0.05	0.11 ± 0.01	-1.64 ± 0.05	0.43 ± 0.05	0.25 ± 0.05
	0.4	0.35 ± 0.05	$10^{-4} \pm 0.01$	-1.57087	0.35 ± 0.05	2.857×10^{-4}
up-down	10^{-6}	0.49 ± 0.05	0.31 ± 0.01	-2.10 ± 0.05	0.58 ± 0.05	0.56 ± 0.05
	10^{-5}	0.49 ± 0.05	0.31 ± 0.01	-2.01 ± 0.05	0.58 ± 0.05	0.56 ± 0.05
	10^{-4}	0.49 ± 0.05	0.31 ± 0.01	-1.99 ± 0.05	0.58 ± 0.05	0.56 ± 0.05
	10^{-3}	0.49 ± 0.05	0.31 ± 0.01	-1.99 ± 0.05	0.58 ± 0.05	0.56 ± 0.05
	10^{-2}	0.49 ± 0.05	0.31 ± 0.01	-1.99 ± 0.05	0.58 ± 0.05	0.56 ± 0.05
	0.05	0.49 ± 0.05	0.29 ± 0.01	-1.90 ± 0.05	0.57 ± 0.05	0.54 ± 0.05
	0.1	0.49 ± 0.05	0.26 ± 0.01	-1.56 ± 0.05	0.55 ± 0.05	0.48 ± 0.05
	0.2	0.44 ± 0.05	0.20 ± 0.01	-1.71 ± 0.05	0.49 ± 0.05	0.43 ± 0.05
	0.3	0.44 ± 0.05	0.12 ± 0.01	-1.66 ± 0.05	0.46 ± 0.05	0.27 ± 0.05
	0.4	0.38 ± 0.05	$10^{-4} \pm 0.01$	-1.57087	0.38 ± 0.05	2.652×10^{-4}

Table B.2: Fit values for the flavor-off-diagonal Schwinger functions.

B.3.6 Schwinger function

In figure B.8, the Schwinger function for the scalar dressing function for the first and second generation, both for flavor-diagonal and flavor-off-diagonal elements, are shown. The third generation's large tree-level mass leads to a too-quick drowning in numerical noise to provide any reasonable results. For a detailed discussion, see section 4.2.4.

Fit parameters for the Schwinger function

The values for the fit-function are listed for the various cases studied in tables B.1 and B.2 for the flavor-diagonal and flavor-off-diagonal elements, respectively.

Appendix C

BSEs of the weak pion decay

C.1 Diagrammatic derivation of the BSEs

In this section, we illustrate the diagrammatic derivation of the weak pion BSEs from the DSEs of the corresponding 4-point functions for a better understanding. The formal derivation has very lengthy expressions. Thus, stating them here is of no use. We recommend using tools like DoFun and FormTracer for the derivation. Keep in mind that DoFun was build to derive DSEs or FRGEs in QCD, and special care has to be taken into account for our study. Nevertheless, it is possible to use these tools for the derivation.

Let us present the procedure for the 4-quark-vertex in the following. The quark-gluon interaction in our Lagrangian (see equation 5.16) generates one-loop-diagrams. The 4-Fermi interaction for the weak sector causes up to 2-loop-diagrams (see our introduction in section 3.4). As a first step, we neglect all the 2-loop-diagrams in our system. For a better understanding of the following discussion, let e, f, g, and h be the flavor of our 4 quarks. Each field has its own master equation for the DSEs (see section 3.4). Without loss of generality, let us start with the master equation of the quark e. Then, the quark e is always connected to the tree-level vertex. We show some diagrams of the resulting DSE in figure C.1, which captures all the relevant features for the derivation of the BSE.

The BSEs are derived under the assumption that the 4-point function exhibits a pole. Let us say that the quarks g and h has the total momentum P equal to the pion pole[1]:

$$\Gamma^{(4)} = \mathcal{N}\frac{\Psi\overline{\Psi}}{P^2 + M_{\pi,\mathrm{Pole}}^2}. \tag{C.1}$$

We multiply the DSE for 4-point function with $P^2 + M_{\pi,\mathrm{Pole}}^2$ and take the limit $P^2 \to -M_{\pi,\mathrm{Pole}}^2$. As a consequence of this, all the terms, which do not have a pole for this particular momentum configuration, in the DSEs vanishe. Note that in our example, this means the total momentum squared of the quarks e and f as well as g and h are fixed to the pion pole squared. Let us now illustrate the last step diagrammatically for the 4-quark-vertex, shown in figure C.1.

The first term is given by the box-diagram via two gluon exchange. It only consists of the quark-gluon-vertex at tree-level, as well as full. None of them has a pole. Hence, this diagram vanishes for the pion BSE.

[1]This also implies that the total momentum of e and f is equal to the negative of the g and h due to momentum conservation.

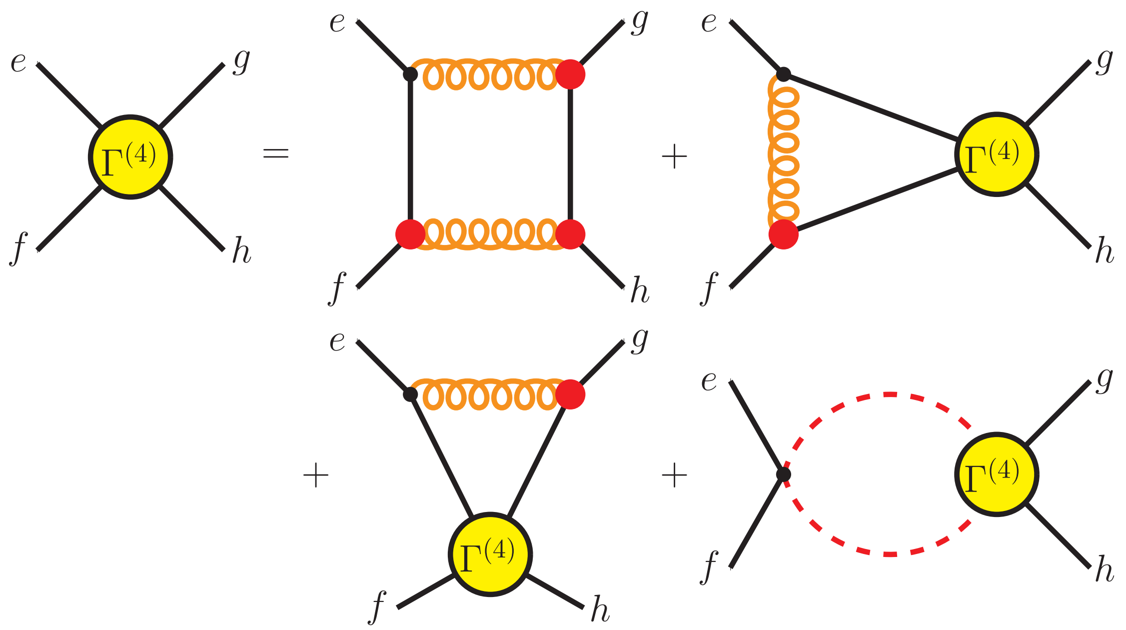

Figure C.1: Diagrammatic representation of the DSEs for the 4-quark-vertex with the flavors e, f, g and h.

The next term is the triangle-diagram with the 4-point function of the quarks. This has a pole for this particular momentum configuration since the quarks g and h are at this vertex and have the total momentum P. So this diagram gives us a contribution to the pion BSE.

The next term (first term in the second line) is again a triangle-diagram, but this time the quarks f and h are at the 4-quark-vertex and the gluon exchange between the quarks e and g. Since the total momentum of the quark f and h are not fixed, this 4-point function has not a pole for this particular momentum configuration. Therefore, this diagram does not contribute to the pion BSE. In pure QCD, all the other diagrams also vanish because they do not have a pole or are not evaluated at their pole. Thus, the pion BSE in the pure QCD has only one contribution given by a gluon exchange (see section 5.4).

The last term arises from the additional 4-Fermi interaction in our system. This diagram has a 2-quark-2-lepton-vertex with the external quarks g and h. Both quarks have the total momentum equal to the pion mass. So under the assumption that this 4-point function has the pion pole as well, this also contributes to the pion BSE representing the decay amplitude Ψ'.

All the other diagrams vanish using the same procedure. We are left with two contributions for the pion BSE. The first one is given by the gluon exchange, which is also present in the pure QCD case, and the second one arising from the effective weak interaction related to the decay process. For self-consistency, we also have to apply the same procedure for the 2-quark-2-lepton DSE. This will provide us with a coupled set of BSEs.

Let us in the following give the detailed expression of the pion amplitude. For this purpose we define the momenta k and q to be the relative momenta of the external and internal quarks, respectively. Then, we get for the momenta of the external and internal quarks the following:

$$k_\pm = k \pm \eta_\pm P, \qquad\qquad q_\pm = q \pm \eta_\pm P. \tag{C.2}$$

The relative and total momenta are defined as:

$$P = k_+ - k_-, \qquad k = \eta_- k_+ + \eta_+ k_- \qquad q = \eta_- q_+ + \eta_+ q_- \qquad \eta_+ + \eta_- = 1. \tag{C.3}$$

Applying the momenta conservation at the quark-gluon-vertex, we get for the gluon momenta:

$$p = k - q. \tag{C.4}$$

We use u, v, w, x, y and z for the combination of all the internal indices of the fermionic fields excluding the momenta. For the gluon fields, we use i and j. With this we may write the expression for BSA as follows:

$$\begin{aligned}\Psi_{u,v}\left(P^2,k^2,P\cdot k\right) = &\int_q \{K_{u,v,w,x}(P,k,q)P^Q_{w,y}(q_+)P^Q_{x,z}(q_-)\Psi_{y,z}(P^2,q^2,P\cdot q)+\\ &+S^{(4),Q,\overline{Q},l,\bar{l}}_{u,v,w,x}(P,k,q)P^l_{w,y}(q_+)P^l_{x,z}(q_-)\Psi'_{y,z}(P^2,q^2,P\cdot q)\Big\}, \\ \Psi'_{u,v}\left(P^2,k^2,P\cdot k\right) = &\int_q \Big\{S^{(4),l,\bar{l},Q,\overline{Q}}_{u,v,w,x}(P,k,q)P^Q_{w,y}(q_+)P^Q_{x,z}(q_-)\Psi_{y,z}(P^2,q^2,P\cdot q)\Big\}.\end{aligned} \tag{C.5}$$

with the Kernel

$$K_{u,v,w,x}(P,k,q) = S^{(3),A,Q,\overline{Q}}_{u,i,w}(k_+,k-q,q_+)P^A_{i,j}(k-q)\Gamma^{(3),A,Q,\overline{Q}}_{w,j,x}(k_-,k-q,q_-). \tag{C.6}$$

C.2 Numerical setup

We insert the form of the BSAs as given in equation (5.20) in the BSEs to project out the dressing functions f_i and g_i. This leads to the relation for the dressing functions given in equation (5.21). Since P^2 is fixed, these dressing functions depends on two Lorentz-invariants. Let θ be the angle between P and k and θ' between P and q. We define $z = \cos(\theta)$ and $\omega = \cos(\theta')$. Using these integration variables and performing the integrals in an appropriate coordinates, we may write the equation (5.21) as follows (see section A.5 with $y = q^2$):

$$\begin{aligned} f_i(k^2,z) = &\int_0^{\Lambda^2} \mathrm{d}\,y \int_{-1}^{1} \mathrm{d}\,\omega\sqrt{1-\omega^2}y\Bigg\{C_1\frac{\alpha\Big((k-q)^2\Big)}{(k-q)^2}M_{i,j}f_j(y,\omega)+\\ &+C_2\alpha_w((k-q)^2)\tilde{M}_{i,j}g_j(y,\omega)\Bigg\}, \\ g_i(k^2,z) = &\int_0^{\Lambda^2} \mathrm{d}\,y \int_{-1}^{1} \mathrm{d}\,\omega\sqrt{1-\omega^2}y\Bigg\{C_2\alpha_w\Big((k-q)^2\Big)M'_{i,j}f_j(y,\omega)\Bigg\},\end{aligned} \tag{C.7}$$

where the constants C_1 and C_2 are given by:

$$\begin{aligned} C_1 =& C_F\frac{4\pi I_{\text{angle}}(2)}{2(2\pi)^4}Z_{2,u}(\mu^2,\Lambda^2)Z_{2,d}(\mu^2,\Lambda^2) = \frac{2}{3\pi^2}Z_{2,u}(\mu^2,\Lambda^2)Z_{2,d}(\mu^2,\Lambda^2),\\ C_2 =& \frac{2}{\pi^3}\sqrt{Z_{2,u}(\mu^2,\Lambda^2)Z_{2,d}(\mu^2,\Lambda^2)Z_{2,e}(\mu^2,\Lambda^2)Z_{2,\nu}(\mu^2,\Lambda^2)}.\end{aligned} \tag{C.8}$$

where $Z_{2,e}$ are the wavefunction renormalization constants of the different particles.

Here, we have chosen the momenta routing such that the BSA on the right hand side depend only on the integration variables y and ω. So by choosing our grid for the BSAs given by our integration nodes, this equation becomes a finite dimensional eigenvalue problem with the matrix $\mathcal{M}$.

$$\mathcal{M} = y \begin{pmatrix} C_1 \frac{\alpha\left((k-q)^2\right)}{(k-q)^2} M & C_2 \alpha_w \left((k-q)^2\right) \tilde{M} \\ C_2 \alpha_w \left((k-q)^2\right) M' & 0 \end{pmatrix}. \tag{C.9}$$

Let us in the following deal with the matrix elements in more detail. The quark and lepton propagator of the flavor e have the following general form:

$$P_e^{Q/l}(p^2) = \tilde{A}_e^{Q/l}(p^2)\,\mathrm{i}\,\not{p} + \tilde{B}_e^{Q/l}(p^2)\mathbb{1}. \tag{C.10}$$

In equation (C.5) for the pion BSE we have quark and lepton propagator of the form $P_{w,y}^{Q/l}(q_+)$ and $P_{x,z}^{Q/l}(q_-)$. Let e and f be the flavor of the first and second propagator, respectively. We define:

$$a^{Q/l} = \tilde{A}_e^{Q/l}(q_+^2)\tilde{A}_f^{Q/l}(q_-^2), \qquad c^{Q/l} = \tilde{A}_e^{Q/l}(q_+^2)\tilde{B}_f^{Q/l}(q_-^2),$$

$$b^{Q/l} = \tilde{B}_e^{Q/l}(q_+^2)\tilde{B}_f^{Q/l}(q_-^2), \qquad d^{Q/l} = \tilde{B}_e^{Q/l}(q_+^2)\tilde{A}_f^{Q/l}(q_-^2), \tag{C.11}$$

$$m_{Q/l}^+ = c^{Q/l} + d^{Q/l}, \qquad m_{Q/l}^- = c^{Q/l} - d^{Q/l}. \tag{C.12}$$

The BSE of the pion in pure QCD has already been investigated in various works. Thus, we do not state the matrix M for the pure QCD part here since it is a very lengthy expression. We refer the reader to the literature in this case. The matrix elements from the decay part are new. Thus, we state them in the following. The matrix M' can directly be obtained from $\tilde{M}$ by replacing the lepton propator quantities by QP quantities due to the symmetry of the BSE. For example, replace a^l by a^Q. Therefore, we only state the matrix $\tilde{M}$ in the following and suppress the index Q. The matrix elements for the contribution to f_1 and f_4 vanish (see our discussion in chapter 5). So we get:

$$\tilde{M}_{1,1} = \tilde{M}_{1,2} = \tilde{M}_{1,3} = \tilde{M}_{1,4} = \tilde{M}_{4,1} = \tilde{M}_{4,2} = \tilde{M}_{4,3} = \tilde{M}_{4,4} = 0. \tag{C.13}$$

The remaining part has a common denominator given by:

$$m = (k \cdot P)^2 - (k \cdot k)(P \cdot P). \tag{C.14}$$

The matrix elements are given by:

$$
\begin{aligned}
\tilde{M}_{2,1} =& \frac{\mathrm{i}}{2m}\Bigg((k\cdot k)\Big(m^{+}(P\cdot P)-2m^{-}(P\cdot q)\Big)+2m^{-}(k\cdot P)(k\cdot q)-m^{+}(k\cdot P)^2\Bigg),\\
\tilde{M}_{2,2} =& \frac{1}{4m}\Bigg((k\cdot P)^2\Big(a(P\cdot P)+4a(q\cdot q)-4b\Big)+(k\cdot k)\Big(4(P\cdot P)(b-a(q\cdot q))+\\
&+8a(P\cdot q)^2-a(P\cdot P)^2\Big)-8a(k\cdot P)(k\cdot q)(P\cdot q)\Bigg),\\
\tilde{M}_{2,3} =& \frac{1}{4m}\Bigg(-(k\cdot P)(k\cdot q)\Big(4(a(q\cdot q)+b)+a(P\cdot P)\Big)+(k\cdot k)(P\cdot q)\times\\
&\times\Big(4(a(q\cdot q)+b)-a(P\cdot P)\Big)+2a(k\cdot P)^2(P\cdot q)\Bigg),\\
\tilde{M}_{2,4} =& -\frac{\mathrm{i}}{2m}\Bigg((k\cdot P)^2\Big(m^{-}(P\cdot q)-2m^{+}(q\cdot q)\Big)+(k\cdot P)(k\cdot q)\times\\
&\times\Big(2m^{+}(P\cdot q)-m^{-}(P\cdot P)\Big)-2m^{+}(k\cdot k)\Big((P\cdot q)^2-(P\cdot P)(q\cdot q)\Big)\Bigg),\\
\tilde{M}_{3,1} =& -\frac{\mathrm{i}}{m}m^{-}\Big((P\cdot P)(k\cdot q)-(k\cdot P)(P\cdot q)\Big),\\
\tilde{M}_{3,2} =& \frac{2}{m}a(P\cdot q)\Big((P\cdot P)(k\cdot q)-(k\cdot P)(P\cdot q)\Big),\\
\tilde{M}_{3,3} =& \frac{1}{4m}\Big((P\cdot P)(k\cdot q)-(k\cdot P)(P\cdot q)\Big)\Big(4(a(q\cdot q)+b)+a(P\cdot P)\Big),\\
\tilde{M}_{3,4} =& -\frac{\mathrm{i}}{2m}\Big((P\cdot P)(k\cdot q)-(k\cdot P)(P\cdot q)\Big)\Big(m^{-}(P\cdot P)-2m^{+}(P\cdot q)\Big).
\end{aligned}
\tag{C.15}
$$

Further details on the numerical implementation is already stated in various literatures. Hence, we conclude our technical discussion on the pion BSEs.

Appendix D

FRG

D.1 Flow equation for the dynamical hadronization

In this section, we derive the Wetterich equation for the dynamical hadronization case with all its details. Let now a part of the fields be scale-dependent, which is the case for the dynamical hadronization. We split $\Phi = (\tilde{\Phi}, \hat{\Phi}_k)$ into a scale-independent part $\tilde{\Phi}$ and scale-dependent part $\hat{\Phi}_k$ and define the IR-regularized functional $Z_k[J]$ and Schwinger functional $W_k[J]$:

$$\mathrm{e}^{W_k[J]} \equiv Z_k\left[J\right] = \int \mathcal{D}\tilde{\Phi} \exp\left[-S[\tilde{\Phi}] - \Delta S_k[\Phi] + \int \left(J\Phi\right)\right]. \tag{D.1}$$

The expectation value ϕ of the field Φ in the presence of the source J is:

$$\phi_i = \left\langle \Phi_i \right\rangle_J = \frac{\delta}{\delta J_i} W_k[J]. \tag{D.2}$$

The IR-regularized effective action is given by:

$$\Gamma_k\left[\phi\right] = \sup_J \left\{-W_k\left[J\right] + \int \left(J\phi\right)\right\} - \Delta S_k\left[\phi\right]. \tag{D.3}$$

We get for the source fields:

$$J_i(p) = (-1)_i^G \frac{\delta}{\delta\phi_i(p)} \left(\Gamma_k\left[\phi\right] + \Delta S_k\left[\phi\right]\right). \tag{D.4}$$

For the 2-point function and the propagator ($\mathcal{P}_k$), we have the relation:

$$\mathcal{P}_{k,ij}(p_1, p_2) = \left[\frac{\delta^2}{\delta\phi_j(p_2)\delta\phi_i(p_1)} \left(\Gamma_k\left[\phi\right] + \Delta S_k\left[\phi\right]\right)\right]^{-1} = (-1)_i^G \frac{\delta^2}{\delta J_i(p_1)\delta J_j(p_2)} W_k[J] \tag{D.5}$$

We get the following useful relation:

$$\left\langle \Phi_i(p_1)\Phi_j(p_2)\right\rangle_J = \frac{\delta^2 W_k[J]}{\delta J_i(p_2)\delta J_j(p_1)} + \phi_i(p_1)\phi_j(p_2) = (-1)_i^G \mathcal{P}_{k,ij}(p_1, p_2) + \phi_i(p_1)\phi_j(p_2). \tag{D.6}$$

For the total derivative of W_k respect to $t = \log(\frac{k}{\Lambda})$, we get:

$$\frac{\mathrm{d}}{\mathrm{d}\,t} W_k[J] = -\left\langle \frac{\mathrm{d}}{\mathrm{d}\,t}\Delta S_k[\Phi]\right\rangle_J + \int (\partial_t J)\phi + \int \hat{J}\left\langle \partial_t \hat{\Phi}\right\rangle_J, \tag{D.7}$$

and of Γ_k:

$$\frac{\mathrm{d}}{\mathrm{d}\,t}\Gamma_k[\phi] = \left\langle \frac{\mathrm{d}}{\mathrm{d}\,t}\Delta S_k[\Phi] \right\rangle_J - \frac{\mathrm{d}}{\mathrm{d}\,t}\Delta S_k[\phi] + \int \hat{J}\left(\partial_t\hat{\phi} - \left\langle \partial_t\hat{\Phi}\right\rangle_J\right). \tag{D.8}$$

This is at the same time:

$$\frac{\mathrm{d}}{\mathrm{d}\,t}\Gamma_k[\phi] = \partial_t|_{\hat{\phi}}\,\Gamma_k[\phi] + \int \frac{\delta}{\delta\hat{\phi}}\Gamma_k\,[\phi]\,\partial_t\hat{\phi}. \tag{D.9}$$

Hence, we get the final expression:

$$\begin{aligned}\partial_t|_{\hat{\phi}_k}\,\Gamma_k[\phi] = &\left\langle \frac{\mathrm{d}}{\mathrm{d}\,t}\Delta S_k[\Phi] \right\rangle_J - \frac{\mathrm{d}}{\mathrm{d}\,t}\Delta S_k[\phi] + \int \frac{\delta}{\delta\hat{\phi}}\left(\Gamma_k\,[\phi] + \Delta S_k\,[\phi]\right)\left(\partial_t\hat{\phi} - \left\langle \partial_t\hat{\Phi}\right\rangle_J\right)\\ &- \int \frac{\delta}{\delta\hat{\phi}}\Gamma_k\,[\phi]\,\partial_t\hat{\phi}.\end{aligned} \tag{D.10}$$

This general expression simplifies for ΔS_k of the form:

$$\Delta S_k\,[\Phi] = \frac{1}{2}\int_q \Phi(q)R_k(q)\Phi(q). \tag{D.11}$$

We get:

$$\begin{aligned}\left\langle \frac{\mathrm{d}}{\mathrm{d}\,t}\Delta S_k[\Phi] \right\rangle_J =&\frac{1}{2}\int_q \left\{(\partial_t R_{k,ij}(q))\left\langle \Phi_i(q)\Phi_j(q)\right\rangle_J + R_{k,ij}(q)\left\langle \partial_t(\Phi_i(q)\Phi_j(q))\right\rangle_J\right\}\\ =&\frac{1}{2}\int_q \Big\{(\partial_t R_{k,ij}(q))\left[(-1)^G_i\mathcal{P}_{k,ij}(q,q) + \phi_i(q)\phi_j(q)\right]\\ &+R_{k,ij}(q)\left\langle \partial_t(\hat{\Phi}_i(q)\hat{\Phi}_j(q))\right\rangle_J\Big\},\end{aligned} \tag{D.12}$$

and:

$$\frac{\mathrm{d}}{\mathrm{d}\,t}\Delta S_k[\phi] =\frac{1}{2}\int_q \left\{(\partial_t R_{k,ij}(q))\phi_i(q)\phi_j(q) + R_{k,ij}(q)\partial_t(\hat{\phi}_i(q)\hat{\phi}_j(q))\right\}. \tag{D.13}$$

Hence, we get for the flow:

$$\begin{aligned}\partial_t|_{\hat{\phi}_k}\,\Gamma_k[\phi] = \int_q \Bigg\{&(-1)^G_i\frac{1}{2}(\partial_t R_{k,ij}(q))\mathcal{P}_{k,ij}(q,q) + \frac{1}{2}R_{k,ij}(q)\left[\left\langle \partial_t(\hat{\Phi}_i(q)\hat{\Phi}_j(q))\right\rangle_J\right.\\ &\left.-\partial_t(\hat{\phi}_i(q)\hat{\phi}_j(q))\right] + \frac{\delta}{\delta\hat{\phi}(q)}\left(\Gamma_k\,[\phi] + \Delta S_k\,[\phi]\right)\left(\partial_t\hat{\phi}(q) - \left\langle \partial_t\hat{\Phi}(q)\right\rangle_J\right)\\ &-\frac{\delta}{\delta\hat{\phi}(q)}\Gamma_k\,[\phi]\,\partial_t\hat{\phi}(q)\Bigg\}.\end{aligned} \tag{D.14}$$

For the last step, let us assume that the derivative of the scale-dependent part of the fields is at most linear. This means:

$$\partial_t\hat{\Phi}_i(q) = (\partial_t A_{i,m}(q))F_m[\phi](q) + (\partial_t B_{i,m}(q))G[\phi](q)\Phi_m(q), \tag{D.15}$$

which fulfils the condition:

$$\left\langle \partial_t \hat{\Phi}_i(q) \right\rangle_J = \partial_t \hat{\phi}_i(q) = (\partial_t A_{i,m}(q)) F_m[\phi](q) + (\partial_t B_{i,m}(q)) G[\phi](q) \phi_m(q). \tag{D.16}$$

This yields:

$$\left\langle \partial_t (\hat{\Phi}_i(q) \hat{\Phi}_j(q)) \right\rangle_J - \partial(\hat{\phi}_i(q) \hat{\phi}_j(q)) = (-1)^G G[\phi](q) \left[(\partial_t B_{i,m}(q)) \mathcal{P}_{k,mj} + \mathcal{P}_{k,im} (\partial_t B_{m,j}(q)) \right].$$

We insert this into the flow equation and get the final equation:

$$\partial_t|_{\hat{\phi}_k} \Gamma_k[\phi] = \frac{1}{2} \mathrm{STr} \left\{ \left[(\partial_t R_k) + G[\phi](\partial_t B) R_k + R_k G[\phi](\partial_t B) \right] \mathcal{P}_k \right\} - \mathrm{Tr} \left\{ \frac{\delta}{\delta \hat{\phi}} \Gamma_k [\phi] \, \partial_t \hat{\phi} \right\} \tag{D.17}$$

D.2 Regulators

D.2.1 Regulators for the Euclidean case

We choose the standard exponential regulator for our calculation. The bosonic and fermionic regulator shape function are given by:

$$r_B(x) = \frac{x^{m-1}}{e^{x^m} - 1}, \qquad r_F(x) + 1 = \sqrt{r_B(x) + 1}, \tag{D.18}$$

where the explicit calculation is done for $m = 2$. This results in the following regulators for the different particles (see equation (3.11)):

$$\begin{aligned} R^i_k(p) &= \hat{R}^i_k(p) p^2, & \hat{R}^i_k(p) &= Z_{i,k}(0) r_B \left(\frac{p^2}{k^2} \right), & i &\in \{\sigma, \pi\}, \\ R^i_k(p) &= \hat{R}^i_k(p) \not{p}, & \hat{R}^i_k(p) &= Z_{i,k}(0) r_F \left(\frac{p^2}{k^2} \right), & i &\in \{Q, l\}. \end{aligned} \tag{D.19}$$

D.2.2 Regulators for the real-time FRG

We define a smooth approximation (Θ_n) for the step function (Θ) and a modified version of this via:

$$\Theta_n(x) = \frac{1}{1 + x^n}, \qquad \Theta_{\alpha,\beta,n}(x) = \alpha \Theta_n \left(\frac{\beta}{x} \right). \tag{D.20}$$

We further define:

$$\Delta m_r(k) = \mu \sqrt{\Theta_{\alpha,\beta,n} \left(\frac{\mu}{k} \right)} \xrightarrow{n \to \infty} \begin{cases} \sqrt{\alpha} \mu, & \text{if } k < \frac{\mu}{\beta} \\ 0, & \text{if } k > \frac{\mu}{\beta} \end{cases}. \tag{D.21}$$

This results in the following regulators for the different particles (see equation (3.11)):

$$\begin{aligned} \hat{R}^i_k(p) &= \left(Z_{i,k}(0) + \frac{\Delta m_r^2(k)}{p^2} \right) r_B \left(\frac{p^2 + \Delta m_r^2(k)}{k^2} \right), & i &\in \{\sigma, \pi\}, \\ \hat{R}^i_k(p)) &= \left(Z_{i,k}(0) + \frac{\Delta m_r(k)}{\sqrt{p^2}} \right) r_F \left(\frac{p^2 + \Delta m_r^2(k)}{k^2} \right), & i &\in \{Q, l\}. \end{aligned} \tag{D.22}$$

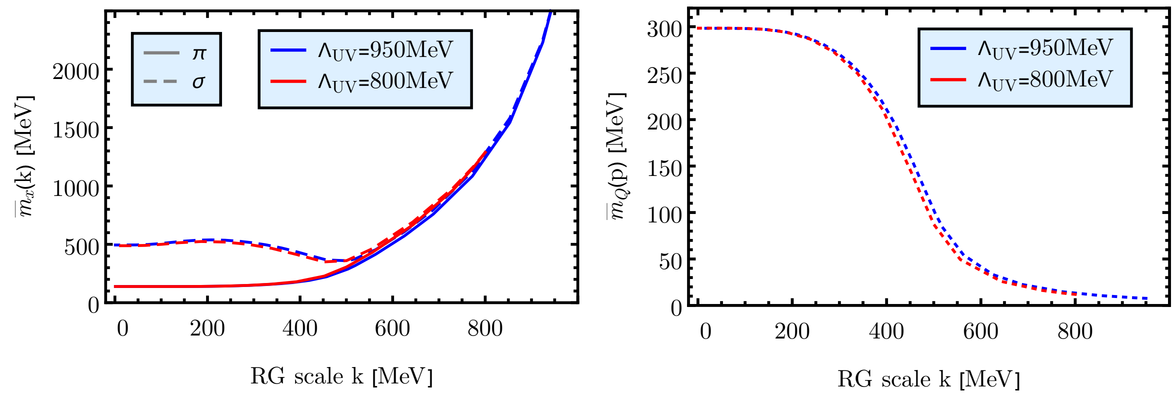

Figure D.1: The flow of the curvature masses for the mesons (left panel) and quark (right panel) for different UV-cutoffs.

D.3 Quark-meson model

D.3.1 Initial values

We choose our initial values to achieve the IR-values for the curvature masses and pion decay-constant, as stated in equation((6.9) and (6.11). We refer the reader to our discussion in 6.1.5; or 6.2.2 and [43] for further details on the relation between curvature and pole masses,.

According to our discussion in 6.1, we start the flow at $\Lambda_{\rm UV} = 950\,\text{MeV}$. The initial mesonic potential is considered to be quadratic (i.e., all higher orders of the mesonic potential vanish at the starting point of the flow):

$$V_{k=\Lambda_{\rm UV}} = a_1(\rho - \rho_0) + \frac{a_2}{2}(\rho - \rho_0)^2 \tag{D.23}$$

where ρ_0 is the expansion point. We set the wavefunction renormalizations to unity at the UV-cutoff.

For completeness, we also state our initial values for our full truncation of the PM considered in this work:

$$a_1 = (2638\text{ MeV})^2, \qquad a_2 = 50, \qquad h_\Lambda = 18.085, \qquad \rho_0 = \frac{1}{2}(28.32\text{ MeV})^2 \tag{D.24}$$

The results of the renormalized quantities in the IR do not depend on the UV-cutoff if it is changed within reasonable bounds and if the initial values (D.24) are changed accordingly. This is demonstrated in figures D.1 and D.2, where these quantities are displayed for two values of the UV-cutoff, $\Lambda_{\rm UV} = 950\,\text{MeV}$ (blue line) and $\Lambda_{\rm UV} = 800\,\text{MeV}$ (red line).

D.3.2 Propagators

Due to the fact that flow equations are evaluated at non-vanishing fields, we have for the 2-point functions:

$$\Gamma^{(2),\pi}(p=0) = V_k'[\rho], \quad \Gamma^{(2),\sigma}(p=0) = V_k'[\rho] + 2\rho V_k''[\rho], \quad \hat{m}_{Q,k}(p) = h_k(p,-p)\sqrt{\frac{\rho}{N_f}}. \tag{D.25}$$

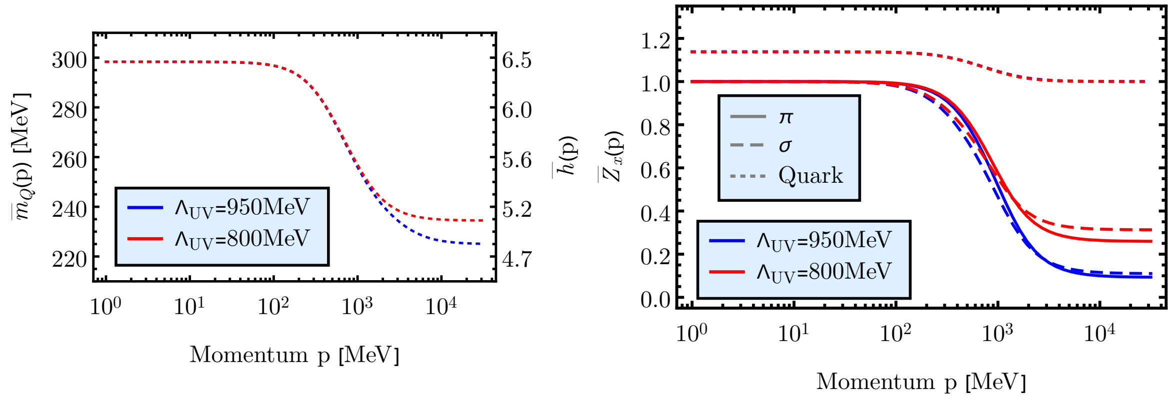

Figure D.2: Momentum-dependence of the quark mass and Yuakawa coupling (left panel), and the wavefunction (right panel) for different UV-cutoffs.

We define the following mesonic propagators:

$$P_i(p) = \frac{1}{\left[Z_{i,k}(p) + \hat{R}_k^i(p)\right] p^2 + \Gamma_i^{(2)}(0)}, \qquad i \in \{\sigma, \pi\}\,. \tag{D.26}$$

In addition, we can define an effective (scalar) QP, entering all loop functions:

$$\hat{P}_Q(p) = \frac{1}{\left[Z_{rQ,k}(p)\right]^2 p^2 + \hat{m}_{Q,k}^2(p)}, \qquad Z_{rQ,k}(p) = Z_{Q,k}(p) + \hat{R}_k^Q(p), \tag{D.27}$$

resulting in the following full QP:

$$P_Q(p) = \hat{P}_Q(p)\left[Z_{rQ,k}(p)\,\mathrm{i}\not{p} + \hat{m}_{Q,k}(p)\mathbb{1}\right]. \tag{D.28}$$

D.3.3 Flow equations

Let us start with the flow equation of the mesonic potential. We take the ansatz for the potential (equation (6.4)) and insert this into the Wetterich equation (3.21). Evaluating the expression for non-vanishing sigma fields ($\rho = \frac{1}{2}\sigma^2$) yields for the part of the potential:

$$\partial_t V_k[\rho] = \frac{1}{2}\int_q q^2 \left\{\dot{\hat{R}}_k^\sigma(q) P_\sigma(q) + (N_f^2 - 1)\dot{\hat{R}}_k^\pi(q) P_\pi(q) - 8 N_c N_f \dot{\hat{R}}_k^Q(q) Z_{rQ,k}(q) \hat{P}_Q(q)\right\}. \tag{D.29}$$

To project out the the flow of $v_{k,i}$'s, we take derivatives of the equation D.29 with respect to ρ and evaluate it at $\rho = \rho_0$:

$$\partial_t v_{k,i} = \partial_\rho^i \partial_t V_k[\rho]\Big|_{\rho=\rho_0}. \tag{D.30}$$

We can get the momentum-independent part of the mesonic 2-point-functions from the mesonic potential via:

$$\Gamma^{(2),\pi}(p=0) = \partial_\rho V[\rho], \qquad \Gamma^{(2),\sigma}(p=0) = \partial_\rho V[\rho] + 2\rho\partial_\rho^2 V[\rho],$$

Therefore, we only solve the momentum-dependent part and used for the momentum independent part (curvature masses) the mesonic potential. This leads us to:

$$\Delta\Gamma_k^{(2),i}(p) = \Gamma_k^{(2),i}(p) - \Gamma_k^{(2),i}(0), \qquad\qquad i \in \{\sigma, \pi\}\,. \tag{D.31}$$

The tadpole-diagram, depicted in the second line in figure 6.1, only contributes to the momentum-independent part of the flow equation as the 4-point functions do not carry any momentum-dependency in our truncation. Thus, it can ignored for our study, and we are left with the polarization diagrams. So we will not state any contributions from the tadpole-diagram in the following. The mesonic wave-function renormalizations are directly related to the 2-point functions by:

$$Z_{i,k}(p) = p^{-2}\Delta\Gamma_k^{(2),i}(p). \tag{D.32}$$

We used computation tools, like DoFun [171] and FormTracer [173], for the derivation of the flow equations. Let us now turn to the expressions for the flow equations and define the relative momentum between the internal and the external momenta $r = q - p$. The contribution to the $\dot{\Gamma}^{(2)}_{\pi,k}(p)$ and $\dot{\Gamma}^{(2)}_{\sigma,k}(p)$ from the quark-loop is the same and given by:

$$\begin{aligned}\dot{\Gamma}^{(2),\kappa}_{Q,k}(p) = \int_q \Big\{ & 12\dot{\hat{R}}^Q_k(q)(q)\hat{P}^2_Q(q)\hat{P}_Q(r)h_k(r,-q)h_k(q,-r)\left[\left(Z^2_{rq,k}(q)q^2 - m^2_{q,k}(q)\right)\times\right. \\ & \left.\times Z_{rQ,k}(r)(p\,q - p^2) + 2m_{q,k}(q)m_{q,k}(r)Z_{rQ,k}(q)q^2\right]\Big\}.\end{aligned} \tag{D.33}$$

The full flow for the 2-point function of the pion is:

$$\dot{\Gamma}^{(2),\pi}k(p) = \dot{\Gamma}^{(2),\kappa}_{Q,k}(p) + \int_q \left\{ \left(\Gamma^{(3)}_{\pi\pi\sigma}(0)\right)^2 \left[\dot{\hat{R}}^\pi_k(q)P^2_\pi(q)P_\sigma(r) + \dot{\hat{R}}^\sigma_k(q)P^2_\sigma(q)P_\pi(r)\right]\right\}, \tag{D.34}$$

and correspondingly the full flow of the sigma is:

$$\begin{aligned}\dot{\Gamma}^{(2)}_{\sigma,k}(p) = \dot{\Gamma}^{(2),\kappa}_{Q,k}(p) + \int_q \Big\{ & 3\left(\Gamma^{(3)}_{\pi\pi\sigma}(0)\right)^2 \dot{\hat{R}}^\pi_k(q)P^2_\pi(q)P_\pi(r) \\ & + \left(\Gamma^{(3)}_{\sigma\sigma\sigma}(0)\right)^2 \dot{\hat{R}}^\sigma_k(q)P^2_\sigma(q)P_\sigma(r)\Big\}.\end{aligned} \tag{D.35}$$

The mesonic 3-point vertices are obtained from the mesonic potential via:

$$\Gamma^{(3)}_{\pi\pi\sigma}(0) = \sigma V^{(2)}_k[\rho]\Big|_{\rho=\rho_0}, \qquad \Gamma^{(3)}_{\sigma\sigma\sigma}(0) = \left[3\sigma V^{(2)}_k[\rho] + \sigma^3 V^{(3)}_k[\rho]\right]\Big|_{\rho=\rho_0}. \tag{D.36}$$

The flow for the wavefunction part of the QP is given by:

$$\begin{aligned}\dot{Z}_{q,k}(p) = -\frac{1}{4p^2}\int_q \Bigg\{ & (p\,q)\dot{\hat{R}}^Q_k(q)(q)\hat{P}^2_Q(q)h_k(-p,q)h_k(-q,p)\left(m^2_{q,k}(q) - Z^2_{rq,k}(q)q^2\right)\times \\ & \times\left(3P_\pi(r) + P_\sigma(r)\right) + 2\hat{P}_Q(r)Z_{rQ,k}(r)(p\,q - p^2)\times \\ & \times h_k(r,p)h_k(-p,-r)\left(3\dot{\hat{R}}^\pi_k(q)P^2_\pi(q) + \dot{\hat{R}}^\sigma_k(q)P^2_\sigma(q)\right)\Bigg\}.\end{aligned} \tag{D.37}$$

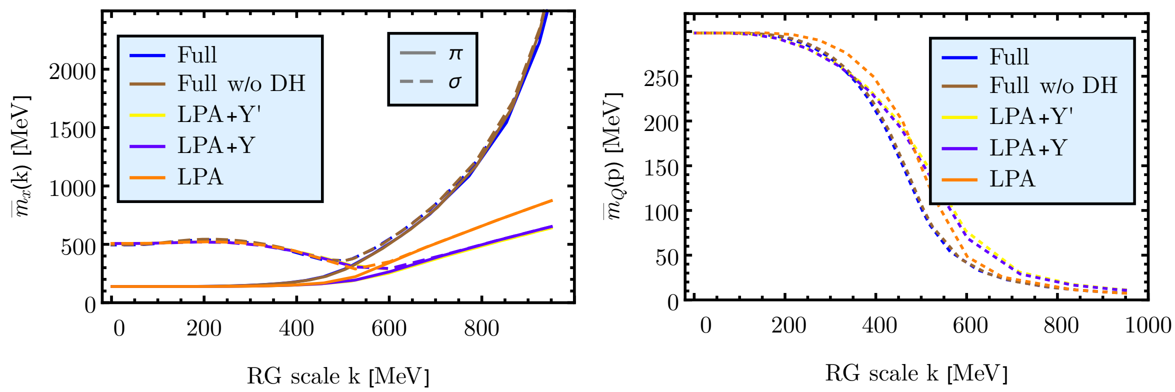

Figure D.3: Flow of the meson masses (left panel) and quark masses at $p = 0$ (right panel) for different truncations.

From the 2-quark-meson-vertex, we obtain the full momentum-dependency of the Yukawa coupling. Anyhow, for the particular one momentum channel in our study (see equation (6.12)), we may also derive the flow equation from the scalar channel of the QP. With this, we get for the Yukawa coupling without the extra contributions from the dynamical hadronization the following:

$$\dot{h}_k(p,-p) = -\frac{1}{4}\int_q \Bigg\{ 2\dot{\hat{R}}_k^Q(q)(q)\hat{P}_Q^2(q)h_k(-p,-q)h_k(q,p)h_k(q,-q)Z_{rQ,k}(q)q^2\left(3P_\pi(r) - P_\sigma(r)\right) \\ + \hat{P}_Q(r)h_k(-p,-r)h_k(r,p)h_k(r,-r)\left(3\dot{\hat{R}}_k^\pi(q)P_\pi^2(q) - \dot{\hat{R}}_k^\sigma(q)P_\sigma^2(q)\right)\Bigg\}. \tag{D.38}$$

The flow of λ_k has a very lengthy expression and thus is not noted here. In the particular momentum channel of equation (6.12), we get the following relation from the dynamical hadronization by setting the flow of λ_k to zero:

$$\begin{aligned} \partial_t\lambda_k(p,-p,p) =& \mathrm{Flow}\lambda_k(p,-p,p) - \dot{A}(p,-p)h_k(p,-p), \\ \dot{A}(p,-p) =& \frac{\mathrm{Flow}\lambda_k(p,-p,p)}{h_k(p,-p)}, \\ \dot{h}_k(p,-p) =& \mathrm{Flow}h_k(p,-p) - \mathrm{Flow}\lambda_k(p,-p,p)\frac{\Gamma^{(1),\kappa}(0)}{h_k(p,-p)}. \end{aligned} \tag{D.39}$$

D.3.4 Truncation schemes

In this section of the appendix, we discuss details on the different truncations schemes for the QMM. In particular, we compare them to our results in section 6.1 and refer to this as the full case. Thus, we set the initial values for different truncations to achieve the same IR values given by the PM. The results are shown in D.3 and D.4.

We consider four additional truncations, apart from the full case, given by:

- Full w/o DH: First, we want to analyze the effects from the dynamical hadronization

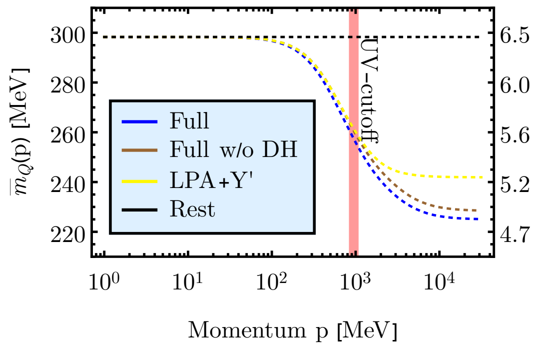

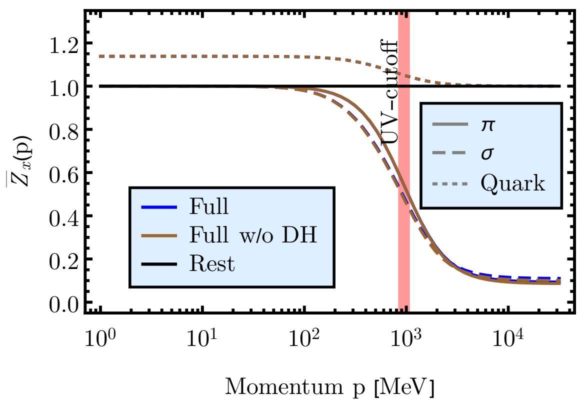

Figure D.4: Momentum-dependence of the quark mass and Yuakawa coupling (left panel), and the wavefunction (right panel) for different truncations.

procedure. Therefore, only the contributions from the dynamical hadronization procedure are neglected.

- LPA + Y': In addition, we neglect the flow of the wavefunction renormalization function and thus set the wavefunctions to unity.
- LPA + Y: Besides, we suppress the momentum-dependence of the Yukawa coupling. Thus, only its flow at vanishing momenta is considered.
- LPA: Finally, also the Yukawa coupling is fixed to a constant. So we are left with the flow of the momentum-independent couplings from the potential.

Let us start with the running of the curvature masses, shown in figure D.3. The most notable effect is the faster decoupling of the meson masses at larger scales. Hence, the behavior gets closer to the one in full QCD. The running of the quark mass is almost unaffected.

The momentum-dependent Yukawa coupling is depicted in the left panel of figure D.4. Below the UV-cutoff, It is mostly independent of the truncation, as long as the momentum-dependency is taken into account. We observe the same pattern for the wavefunctions, as shown in the right panel of figure D.4. These findings are in according to our discussion about the different contributions generating momentum-dependencies in 6.1. This concludes our presentation of the results from the different truncation schemes.

D.4 Regulator dependencies for the real-time FRG

Let us now discuss an issue caused by modifying the regulator with an additional mass-term in the real-time FRG framework. The quantum fluctuations are integrated out step by step in the FRG, as stated in the introduction. Especially, the regulator determines how the fluctuations are integrated out. In practice, the regulator singles out momentum-shells for the integration.

To be more precise, the regulator shape function singles out momenta for the propagator around unity ($x \approx 1$). This means the following for the modified regulator in the real-time

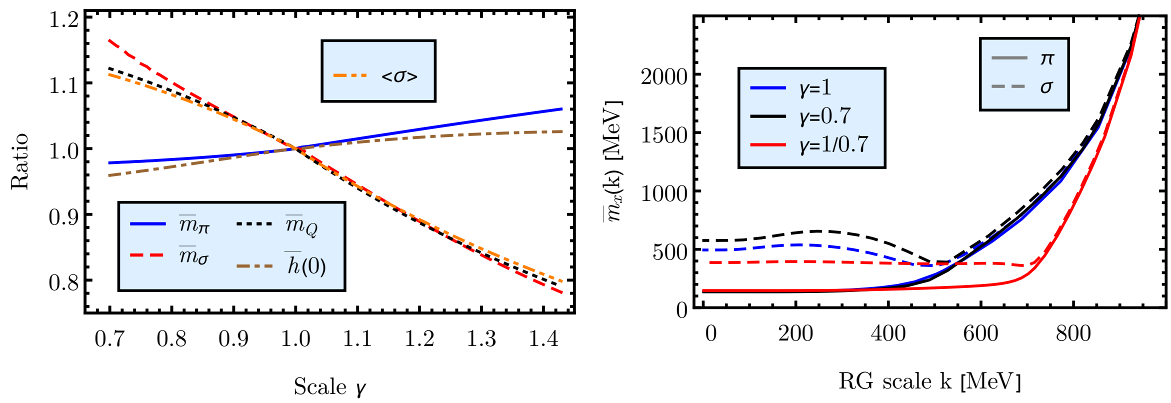

Figure D.5: Ratio of the the different quatities (left panel) and the flow of the meson masses (right panel) for different scale shifting.

FRG framework (see section D.2.2):

$$p^2 \approx k^2 - \Delta m_r^2(k). \tag{D.40}$$

So we may integrate out the different fields at different scales for different values of the mass-shifting. Since the different fields in our system may have different masses, we want to do this. Therefore, we investigate the effects of integrating out bosonic and fermionic fields at different scales for our QMM to get an insight.

D.4.1 Scale shifted regulators

For this purpose, we define bosonic and fermionic scale shifting function as follows:

$$f_i(k) = \Theta_{1-\gamma_i,\beta_i,n_i}\left(\frac{k}{\Lambda}\right) + \gamma_i \xrightarrow{n\to\infty} \begin{cases} 1, & \text{if } k > \beta\Lambda \\ \gamma_i, & \text{if } k < \beta\Lambda \end{cases}, \qquad i \in \{B, F\}, \tag{D.41}$$

where β_i and γ_i ($\in [0,1]$) are parameters.

As a first step, we analyze the impact of the scale shifting without the mass shifting term. This results in the following regulators for the different particles:

$$\begin{aligned} \hat{R}_k^i(p) =& Z_{i,k}(0) r_B\left(\frac{p^2}{f_B^2(k)k^2}\right), \qquad & i \in \{\sigma, \pi\}, \\ \hat{R}_k^i(p)) =& Z_{i,k}(0) r_F\left(\frac{p^2}{f_F^2(k)k^2}\right), \qquad & i \in \{Q, l\}. \end{aligned} \tag{D.42}$$

The scale shifting function enable us to start the flow equation unmodified in the UV ($\beta_i < 1$). Around the scale $\beta_i\Lambda$, we start to shift the scale of the corresponding fields to lower values ($\gamma_i k$). Thus, the corresponding fields are integrated out faster ($\gamma_i < 1$).

D.4.2 Scale-dependencies of the quark-meson model

We only shift the scale of one kind of field at the same time since γ_i corresponds to the relative shift of the scales between the fermionic and bosonic fields. Therefore, we define:

$$\gamma = \begin{cases} \gamma_B, & \text{if } \gamma_B < 1 \\ 1, & \text{if } \gamma_B = \gamma_F = 1 \\ 1/\gamma_F, & \text{if } \gamma_F < 1 \end{cases} . \tag{D.43}$$

We show the relative ratio of the different quantities (left panel) and the flow of the meson masses (right panel) for different values of the scale shifting in figure D.5.

The quarks only interact via the mesons with each other in our system. Dynamical chiral symmetry is related to a strong enough interaction between the quarks. $\gamma > 1$ means that the fermionic fields are integrated out faster during the flow. So if we have integrated out all the quarks before we even start to integrate out the bosons ($\gamma = \infty$), there is no interaction between the quarks. Hence, no dynamical chiral symmetry breaking will appear. Therefore, the effects of the dynamical chiral symmetry breaking are reduced for $\gamma > 1$. This is seen for the flow of the curvature mass (red) in the left panel of figure D.5, as the difference between the meson masses, is shrunk. This also explains the decreasing of the sigma condensate for increasing γ as it is directly related to dynamical chiral symmetry breaking. Therefore, the quark mass and sigma mass is also decreased. This concludes our brief presentation of the results for scale shifted regulators.

Appendix E

List of abbreviations

BSA	Bethe-Salpeter-amplitude
BSE	Bethe-Salpeter-equation
C	Charge conjugation
DSE	Dyson-Schwinger-equation
FRG	Functional-Renormalization-Group
FRGE	Functional-Renormalization-Group equation
IR	Infrared
P	Parity
PM	Physical model
QCD	Quantum chromodynamics
QCDM	QCD related model
QFT	Quantum field theory
QMM	Quark-meson model
QP	Quark propagator
RG	Renormalization-Group
UV	Ultraviolet

Appendix F

Bibliography

[1] Abbott, B. P. *et al.*: *Observation of Gravitational Waves from a Binary Black Hole Merger*. Phys. Rev. Lett., 116(6):061102, 2016.

[2] Abbott, B. P. *et al.*: *GW151226: Observation of Gravitational Waves from a 22-Solar-Mass Binary Black Hole Coalescence*. Phys. Rev. Lett., 116(24):241103, 2016.

[3] Abadie, J. *et al.*: *Calibration of the LIGO Gravitational Wave Detectors in the Fifth Science Run*. Nucl. Instrum. Meth., A624:223–240, 2010.

[4] Accadia, T. *et al.*: *Calibration and sensitivity of the Virgo detector during its second science run*. Class. Quant. Grav., 28:025005, 2011. [Erratum: Class. Quant. Grav.28,079501(2011)].

[5] Faber, Joshua A. and Frederic A. Rasio: *Binary Neutron Star Mergers*. Living Rev. Rel., 15:8, 2012.

[6] Koutarou Kyutoku: *The Black Hole-Neutron Star Binary Merger in Full General Relativity. Dependence on Neutron Star Equation of State* . Springer Verlag, 2013.

[7] Foucart, Francois, Evan O'Connor, Luke Roberts, Matthew D. Duez, Roland Haas, Lawrence E. Kidder, Christian D. Ott, Harald P. Pfeiffer, Mark A. Scheel, and Bela Szilagyi: *Post-merger evolution of a neutron star-black hole binary with neutrino transport*. Phys. Rev., D91(12):124021, 2015.

[8] Abbott, B. P. *et al.*: *GW170817: Observation of Gravitational Waves from a Binary Neutron Star Inspiral*. Phys. Rev. Lett., 119(16):161101, 2017.

[9] Rosswog, Stephan and M. Liebendoerfer: *High resolution calculations of merging neutron stars. 2: Neutrino emission*. Mon. Not. Roy. Astron. Soc., 342:673, 2003.

[10] Sekiguchi, Yuichiro, Kenta Kiuchi, Koutarou Kyutoku, and Masaru Shibata: *Gravitational waves and neutrino emission from the merger of binary neutron stars*. Phys. Rev. Lett., 107:051102, 2011.

[11] Neilsen, David, Steven L. Liebling, Matthew Anderson, Luis Lehner, Evan O'Connor, and Carlos Palenzuela: *Magnetized Neutron Stars With Realistic Equations of State and Neutrino Cooling*. Phys. Rev., D89(10):104029, 2014.

[12] Palenzuela, Carlos, Steven L. Liebling, David Neilsen, Luis Lehner, O. L. Caballero, Evan O'Connor, and Matthew Anderson: *Effects of the microphysical Equation of State in the mergers of magnetized Neutron Stars With Neutrino Cooling.* Phys. Rev., D92(4):044045, 2015.

[13] Sekiguchi, Yuichiro, Kenta Kiuchi, Koutarou Kyutoku, and Masaru Shibata: *Dynamical mass ejection from binary neutron star mergers: Radiation-hydrodynamics study in general relativity.* Phys. Rev., D91(6):064059, 2015.

[14] Foucart, Francois, Roland Haas, Matthew D. Duez, Evan O'Connor, Christian D. Ott, Luke Roberts, Lawrence E. Kidder, Jonas Lippuner, Harald P. Pfeiffer, and Mark A. Scheel: *Low mass binary neutron star mergers : gravitational waves and neutrino emission.* Phys. Rev., D93(4):044019, 2016.

[15] Caballero, O. L.: *Neutrino emission, Equation of State and the role of strong gravity.* In *11th Latin American Symposium on Nuclear Physics and Applications Medellin, Colombia, November 30-December 4, 2015*, 2016. `https://inspirehep.net/record/1426803/files/arXiv:1603.02755.pdf`.

[16] Suwa, Yudai and Kohta Murase: *Probing the central engine of long gamma-ray bursts and hypernovae with gravitational waves.* Phys. Rev., D80:123008, 2009.

[17] Hasenfratz, Peter and Reto von Allmen: *Towards Weyl fermions on the lattice without artefacts.* JHEP, 02:079, 2008.

[18] Alkofer, Reinhard and Lorenz von Smekal: *The infrared behavior of QCD Green's functions: Confinement, dynamical symmetry breaking, and hadrons as relativistic bound states.* Phys. Rept., 353:281, 2001.

[19] Fischer, Christian S.: *Infrared properties of QCD from Dyson-Schwinger equations.* J.Phys.G, G32:R253–R291, 2006.

[20] Alkofer, Reinhard, Christian S. Fischer, Felipe J. Llanes-Estrada, and Kai Schwenzer: *The quark-gluon vertex in Landau gauge QCD: Its role in dynamical chiral symmetry breaking and quark confinement.* Annals Phys., 324:106–172, 2009.

[21] Bashir, Adnan, Lei Chang, Ian C. Cloet, Bruno El-Bennich, Yu Xin Liu, *et al.*: *Collective perspective on advances in Dyson-Schwinger Equation QCD.* Commun.Theor.Phys., 58:79–134, 2012.

[22] Sanchis-Alepuz, Helios and Richard Williams: *Recent developments in bound-state calculations using the Dyson-Schwinger and Bethe-Salpeter equations.* 2017.

[23] Roberts, Craig D.: *Three Lectures on Hadron Physics.* J. Phys. Conf. Ser., 706(2):022003, 2016.

[24] Williams, Richard, Christian S. Fischer, and Walter Heupel: *Light mesons in QCD and unquenching effects from the 3PI effective action.* Phys. Rev., D93(3):034026, 2016.

[25] Sanchis-Alepuz, Helios and Richard Williams: *Hadronic Observables from Dyson-Schwinger and Bethe-Salpeter equations.* J. Phys. Conf. Ser., 631(1):012064, 2015.

[26] Eichmann, Gernot, Helios Sanchis-Alepuz, Richard Williams, Reinhard Alkofer, and Christian S. Fischer: *Baryons as relativistic three-quark bound states.* Prog. Part. Nucl. Phys., 91:1–100, 2016.

[27] Wetterich, Christof: *Exact evolution equation for the effective potential.* Phys.Lett., B301:90–94, 1993.

[28] Gies, Holger: *Introduction to the functional RG and applications to gauge theories.* Lect.Notes Phys., 852:287–348, 2012.

[29] Pawlowski, Jan M.: *Aspects of the functional renormalisation group.* Annals Phys., 322:2831–2915, 2007.

[30] Braun, Jens: *Fermion Interactions and Universal Behavior in Strongly Interacting Theories.* J.Phys., G39:033001, 2012.

[31] Maris, Pieter, Craig D. Roberts, and Peter C. Tandy: *Pion mass and decay constant.* Phys.Lett., B420:267–273, 1998.

[32] Maris, Pieter and Craig D. Roberts: *pi and K meson Bethe-Salpeter amplitudes.* Phys. Rev., C56:3369–3383, 1997.

[33] Sauli, Vladimir: *Solving the BSE with an Integral Representation in Minkowski Space.* Few Body Syst., 49(1-4):223–231, 2010.

[34] Sauli, V.: *Pions and excited scalars in Minkowski space DSBSE formalism.* Int. J. Theor. Phys., 54(11):4131–4141, 2015.

[35] Hobbs, T. J., Mary Alberg, and Gerald A. Miller: *Euclidean bridge to the relativistic constituent quark model.* Phys. Rev., C95(3):035205, 2017.

[36] Gigante, V., J. H. Alvarenga Nogueira, E. Ydrefors, and C. Gutierrez: *Study of the homogeneous Bethe-Salpeter equation in the 2+1 Minkowski space.* Int. J. Mod. Phys. Conf. Ser., 45:1760055, 2017.

[37] Paula, W. de, T. Frederico, G. Salmè, and Michele Viviani: *Numerical studies of the Bethe–Salpeter equation for a two-fermion bound state.* J. Phys. Conf. Ser., 981(1):012020, 2018.

[38] Williams, Richard: *Vector mesons as dynamical resonances in the Bethe–Salpeter framework.* Phys. Lett., B798:134943, 2019.

[39] Frederico, Tobias, Dyana C. Duarte, Wayne de Paula, Emanuel Ydrefors, Shaoyang Jia, and Pieter Maris: *Towards Minkowski space solutions of Dyson-Schwinger Equations through un-Wick rotation.* 2019.

[40] Floerchinger, Stefan: *Analytic Continuation of Functional Renormalization Group Equations.* JHEP, 1205:021, 2012.

[41] Pawlowski, Jan M. and Nils Strodthoff: *Real time correlation functions and the functional renormalization group.* Phys. Rev., D92(9):094009, 2015.

[42] Strodthoff, Nils: *Self-consistent spectral functions in the O(N) model from the functional renormalization group.* Phys. Rev., D95(7):076002, 2017.

[43] Pawlowski, Jan M., Nils Strodthoff, and Nicolas Wink: *Finite temperature spectral functions in the O(N)-model.* Phys. Rev., D98(7):074008, 2018.

[44] Kamikado, Kazuhiko, Nils Strodthoff, Lorenz von Smekal, and Jochen Wambach: *Real-Time Correlation Functions in the O(N) Model from the Functional Renormalization Group.* Eur.Phys.J., C74:2806, 2014.

[45] Tripolt, Ralf Arno, Nils Strodthoff, Lorenz von Smekal, and Jochen Wambach: *Spectral Functions for the Quark-Meson Model Phase Diagram from the Functional Renormalization Group.* Phys.Rev., D89:034010, 2014.

[46] Tripolt, Ralf Arno, Lorenz von Smekal, and Jochen Wambach: *Flow equations for spectral functions at finite external momenta.* Phys.Rev., D90(7):074031, 2014.

[47] Jung, Christopher, Fabian Rennecke, Ralf Arno Tripolt, Lorenz von Smekal, and Jochen Wambach: *In-Medium Spectral Functions of Vector- and Axial-Vector Mesons from the Functional Renormalization Group.* Phys. Rev., D95(3):036020, 2017.

[48] Yokota, Takeru, Teiji Kunihiro, and Kenji Morita: *Functional renormalization group analysis of the soft mode at the QCD critical point.* PTEP, 2016(7):073D01, 2016.

[49] Wang, Ziyue and Pengfei Zhuang: *Meson spectral functions at finite temperature and isospin density with the functional renormalization group.* Phys. Rev., D96(1):014006, 2017.

[50] Yokota, Takeru, Teiji Kunihiro, and Kenji Morita: *Tachyonic instability of the scalar mode prior to the QCD critical point based on the functional renormalization-group method in the two-flavor case.* Phys. Rev., D96(7):074028, 2017.

[51] Bluhm, M., Y. Jiang, M. Nahrgang, J. M. Pawlowski, F. Rennecke, and N. Wink: *Time-evolution of fluctuations as signal of the phase transition dynamics in a QCD-assisted transport approach.* In *27th International Conference on Ultrarelativistic Nucleus-Nucleus Collisions (Quark Matter 2018) Venice, Italy, May 14-19, 2018*, 2018.

[52] Gies, Holger and Christof Wetterich: *Renormalization flow of bound states.* Phys.Rev., D65:065001, 2002.

[53] Floerchinger, S. and C. Wetterich: *Exact flow equation for composite operators.* Phys.Lett., B680:371–376, 2009.

[54] Floerchinger, S.: *Exact Flow Equation for Bound States.* Eur. Phys. J., C69:119–132, 2010.

[55] Wilson, Kenneth G.: *Renormalization group and critical phenomena. 1. Renormalization group and the Kadanoff scaling picture.* Phys.Rev., B4:3174–3183, 1971.

[56] Wilson, Kenneth G.: *Renormalization group and critical phenomena. 2. Phase space cell analysis of critical behavior.* Phys.Rev., B4:3184–3205, 1971.

[57] Wilson, K.G. and J. B. Kogut: *The Renormalization group and the epsilon expansion.* Phys.Rept., 12:75–200, 1974.

[58] Binney, J. J., N. J. Dowrick, A. J. Fisher, and M. E. J. Newman: *The Theory of critical phenomena: An Introduction to the renormalization group.* 1992.

[59] Collins, John C.: *Renormalization. An Introduction to Renormalization, The Renormalization Group, and the Operator Product Expansion*, volume 26 of *Cambridge Monographs on Mathematical Physics.* Cambridge University Press, Cambridge, 1986, ISBN 9780521311779, 9780511867392. `http://www-spires.fnal.gov/spires/find/books/www?cl=QC174.17.R46C65::1985`.

[60] Zinn-Justin, Jean: *Quantum field theory and critical phenomena.* Int. Ser. Monogr. Phys., 4. edition, 2002.

[61] Delamotte, Bertrand: *A Hint of renormalization.* Am. J. Phys., 72:170, 2004.

[62] Hollowood, T. J.: *Renormalization Groups and Fixed Points in Quantum Field Theory.* Springer-Verlag, 2013.

[63] Fischer, Christian S.: *Non-perturbative propagators, running coupling and dynamical mass generation in ghost - antighost symmetric gauges in QCD.* PhD thesis, Tübingen University, 2003.

[64] Abbott, B. P. *et al.*: *GW150914: The Advanced LIGO Detectors in the Era of First Discoveries.* Phys. Rev. Lett., 116(13):131103, 2016.

[65] Abbott, B. P. *et al.*: *Astrophysical Implications of the Binary Black-Hole Merger GW150914.* Astrophys. J., 818(2):L22, 2016.

[66] Acernese, F. *et al.*: *Advanced Virgo: a second-generation interferometric gravitational wave detector.* Class. Quant. Grav., 32(2):024001, 2015.

[67] J. Hough, B. J. Meers, G. P. Newton N. A. Robertson H. Ward *et al.*: *Proposal for a Joint German-British interferometric gravitational wave detector.* 1989.

[68] Aso, Yoichi, Yuta Michimura, Kentaro Somiya, Masaki Ando, Osamu Miyakawa, Takanori Sekiguchi, Daisuke Tatsumi, and Hiroaki Yamamoto: *Interferometer design of the KAGRA gravitational wave detector.* Phys. Rev., D88(4):043007, 2013.

[69] Iyer, B. *et al.*: *LIGO-INDIA: proposal for an interferometric gravitational-wave observatory.* LIGO Public documents, 2011.

[70] Sathyaprakash, B. S. and B. F. Schutz: *Physics, Astrophysics and Cosmology with Gravitational Waves.* Living Rev. Rel., 12:2, 2009.

[71] Baubock, Michi, Dimitrios Psaltis, and Feryal Ozel: *Effects of Spot Size on Neutron-Star Radius Measurements from Pulse Profiles.* Astrophys. J., 811(2):144, 2015.

[72] Bogdanov, Slavko, Jonathan E. Grindlay, and George B. Rybicki: *Thermal X-rays from Millisecond Pulsars: Constraining the Fundamental Properties of Neutron Stars.* Astrophys. J., 689:407, 2008.

[73] Watts, Anna L. *et al.*: *Colloquium : Measuring the neutron star equation of state using x-ray timing*. Rev. Mod. Phys., 88(2):021001, 2016.

[74] Hirata, K. *et al.*: *Observation of a Neutrino Burst from the Supernova SN 1987a*. Phys. Rev. Lett., 58:1490–1493, 1987. [,727(1987)].

[75] Bionta, R. M. *et al.*: *Observation of a Neutrino Burst in Coincidence with Supernova SN 1987a in the Large Magellanic Cloud*. Phys. Rev. Lett., 58:1494, 1987.

[76] Shapiro, S. L. and S. A. Teukolsky: *Black holes, white dwarfs, and neutron stars: The physics of compact objects*. 1983, ISBN 9780471873167.

[77] Haensel, P., A. Y. Potekhin, and D. G. Yakovlev: *Neutron stars 1: Equation of state and structure*. Astrophys. Space Sci. Libr., 326:pp.1–619, 2007.

[78] Baym, Gordon, Tetsuo Hatsuda, Toru Kojo, Philip D Powell, Yifan Song, and Tatsuyuki Takatsuka: *From hadrons to quarks in neutron stars: a review*. Rep. Prog. Phys., 81:056902, 2018.

[79] Baym, G. and C. Pethick: *Neutron Stars*. Ann. Rev. Nucl. Part. Sci., 25:27–77, 1975.

[80] Baym, G. and C. Pethick: *Physics of Neutron Stars*. Ann. Rev. Astron. Astrophys., 17:415–443, 1979.

[81] Hell, Thomas and Wolfram Weise: *Dense baryonic matter: constraints from recent neutron star observations*. Phys. Rev., C90(4):045801, 2014.

[82] Lattimer, James M.: *The nuclear equation of state and neutron star masses*. Ann. Rev. Nucl. Part. Sci., 62:485–515, 2012.

[83] Gil-Botella, Inés: *Detection of Supernova Neutrinos*. In *NuPhys2015: Prospects in Neutrino Physics (NuPhys) London, UK, December 16-18, 2015*, 2016. `https://inspirehep.net/record/1456749/files/arXiv:1605.02204.pdf`.

[84] Mirizzi, Alessandro, Irene Tamborra, Hans Thomas Janka, Ninetta Saviano, Kate Scholberg, Robert Bollig, Lorenz Hudepohl, and Sovan Chakraborty: *Supernova Neutrinos: Production, Oscillations and Detection*. Riv. Nuovo Cim., 39(1-2):1–112, 2016.

[85] Tamborra, Irene: *Supernova Neutrinos: Theory*. In *Proceedings, Prospects in Neutrino Physics (NuPhys2015): London, UK, December 16-18, 2015*, 2016.

[86] Abbott, B. P. *et al.*: *Multi-messenger Observations of a Binary Neutron Star Merger*. Astrophys. J., 848(2):L12, 2017.

[87] Bhat, Sajad A. and Debades Bandyopadhyay: *Neutron star equation of state and GW170817*. J. Phys., G46(1):014003, 2019.

[88] Baker, T., E. Bellini, P. G. Ferreira, M. Lagos, J. Noller, and I. Sawicki: *Strong constraints on cosmological gravity from GW170817 and GRB 170817A*. Phys. Rev. Lett., 119(25):251301, 2017.

[89] Carson, Zack, Andrew W. Steiner, and Kent Yagi: *Constraining nuclear matter parameters with GW170817*. Phys. Rev., D99(4):043010, 2019.

[90] Hayato, Y. *et al.*: *Search for Neutrinos in Super-Kamiokande Associated with the GW170817 Neutron-star Merger.* Astrophys. J., 857(1):L4, 2018.

[91] Yamamoto, Naoki: *Chiral transport of neutrinos in supernovae: Neutrino-induced fluid helicity and helical plasma instability.* Phys. Rev., D93(6):065017, 2016.

[92] Yamamoto, Naoki: *Scaling laws in chiral hydrodynamic turbulence.* Phys. Rev., D93(12):125016, 2016.

[93] Sen, Srimoyee and Naoki Yamamoto: *Chiral Shock Waves.* Phys. Rev. Lett., 118(18):181601, 2017.

[94] Yamamoto, Naoki: *Chiral transport of neutrinos in supernovae.* EPJ Web Conf., 137:09013, 2017.

[95] Masada, Youhei, Kei Kotake, Tomoya Takiwaki, and Naoki Yamamoto: *Chiral magneto-hydrodynamic turbulence in core-collapse supernovae.* Phys. Rev., D98(8):083018, 2018.

[96] Griffiths, David: *Introduction to elementary particles.* Physics textbook. Wiley-VCH Verlag, 2008.

[97] Peskin, Michael Edward and Daniel V. Schroeder: *An Introduction to quantum field theory.* Addison-Wesley, Reading, 1995.

[98] Greiner, W. and J. Reinhardt: *Field quantization.* Springer-Verlag Berlin Heidelberg New York, 1996.

[99] Weinberg, Steven: *The Quantum theory of fields. Vol. 1: Foundations.* Cambridge University Press, Cambridge, 1995. Cambridge, UK: Univ. Pr. (1995) 609 p.

[100] Weinberg, Steven: *The quantum theory of fields. Vol. 2: Modern applications.* Cambridge University Press, Cambridge, 1996. Cambridge, UK: Univ. Pr. (1996) 489 p.

[101] Mandl, F. and Graham Shaw: *Quantum Field Theory.* Wiley Verlag, 2. edition, 2010.

[102] Zinn-Justin, Jean: *Path Integrals in Quantum Mechanics.* Oxford University Press, 2005.

[103] Bohm, M., Ansgar Denner, and H. Joos: *Gauge theories of the strong and electroweak interaction.* Teubner, Stuttgart, 2001. Stuttgart, Germany: Teubner (2001) 784 p.

[104] Greiner, W. and B. Müller: *Gauge Theory of Weak Interaction.* Springer-Verlag, 4. edition, 2009.

[105] Greiner, W. und Reinhardt, J.: *Quantum Electrodynamics.* Springer-Verlag, 4th edition, 2009.

[106] Scheck, Florian: *Electroweak and Strong Interactions.* Springer-Verlag, 2012.

[107] Kugo, Taichiro: *Eichtheorie.* Springer-Verlag Berlin Heidelberg, 1997.

[108] Yndurain, Francisco J.: *The Theory of Quark and Gluon Interactions.* Theoretical and Mathematical Physics. Springer, Berlin, Germany, 2006, ISBN 9783540332091, 9783540332107.

[109] W. Greiner, S. Schremm und E. Stein: *Quantum Chromodynamics.* Springer-Verlag, 3. edition, 2007.

[110] Cheng, T.P. and L.F. Li: *Gauge theory of elementary particle physics.* Osford University Press, 1984.

[111] Pennington, M. R.: *Swimming with quarks.* J. Phys. Conf. Ser., 18:1–73, 2005.

[112] Kühnel, W.: *Matrizen und Lie-Gruppen.* ViewegTeubner Verlag, 1st edition, 2011.

[113] Iachello, F.: *Lie-Algebras and Applications.* Springer-Verlag, 2006.

[114] Böhm, M.: *Lie-Gruppen und Lie-Algebren in der Physik.* Springer-Verlag, 2011.

[115] Faddeev, L.D. and V.N. Popov: *Feynman Diagrams for the Yang-Mills Field.* Phys.Lett., B25:29–30, 1967.

[116] Gribov, V. N.: *Quantization of non-Abelian gauge theories.* Nucl. Phys., B139:1, 1978.

[117] Singer, I. M.: *Some Remarks on the Gribov Ambiguity.* Commun. Math. Phys., 60:7–12, 1978.

[118] Greensite, J.: *Faddeev-Popov spectra at the Gribov horizon.* Phys. Rev., D81:114011, 2010.

[119] Huber, Markus Q., Reinhard Alkofer, and Silvio P. Sorella: *Infrared analysis of Dyson-Schwinger equations taking into account the Gribov horizon in Landau gauge.* Phys. Rev., D81:065003, 2010.

[120] Zwanziger, Daniel: *An improved model of color confinement.* 2011. Gribov-Zwanziger scenario.

[121] Dudal, D., S.P. Sorella, and N. Vandersickel: *The dynamical origin of the refinement of the Gribov-Zwanziger theory.* Phys.Rev., D84:065039, 2011.

[122] Vandersickel, N. and Daniel Zwanziger: *The Gribov problem and QCD dynamics.* 2012.

[123] Dudal, David and Silvio Paolo Sorella: *The Gribov horizon and spontaneous BRST symmetry breaking.* Phys.Rev., D86:045005, 2012.

[124] Maas, Axel: *More on the properties of the first Gribov region in Landau gauge.* Phys. Rev., D93(5):054504, 2016.

[125] Maas, Axel: *Dependence of the propagators on the sampling of Gribov copies inside the first Gribov region of Landau gauge.* 2017.

[126] Huber, Markus Q.: *Nonperturbative properties of Yang-Mills theories.* habilitation, Graz U., 2018.

[127] Gross, David J. and Frank Wilczek: *Ultraviolet Behavior of Nonabelian Gauge Theories.* Phys. Rev. Lett., 30:1343–1346, 1973.

[128] Politzer, H. David: *Reliable Perturbative Results for Strong Interactions?* Phys. Rev. Lett., 30:1346–1349, 1973.

[129] Weinberg, Steven: *A Model of Leptons.* Phys. Rev. Lett., 19:1264–1266, 1967.

[130] Salam, Abdus: *Weak and Electromagnetic Interactions.* Conf. Proc., C680519:367–377, 1968.

[131] Greensite, Jeff: *An introduction to the confinement problem.* Lect. Notes Phys., 821:1–211, 2011.

[132] Koch, Volker: *Aspects of chiral symmetry.* Int.J.Mod.Phys., E6:203–250, 1997.

[133] Noether, Emmy: *Invariant Variation Problems.* Gott. Nachr., 1918:235–257, 1918. [Transp. Theory Statist. Phys.1,186(1971)].

[134] Matthews, P. T. and Abdus Salam: *Relativistic field theory of unstable particles.* Phys. Rev., 112:283–287, 1958.

[135] Eden, R. J., P. V. Landshoff, D. I. Olive, and J. C. Polkinghorne: *The analytic S-matrix.* Cambridge University Press, 1966.

[136] Nussenzveig, H. M.: *Causality and Dispersion Relations*, volume 95. Academic Press, 1972.

[137] Fonda, L., G. C. Ghirardi, and A. Rimini: *Decay Theory of Unstable Quantum Systems.* Rept. Prog. Phys., 41:587–631, 1978.

[138] Gunson, J. and J. G. Taylor: *Unstable particles in general field theory.* In *Proceedings, 10th International Conference on High-Energy Physics (ICHEP 60): Rochester, NY, USA, 25 Aug - 1 Sep 1960*, pages 245–246, 1960.

[139] Pelaez, J. R.: *From controversy to precision on the sigma meson: a review on the status of the non-ordinary* $f_0(500)$ *resonance.* Phys. Rept., 658:1, 2016.

[140] Salpeter, E. E.: *Wave Functions in Momentum Space.* Phys. Rev., 84:1226–1231, 1951.

[141] Salpeter, E.E. and H.A. Bethe: *A Relativistic equation for bound state problems.* Phys.Rev., 84:1232–1242, 1951.

[142] LePage, W. R.: *Complex Variables and the Laplace Transform for Engineers.* Dover Publications, 1980.

[143] Forster, O.: *Lectures on Riemann Surfaces.* Springer Verlag, 1984.

[144] Nearing, J.: *Mathematical Tools for Physics.* Dover Publications, http://www.physics.miami.edu/ nearing/mathmethods/, 2010.

[145] Mandelstam, S.: *Determination of the pion - nucleon scattering amplitude from dispersion relations and unitarity. General theory.* Phys. Rev., 112:1344–1360, 1958.

[146] Mandelstam, Stanley: *Analytic properties of transition amplitudes in perturbation theory.* Phys. Rev., 115:1741–1751, 1959.

[147] Blankenbecler, R.: *Unphysical Riemann sheets.* In *Proceedings, 10th International Conference on High-Energy Physics (ICHEP 60): Rochester, NY, USA, 25 Aug - 1 Sep 1960*, pages 247–254, 1960.

[148] Grama, C., N. Grama, and I. Zamfirescu: *Riemann surface approach to bound and resonant states: Exotic resonant states for a central rectangular potential.* Phys. Rev. A, 61:032716, 2000.

[149] Passarino, Giampiero, Christian Sturm, and Sandro Uccirati: *Higgs Pseudo-Observables, Second Riemann Sheet and All That.* Nucl. Phys., B834:77–115, 2010.

[150] Wolkanowski, Thomas: *Resonances and poles in the second Riemann sheet.* Master's thesis, Frankfurt U., 2013.

[151] Schlessinger, L.: *Use of Analyticity in the Calculation of Nonrelativistic Scattering Amplitudes.* Phys. Rev., 167(5):1411–1423, 1968.

[152] Tripolt, Ralf Arno, Philipp Gubler, Maksim Ulybyshev, and Lorenz von Smekal: *Numerical analytic continuation of Euclidean data.* 2018.

[153] Alkofer, Reinhard, W. Detmold, C. S. Fischer, and P. Maris: *Analytic properties of the Landau gauge gluon and quark propagators.* Phys. Rev., D70:014014, 2004.

[154] Maas, Axel: *Describing gauge bosons at zero and finite temperature.* Phys.Rept., 524:203–300, 2013.

[155] Dyson, F. J.: *The S matrix in quantum electrodynamics.* Phys. Rev., 75:1736–1755, 1949.

[156] Schwinger, Julian S.: *Gauge Invariance and Mass.* Phys. Rev., 125:397–398, 1962.

[157] Schwinger, Julian S.: *Gauge Invariance and Mass. 2.* Phys. Rev., 128:2425–2429, 1962.

[158] Maas, Axel: *Solving a set of truncated Dyson-Schwinger equations with a globally converging method.* Comput.Phys.Commun., 175:167–179, 2006.

[159] Roberts, Craig D. and Anthony G. Williams: *Dyson-Schwinger equations and their application to hadronic physics.* Prog.Part.Nucl.Phys., 33:477–575, 1994.

[160] Fischer, Christian S.: *Infrared properties of QCD from Dyson-Schwinger equations.* J. Phys., G32:R253–R291, 2006.

[161] Huber, Markus Q. and Lorenz von Smekal: *Spurious divergences in Dyson-Schwinger equations.* JHEP, 06:015, 2014.

[162] Haag, R.: *Local quantum physics: Fields, particles, algebras.* Springer, Berlin, 1992. Berlin, Germany: Springer (1992) 356 p. (Texts and monographs in physics).

[163] Berges, Juergen, Nikolaos Tetradis, and Christof Wetterich: *Non-perturbative renormalization flow in quantum field theory and statistical physics.* Phys. Rept., 363:223–386, 2002.

[164] Schaefer, Bernd Jochen and Jochen Wambach: *Renormalization group approach towards the QCD phase diagram.* Phys.Part.Nucl., 39:1025–1032, 2008.

[165] Gies, Holger and Christof Wetterich: *Universality of spontaneous chiral symmetry breaking in gauge theories.* Phys.Rev., D69:025001, 2004.

[166] Braun, Jens, Leonard Fister, Jan M. Pawlowski, and Fabian Rennecke: *From Quarks and Gluons to Hadrons: Chiral Symmetry Breaking in Dynamical QCD.* Phys. Rev., D94(3):034016, 2016.

[167] Mitter, Mario, Jan M. Pawlowski, and Nils Strodthoff: *Chiral symmetry breaking in continuum QCD.* Phys.Rev., D91:054035, 2015.

[168] Cyrol, Anton K., Mario Mitter, Jan M. Pawlowski, and Nils Strodthoff: *Nonperturbative quark, gluon, and meson correlators of unquenched QCD.* Phys. Rev., D97(5):054006, 2018.

[169] Cyrol, Anton K., Leonard Fister, Mario Mitter, Jan M. Pawlowski, and Nils Strodthoff: *Landau gauge Yang-Mills correlation functions.* Phys. Rev., D94(5):054005, 2016.

[170] Cyrol, Anton K., Mario Mitter, Jan M. Pawlowski, and Nils Strodthoff: *Nonperturbative finite-temperature Yang-Mills theory.* Phys. Rev., D97(5):054015, 2018.

[171] Huber, Markus Q. and Jens Braun: *Algorithmic derivation of functional renormalization group equations and Dyson-Schwinger equations.* Comput.Phys.Commun., 183:1290–1320, 2012.

[172] Huber, Markus Q., Anton K. Cyrol, and Jan M. Pawlowski: *DoFun 3.0: Functional equations in Mathematica.* 2019.

[173] Cyrol, Anton K., Mario Mitter, and Nils Strodthoff: *FormTracer - A Mathematica Tracing Package Using FORM.* Comput. Phys. Commun., C219:346–352, 2017.

[174] Hopfer, Markus, Andreas Windisch, and Reinhard Alkofer: *The Quark-Gluon Vertex in Landau gauge QCD.* PoS, ConfinementX:073, 2012.

[175] Windisch, Andreas, Markus Hopfer, and Reinhard Alkofer: *Towards a self-consistent solution of the Landau gauge quark-gluon vertex Dyson-Schwinger equation.* Acta Phys.Polon.Supp., 6:347–352, 2013.

[176] Williams, Richard: *The quark-gluon vertex in Landau gauge bound-state studies.* Eur. Phys. J., A51(5):57, 2015.

[177] Blum, Adrian L., Reinhard Alkofer, Markus Q. Huber, and Andreas Windisch: *Three-point vertex functions in Yang-Mills Theory and QCD in Landau gauge.* EPJ Web Conf., 137:03001, 2017.

[178] Oliveira, Orlando, Ayse Kizilersu, Paulo J. Silva, Jon Ivar Skullerud, Andre Sternbeck, and Anthony G. Williams: *Lattice Landau gauge quark propagator and the quark-gluon vertex.* In *Excited QCD 2016 Costa da Caparica, Portugal, March 6-12, 2016*, 2016. `http://inspirehep.net/record/1466442/files/arXiv:1605.09632.pdf`.

[179] Maris, Pieter and Peter C. Tandy: *Bethe-Salpeter study of vector meson masses and decay constants.* Phys. Rev., C60:055214, 1999.

[180] Goecke, Tobias, Christian S. Fischer, and Richard Williams: *Leading-order calculation of hadronic contributions to the muon $g-2$ using the Dyson-Schwinger approach.* Phys. Lett., B704:211–217, 2011.

[181] Sanchis-Alepuz, Hèlios, Christian S. Fischer, and Stanislav Kubrak: *Pion cloud effects on baryon masses.* Phys. Lett., B733:151–157, 2014.

[182] Hilger, T., M. Gomez-Rocha, and A. Krassnigg: *Light-quarkonium spectra and orbital-angluar-momentum decomposition in a Bethe-Salpeter-equation approach.* 2015.

[183] Hilger, T., M. Gómez-Rocha, A. Krassnigg, and W. Lucha: *Aspects of open-flavour mesons in a comprehensive DSBSE study.* Eur. Phys. J., A53(10):213, 2017.

[184] Chen, Chen, Bruno El-Bennich, Craig D. Roberts, Sebastian M. Schmidt, Jorge Segovia, and Shaolong Wan: *Structure of the nucleon's low-lying excitations.* Phys. Rev., D97(3):034016, 2018.

[185] Serna, Fernando E., Bruno El-Bennich, and Gastao Krein: *Charmed mesons with a symmetry-preserving contact interaction.* Phys. Rev., D96(1):014013, 2017.

[186] Carbonell, J., T. Frederico, and V. A. Karmanov: *Bound state equation for the Nakanishi weight function.* Phys. Lett., B769:418–423, 2017.

[187] Stadler, Alfred, Sofia Leitao, M. T. Pena, and Elmar P. Biernat: *Heavy and heavy-light mesons in the Covariant Spectator Theory.* Few Body Syst., 59(3):32, 2018.

[188] Castro, A., E. Ydrefors, W. De Paula, T. Frederico, J. H. De Alvarenga Nogueira, and P. Maris: *The Bethe-Salpeter approach to bound states: from Euclidean to Minkowski space.* J. Phys. Conf. Ser., 1291(1):012006, 2019.

[189] Fischer, Christian S. and Richard Williams: *Beyond the rainbow: effects from pion back-coupling.* Phys. Rev., D78:074006, 2008.

[190] Williams, Richard: *Bethe-Salpeter studies of mesons beyond rainbow-ladder.* 2009. Bethe-Salpeter mesons.

[191] Williams, Richard and Christian S. Fischer: *Bethe-Salpeter equations: mesons beyond the rainbow-ladder truncation.* 2009. Bethe-Salpeter mesons.

[192] Mian, Walid Ahmed and Axel Maas: *Quark Propagator with electroweak interactions in the Dyson-Schwinger approach.* EPJ Web Conf., 137:05015, 2017.

[193] Maas, Axel and Walid Ahmed Mian: *Influence of broken flavor and C and P symmetry on the quark propagator.* Eur. Phys. J., A53(2):22, 2017.

[194] Olive, K.A. *et al.*: *Review of Particle Physics.* Chin.Phys., C38:090001, 2014.

[195] Maas, Axel, Jochen Wambach, Burghard Gruter, and Reinhard Alkofer: *High-temperature limit of Landau-gauge Yang-Mills theory.* Eur.Phys.J., C37:335–357, 2004.

[196] Maas, Axel: *The high-temperature phase of Yang-Mills theory in Landau gauge.* 2005.

[197] Mian, Walid Ahmed, Axel Maas, Mario Mitter, Jan Martin Pawlowski, Helios Sanchis-Alepuz, and Nicolas Wink: *Formulating electroweak pion decays in functional methods.* PoS, Hadron2017:234, 2018.

[198] Blank, M. and A. Krassnigg: *Matrix algorithms for solving (in)homogeneous bound state equations.* 2010. Bethe-Salpeter; numerics.

[199] Weil, Esther, Gernot Eichmann, Christian S. Fischer, and Richard Williams: *Electromagnetic decays of the neutral pion investigated in the Dyson-Schwinger formalism.* J. Phys. Conf. Ser., 1024(1):012032, 2018.

[200] Weil, Esther, Gernot Eichmann, Christian S. Fischer, and Richard Williams: *Electromagnetic decays of the neutral pion.* Phys. Rev., D96(1):014021, 2017.

[201] Llewellyn-Smith, C. H.: *A relativistic formulation for the quark model for mesons.* Ann. Phys., 53:521–558, 1969.

[202] Ellwanger, Ulrich: *FLow equations for N point functions and bound states.* Z. Phys., C62:503–510, 1994. [,206(1993)].

[203] Ellwanger, U. and C. Wetterich: *Evolution equations for the quark - meson transition.* Nucl.Phys., B423:137–170, 1994.

[204] Jakovác, Antal and András Patkós: *Bound states in Functional Renormalization Group.* Int. J. Mod. Phys., A34(27):1950154, 2019.

[205] Jakovác, A. and A. Patkós: *Interacting two-particle states in the symmetric phase of the chiral Nambu-Jona-Lasinio model.* 2019.

[206] Paris-Lopez, J., R. Alkofer, A. Maas, W. Mian, M. Mitter, J. Pawlowski, and H. Sanchis-Alepuz: *Calculating hadron properties from dynamical hadronization in the Functional Renormalisation Group.* Journal of Physics: Conference Series, 1024:012009, may 2018. https://doi.org/10.1088%2F1742-6596%2F1024%2F1%2F012009.

[207] Alkofer, Reinhard, Axel Maas, Walid Ahmed Mian, Mario Mitter, Jordi Paris-Lopez, Jan M. Pawlowski, and Nicolas Wink: *Bound state properties from the functional renormalization group.* Phys. Rev., D99(5):054029, 2019.

[208] Pawlowski, Jan M. and Fabian Rennecke: *Higher order quark-mesonic scattering processes and the phase structure of QCD.* Phys. Rev., D90(7):076002, 2014.

[209] Rennecke, Fabian and Bernd Jochen Schaefer: *Fluctuation-induced modifications of the phase structure in (2+1)-flavor QCD.* 2016.

[210] Rennecke, Fabian: *The Chiral Phase Transition of QCD.* PhD thesis, Heidelberg U., 2015.

[211] Markó, Gergely, Urko Reinosa, and Zsolt Szép: *Loss of solution in the symmetry improved ϕ-derivable expansion scheme.* Nucl. Phys., B913:405–424, 2016.

[212] Helmboldt, Alexander J., Jan M. Pawlowski, and Nils Strodthoff: *Towards quantitative precision in the chiral crossover: masses and fluctuation scales.* Phys.Rev., D91(5):054010, 2015.

[213] Braun, Jens, Marc Leonhardt, and Jan M. Pawlowski: *Renormalization group consistency and low-energy effective theories.* 2018.

[214] Kugo, Taichiro and Izumi Ojima: *Local Covariant Operator Formalism of Nonabelian Gauge Theories and Quark Confinement Problem.* Prog. Theor. Phys. Suppl., 66:1, 1979.

[215] Osterwalder, Konrad and Robert Schrader: *Axioms for Euclidean Green's Functions. 2.* Commun. Math. Phys., 42:281, 1975.

[216] Mack, G.: *Osterwalder-Schrader Positivity in Conformal Invariant Quantum Field Theory.* Lect. Notes Phys., 37:66–91, 1975.

[217] Glimm, J. and Arthur M. Jaffe: *Quantum Physics. A Functional Integral Point Of View*. 1987.